Structure and properties of zinc 1,3-bdc metal-organic frameworks

Emily G. Meekel

Balliol College, Oxford



A thesis submitted to the University of Oxford for the degree of Doctor of Philosophy

Inorganic Chemistry Laboratory

University of Oxford

Trinity 2023

The work presented in this thesis was carried out between October 2019 and June 2023 in the Inorganic Chemistry Laboratory, University of Oxford under the supervision of Prof. Andrew L. Goodwin. All of the work is my own unless otherwise stated, and has not been submitted previously for any degree at this or any other university.

Emily Gabrielle Meekel

June 2023

Summary

Complexity in material design is widely recognised as a means of introducing unique properties that may be beneficial for various applications. The project described in this thesis aims to explore the efficiency of introducing such complexity into materials through the incorporation of low-symmetry components. Due to their ability of offering control over the geometry of building blocks, metal-organic frameworks (MOFs) were selected as the platform for this exploration.

The presented results revolve around the structures and chemical/physical properties of five crystalline MOFs obtained by combining zinc with the low-symmetry bent linker 1,3-benzene dicarboxylic acid (1,3-bdc): TRUMOF-1, MOX-2, MOX-3, MOX-4, and MOX-5. As highlighted in Chapter 3, these structures exhibit significant disparity in their topologies, with that of TRUMOF-1 being particularly intriguing due to its aperiodic nature.

The true structure of TRUMOF-1, as described in Chapter 7, was characterised using a Truchet-tile analogy. Its maze-like pore network was found to adsorb different types of gases and, more interestingly, enhance its elastic stability through the internal reorganisation of different local motifs. Being the first topologically aperiodic material to be reported, TRUMOF-1 likely possesses many other interesting properties with the potential for various applications, including error-correcting memory storage.

Our findings ultimately confirm the efficacy of incorporating low-symmetry components in obtaining complex materials. The role of 1,3-bdc in introducing this complexity, both through its bent shape and the flexibility of the carboxylate torsion angles, is discussed in Chapter 8.

Yet, there is still a need for a systematic approach to purposely synthesise complex structures such as TRUMOF-1. The difficulty in finding suitable synthetic parameters, together with the ultimate goal of controlling the complexity, are important aspects to focus on in future research.

Acknowledgements

Throughout my DPhil project, I have had the privilege to work with, and receive support from a wide range of individuals, for which I am extremely grateful. I would like to begin by expressing my gratitude to my supervisor, Andrew Goodwin, for giving me the opportunity to be part of such a fantastic project and allowing me the freedom to make it my own. His brilliance and enthusiasm for science, paired with humility, never ceases to amaze me. I am truly fortunate to have had such an exceptional supervisor, and I could not have asked for a better mentor.

I would also like to thank my examiners, Jin-Chong Tan and Monique van der Veen, for reading my thesis, their invaluable discussions and thoughtful suggestions, which have contributed to the quality of this work.

My DPhil experience would not have been the same without the continuous support from the Goodwin group, be it through science or friendship. I want to extend special mentions to Arianna and Ella S. for their invaluable guidance, introducing me to the experimental and computational aspects of crystallography, and for showing me how to be a confident woman in academia. I would also like to express my gratitude to Johny for his companionship throughout this journey, his exceptional ability to think outside the box, and his continuous words of encouragement. And to Tom, I am truly indebted for his talent in helping me articulate my scattered thoughts, and for always pushing me beyond my limits (including conquering the summit of Ben Nevis). I would also like to acknowledge Quentin for his reliable presence in not bringing lunch, which inadvertently exposed me to various lunch venues in Oxford, adding delightful culinary adventures to my DPhil experience. Last but not least, I extend my thanks to Emma, John, Elodie, Nikolaj, Harry, Xiao, and Phil for their support, assistance, and friendship throughout my DPhil journey.

The help I received during my DPhil project extends beyond the Goodwin group. I would first like to thank Simon for his assistance with collection of diffraction data both in-house and at the I11 beamline, as well as Amber, who introduced me to the practical aspects of crystallography and brought me along for my first beamtime. I am extremely grateful to Claire for hosting me in Edinburgh, sharing her expertise

in high-pressure crystallography, and providing valuable insights into early career academia. Together with Philly and Josh, I appreciate her company during our high-pressure beamtime at I19. I would also like to express my gratitude towards Cameron Kepert and his group members Dave, Rob, Hunter, and Andrew for hosting me in Sydney for two months, patiently guiding me through experiments and showing me around their beautiful city. Additionally, I extend my thanks to Lauren, Caroline, and especially Caite, for making my time in Sydney such a fruitful and enjoyable experience. Finally, I am grateful to Giovazzio for allowing me to bring my samples to his beamtime, and his enthusiasm for X-ray absorption as well as skiing (and lending me a hand in doing both).

As for my non-(inorganic) chemistry friends, I would like to thank my fellow DPhil girls Linda, Moa, Mia, Momo, Zoe and especially Hannah. There is no limit to their support and without our friendship, my time in Oxford would not have been the same. I am also grateful to Ella J. for providing reminiscence of our time in Glasgow and always patiently listening to me vent about work. And finally, I would not have been able to complete my DPhil project as successfully without the balance of making music. Thank you to Annie, Roshan, Rupert, Nora, Will, Joel G., Nathan, Janathan, Josh, Jossy, Kyle, Phoebe, Rachel, Olive, Erin, Eleanor, Maisie, Charlie, Matthew, Joel K., Abi, Dec, Izzy, and especially Logan, for making music with me.

Finally, there are a number of people I need to thank back home. Tessa, Robin, Ellen, Lotte en Sien, dankjulliewel voor onze hechte vriendschap. Ik kijk er altijd naar uit jullie weer te zien en heb genoten van jullie bezoeken aan Oxford. Lieve Victor, dankjewel voor je geduld en constante steun. Ik ben elke dag dankbaar dat ik zo een lieve en zorgzame vriend heb; zonder jou hadden mijn laatste 4 jaar er heel anders uitgezien. En mijn kleine (niet zo klein meer) Phoebe, bedankt voor al je oprechte liefde tijdens mijn tijd in Oxford. Tenslotte, mam en pap, er zijn niet genoeg woorden om mijn dankbaarheid naar jullie uit te drukken. Zonder jullie onvoorwaardelijke steun was deze DPhil niet mogelijk geweest. Ook al woon ik al 10 jaar ver weg en antwoord ik soms niet op jullie berichtjes als ik het druk heb, jullie blijven altijd in mijn hart, waar ik ook ben.

For mama & papa

Contents

1 Introduction **1**

1.1 Overview . . . 1

1.2 Complexity in materials . . . 2

1.3 Aperiodic tilings . . . 12

1.4 Metal-organic frameworks . . . 19

1.5 Thesis aim and outline . . . 35

2 Methods **41**

2.1 Summary . . . 41

2.2 X-ray crystallography . . . 42

2.3 Spectroscopy techniques . . . 67

2.4 Topology determination . . . 73

2.5 Mechanical and thermal stability . . . 73

2.6 Gas adsorption . . . 81

3 Synthesis and average structure analysis **85**

3.1 Summary and acknowledgements . . . 85

3.2 TRUMOF-1 . . . 86

3.3 MOX-2 . . . 92

3.4 MOX-3 . . . 96

3.5 MOX-4 . . . 100

3.6 MOX-5 . . . 104

3.7 Conclusion and Outlook . . . 109

4 Flexibility of MOX-2 and MOX-4 **113**

4.1 Summary and acknowledgements . . . 113
4.2 Background . . . 113
4.3 Variable Temperature X-ray diffraction . . . 115
4.4 High-pressure X-ray diffraction . . . 121
4.5 Summary and conclusion . . . 125

5 MOX-3 thermal diffuse scattering 129
5.1 Summary and acknowledgements . . . 129
5.2 Methods . . . 129
5.3 Results and discussion . . . 130
5.4 Conclusion . . . 133

6 Correlated disorder in MOFs 135
6.1 Introduction . . . 135
6.2 Vacancy correlations . . . 137
6.3 Compositional disorder . . . 140
6.4 Orientational disorder . . . 144
6.5 Conclusions and outlook . . . 147

7 TRUMOF-1: an atomic-scale realisation of a Truchet-tiling 149
7.1 Summary and acknowledgements . . . 149
7.2 Chemical and physical properties . . . 150
7.3 Building the structural model . . . 154
7.4 Model validation . . . 161
7.5 Intermezzo . . . 166
7.6 Elastic behaviour . . . 168
7.7 Conclusion and Outlook . . . 175

8 Summary and perspective 177
8.1 Summary and acknowledgements . . . 177
8.2 The Zn-1,3-bdc MOF phase space . . . 177
8.3 Torsion angle variations TRUMOF-1 . . . 180
8.4 Torsion angle variations 1,3-bdc *vs* 1,4-bdc in Zn-MOFs . . . 181

8.5 Conclusion and discussion 183

Bibliography **187**

Appendix A **207**

A1 TRUMOF-1 208

A2 MOX-2 210

A3 MOX-3 211

A4 MOX-4 215

A5 MOX-5 217

Appendix B **217**

B1 Variable-temperature diffraction data 218

B2 High-pressure diffraction data 237

Appendix C **258**

C1 MOF-5 preparation 259

C2 EXAFS 261

C3 Heat of adsorption 262

C4 Atomic displacement parameters 263

C5 High-pressure diffraction data 264

Appendix D **275**

D1 Failed synthesis attempts 276

Publications

Parts of this thesis that have already been published are listed below along with the chapter which contains the work.

- Correlated disorder in metal–organic frameworks
  E. G. Meekel and A. L. Goodwin, *CrystEngComm*, **23**, 2915–2922 (2021)
  Chapter 6

- Truchet-tile structure of a topologically aperiodic metal–organic framework
  E. G. Meekel, E. M. Schmidt, L. J. Cameron, A. D. Dharma, H. J. Windsor, S. G. Duyker, A. Minelli, T. Pope, G. O. Lepore, B. Slater, C. J. Kepert and A. L. Goodwin, *Science*, **379**, 357–361 (2023)
  Chapter 7

- Torsional flexibility in zinc-benzenedicarboxylate metal–organic frameworks
  E. G. Meekel, T. C. Nicholas, B. Slater and A. L. Goodwin, *CrystEngComm*, **23**, 673–680 (2024)
  Chapter 8

List of Figures

1.1 Examples of complex materials found in nature 2
1.2 Examples of ordered systems with low-symmetry components 4
1.3 Hierarchical structure of complex materials 5
1.4 The effect of proton disorder on diffraction patterns of square ice . . 7
1.5 Examples of local symmetry lowering arising from distortions 8
1.6 Geometrical frustration on the Ising triangular lattice 10
1.7 Examples of materials with dynamic disorder 12
1.8 Periodic tilings to understand the topology of zeolites 13
1.9 Quasicrystal diffractogram and symmetry-matching Penrose tiling . 14
1.10 Aperiodic monotiles 15
1.11 Truchet tiles and tilings as described by Sébastian Truchet 16
1.12 Truchet tilings as a platform for data storage 17
1.13 Design approach to generating procrystalline networks 18
1.14 Key MOF properties 19
1.15 The structures of well-known MOFs 20
1.16 MOF topologies 21
1.17 The diversity of the Fe-1,4-bdc phase space 22
1.18 Isoreticular and multivariate chemistry 24
1.19 The concept of geometry mismatch 25
1.20 Examples of mismatching building blocks 26
1.21 Porosity in MOFs 28
1.22 Structure of the framework with the largest NLC to be reported . . 30
1.23 The structure of Ag(mIm), which exhibits both NTE and NLC . . . 32
1.24 The breathing effect in MIL-53 and MIL-88B 33

1.25 Negative gas adsorption as observed for DUT-49 34
1.26 Origin complexity of 1,3-bdc as compared to 1,4-bdc 35
1.27 Schematic of the torsion potential curves for 1,3- and 1,4-bdc 36

2.1 The seven crystal classes 43
2.2 Scattering of waves by two atoms 45
2.3 Graphical representations of X-ray sources used in this thesis 55
2.4 Schematic showing the different types of disorder 57
2.5 Diffuse scattering calculated from displacive and occupational disorder 58
2.6 Diffuse scattering calculated from the size effect 59
2.7 Pictures of our in-house diffractometer 61
2.8 2D-ΔPDFs calculated from displacive and occupational disorder . . 65
2.9 2D-ΔPDF calculated from the size effect 66
2.10 Schematic of directional elastic properties of materials 74
2.11 Experimental DAC set-up 76

3.1 Batch of TRUMOF-1 crystals 86
3.2 NMR spectra of acid-digested TRUMOF-1 crystals 88
3.3 The bulk phase of TRUMOF-1 89
3.4 Structural features of TRUMOF-1 91
3.5 Batch of MOX-2 crystals 92
3.6 MOX-2 single crystal and powder refinement 93
3.7 Structural features and topology of MOX-2 95
3.8 MOX-3 single crystal refinement 97
3.9 Diffuse scattering observed in the $hk0$ layer for MOX-3 samples . . . 98
3.10 Structural features and topology of MOX-3 99
3.11 Batch of MOX-4 crystals 101
3.12 MOX-4 single crystal and powder refinement 102
3.13 Structural features and topology of MOX-4 104
3.14 Batch of MOX-5 crystals 105
3.15 Asymmetric unit of MOX-5 at 298 K 106
3.16 Reconstructed diffraction layers MOX-5α 107

3.17 Structural features and topology of MOX-5 108
3.18 Summary of Zn-1,3-bdc MOF structures obtained in this thesis . . . 109

4.1 Comparison of wine-rack compositions MOX-2 and MOX-4 114
4.2 Variable temperature behaviour of MOX-2 117
4.3 Variable temperature behaviour of MOX-4 118
4.4 Thermal variation in linker distance and framework angle 120
4.5 Maximum Zn column separation in MOX-4 121
4.6 Behaviour of MOX-2 and MOX-4 under pressure 123
4.7 Compressibility of linker distance and framework angle 124

5.1 Reconstructed $0kl$, $h0l$, $hk0$, and hhl layers collected for MOX-3 . . 130
5.2 $uv0$ cut of the 3D-ΔPDF calculated for MOX-3 with X = Br 131
5.3 Calculation of TDS based on a coarse grained hexagonal lattice . . 132

6.1 Random *vs* correlated disorder in MOFs 136
6.2 Correlated vacancies in UiO-66 137
6.3 Correlated vacancies in other MOFs 139
6.4 Determining correlations in compositionally disordered MOFs Pt. I 141
6.5 Determining correlations in compositionally disordered MOFs Pt. II 143
6.6 Orientational disorder in MOFs 145
6.7 Barocaloric cooling strategy using MOF order/disorder transitions . 146

7.1 Characterisation of chemical properties of TRUMOF-1 151
7.2 Adsorption and desorption isotherms of TRUMOF-1 152
7.3 Representative Truchet tilings 154
7.4 Building a 3D Truchet tiling 156
7.5 DFT geometry optimisation of TRUMOF-1 MC models 159
7.6 The local crystal structure of TRUMOF-1 160
7.7 Reconstructed SCXRD patterns collected from TRUMOF-1 161
7.8 Validation of the TRUMOF-1 Truchet tile model Pt. I 163
7.9 Validation of the TRUMOF-1 Truchet tile model Pt. II 164
7.10 Validation of the TRUMOF-1 Truchet tile model Pt. III 165
7.11 Pore structure of TRUMOF-1 and its properties 166

7.12 Heterogeneous microstructures known to enhance elastic stability . . 168
7.13 Pressure-induced changes in the average structure of TRUMOF-1 . 169
7.14 Mechanical stability of our simplified models for MOF-5 172
7.15 Microscopic mechanism of TRUMOF-1 under hydrostatic pressure . 175

8.1 Summary of crystalline Zn-1,3-bdc MOFs obtained in this thesis . . 178
8.2 Distribution of 1,3-bdc torsion angles in TRUMOF-1 approximants 180
8.3 Distribution of (5-X-)1,3-bdc and (2-X-)1,4-bdc torsion angles . . . 182
A4.4 Comparison difference peaks Pawley fit MOX-2 and MOX-4 216
B1.5 Thermal variation of MOX-2 and MOX-4 structures 236
B2.6 Pressure-induced variation of MOX-2 and MOX-4 structures 258
C1.7 Pawley refinement of MOF-5 powder sample 260
C2.8 Zn K-edge EXAFS measurements and derived functions 261
C3.9 Heat of adsorption of TRUMOF-1 262
C4.10 U(T) plots used to derive experimental U_{ij} values 263
C5.11 Analysis of high-pressure data TRUMOF-1 273
C5.12 Orientational dependence of various elastic moduli of MOF-5 275
C5.13 Orientational dependence of various elastic moduli of TRUMOF-1 . 275

List of Tables

2.1 Typical data collection of a high-pressure diffraction experiment . . 78

3.1 MOX-3 unit cell parameters for MOX-3 single crystals 97

4.1 Thermal expansion coefficients of MOX-2 117
4.2 Thermal expansion coefficients of MOX-4 119
4.3 Thermal expansion coefficients of θ and r 120
4.4 Compressibility of MOX-2 and MOX-4 122
4.5 EoS parameters of MOX-2 and MOX-4 123
4.6 Compressibility of θ and r 125

7.1 Heat of adsorption of various gases in TRUMOF-1 and MOF-5 . . . 153
7.2 Bulk moduli of TRUMOF-1 170
7.3 Quantified anisotropy of the simple models 174

8.1 *Syn*:*anti* ratio of 1,3-bdc in TRUMOF-1 approximants 181
8.2 *Syn*:*anti* ratio of (5-X-)1,3-bdc and (2-X-)1,4-bdc in Zn-MOFs . . . 183
A1.3 Refined site occupancies in TRUMOF-1 208
A1.4 Crystallographic information for TRUMOF-1 at 100 K 209
A2.5 Crystallographic information for MOX-2 210
A3.6 Crystallographic information for MOX-3 for X = Br 211
A3.7 Crystallographic information for MOX-3 for X = Cl 212
A3.8 Crystallographic information for MOX-3 for X = Cl/Br 213
A3.9 Crystallographic information for MOX-3 for X = I 214
A4.10 Crystallographic information for MOX-4 215
A5.11 Crystallographic information for MOX-5 217

B1.12 Crystallographic information for MOX-2 at 300 K 219
B1.13 Crystallographic information for MOX-2 at 250 K 220
B1.14 Crystallographic information for MOX-2 at 225 K 221
B1.15 Crystallographic information for MOX-2 at 200 K 222
B1.16 Crystallographic information for MOX-2 at 175 K 223
B1.17 Crystallographic information for MOX-2 at 150 K 224
B1.18 Crystallographic information for MOX-2 at 125 K 225
B1.19 Crystallographic information for MOX-2 at 100 K 226
B1.20 Crystallographic information for MOX-4 at 300 K 227
B1.21 Crystallographic information for MOX-4 at 275 K 228
B1.22 Crystallographic information for MOX-4 at 250 K 229
B1.23 Crystallographic information for MOX-4 at 225 K 230
B1.24 Crystallographic information for MOX-4 at 200 K 231
B1.25 Crystallographic information for MOX-4 at 175 K 232
B1.26 Crystallographic information for MOX-4 at 150 K 233
B1.27 Crystallographic information for MOX-4 at 125 K 234
B1.28 Crystallographic information for MOX-4 at 100 K 235
B2.29 Crystallographic information for MOX-2 at 0.1(1) GPa 237
B2.30 Crystallographic information for MOX-2 at 0.26(1) 238
B2.31 Crystallographic information for MOX-2 at 0.52(3) GPa 239
B2.32 Crystallographic information for MOX-2 at 0.72(3) GPa 240
B2.33 Crystallographic information for MOX-2 at 0.81(4) GPa 241
B2.34 Crystallographic information for MOX-2 at 0.96(5) GPa 242
B2.35 Crystallographic information for MOX-2 at 1.18(3) GPa 243
B2.36 Crystallographic information for MOX-2 at 1.42(2) GPa 244
B2.37 Crystallographic information for MOX-2 at 1.77(7) GPa 245
B2.38 Crystallographic information for MOX-2 at 2.00(7) GPa 246
B2.39 Crystallographic information for MOX-4 at 0.00 GPa 247
B2.40 Crystallographic information for MOX-4 at 0.15(1) GPa 248
B2.41 Crystallographic information for MOX-4 at 0.24(2) GPa 249
B2.42 Crystallographic information for MOX-4 at 0.44(3) GPa 250

B2.43 Crystallographic information for MOX-4 at 0.6 GPa 251
B2.44 Crystallographic information for MOX-4 at 0.92(4) GPa 252
B2.45 Crystallographic information for MOX-4 at 1.33(4) GPa 253
B2.46 Crystallographic information for MOX-4 at 1.46(6) GPa 254
B2.47 Crystallographic information for MOX-4 at 1.62 GPa 255
B2.48 Crystallographic information for MOX-4 at 1.79 GPa 256
B2.49 Crystallographic information for MOX-4 at 2.09 GPa 257
C2.50 Pearson correlation functions calculated from EXAFS data 261
C5.51 Crystallographic information for TRUMOF-1 at 0.11 GPa 264
C5.52 Crystallographic information for TRUMOF-1 at 0.30(3) GPa 265
C5.53 Crystallographic information for TRUMOF-1 at 0.59(1) GPa 266
C5.54 Crystallographic information for TRUMOF-1 at 0.73(2) GPa 267
C5.55 Crystallographic information for TRUMOF-1 at 1.14(5) GPa 268
C5.56 Crystallographic information for TRUMOF-1 at 1.35(6) GPa 269
C5.57 Crystallographic information for TRUMOF-1 at 1.47(4) GPa 270
C5.58 Crystallographic information for TRUMOF-1 at 1.66(1) GPa 271
C5.59 Crystallographic information for TRUMOF-1 at 1.81(2) GPa 272
C5.60 TRUMOF-1 pore volume and contents as a function of pressure . . 274
D1.61 Representative selection of unsuccesful reactions 277
D1.62 Representative selection of unsuccesful reactions continued 278

Abbreviations

1,3-bdc	1,3-benzene dicarboxylic acid
1,4-bdc	1,4-benzene dicarboxylic acid
2θ	scattering angle (diffraction)
2,5-tdc	thiopene dicarboxylic acid
2,6-ndc	2,6-napthalene dicarboxylic acid
1D	one-dimensional
2D	two-dimensional
3D	three-dimensional
3D-ΔPDF	3D difference pair distribution function
AMPh	phenylamide substituent
APT	atom probe tomography
B	bulk modulus
BET	Brunauer-Emmett-Teller
BM	Birch-Murnaghan
bcdc	9-(4-carboxyphenyl)-9H-carbazole-3,6-dicarboxylate
btc	1,3,5-benzene tricarboxylic acid
CAU	Christian-Albrechts University
CCD	charged-coupled device
CCDC	Cambridge crystallographic data centre
cdc	9H-carbazole-3,6-dicarboxylate
CID	coordination polymer with an interdigitated structure
CSD	Cambridge structural databas
CIF	crystallographic information file
CMR	collosal magnetoresistance

DAC	diamond anvil cell
DCM	dichloromethane
DEF	diethyl formamide
DFT	density functional theory
DMF	N,N-dimethylformamide
DMSO	dimethyl sulfoxide
dot	2,5-dioxidoterephthalate
DUT	Dresden University of Technology
E	elastic or Young's modulus
EA	ethyl acetate
EoS	equation of state
ESRF	European Synchrotron Radiation Facility
EXAFS	extended X-ray absorption fine structure
G	shear modulus
GCMC	grand canonical Monte-Carlo
GUA	guanidinium
GULP	General Utility Lattice Program
HKUST	Hong Kong University of Science and Technology
HRTEM	high-resolution transmission electron microscopy
Im	imidazole
IR	infrared
IUCr	international union of crystallography
JT	Jahn-Teller
LJ	Lennard-Jones
MC	Monte Carlo
mIm	methyl imidazole
MIL	Matériaux de l'Institut Lavoisier
MOF	metal-organic framework
MTV	multivariate
NLC	negative linear compressibility
NMR	nuclear magnetic resonance

NTE	negative thermal expansion
PBA	Prussian blue analogue
PDF	pair distribution function
PMN	$PbMg_{1/3}Nb_{2/3}O_3$
PTE	positive thermal expansion
PTM	pressure transmitting medium
PXRD	powder X-ray diffraction
REDOR	rotational-echo double-resonance
RMC	reverse Monte Carlo
RUM	rigid unit mode
SBU	secondary building unit
SED	scanning electron diffraction
SCXRD	single-crystal X-ray diffraction
SLI	sequential linker installation
SOJT	second-order Jahn-Teller
STEM-EDX	scanning transmission electron microscopy–energy dispersive X-ray
TDS	thermal diffuse scattering
TGA	thermogravimetric analysis
THF	tetrahydrofuran
UFF	universal force field
UiO	Universitetet i Oslo
TCNQ	7,7,8,8-tetracyanoquinodimethane
XANES	X-ray absorption near-edge spectra
XAS	X-ray absorption spectroscopy
ZIF	zeolitic imidazolate framework

Chapter 1

Introduction

1.1 Overview

This is a thesis about complexity, and how — despite the negative connotations often associated with the term — it may lead to several unusual material properties. Various strategies exist for introducing complexity into materials, such as chemical substitution, which involves the incorporation of multiple components on the same crystallographic site. The approach taken in this thesis is that of reducing the symmetry of building blocks. Accordingly, the first section of this introduction delves into the diverse levels of complexity observed in materials resulting from the incorporation of symmetry-lowering components.

Whilst not the sole definition, a material is considered complex if its structure contains a variety of local environments. The classic theory of crystallography fails to accurately describe such systems because it only probes the average structure. Instead, these complex materials may be better understood by comparing them to aperiodic tilings, which similarly lack a periodic translation of the building blocks *i.e.* the tiles. Moreover, the discovery of aperiodic tilings may inspire design of future-generation complex materials as influenced by the tile geometry and connectivity. Both of these aspects are explored in the second section of this chapter.

In order to design a complex material by incorporating low symmetry components, it is crucial to find a platform that allows for full control over the geometry of the building units. Such a platform is offered by metal-organic frameworks (MOFs), as they are realised through the assembly of metal clusters and organic linkers. However, the exploitation of MOFs to realise novel complex materials is not as extensively explored by the scientific community, given the multitude of other remarkable properties they possess; *e.g.* high porosity and flexibility. Consequently, MOFs have gained significant attention and have become highly attractive for a wide range of real-life applications. The third section of this chapter examines the

most notable properties that have contributed to this extensive interest in MOFs.

These individual sections provide the necessary scientific context of the aim of this thesis, which is described in the final section. Along with this introduction, there are a total of 8 chapters in this thesis. The content of each will be summarised at the end of this current chapter.

1.2 Complexity in materials

Biomolecules such as proteins are often described as large and complex. For example: the structures of proteins consist of long chains of amino acid residues arranged in sheets and helices, in turn folded as guided by interactions between the protein backbone (Fig. 1.1a) [1]. Whilst complex, this arrangement is intricately designed by nature in order to regulate cellular processes.

Such complex natural substances are often key in developing next-generation materials. A notable example is nacre, also known as mother-of-pearl, which forms the inner lining of mussel and mollusk shells (Fig. 1.1b) [4]. Its structure consists of inorganic polygonal aragonite ($CaCO_3$) platelets bonded by a thin layer of or-

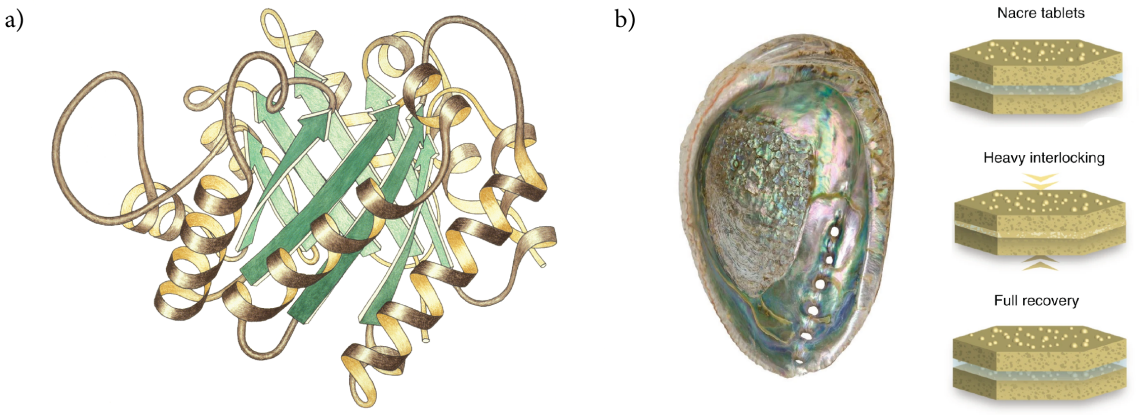

Figure 1.1: Examples of complex materials found in nature. (a) Drawing of the protein triose phosphate isomerase. The green arrows and brown spirals represent the central 8-stranded β-barrels and surrounding ring of 8 α-helices, respectively. (b) Example of a mollusk shell lined with mother-of-pearl, or nacre, which was found to be extremely resilient due to the interlocking of thin tablets as permitted by the organic layer moving out. Figure (a) adapted by Jane Richardson from Ref. 2 and figure (b) adapted from Ref. 3 with permission from Springer Nature.

ganic material. The ultrahigh resilience for which nacre is known arises from its hierarchical structure: the platelets are actually multi-sided tablets of only a few nanometers in size, that can move collectively and spring back in response to applied and removed forces, respectively [3]. This structure has inspired the synthesis of novel complex materials, including impact-resistant body armour [5] and strong glass [6].

Nature clearly demonstrates that complexity in materials can result in optimised properties. Consequently, the design of complex materials has become a significant concept in the field [7]. An efficient approach is to introduce degrees of freedom to a system by reducing the local symmetry of components. Generally, there are two mechanisms to achieve such symmetry lowering: (i) distortions and (ii) molecular shape. The following section will explore this concept through examples from the literature, arranged in ascending order of complexity: order, hierarchical order, and disorder.

1.2.1 Order

If the real structure of a material can be accurately described by the periodic translation of its average unit cell, it is considered ordered and thus, typically, not complex. This characterisation may apply to systems that contain low-symmetry components if the interactions between them are strong enough to yield long-range order.

Examples are the alkali cyanides such as NaCN and KCN, where the alignment of the CN^- rod is ordered antiferroically *i.e.* the up/down alignments are alternated (Fig. 1.2a) [8]. Similarly, the orientation of the planar imidazolium cation captured in the pores of cyanoelpasolites — analogues of $A_2BB'O_6$ double perovskites — is translated periodically (Fig. 1.2b) [9]. However these ordered configurations are only stable at lower temperatures. Beyond a certain threshold, both systems become disordered due to the degrees of freedom associated with the low symmetry components: the CN^- anions may align up or down and therefore behave as an Ising variable, while the planar imidazolium cation aligns to one of the four planes normal to the $\langle 111 \rangle$ cube diagonals, thus behaving as a four-state Potts degrees of freedom. The ordered configuration of such materials is therefore the lowest in energy; there

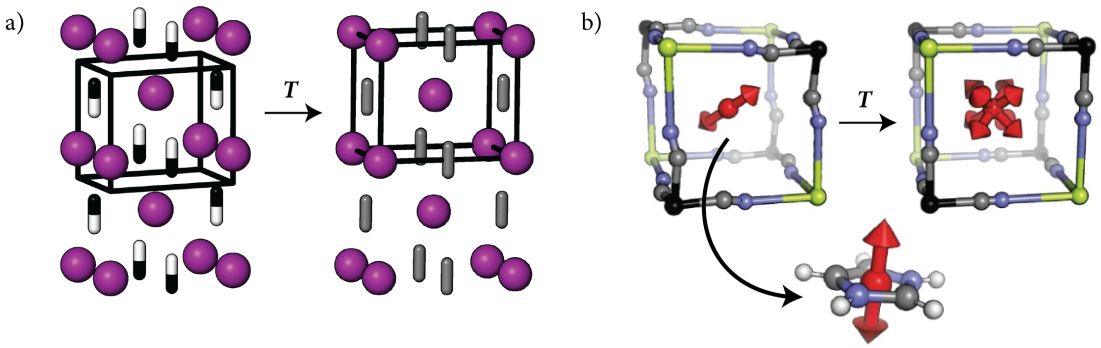

Figure 1.2: Examples of systems where low-symmetry components are distributed in an ordered arrangement. (a) Transition of the low-temperature, ordered $Pmmn$ phase of KCN to the high-temperature, disordered $Fm\bar{3}m$ phase, in which there are no interactions between the CN^- anions. The colour scheme is as follows: K = purple spheres, C = black sticks, N = white sticks, disordered C/N = grey sticks. (b) Transition of the lower-temperature, ordered phase of imidazolium cyanoelpasolite to the high-temperature, disordered phase. This disorder arises from the alignment of the imidazolium cation (H_2Im^+) over four different orientations, as indicated with the red arrow. The colour scheme is as follows: Co = black spheres, Rb = green spheres, C = grey spheres, N = blue spheres, H = white spheres, quadrupole = red arrow. Figure (b) adapted from Ref. 7 with permission from Springer Nature.

is only one possibility and hence the temperature has to be low for it to be realised. As the temperature increases, the system can explore a higher, but shallower, energy landscape containing numerous local minima, each leading to a different disordered configuration.

1.2.2 Hierarchical order

For some ordered materials, large quantities of information may still be required to describe their structure. Proteins, for example, can crystallise, allowing the determination of their structure through single-crystal diffraction experiments [1]. However, whilst crystallographic descriptors successfully account for protein structures, there are four structural levels to consider: the primary, secondary, tertiary, and quaternary protein structures (Figs. 1.3a–d). Thus, despite their ordered nature, the hierarchical structure of proteins is the source of their complexity [10].

Similar to proteins, the structure of relaxor ferroelectrics varies over different length scales [11]. However in contrast, crystallographic descriptors fail to accurately

characterise their structure. In the case of $PbMg_{1/3}Nb_{2/3}O_3$ (PMN), for example, the structural variation arises from both cation off-centering and the (non-random) distribution of the Nb^{5+} and Mg^{2+} ions (Figs. 1.3e–h) [12]. The interplay between these two deviations gives rise to polar nanoregions (PNRs), which are responsible for the unusual response of PMN to electric fields. To obtain an accurate map of this coupling, a complex model of PMN was generated, consisting of over 320,000 atoms [13].

Likewise, the classic theory of crystallography fails to describe the reduced symmetry of domains in the bulk tetragonal phase of the superconductor FeSe, in this

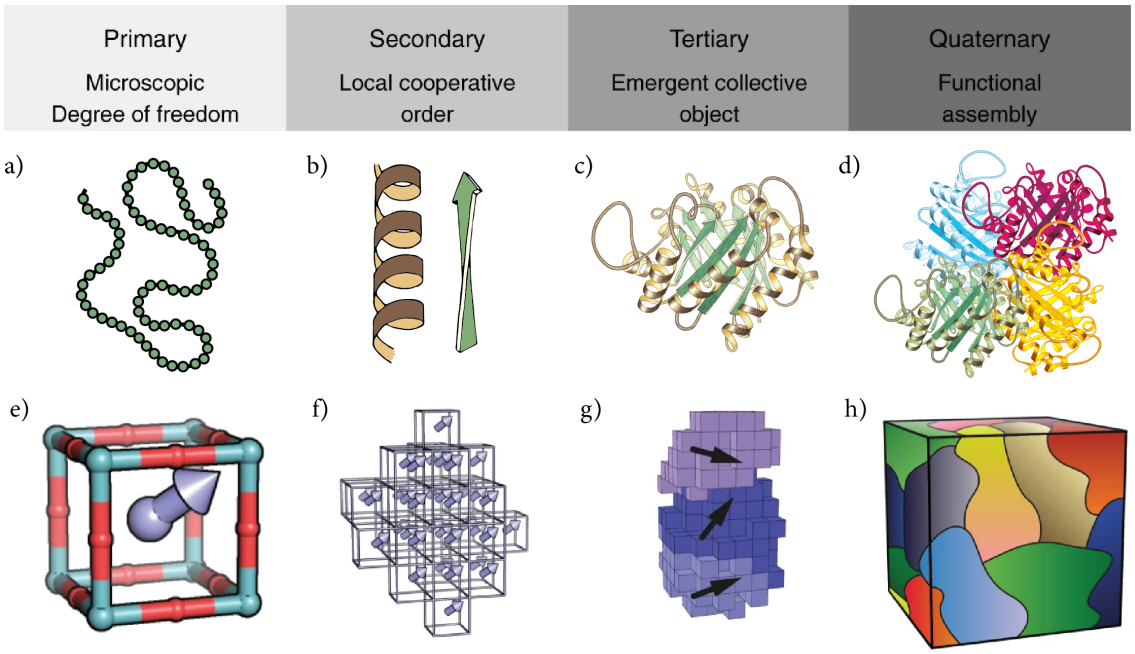

Figure 1.3: Hierarchical structure of proteins (a)–(d) and the relaxor ferroelectric $PbMg_{1/3}Nb_{2/3}O_3$ (PMN) (e)–(h), as divided into the primary, secondary, tertiary, and quaternary level. (a) The sequence of amino acids, which make up the backbone of a protein. (b) The arrangement of amino-acid chains into α-helices (left) and β-sheets (right). (c) Assembly of folded α-helices and β-sheets into a sub-unit. (d) Assembly of multiple sub-units, giving the final protein configuration. (e) Unit cell of PMN, showing the cation is displaced from its high-symmetry position (as indicated with the arrow) at the centre of cell. (f) Assembly of unit cells, where neighbouring unit cells coalign according to their displacements, forming domains with a collective polarisation. (g) Formation of larger structures from the assembly of nearly aligned domains. (h) The bulk structure of PMN, which consists of a dense packing of the large structures. Here, the different colours represent the different orientations of the larger structures, with the gradation reflecting the presence of nearly-aligned sub-domains. Figures (e)–(h) adapted from Ref. 10 with permission from Springer Nature.

case caused by covalent interactions. The subsequent emergence of local environments give rise to significant atomic and electronic anomalies [14]. To elucidate the hierarchical structure of FeSe, a combination of pair distribution function (PDF) experiments and density functional theory (DFT) simulations was employed, which both indicated non-Gaussian distributions in bond distances.

Although not directly related to local symmetry lowering, the atomic order in nanoparticles also demonstrates limitations of the nanoscale [13]. When attempting to determine the local arrangement of atoms in such particles, several factors need to be considered, including the interactions between surface and bulk atoms, as well as the distinction between individual nanoparticles and the ensemble of multiple. Once again, PDF proved particularly useful, as it captures the distribution of interatomic separations over multiple lengthscales. For instance, in conjunction with the Liga algorithm, PDF was utilised to solve the three-dimensional (3D) structure of C_{60} and other nanomaterials [15].

However, the question arises whether it is at all necessary to determine the atomic positions of such hierarchical complex structures in order to comprehend the underlying physics. It may be a better alternative to focus on the interactions between components, which is generally the approach of direct modelling. Herein, a specific interaction model is used to drive a simulation (*e.g.* Monte Carlo), which is then evaluated by comparing the results to experimental observations [16]. In this way, the output is the physics itself; being how the individual components of a system interact to produce the various effects that are observed experimentally.

1.2.3 Disorder

Unlike ordered materials, a material is considered disordered when its real structure cannot be described by the periodic translation of its average unit cell [17]. Hence, the traditional language of crystallography falls short in accurately describing such systems; additional information is needed. Therefore, by definition, disordered materials are complex.

It is important to acknowledge that disorder can manifest in various degrees,

depending on the interactions between the disordered components. If absent, a material is said to be randomly disordered; there is no short- nor long-range order as the disordered components do not influence the state of one another. However, more often than not, interactions between the components are present, leading to short-range order. This is known as correlated disorder [17].

This distinction between random and correlated disorder is perhaps best demonstrated with the simple toy model of square ice — the two-dimensional (2D) analogue of water ice — given in Fig. 1.4. In this model, water molecules are arranged periodically on a 2D square lattice. The positions of the oxygen atoms are translated periodically in all configurations, though the positions of the protons vary. The ordered (Fig. 1.4a) and randomly disordered (Fig. 1.4c) configuration of square ice demonstrate two extremes: in the former, all molecules appear identical, whilst in the latter, they are all distinct. The correlated disordered configuration (Fig. 1.4b) strikes a balance between the two; although disordered, the water molecules interact in such a way that each proton points towards an oxygen atom of a neigh-

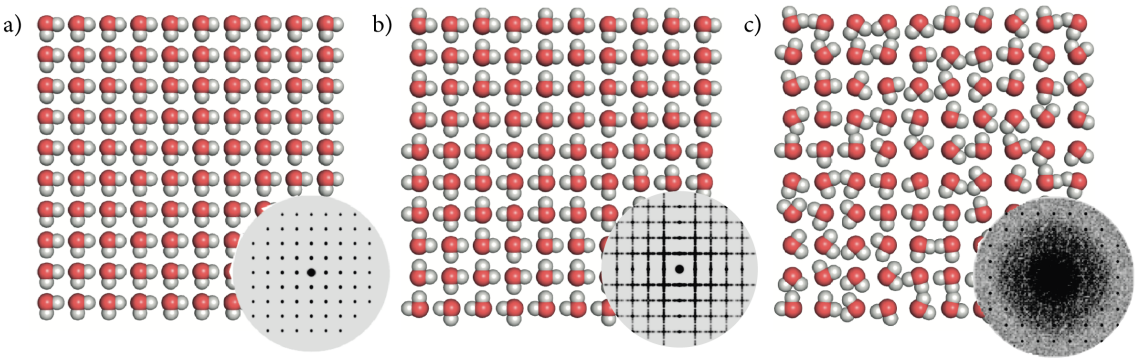

Figure 1.4: The effect of proton disorder on the diffraction pattern of square ice. For each configuration (a–c), the position of the oxygen atom is periodic, resulting in well-defined Bragg peaks in the diffraction patterns (given in the bottom right corner of each configuration). Each configuration shows a different degree of proton order. In (a) the proton positions are long-range ordered *i.e.* all water molecules look the same. As such, the corresponding diffraction patterns contains sharp Bragg peaks only. In (b) the proton positions are correlated, but disordered — they are subject to so-called 'ice rules', which state that each oxygen is near two protons and far from two others. Consequently, all –O–H bonds point along a common direction for each individual row or column, though there is no correlation across the rows and columns. The corresponding diffraction patterns contains both sharp Bragg peaks as well as highly structured diffuse scattering. Finally, in (c) the orientations of the water molecules are random. As a consequence, there is broad, featureless diffuse scattering on top of the Bragg peaks. Figure adapted from Ref. 17 with permission from Springer Nature.

bouring molecule. As a result, all –O–H bonds align along a common direction for each individual row and column of the lattice. Importantly, these configurations exhibit different scattering behaviours, in turn highlighting the sensitivity of scattering techniques to disorder. The intensity originating from the disordered components is known as diffuse scattering, which appears structured when interactions are well-defined (Fig. 1.4b) and broad when weak or absent (Fig. 1.4c). Thus, scattering techniques can serve as powerful tools for characterising complexity in materials.

There are numerous examples of systems that display (correlated) disorder as a consequence of symmetry lowering. This includes the examples of alkali cyanides [8] and cyanoelpasolites [9] mentioned above, which exhibit disorder in the orientation of the low-symmetry CN^- anion and imidazolium cation, respectively (Fig. 1.2), as well as the relaxor ferroelectric PMN (Fig. 1.3b) [12] and the superconductor FeSe [14], in which the disorder arises from local distortions.

The Jahn-Teller (JT) effect is another phenomenon known to introduce complexity in materials by reducing the symmetry of structural components through a distortion. The resulting disorder tends to be correlated as neighbouring units share a common vertex [7]. The manganite perovskite $LaMnO_3$, for example, undergoes

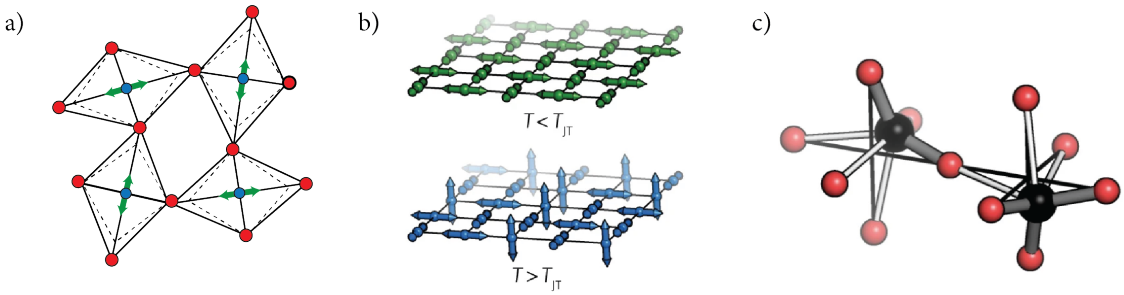

Figure 1.5: Examples of local symmetry lowering arising from distortions. (a) Schematic representation of $LaMnO_3$ in the xy plane, showing the checkerboard arrangement of JT-distorted octahedra. The directions of the distortion is highlighted for each octahedra with green arrows. The ideal geometric templates for JT-distorted octahedra are given in the dashed black lines. Colour scheme is as follows: Mn = blue, O = red. La atoms omitted for clarity. (b) The orbital order-disorder transition in $LaMnO_3$, which involves a progression from alternating $Q_{2,xy}$ distortions at $T < T_{\mathrm{JT}}$ to a correlated disordered population of all six Q_2 states at $T > T_{\mathrm{JT}}$. (c) Correlated off-centring of Ti^{4+} ions in $BaTiO_3$ driven by second-order Jahn–Teller (SOJT) effects. The distortions strengthen some Ti–O bonds at the expense of others. Colour scheme is as follows: Ti = black, O = red. Figures (b) and (c) adapted from Ref. 7 with permission from Springer Nature.

a JT distortion where one pair of M–O bonds is elongated, one is shortened, and one remains unchanged. Due to the tendency of long Mn–O bonds to avoid sharing the same O atom (an effect of covalency), a direction-dependent antiferroic coupling arises between neighbouring states (Fig. 1.5a). These interactions directly impact the occupancy of the e_g orbitals of the Mn^{3+} sublattice, which can explain some of the physical behaviour exhibited by $LaMnO_3$. Its orbital order–disorder transition at $T_{JT} = 750$ K, for example, couples to a switch from anisotropic to isotropic magnetism as well as a hundredfold decrease in resistivity (Fig. 1.5b) [18–20]. Moreover, introducing further complexity through doping to form the mixed-valence series $La_{1-x}Ca_xMnO_3$, leads to a decrease in the fraction of JT-active sites, stabilisation of the orbital disordered state, and lowering of T_{JT} [21]. In fact, for $x \simeq \frac{1}{3}$, T_{JT} is commensurate with the magnetic ordering temperature ($\simeq$300 K), and the system exhibits a collosal magnetoresistance (CMR) effect, whereby its electrical conductivity is strongly perturbed by an applied magnetic field [22].

Second-order Jahn-Teller (SOJT) distortions remove local inversion symmetry so as to allow mixing between orbitals of different symmetries. This mixing leads to the strengthening of certain bonding interactions at the expense of others, which can provide a source of coupling between neighbouring states. In the case of $BaTiO_3$, for example, off-centering of the Ti^{4+} cation towards the face of the TiO_6 coordination polyhedron strengthens three mutually perpendicular Ti–O bonds, while weakening the other three (Fig. 1.5c) [23, 24]. The tendency for each oxygen atom to participate in one strong and one weak Ti–O bond drives an anisotropic interaction that couples local displacements into polar chains which, in turn, result in the emergence of bulk polarisation and a ferroelectric response [23, 25, 26].

Geometrical frustration

Complexity through disorder may be carefully designed by considering the lattice on which low-symmetry components reside. If the combination of the lattice, degrees of freedom, and interactions leads to frustration, for example, the disorder will be correlated since the components cannot simultaneously satisfy all pairwise interactions between them [27].

The simplest example to demonstrate this concept is that of the triangular Ising antiferromagnet. In this model, Ising spins — which are constrained to point either up or down — are positioned at the corners of the triangular lattice (Fig 1.6a). If two neighbouring spins couple antiferromagnetically (*i.e.* one is pointing up and the other is pointing down), then there is no arrangement in which the third neighbour can couple antiferromagnetically to both. As a result, the system becomes frustrated, lacking a unique ground state. All macroscopic configurations are essentially degenerate, leading to an extensive residual entropy at 0 K [28].

Geometrical frustration translates across multiple length-scales. For instance, columnal aggregates of molecules based on 1,3,5-benzene tricarboxamide tile a triangular lattice to maximise packing efficiency of a single crystal [29]. Each column has a macroscopic dipole moment, and neighbouring columns tend to align antiferroelectrically such that the dipoles cancel, resulting in a geometrically frustrated distribution [30]. Therefore, its ferroelectric behaviour may be tuned as a function of steric and electrical interactions. Likewise, the resonating valence bond model that governs the electronic structure of graphene can be mapped onto the triangular antiferromagnet (Fig. 1.6c) [31]. On an even larger length-scale, the 'feline foamy

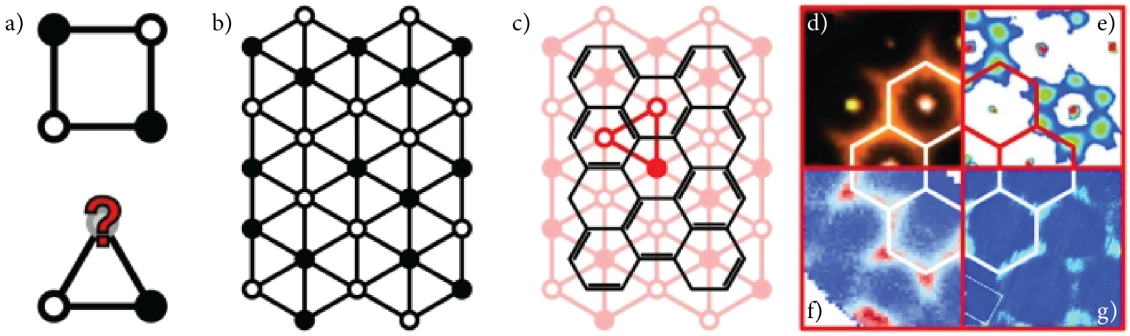

Figure 1.6: Geometrical frustration on the Ising triangular lattice. (a) Antiferromagnetic interactions between Ising spins are fully satisfied on a square lattice, but not on a triangular lattice. (b) One of many possibilities of an extended triangular lattice, where each triangle adopts either a one-up-two-down or a one-down-two-up arrangement. (c) This model can be used to explain the arrangement of π-bonds in the resonant valence bond model of graphene. The structural parallels between systems which show frustration on the triangular lattice is reflected in their scattering functions for (d) the Gag protein; (e) orbital orientations in $Ba_3CuSb_2O_9$; (f) the emergent spin structure of β-Mn and (g) the electronic structure of graphene. Figures adapted from Ref. 17 with permission from Springer Nature.

virus' also packs in a triangular lattice, as driven by steric interactions [32]. Despite having different driving forces, these various systems exhibit the same signatures in reciprocal space as a result of this geometric frustration (Figs. 1.6d–g)) [17].

Dynamical disorder

In some cases, the configurational landscape of disordered states is sufficiently shallow to be navigated thermally. As a result, the disorder is no longer static, but dynamic in nature. This dynamic disorder may be correlated, being that the atomic displacements can be described by the collective movement of the lattice, which is known as phonons [33].

This aspect is well-demonstrated with the case of rock-salt thermoelectrics PbTe and PbO, where symmetry-lowering effects come into play [34, 35]. The Pb^{2+} cation, with its $6s^26p^0$ configuration, is susceptible to a SOJT distortion, leading to an off-centering of the cation and the formation of stronger Pb-chalcogenide interactions at the expense of others. In this case, the barrier height for interconverting between equivalent off-centering directions is determined by the relative energies of the Pb and chalcogenide orbitals [36–38]. As such, the distortions in PbO are static, whilst those in PbTe are dynamic. The latter results in a particularly soft branch in the phonon dispersion, leading to the mixing with acoustic branches and amplification of anharmonic scattering, which in turn slows down thermal transport [34]. A similar mechanism is responsible for the anomalously large dielectric response observed in many bismuth pyrochlores, such as $Bi_2Ti_2O_7$, where the dynamic off-centering of the Bi^{3+} plays a key role [39, 40].

Phonons are typically characterised using inelastic scattering techniques [41–44]. It is important to consider the relevant timescale of these methods, as scattering periods are generally shorter than those of the atomic vibrations. Another experimental feature related to phonons is thermal diffuse scattering (TDS), although its interpretation is more complex. It is most often used for comparing experimental data with simulations based on calculated models, or for tracking phase transitions under varying temperature or pressure conditions [44]. An example of the former is the case of β-quartz, for which streaks of diffuse scattering appear in its diffraction

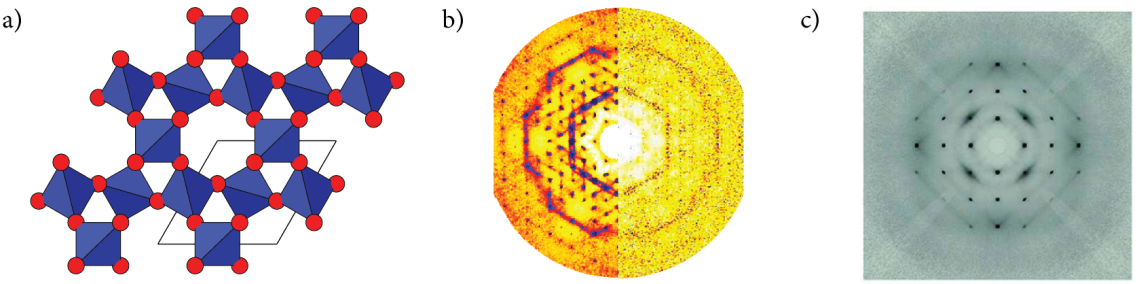

Figure 1.7: Examples of materials with dynamic disorder. (a) The structure of β-quartz, which can be described as connected SiO_4 tetrahedra. Colour scheme is as follows: Si = blue tetrahedra and O = red spheres. (b) Experimental (left) and calculated (right) reconstructed *hk*0 total scattering layer of β-quartz. (c) The (200) cross section of total neutron scattering of crystalline CBr_4. Figures (a) and (b) adapted from Ref. 45 with permission from MinSoc, and figure (c) adapted from Ref. 47 with permission from the IUCr.

pattern (Figs. 1.7a, b) [45]. These streaks are particularly important since they are attributed to the motion of linked polyhedra, known as rigid unit modes (RUMs), which are usually low in energy [46].

Plastic crystals can also be regarded as a form of dynamical disorder [48–50]. Such crystals are characterised by the free rotation of molecular moieties over a number of different configurations *i.e.* orientational and displacive disorder. The high-temperature, cubic ($Fm\bar{3}m$) phase of carbon tetrabromide (CBr_4) is an example of such a plastic crystal [51–55]. Similar to other plastic crystals, CBr_4 undergoes a phase transition to an ordered, monoclinic phase at low temperatures [56]. In the high-temperature plastic phase, the CBr_4 molecules are free to rotate, but do not do so independently from each other. Hence, there are strong nearest-neighbour intermolecular orientational and associated displacive correlations, resulting in structured diffuse scattering contributions to the corresponding diffraction pattern (Fig. 1.7c) [57, 58].

1.3 Aperiodic tilings

In materials chemistry, it is often useful to interpret crystal structures in terms of periodic tilings. This approach can be particularly useful to describe the connectivity (*i.e.* topology) of framework materials, such as zeolites (Fig. 1.8) [59].

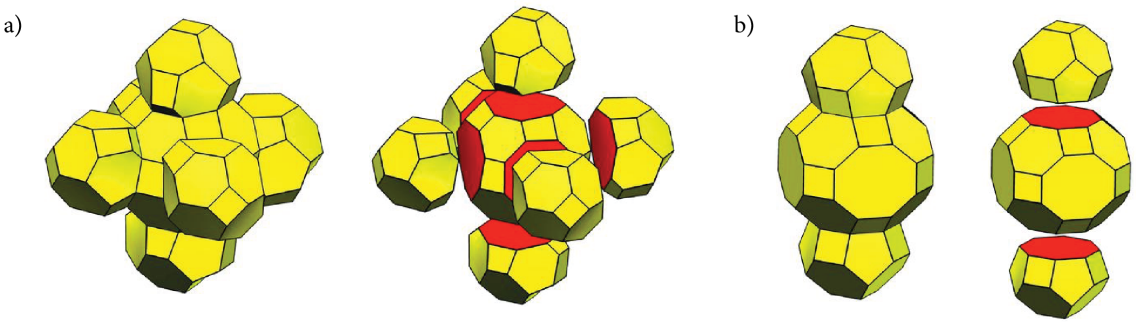

Figure 1.8: Periodic tilings corresponding to the zeolite (a) **LTN** and (b) **UFI** net topologies. Two representative tilings are given for both cases to demonstrate the range of structural interpretations into tilings. In this case, the larger tiles (left) are split into smaller components (right) to allow for the faces that correspond to weak zeolite rings (highlighted in red). Figures adapted from Ref. 59 with permission from the IUCr.

However, in the case of complex materials, the structure cannot always be described by the periodic arrangement of the same tile. Instead, the concept of aperiodic tilings becomes more relevant as these tilings lack translational periodicity and may therefore capture the complexity of a particular system. This section will explore several aperiodic tilings that have either contributed to our understanding of complex materials or have the potential to inspire the design and realisation of next-generation complex crystal structures.

1.3.1 Penrose tilings and quasicrystals

In 1982, Dan Shechtman observed a diffraction pattern with 5-fold rotational symmetry for the metallic alloy Al_6Mn [60]. This discovery was significant because, at that time, it was believed that only 2-, 3-, 4-, or 6-fold rotational symmetry was possible in crystal structures. This observation thus challenged the conventional understanding of crystallography and led to the discovery of a new class of materials called quasicrystals, for which he was awarded the Nobel Prize in Chemistry in 2011 [61].

The unusual symmetry observed in diffraction patterns of quasicrystals stems from a lack of translational periodicity, despite the sharp Bragg peaks indicating the presence of long-range order. Penrose tilings, although discovered before the discovery of quasicrystals, played a crucial role in understanding and describing these

diffraction patterns by providing a mathematical framework for their interpretation (Fig. 1.9) [62]. In fact, these tilings enabled the derivation of a structural model for Al_6Mn based on the polyhedral units present in the crystallographic phase [63].

Accordingly, Penrose tilings are a type of aperiodic tiling that covers 2D space in an aperiodic manner, exhibiting 5- or 10-fold rotational symmetry. The original set of Penrose tiles consisted of four different shapes, but later, Roger Penrose achieved an aperiodic tiling using only two differently shaped tiles (Fig. 1.9b) [65]. For almost 50 years it was considered that two was the minimum number of tiles required to create an aperiodic tiling. That is, until this year, when the first set of aperiodic monotiles was discovered [66].

Dozens of quasicrystals have been identified since Shechtman's discovery; these include the naturally occurring icosahedrite [67], and soft-matter quasicrystals [68, 69]. The origin of their aperiodicity is still subject to ongoing research and hence it is not yet fully understood how the unique atomic arrangement in quasicrystals gives rise to distinctive properties, such as their high electrical resistivity [64, 70]. Notably, a recently reported design strategy based on the assembly of 'patchy particles' provides a potential route towards functional quasicrystalline materials of different symmetries [71]. Simulations show that this approach may be realised using poly-

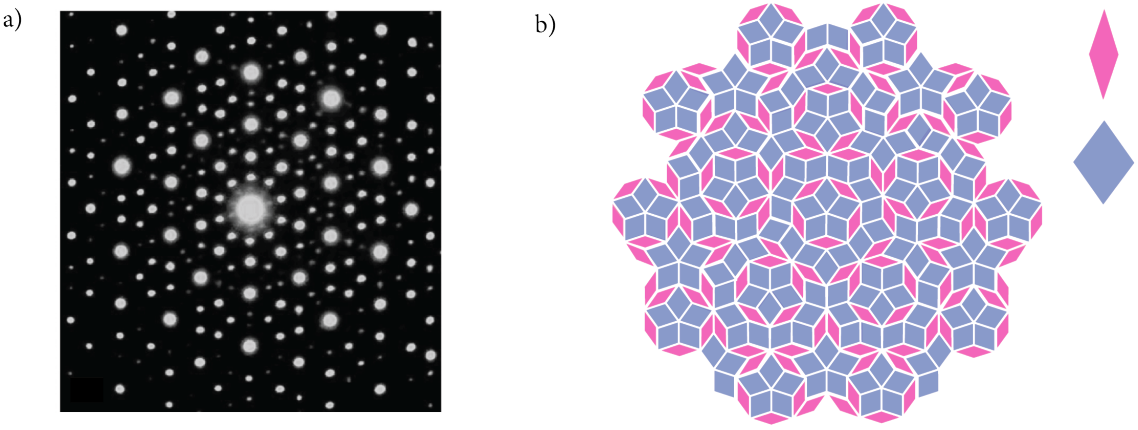

Figure 1.9: Quasicrystal diffractogram and symmetry-matching Penrose tiling. (a) Electron diffraction pattern of icosahedral $Al_{65}Cu_{20}Fe_{15}$ quasicrystals, showing sharp Bragg peaks of a 5-fold rotational symmetry. (b) Penrose tiling showing similar 5-fold rotational symmetry, built from two differently shaped tiles. Figure (a) adapted from Ref. 64 with permission from Elsevier.

hedral DNA origami particles, as they have specific interactions between vertices arising from single-stranded DNA 'sticky ends' [72].

1.3.2 Monotilings

The quest for an aperiodic tiling enforced by just one tile had been a long-standing challenge since the discovery of Penrose tilings in 1974. Whilst several monotiles had been proposed over the years, many of them did not meet the strict criteria for a fully aperiodic tiling. The Schmitt-Conway-Danzer tile, for example, is considered 'weakly aperiodic' as it can be translated along a screw axis (Fig. 1.10a) [73]. Similarly, the Socolar-Taylor tile (Fig. 1.10b), despite displaying local aperiodic patterns, is not fully connected [74, 75]. Its 3D analogue (the '3D-Einstein tile') is periodic in the third dimension, despite demonstrating aperiodicity within each layer (Fig. 1.10c) [74, 75].

These examples illustrate the challenges encountered in the search for a fully aperiodic monotile. However, recent progress has been made, and in a groundbreaking discovery, the first set of aperiodic monotiles to cover 2D space was reported this year: the 'Einstein' tile (Fig. 1.10d) [66]. This discovery represents a significant milestone in aperiodic tiling and opens up new possibilities for exploring the design and realisation of complex crystal structures with only one tile *i.e.* (low-symmetry) component. A remarkable feature of the hat-shaped Einstein tile is that the lengths of its 13 sides could be altered to result in tiles that can still be arranged into a

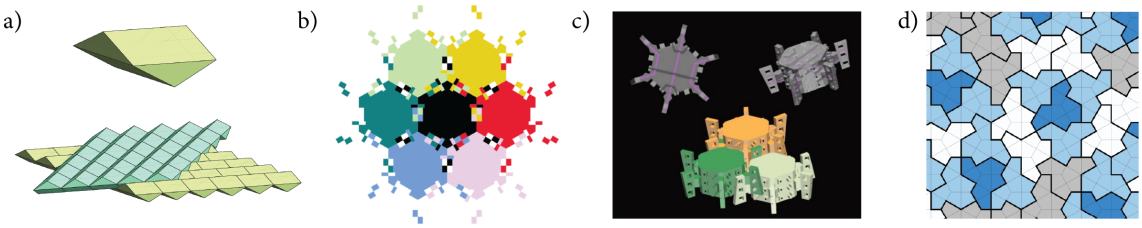

Figure 1.10: Aperiodic monotiles. (a) The Schmitt-Conway-Danzer tile and the space-filling tiling it forces. (b) The Socolar-Taylor tiling, where each tile has a different colour. The tiles are not fully connected. (c) Tiling of the 3D-analogue of (b), which is not periodic in the third dimension. (d) The Einstein tiling, which is the first aperiodic monotile to be reported. Figures (a)–(c) adapted from Refs. 74 and 75 with permission from Elsevier B. V. and Springer Nature, respectively. Figure (d) adapted from Ref. 66.

seamless, aperiodic tiling. Thus, this shape opens the door to an infinite number of Einstein tiles.

Yet, the Einstein monotile received some criticism as it is weakly chiral and therefore relies on a reflection to achieve the aperiodic tiling. Hence one may argue it is not fully aperiodic — a ceramic tiling of the Einstein tile, for example, would need two different sets of glazed tiles. However, the same authors have most recently derived a monotile from the original Einstein tile that exhibits strictly chiral aperiodicity: the 'Spectre' monotile [76].

Whilst there are currently no known materials that directly map onto the Einstein or Spectre tiling, the discovery of these aperiodic monotiles has significant implications for the design and understanding of future-generation complex materials.

1.3.3 Truchet tilings

As opposed to the Einstein tile, the aperiodicity of Truchet tiles arises from the decoration — rather than the shape — of the tile. These were first described in 1704 by the French priest Sébastian Truchet, who arranged a single square tile painted in a different colour on either side of its diagonal in a number of visually appealing patterns, including both ordered and disordered arrangements (Fig. 1.11) [77].

These Truchet tilings have now been generalised to encompass any periodic covering of space, whether partial or complete, using one or more tiles that have been decorated to reduce their symmetry [78]. Breaking colour-inversion symmetry, for

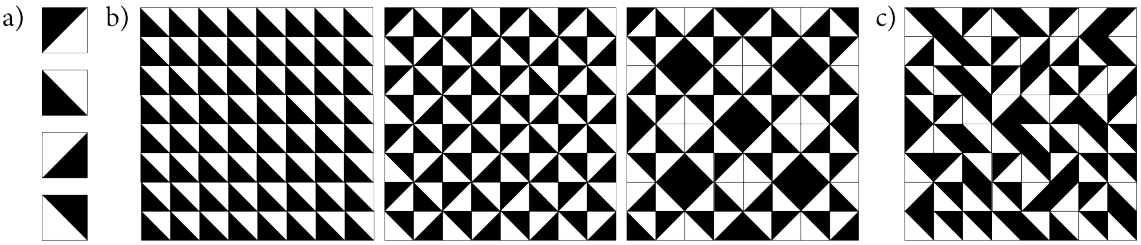

Figure 1.11: Truchet tiles and tilings as described by Sébastian Truchet. (a) Single square tile and its four possible orientations, arranged in (b) periodic and (c) random tiling patterns.

example, gives barcodes and QR codes as simple Truchet tilings in one and two dimensions, respectively: each strip or pixel encodes a binary state that is exploited in their application as machine-readable information stores (Figs. 1.12a, b). More complex Truchet tilings store information in aperiodic patterns of loops and networks in two or three dimensions (Figs. 1.12c, d) [79].

Indeed, Truchet tiles offer a platform for data storage by arranging 'N' bits in a periodic array, in turn encoding information by adopting one of n degenerate states, resulting in a total of n^N possible configurations. What makes them particularly interesting is that for certain decorations, achieving a fully connected pattern may require specific neighbouring tile orientations. Such Truchet tilings exhibit correlated disorder, in turn providing an unconventional platform for data storage as

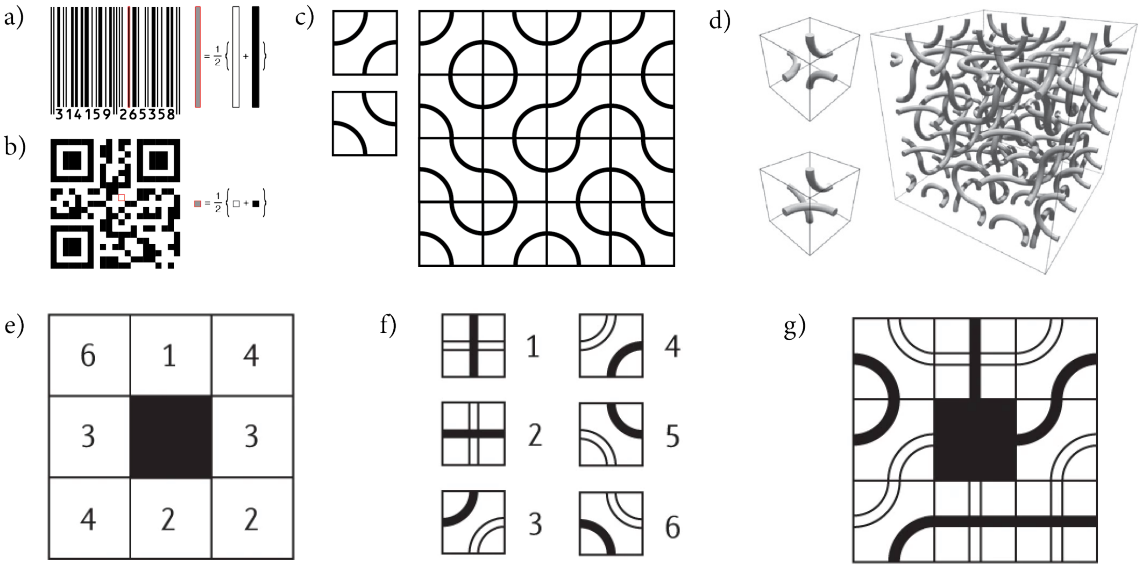

Figure 1.12: Truchet tilings as a platform for data storage. (a) Barcodes and (b) QR codes, which store information in tilings of strips or pixels that break colour-inversion symmetry. The average tile colour, grey, is invariant under colour inversion, but individual strips or pixels (examples outlined in red) store information in the way in which colour-inversion symmetry is broken. The patterns formed are Truchet tilings in the sense that individual tiles are lower in symmetry than the configurational average. Graphic of a (c) two- and (d) three-dimensional Truchet tiling, the latter forming a network of so-called Truchet pipes. (e) Information stored in a conventional array of bits (here 1–6), which is irrecoverable if a single bit is erased (black square). (f) Mapping Truchet tiles to bit states. (g) The information encoded within each bit is no longer independent of its neighbours, such that the loss of one tile does not imply loss of information. Here, it is clear that the missing tile must correspond to state '5'. Figure (d) adapted from Ref. 79 with permission from Elsevier B.V., figures (e)–(g) adapted from Ref. 7 with permission from Springer Nature.

each bit depends on its neighbours. Therefore, if any one state is erased, information may be recovered, rather than completely lost, by inspecting neighbouring bits (Figs. 1.12e–g). This suggests that if a complex, disordered crystal were to map onto such a Truchet tiling, it may provide a unique opportunity for high-density data storage and manipulation with intrinsic error-correcting capabilities [7].

The concept of the 'procrystalline state' attempts to relate such correlated disordered (monotile) Truchet tilings to materials by referring to the tiles as low-symmetry, identical fundamental structural units *i.e.* neighbourhoods, which are positioned periodically but orientationally permuted as permitted by the point symmetry of the high-symmetry lattice on which they reside [80]. Similar to any other material that exhibits correlated disorder, procrystalline structures are characterised by diffuse scattering, as demonstrated through computationally generated procrystalline networks (Fig. 1.13). To realise such complex materials, it is crucial to have full control over building unit geometry.

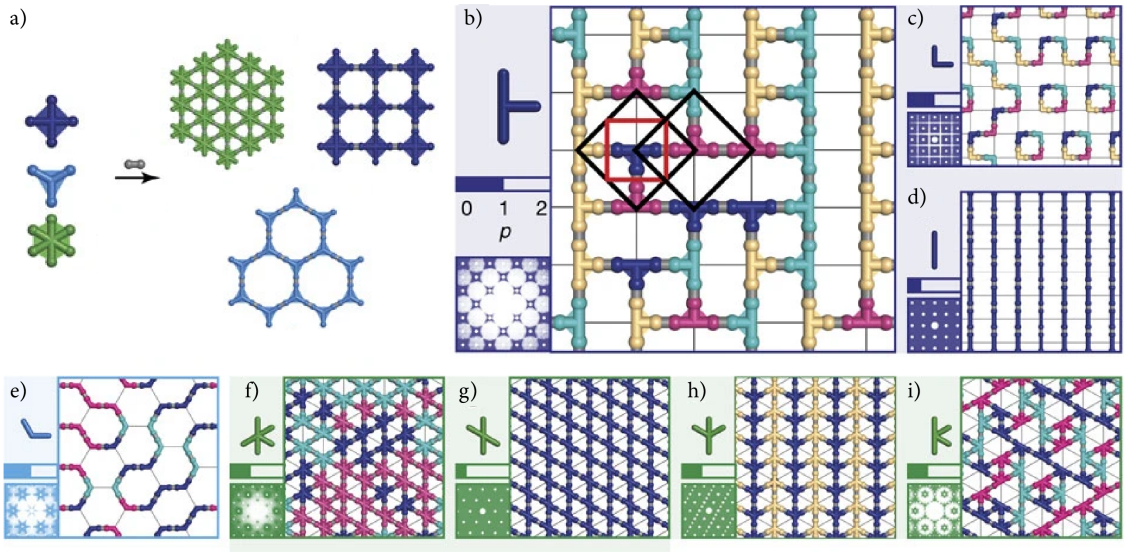

Figure 1.13: Design approach to generating procrystalline networks. (a) High-symmetry lattices, as composed from high-symmetry building blocks: square (indigo), hexagonal (blue), and triangular (green). (b) – (i) Various ordered and disordered states, as composed from the arrangement of low- and high-symmetry nodes on these high-symmetry lattices. For each panel, the node geometry is shown in the top-left corner, followed by a bar to indicate the propensity for the disorder qualitatively. The representative network is shown in the main image, with the nodes coloured according to their orientation. The corresponding X-ray diffraction pattern is given in the bottom-left corner of each panel. Figures adapted from Ref. 80 with permission from Springer Nature.

Metal-organic frameworks (MOFs) are suitable candidates as they offer this prerequisite due to their composition: metal-containing clusters — often referred to as secondary building units or SBUs — interconnected by organic linkers to form a continuous network [81]. The ability to design and control the geometry of MOFs offers an opportunity to explore and realise such complex materials.

1.4 Metal-organic frameworks

The historical focus of the MOF community has been on exploiting the seemingly-infinite possibilities of metal and linker combinations, which in turn influence the structure and properties of MOFs [82, 83]. Approximately 90,000 MOFs have been synthesised to date, with over 500,000 further systems predicted computationally [84, 85]. Some MOFs have been commercialised. TruPick, for example, is a MOF adsorbent designed to store and release 1-methylcyclopropene for fruit and vegetable ripening [86]. Likewise, CALF-20 is a MOF optimised for CO_2 capture in industrial processes [87].

In general, MOFs compare to other frameworks as being particularly versatile, porous, and flexible (Fig. 1.14). The following sections will explore these three aspects of MOF chemistry in more detail.

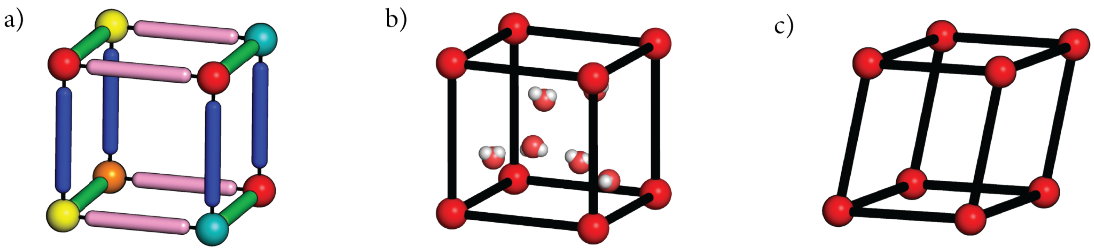

Figure 1.14: The three properties that set MOF apart from other framework materials: (a) Versatility, (b) porosity, and (c) flexibility.

1.4.1 Versatility

The chemical versatility of MOFs stems from their ability to incorporate various metals and linkers into their structures, including different types within the same framework. This diversity is demonstrated with Figure 1.15, which shows a number of different MOFs that are particularly well-known within the field for their remarkable properties.

MOF-5 ($Zn_4O(1,4\text{-bdc})_3$, 1,4-bdc = 1,4-benzene dicarboxylic acid) holds special importance in the field because it was the first MOF that demonstrated to remain stable after evacuation of the solvent [88]. Even today, it is widely studied for its straightforward synthesis, ease of crystallisation, and high porosity [89]. A drawback, however, is its instability with regards to water; MOF-5 tends to gradually

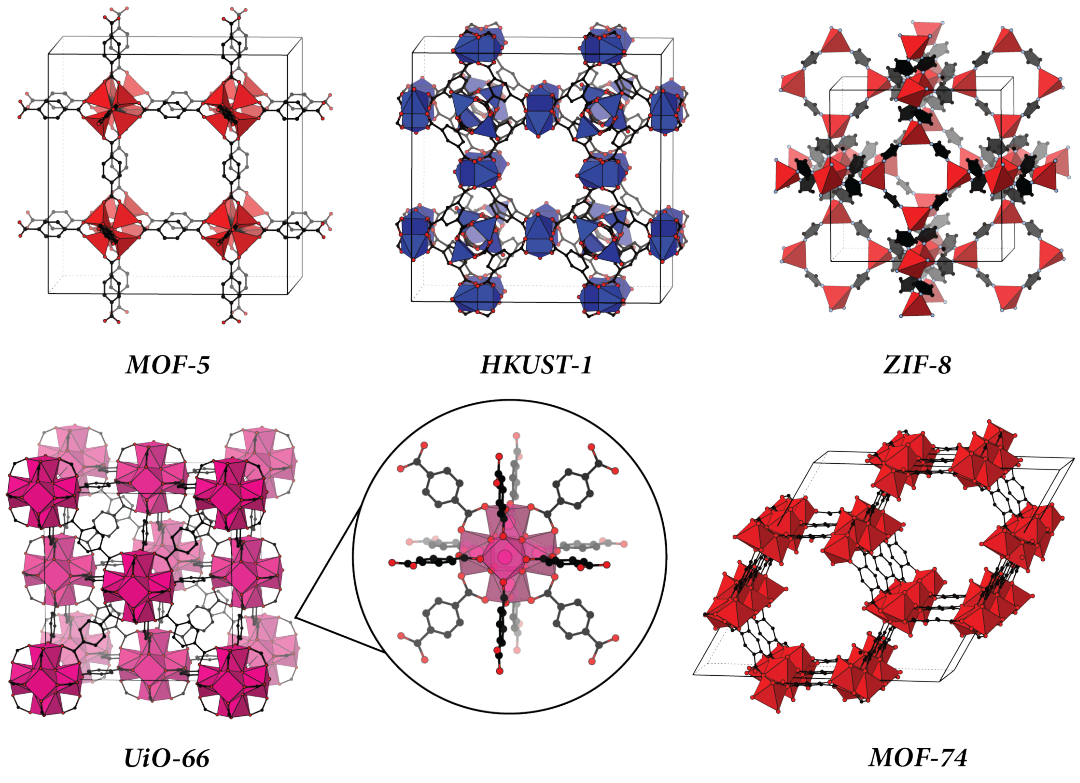

Figure 1.15: The structure of MOFs often mentioned in this thesis, positioned within a unit cell: (Top, from left to right) MOF-5, HKUST-1, ZIF-8, (bottom, from left to right) UiO-66 and its 12-connecting Zr SBU, and MOF-74. Colour scheme is as follows: C = black spheres, O = red spheres, Zn = red polyhedra, Cu = blue polyhedra, Zr = pink spheres and polyhedra. H atoms are omitted for clarity.

disintegrate when left in humid air [90].

Other notable MOFs include HKUST-1 (Cu_3(1,3,5-btc)$_2$(H_2O)$_3$, 1,3,5-btc = 1,3,5-benzene tricarboxylic acid, HKUST = Hong Kong University of Science and Technology) [91], ZIF-8 (Zn(mIm)$_2$, mIm = methyl imidazole) [92], UiO-66 (Zr_6O_4(OH)$_4$(1,4-bdc)$_{12}$, UiO = Universitetet i Oslo) [93], and MOF-74 (Zn_2(2,5-dot)(DMF)$_2$ · (H_2O)$_2$, 2,5-dot = 2,5-dioxidoterephthalate, DMF = dimethyl formamide) [94].

HKUST-1, UiO-66 and ZIF-8 are similarly cubic, albeit more stable than MOF-5. UiO-66 is particularly stable as permitted by the high connectivity of the Zr cluster [93]. The stability of HKUST-1 arises from the tritopic linker 1,3,5-btc, as opposed to the ditopic linker 1,4-bdc present in MOF-5 and UiO-66 [91]. ZIF-8 represents a well-known example of a zeolitic-imidazolate framework (ZIF). ZIFs have structures analogous to zeolites, whereby Si–O–Si connectivity of the latter is mimicked by M–Im–M connectivity in the former [95]. MOF-74, on the other hand, is trigonal, and best known for its honeycomb structure [94]. This structural motif exposes the metal sites, making it suitable for applications such as catalysis [96] and molecular separation [97].

To capture the wide variety of MOF structures, they are often characterised by their connectivity or underlying net *i.e.* topology. This approach is in a way similar to reducing the abundance of inorganic compounds onto certain structure types *e.g.* rocksalt and zinc blende [98]. The structure of MOF-5, for example, is

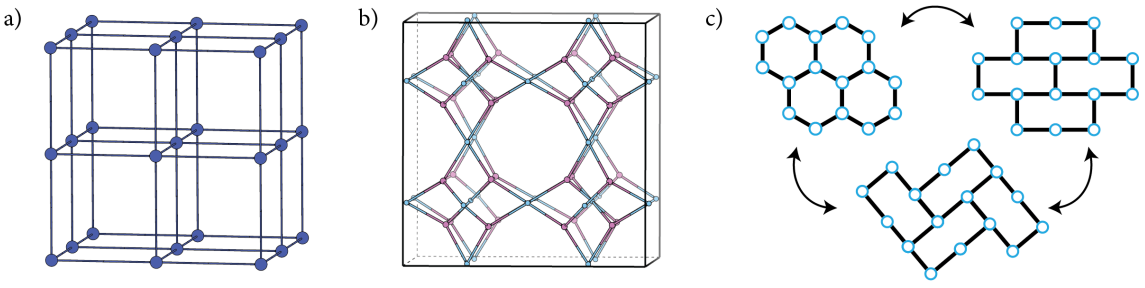

Figure 1.16: MOF topologies. (a) The **pcu** topology, which describes the net of MOF-5. (b) The **tbo** topology, which describes the net of HKUST-1. (c) Three representations of a 3-c net that are geometrically different but topologically identical, because they can be transformed into each other without breaking and reconnecting edges.

characterised by the **pcu** topology, which refers to 6-c octahedral nodes connected by 2-c edges (Fig. 1.16a). HKUST-1, on the other hand, is described by the **tbo** net, which refers to (3,4)-c square planar nodes (Fig. 1.16b). It is important to note that the topology solely captures the framework's connectivity and not its geometry (Fig. 1.16c). Hence, seemingly different MOFs may be characterised by the same underlying net.

MOF phase space

MOF structures are diverse not only in terms of their composition: variations in synthesis can result in different topologies even with the same contribution of metal and linker. In this thesis, I use the term 'phase space' to describe this diversity.

To illustrate this concept, I will discuss the example of the Fe-1,4-bdc phase space, which is particularly rich and well-studied [100]. It is of particular importance for the Fe-frameworks MIL-101, MIL-88B, and MIL-53 (MIL = Matériaux de l'Institut Lavoisier) because of their unique properties [99, 101].

Namely, the rigid and large-pore framework MIL-101 exhibits exceptionally high porosity (surface area = 4470 m^2g^{-1}) [102]; the flexible MIL-88B undergoes continuous breathing upon solvation/desolvation [103–105]; and the similarly flexible MIL-53 exhibits well-defined phase transitions between large and narrow pore phases during the process of solvation/desolvation and gas adsorption [106, 107]. Moreover,

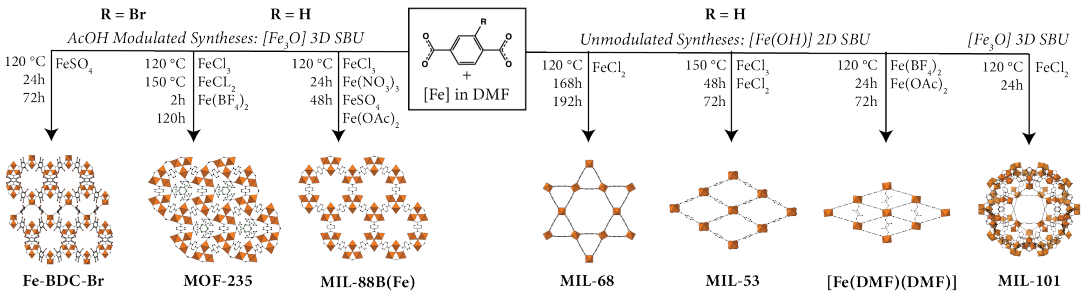

Figure 1.17: Scheme showing the diversity of the Fe-1,4-bdc MOF phase space together with the synthetic parameters established in Ref. 99 responsible for obtaining each phase. Colour scheme is as follows: Zn = orange polyhedra, O = orange polyhedra corners, C = black spheres, Br = brown spheres, N = blue spheres, Cl = green spheres. H atoms are omitted for clarity.

Fe-1,4-bdc MOFs are particularly attractive for biomedical applications due to the biocompatibility of the Fe metal [108].

Other phases within the Fe-1,4-bdc phase space include MIL-68, which is a large pore polymorph of MIL-53 with a rigid kagomé topology [109]; [Fe(DMF)(1,4-bdc)], which is the Fe^{2+} derivative of MIL-53 [106]; and MOF-235, a MOF with the same topology as MIL-88B but containing $[FeCl_4]^-$ counterions in the pores [110].

A recent study showed that synthetic parameters such as reaction time and temperature have a significant impact on the resulting Fe-1,4-bdc MOF phase, as well as the addition of an acid modulator and composition of the metal salt starting material (Fig. 1.17) [111]. In fact, two new Fe-1,4-bdc phases were discovered, underscoring the structural diversity to MOF systems that have already received significant study.

These findings highlight both the complexity of MOF phase spaces and the importance of systematically exploring and understanding the effects of synthetic parameters in controlling the formation of specific structures to ultimately enable the design and synthesis of MOFs with tailored properties and functionalities.

Isoreticular chemistry

The intricacy of MOF phase spaces complicates the targeted design of MOF structures, which is another pivotal factor in realising MOFs for the applications they carry such potential for. An important development in this regard was the concept of isoreticular chemistry [112]. This approach allows for the tailoring of MOF functionality and pore size whilst maintaining the topology.

The prototypical family of isoreticular MOFs is the IRMOF series [112]. These expand on MOF-5 — therefore oftentimes referred to as IRMOF-1 instead — while maintaining the **pcu** topology by replacing the 1,4-bdc linker with other ditopic linear analogues (Fig. 1.18a). Incorporating a longer linker, for example, results in enhanced gas sorption activities due to the larger pores [112], and the amino-functionalisation of 1,4-bdc (IRMOF-3) improves its catalytic performance for condensation reactions [116].

The application of isoreticular chemistry is not restricted to MOF-5 and the IRMOF series: both UiO-66 [117, 118] and MIL-53 [119] have reported isoreticular analogues, and MIL-88B is a member of the isoreticular MIL-88 series [104]. And by replacing the 2,5-dot linkers with elongated analogues, the size of the hexagonal pores in MOF-74 can be increased to a diameter of 85 Å, as granted by the packing of the organic linkers preventing interpenetration (Fig. 1.18b) [113].

It was later discovered that IRMOFs can accommodate more than one type of functionalised linker (Fig. 1.18c), which, for certain linker combinations and ratios, may result in selective gas uptake [114]. The ability to incorporate multiple linkers within the same framework adds to the versatility and complexity of MOFs, in turn leading to the emergence of another branch in the field known as 'multivariate'

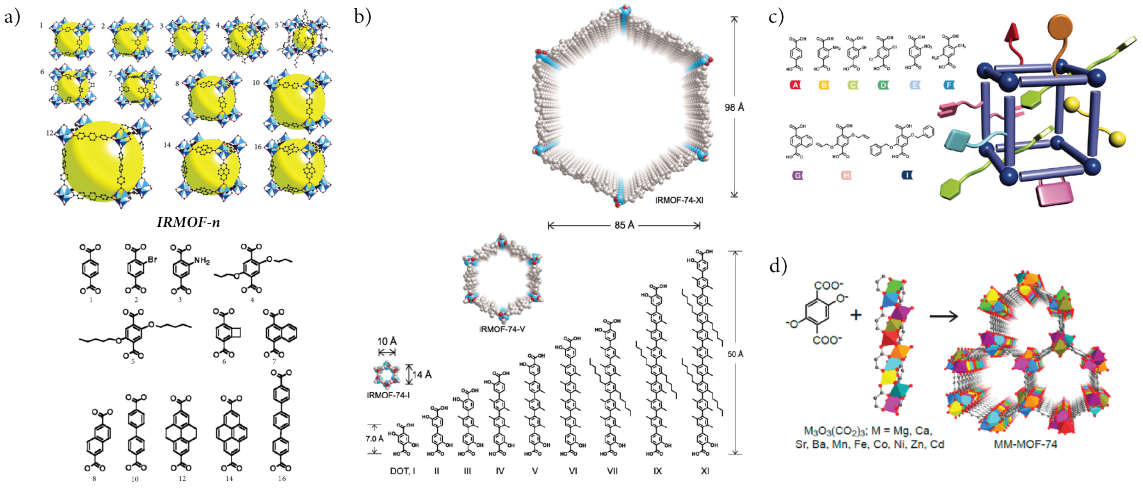

Figure 1.18: Isoreticular and multivariate chemistry. (a) Framework stuctures of the IRMOF series, showing the relevant linkers at the bottom. Colour scheme is as follows: Zn = red poyhedra, O = red spheres, C = black spheres, Br = brown spheres, N = blue spheres. The large yellow spheres represent the largest van der Waals spheres that would fit in the cavities without touching the framework. H atoms have been omitted, and only one orientation of disordered atoms are shown for clarity. (b) Framework structures of MOF-74 and its isoreticular analogues IRMOF-74-V and IRMOF-74-XI, indicating the size of the pores in Å. The relevant linker structure and lengths are shown at the bottom. Colour scheme is as follows: C = grey spheres, O = red spheres, M (Mg and Zn) = blue spheres. (c) Graphic representation of MTV-MOF-5, showing the relevant linkers on the left. (d) The structure of mixed-metal MOF-74. Colour scheme is as follows: C = grey spheres, O = red spheres, M (Mg, Ca, Sr, Ba, Mn, Fe, Co, Ni, Zn, and Cd) = coloured polyhedra. Figure (a) adapted from Ref. 112 with permission from AAAS, figure (b) adapted from Ref. 113 with permission from AAAS, figure (c) adapted from Ref. 114 with permission from AAAS, and figure (d) adapted from Ref. 115 with permission from ACS.

(MTV) MOFs [120]. This concept it not limited to the incorporation of different linkers; some MOFs can also host multiple metals within the same structure. For instance, MOF-74 has been synthesised with up to 10 divalent metals in its structure (Fig. 1.18d) [115].

Geometry mismatch

Whilst isoreticular chemistry can introduce complexity through composition (*i.e.* MTV-MOFs), it does not affect the topology of MOF structures. The concept of geometry mismatch aims to steer away from this method in order to achieve more complex, non-default topologies [121]. The approach of geometry mismatch shares similarities with realising the procrystalline state, being the combination of seemingly incompatible building blocks *via* the incorporation of low-symmetry linkers (*e.g.* twisted, zigzag, or bent) into MOF structures (Fig. 1.19).

For example, the combination of a 4-c Cu paddle wheel and 1,4-bdc typically results in the 2D MOF-2, characterised with the **sql** topology [81]. This low dimensionality of MOF-2 is caused by the 1,4-bdc linker carboxylates being coplanar.

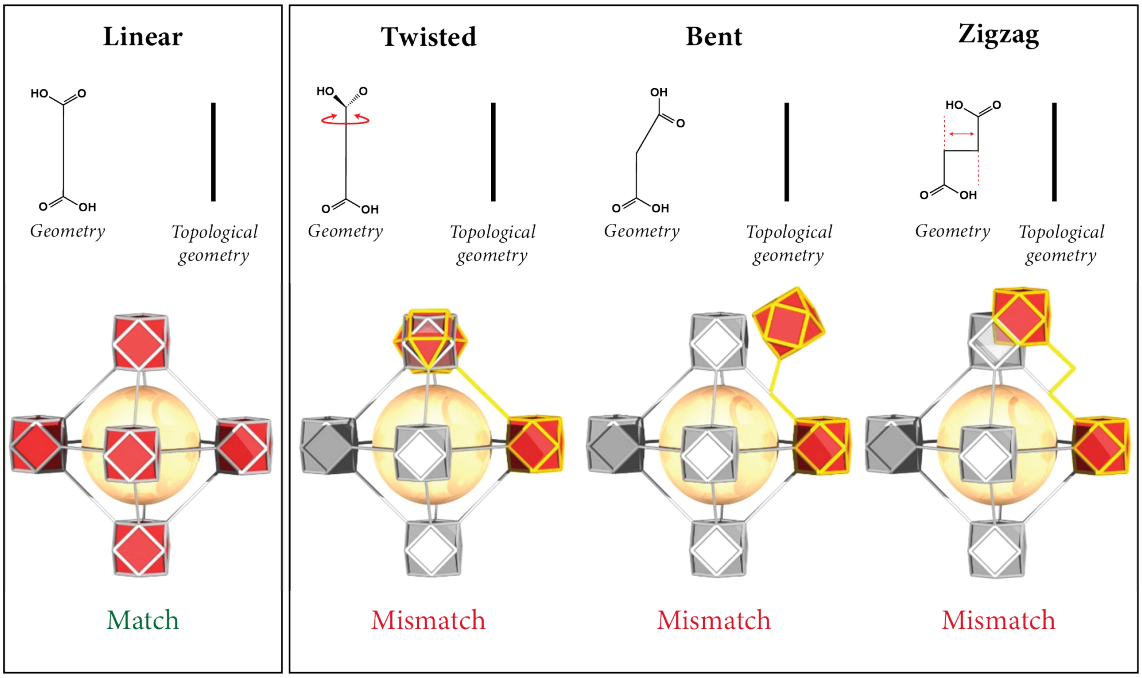

Figure 1.19: Graphic showing the concept of geometry mismatch, in which non-default topologies are achieved by incorporating linkers that are twisted, bent, or zigzag. Figure adapted from Ref. 121.

However, by introducing a bromine group onto the 1,4-bdc ring (*i.e.* 2-Br-1,4-bdc), steric hindrance is initiated, in turn causing one of the carboxylates to twist by 90°. As a consequence, the combination of 2-Br-1,4-bdc with the same 4-c Cu paddle wheel results in a 3D structure with the **nbo** topology [122].

Zigzag ligands such as 2,6-naphthalene dicarboxylic acid (2,6-ndc) are particularly interesting as they can be characterised by the transversal parameter, which takes into account both the width (w) and the height (h) of the linker, reflecting their ability to elongate transversally [123]. This stretching in turn breaks the colinearity of carboxylates. As a consequence, zigzag linkers do not match the perfect alignment of (UiO-66 characteristic) hexanuclear Zr-clusters, for example, which leads to MOFs of the **bcu** — rather than the expected **fcu** — topology (Fig. 1.20a). Notably, the **bcu** net is derived from the **fcu** topology, with four missing ligands on each metal cluster.

Bent ditopic linkers are best known to give rise to discrete metal–organic polyhedra (MOPs) when combined with paddle-wheel metal clusters [124, 125]. In this case, the influence of the angle of the bend is clear, enabling isolation of MOPs of various geometries and distinct metal/ligand content. In combination with metal

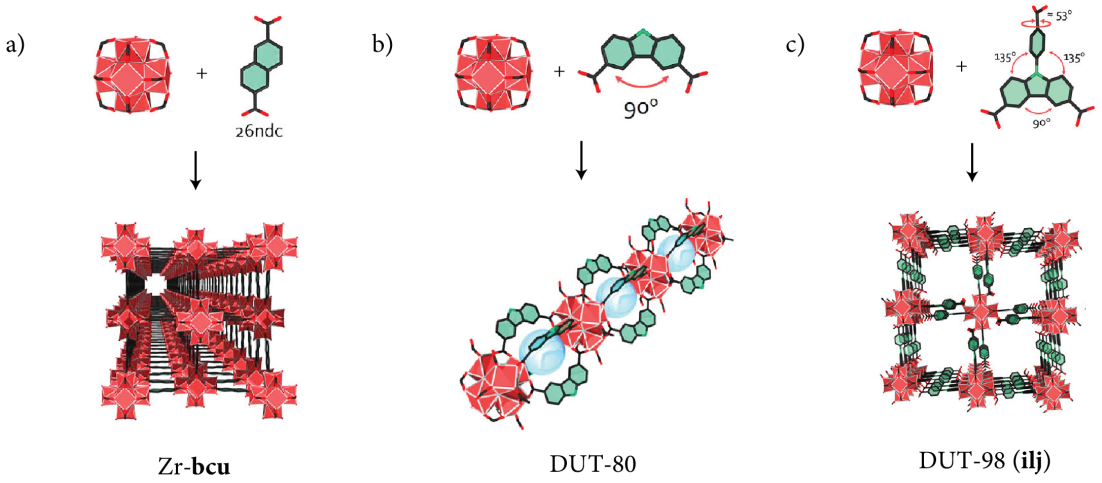

Figure 1.20: Examples of MOFs with non-default topologies resulting from combining Zr-clusters with low-symmetry linkers. (a) The linker 2,6-ndc, which in combination with the Zr-cluster gives rise to a MOF of the **bcu** topology. (b) The linker cdc, which in combination with the Zr-cluster gives rise to the 1D-polymer DUT-80. (c) The linker bcdc, which in combination with the Zr-cluster gives rise to DUT-98 of the topology **ilj**. Figures adapted from Ref. 121 with permission from ACS.

clusters of other geometries, however, the predictability of the topology becomes much more complex since the numerous possibilities of angles and ways of orienting the linkers around the metal clusters prevent straightforward rationalisation. Combining the 90°-bend linker 9H-carbazole-3,6-dicarboxylate (cdc) with the hexanuclear Zr-cluster, for example, results in the one-dimensional (1D) coordination polymer DUT-80, where the 8-c Zr clusters are quadruple-bridged to each other (Fig. 1.20b) [126]. The influence of the angle between linker carboxylates is significant; combining the Zr-cluster with linkers bent at a larger angle of 150° resulted in MOFs of the **reo** topology [127].

Geometry mismatch does not only apply to ditopic linkers; polytopic linkers of various angles and/or twists may also be considered to obtain a high variety of topologies. For example, the 1D coordination polymer DUT-80 mentioned above could be connected *via* the tritopic ligand 9-(4-carboxyphenyl)-9H-carbazole-3,6-dicarboxylate (bcdc) — thus maintaining the 90° bend — to give the unprecedented (3,12)-c net belonging to DUT-98, which, with the topology **ilj**, exhibits high structural flexibility (Fig. 1.20c) [126].

1.4.2 Porosity

A characteristic of conventional framework materials is the formation of non-close-packed open structures, facilitated by strong directional bonding. Zeolites, which exhibit high porosity, serve as a prime example; in turn used as commercial adsorbents and catalysts [128]. In MOFs, however, the metal clusters are connected by organic linkers that are longer than the single atoms typically observed for most other frameworks. As a result, MOFs have a significantly more open structure and thus higher porosity than frameworks of the same topology. This unique property has been the focal point of MOF chemistry ever since their discovery [129–131]. Consequently, scientists have attempted to achieve extreme porosity by incorporating long, rigid organic linkers in MOF structures. The current record surface area is held by DUT-60 (7839 m^2 g^{-1}): a single gram could cover one-and-a-half football fields (Fig 1.21a) [132]. The largest predicted surface area for a MOF, however, currently stands at 14937 m^2 g^{-1} [133].

Because of their high surface area and internal volume, MOFs have been extensively investigated for various applications involving gas adsorption (*e.g.* storage) [81, 112, 135, 136]. The most promising applications exploit both the porosity and chemical tunability of MOFs, rather than relying solely on pore volume and geometric structure. Examples of such applications include gas separation [137, 138] and catalysis [139]. The separation of CO_2 gas has been particularly important due to its environmental relevance [140–142]. MOF structures with open metal sites (*e.g.* HKUST-1, MOF-74) are particularly suitable for these applications as they allow for interactions between the guest (*i.e.* the gas) and the metal cations [139, 140, 143–145]. This property enables MOFs to combine the advantages of heterogeneous catalysis, such as stability and ease of recyclability, with those of homogeneous catalysis, such as well-defined active sites and high active site concentration for specific activity [139]. In addition to open metal sites, catalytic activity in MOFs may originate from catalytically-active linkers [146, 147] and encapsulated molecular or nanoparticle catalysts [148, 149]. Porous MOFs have also been exploited for biomedical applications, including targeted and pharmacokinetically

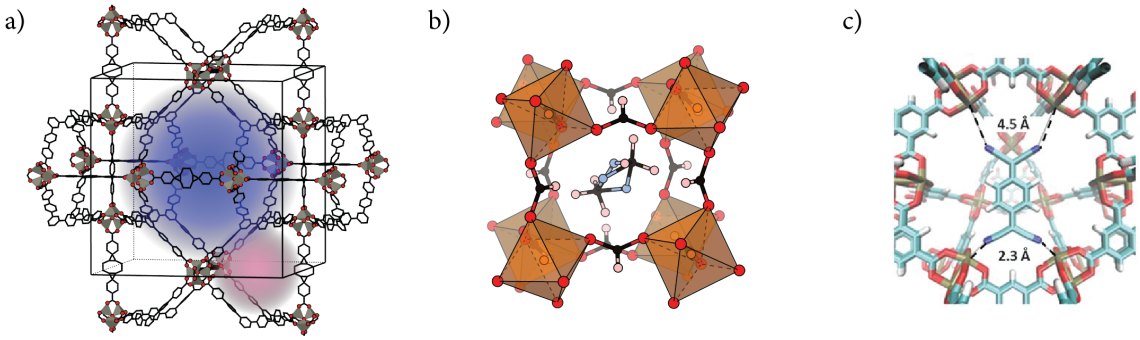

Figure 1.21: Porosity in MOFs. (a) Unit cell of DUT-60, which holds the current record internal surface area for a MOF. Colour scheme is as follows: Zn = grey tetrahedra, C = black spheres, O = red spheres. H atoms are omitted for clarity. The large blue and pink spheres indicate the two different pore environments. (b) Crystal structure of the ferromagnetic and antiferroelectric perovskite MOF dimethylammonium manganese $[(CH_3)_2NH_2][Mn(HCOO)_3]$, showing a single ReO_3 type captivity containing one Me_2NH_2 cation, with the N atom disordered over three sites. Colour scheme is as follows: Fe = purple polyhedra, C = black spheres, O = red spheres, N = blue spheres, H = pink spheres. (c) The lowest energy configuration of TCNQ@HKUST-1, showing the arrangement of the TCNQ molecule in the cavity bridged to the copper paddlewheels along the (111) lattice plane, as calculated from DFT. Figure (c) adapted from Ref. 134.

controlled drug delivery [150–152].

In this way, host-guest interactions play a crucial role in MOF chemistry. These interactions are inherently non-covalent, and thus the configuration of guest molecules tends to be disordered. In some cases, for example if MOFs are charged, the interactions are sufficiently strong to induce the ordering of guest orientations. One example is the ordering of the imidazolium cation in cyanoelpasolites at lower temperatures, as highlighted in section 1.2.1 [9]. Similarly, the Me_2NH_2 cation groups positioned within the pores of the MOF perovskite $[(CH_3)_2NH_2][Mn(HCOO)_3]$ order antiferroically at ∼8.5 K through hydrogen bonding (Fig. 1.21b) [153]. The dipolar ordering occurring via the 'A' site of the perovskite enables the magnetic 'B' sites to create a class of materials displaying simultaneous magnetic and electric order, known as multiferroics [154].

One further example illustrating how functional properties may arise from ordering of guests in MOF pores is the host-guest system TCNQ@HKUST-1 (TCNQ = 7,7,8,8-tetracyanoquinodimethane) [134]. In this system, the TCNQ is preferentially arranged along the (111) lattice plane to bridge the binuclear copper paddlewheels of HKUST-1, thereby introducing tunable electrical conductivity to an otherwise insulating parent material (Fig. 1.21c) [155].

1.4.3 Flexibility

In this thesis, the term 'flexibility' refers to the large-scale structural behaviour displayed by MOFs upon exposure to external stimuli (*e.g.* pressure). By 'large-scale,' I refer to observable (static) changes in the overall structure, as opposed to localised alterations. These changes may be readily detected through methods such as powder and single crystal diffraction. Flexibility includes the anomalous phenomena of negative thermal expansion (NTE), negative linear compressibility (NLC), and negative Poisson's ratio (NPR) [156], as well as guest-responsive behaviour such as the 'breathing effect' [157].

NTE, NLC and NPR

NTE and NLC both involve a reduction in total volume with an expansion along a specific direction upon heating and under hydrostatic pressure, respectively [158, 159]. Materials that exhibit NPR, often referred to as 'auxetic' materials, on the other hand, expand laterally when stretched longitudinally [160, 161].

MOFs may exhibit either NTE or NLC as permitted through their structure consisting of rigid struts and flexible hinges [163]. The strength of the NTE and/or NLC effect depends on the relative softness of the hinges and hardness of the struts. MOFs with topologies resembling a wine-rack or honeycomb motif are often predisposed to exhibit NTE and NLC, as they are stiffer and more compressible in specific directions. Materials that display NTE are particularly attractive for applications including electronics [164, 165], aerospace technologies [166], high precision optical mirrors [164], fibre optic coating [167], and even tooth fillings [168], whilst those ex-

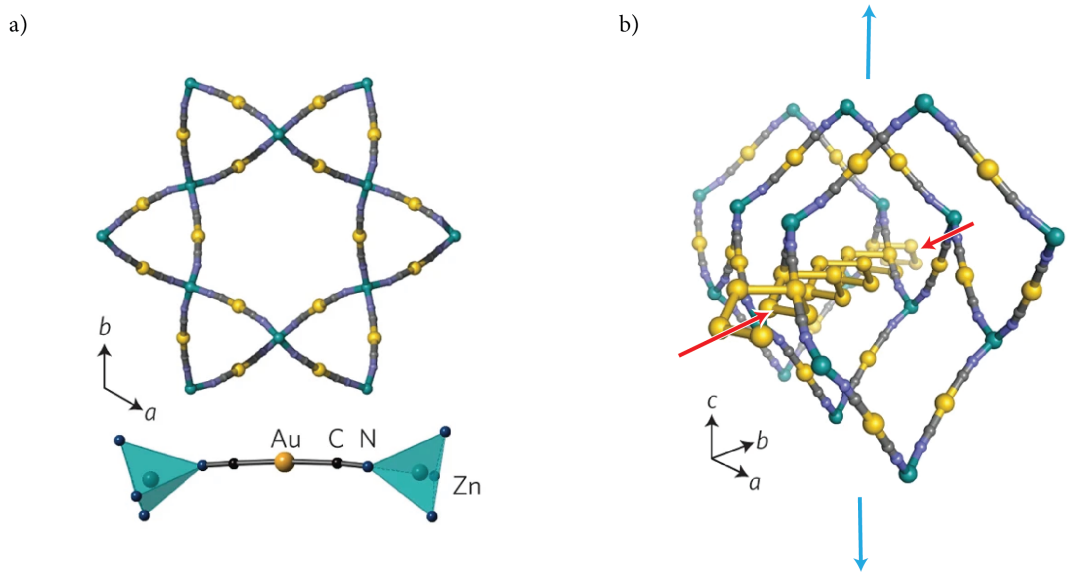

Figure 1.22: The structure of $Zn[Au(CN)_2]_2$, which exhibits both NTE and NLC. (a) One of the six β-quartz-like nets of $Zn[Au(CN)_2]_2$ viewed down its crystallographic *c*-axis, showing how it consists out of ZnN_4 tetrahedra connected *via* flexible dicyanoaurate (N–C–Au–C–N) molecular linkers. (b) Alternative view of the net shown in (a) to highlight the honeycomb-like nature of the hexagonal pores of $Zn[Au(CN)_2]_2$, and also the cross-bracing effect of helical aurophilic chains running perpendicular to the *c*-axis. Colour scheme is as follows: Au = gold spheres, Zn = teal spheres and tetrahedra, C = black spheres, and N = dark blue spheres. Figures adapted from Ref. 162 with permission from Springer Nature.

hibiting NLC are suitable for piezoresponsive applications such as pressure sensors and 'smart' body armour [169–171].

It is important to note that NTE and NLC are not thermodynamically linked, yet they are related by moiety flexibility favoured by both conditions [172, 173].

Although not a MOF, the largest and most persistent NLC to be reported for a material has been observed for a framework: $Zn[Au(CN)_2]$, with K = –42 (5) TPa^{-1} (that is, a $\sim$ 4.2% reduction in length for each 1 GPa increase in pressure), at $0 < p < 1.8$ GPa [162]. This large effect arises from helical aurophilic ($Au^+ \ldots Au^+$) chains acting as springs, which in turn amplify the perpendicular uniaxial expansion of the honeycomb structure along the c-axis by contracting under pressure (Fig. 1.22). $Zn[Au(CN)_2]_2$ also exhibits NTE, albeit with a much reduced relative magnitude than the NLC because the spring-like response is induced by pressure. Other examples of metallocyanides that express significant NLC and NTE include $Ag_3[Co(CN)_6]$ [172, 174] and $KMn[Ag(CN)_2]_3$ [175]. In both cases, this behaviour is attributed to covalent bonds acting as hinges in the wine-rack topology, where the dimensions of the flexible cyanide lattice are dictated by low-energy $Ag^+ \ldots Ag^+$ interactions.

In all these systems, the NTE and NLC occur in the same direction. However, this is not always the case. In $[Ag(ethylenediamine)]NO_3$, for example, the two phenomena occur in perpendicular directions due to positive coupling between thermal expansivity and compressibility as a result of void-filling NO_3^- anions [176].

Prototypical MOFs such as HKUST-1, MIL-53, and MOF-5 (as well as its isoreticular analogues) have also been found to exhibit NTE [177–182]. In the case of MOF-5, this behaviour is attributed to the twisting, rotation, and libration of the 1,4-bdc linker — also referred to as the 'trampoline mode' [179, 183] — as well as an acoustic mode [180]. The wine-rack topology of MIL-53 is responsible for its NTE and NLC effects [178].

Another MOF, Ag(mIm), displays NLC (K = –4.32 TPa^{-1}) along the c-axis at $0 < p < 1$ GPa, after which it switches to positive linear compressibility [184]. In this case, chains of $Ag^+ \ldots Ag^+$ interactions parallel to the a-axis act as spindles

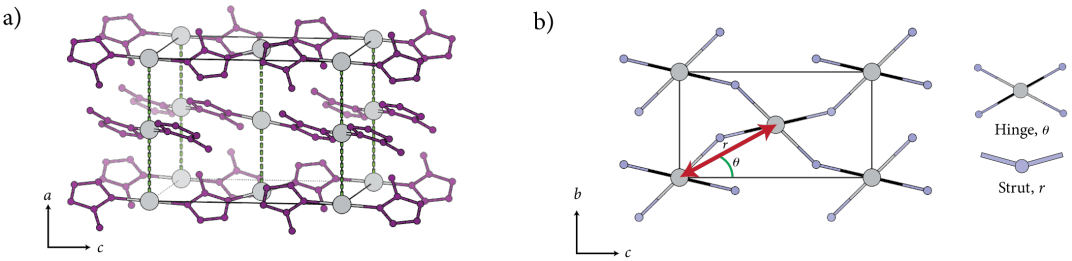

Figure 1.23: The structure of Ag(mIm), which exhibits both NTE and NLC. (a) The crystal structure of Ag(mIm). The $Ag^{+} \ldots Ag^{+}$ interactions are represented with dotted green lines along the *a*-axis. Colour scheme is as follows: Ag = grey spheres, mIm anions = purple spheres. H atoms are omitted for clarity. (b) Alternative representation of the structure shown in (a) (looking down the *a*-axis) in terms of hinges and struts, as expressed in θ and r, respectively.

of the Ag–mIm–Ag hinges, with the mIm linkers serving as struts (Fig. 1.23). Competition between the flexing of the hinge angle (θ) and strut length (r) dictates the compressibility; with the former and latter dominating at lower and higher pressures, respectively.

Whilst it is well-established which structural features of frameworks tend to result in NTE and NLC, the correlation for NPR remains to be identified [185]. Generally, NPR is prevalent in MOFs with lower-than-cubic symmetry. However, it is worth noting that studies on auxetic behavior in MOFs are typically limited to calculations of elastic tensors using techniques such as DFT, primarily due to the specificity of the NPR direction and the non-trivial nature of experimental setups.

Using both Raman and IR spectroscopy as well as DFT calculations, for example, an auxetic response of –0.3 was found in HKUST-1 along the $\langle 110 \rangle$ direction [186]. The hypothesised mechanism responsible for this observation involves the low-energy vibrations of the inorganic–organic clusters, resulting in a rotation when stretched. This rotation allows for elongation in the transverse $\langle 1\bar{1}0 \rangle$ direction.

Guest-responsive behaviour

I previously highlighted the importance of host-guest interactions in MOF chemistry. These interactions may also contribute to the flexible behaviour of MOFs, such as the 'breathing effect'. This phenomenon involves the reversible expansion and

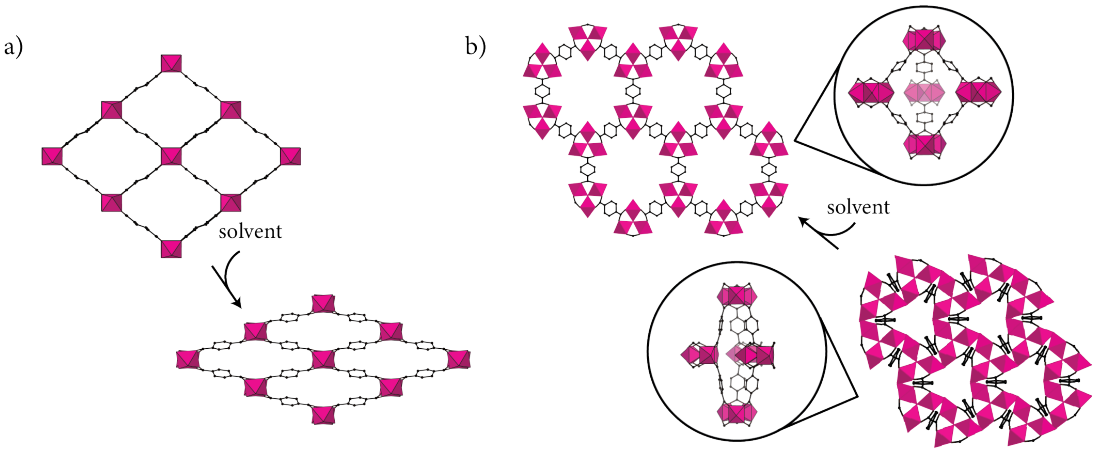

Figure 1.24: The breathing effect, as demonstrated by the *op* and *cp* phase of (a) MIL-53 and (b) MIL-88B, which is stimulated by the addition/removal of guest molecules. The colour scheme is as follows: Cr = pink spheres, C = black spheres. Guest molecules and H atoms are omitted for clarity.

contraction of the framework upon guest uptake or removal [157]. As mentioned previously, both MIL-53 and the MIL-88 series exhibit the breathing effect, of which MIL-88C was found to expand up to 270% in volume upon guest adsorption [187–189]. Accordingly, these MOFs exist in open-pore (*op*) and closed-pore (*cp*) forms (Fig. 1.24). In the case of MIL-53, the *op* form is achieved upon the removal of solvent molecules, whereas in the MIL-88 series the opposite is observed (*i.e.* upon the uptake of guests). Due to this flexibility, MIL-53 and the MIL-88 series are excellent gas adsorbents, with the selectivity strongly dependent on the nature of the organic linker. In fact, the swelling amplitude of the MIL-88 MOFs was found to be tunable by introducing functional groups onto the linkers, showing a clear dependence on steric hindrance [105].

Such guest responsive behaviour is not limited to the breathing effect; other examples include the reversible gate-opening of ZIF-7 and ZIF-8 through ligand rotations [142, 190], which in turn is responsible for the capability of the ZIFs to admit molecules that would appear too large to fit through the pores [191, 192], and gating of doubly interpenetrated MOFs [193]. Particularly interesting is the molecular buckling observed for DUT-49 upon adsorption of methane gas [194]. Namely, DUT-49 undergoes a colossal framework transformation causing the spon-

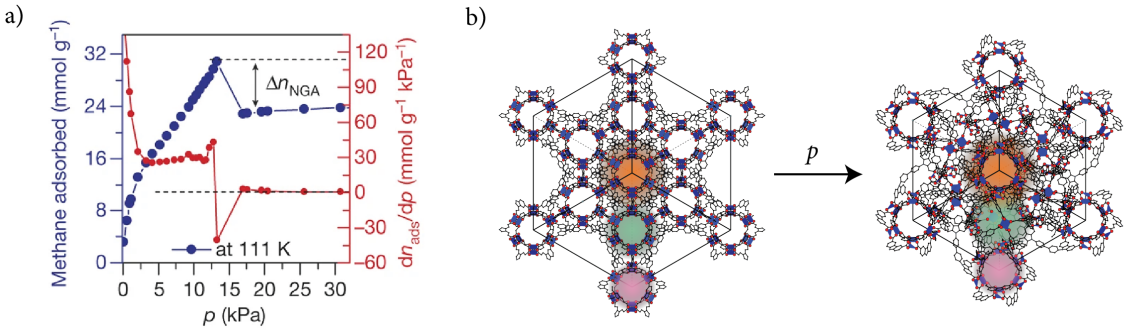

Figure 1.25: Negative gas adsorption as observed for DUT-49. (a) The adsorption isotherms (blue) and corresponding derivatives (red) of DUT-49 for methane gas at 111 K. (b) The structure of DUT-49 before (left) and after (right) the desorption of methane gas, showing the buckling of molecular components. The three different pore environments are indicated with the orange, green, and pink sphere. The colour scheme is as follows: Cu = dark blue polyhedra, C = black spheres, O = red spheres, N = blue spheres. H atoms are omitted for clarity.

taneous desorption of gas despite the increase in pressure, also known as negative gas adsorption (NGA) (Fig. 1.25).

Notably, the connectivity of the bonds is preserved in all these examples. However this preservation does not always apply; MOF-123 transforms to its interpenetrated analogue, MOF-257, upon coordination to DMF [195]. This process is fully reversible.

Softness

Finally, it is important to note that, while certain MOF topologies allow for flexibility-related phenomena such as the breathing effect, all MOFs are flexible with regard to their compressibility. Namely, the relatively weak nature of the bonds (compared to *e.g.* the Si–O bonds in zeolites) and openness of the frameworks make MOFs rather soft; *i.e.* they have a low bulk modulus. MOFs with a higher connectivity — and therefore higher density — tend to be more difficult to compress. For example, the very open MOF-5 has a bulk modulus of 12.3–20.0 GPa [182, 196–205] and was computationally found to collapse at ∼2 GPa [206], whilst HKUST-1 has a bulk modulus of ∼30 GPa [204, 207, 208] and remains crystalline up to 4.2 GPa [207].

1.5 Thesis aim and outline

The objective of this thesis is to introduce complexity in MOF structures by lowering the symmetry of their constituent building blocks. In this regard, two components need to be considered: the (i) metal cluster and (ii) organic linker. Incorporating a low-symmetry linker is a more straightforward task compared to reducing the symmetry of the SBU, as most clusters have relatively high symmetries. Therefore, the focus was directed towards the linker component. However, there is a vast number of potential low-symmetry linker candidates to choose from. Given the importance of 1,4-bdc as an element of many canonical MOFs, we have focused on isophthalic acid, also known as 1,3-benzene dicarboxylic acid (1,3-bdc). It consists of a single benzene molecule with two carboxylate groups attached to the 1- and 3-carbon atoms, resulting in a bent configuration (Fig. 1.26a). As a result, the D_{2h} point group symmetry of 1,4-bdc is reduced to C_{2v} (Fig. 1.26b).

In addition to this point symmetry lowering, it is important to note that the resonance effects of 1,3-bdc may differ from 1,4-bdc as they are governed by a different electronic structure. In turn, this difference may have an impact on the flexibility in torsional motion of the carboxylates with regards to the benzene ring *i.e.* the torsion angle (Fig. 1.26c), possibly introducing further complexity.

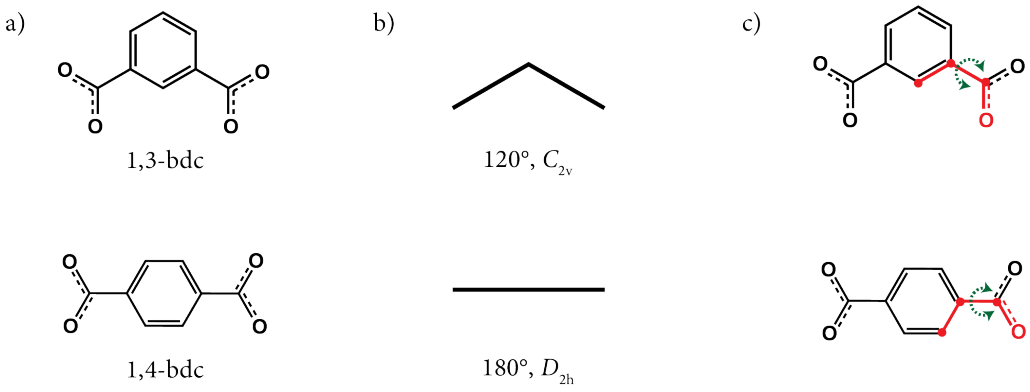

Figure 1.26: Origin complexity of (a) 1,3-bdc as compared to 1,4-bdc: (b) the bent *vs* linear shape and (c) difference in torsion angle flexibility. For both 1,4- and 1,3-bdc, the dihedral angle corresponding to the torsion angle is indicated in (c) for one of the carboxylates by highlighting the relevant C–C–C–O bonds in red.

However, to the best of my knowledge, the literature does not report on the (individual) torsional motion of organic linker carboxylates in MOF structures. Instead, studies have focused on the rotor behaviour of organic linkers — including 1,4-bdc and 1,3-bdc — in MOF structures *i.e.* the rotational motion of the benzene ring whilst the carboxylate groups remain planar [209]. In the case of 1,4-bdc, the linker typically adopts a planar conformation due to resonance effects. This is observed in MOF-5, for example [88], for which solid-state NMR and DFT calculations estimated the rotational energy barrier of 1,4-bdc to be $\sim$ 50 kJ mol^{-1} [210] and within the range of 51–63 kJ mol^{-1} [211, 212], respectively. Accordingly, the torsional potential curve of 1,4-bdc exhibits an energy minimum at 0° and a maximum at 90°, signifying that there is an energy barrier to overcome for the benzene ring to rotate (Fig. 1.27) [213] . The energetic landscape of 1,3-bdc, on the other hand, is characterised by a shallow potential well at low rotational angles (Fig. 1.27) [214, 215]. As a consequence, the benzene ring may undergo large-amplitude oscillations or librations, but no full (*i.e.* 90°) rotations.

Clearly, these benzene ring rotations differ from the individual torsional motions of the carboxylates, as is considered in this thesis. Yet, these earlier studies underscore the contrast between the two linkers, driven by their distinct electronic

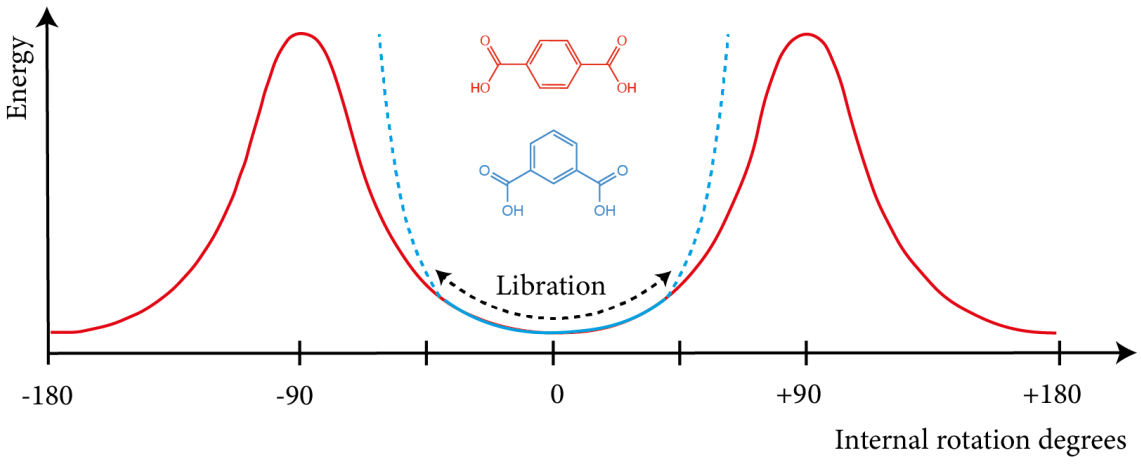

Figure 1.27: Schematic of the torsion potential curves for 1,3- and 1,4-bdc when considered as rotors (*i.e.* rotation of the benzene ring as opposed to individual carboxylates), showing that in the case of 1,3-bdc, large amplitude rotations are hampered by the angle of connectivity, in turn only enabling small-amplitude librations, whereas 1,4-bdc may achieve rotations up to 90°. Figure adapted from Ref. 209 with permission from MDPI.

structures.

Interestingly, there are relatively few reports in the literature on MOF structures with 1,3-bdc incorporated. This point was noted in Ref. 121 in the context of UiO-66 analogues. Instead, the linker is commonly encountered in studies on the formation of discrete molecular cages [124, 216].

Given that the combination of 1,4-bdc and Zn (typically) results in the well-known MOF-5, we decided to focus on understanding the phase space accessible by combining 1,3-bdc with Zn. Again, there is little account of Zn-1,3-bdc MOFs in the literature, possibly indicating the phase space to be so complex (or, sparse) that it had not yet been successfully studied.

The complexity we sought to explore may take on multiple different forms. First, the incorporation of the low-symmetry linker onto a periodic lattice can introduce structural complexity due to the increased degrees of freedom [7, 80]. Second, the Zn-1,3-bdc phase space itself may exhibit complexity, such as a lack of phase reproducibility or challenges in applying reticular chemistry principles. To investigate these aspects, synthesis experiments were repeated under different conditions, including the addition of substituted and elongated 1,3-bdc linkers to explore the applicability of reticular chemistry. Furthermore, the significance of the 120° bend was investigated by introducing other bent linkers, such as 2,5-thiopene dicarboxylic acid (2,5-tdc).

The main characterisation technique employed in this thesis is that of single crystal X-ray diffraction (SCXRD), which, in conjunction with powder X-ray diffraction (PXRD), enabled the analysis of the obtained Zn-1,3-bdc MOF structures. These experiments were conducted under both ambient and extreme conditions to probe the flexibility or softness of the MOF samples. Gas adsorption experiments were also performed to measure porosity, and other experimental techniques including extended X-ray absorption fine structure (EXAFS) aided in determining the chemical environment of samples. In addition, computational approaches such as Monte Carlo (MC) modelling and density functional theory (DFT) aided in the validation

of experimental data. Chapter 2 provides a comprehensive overview of the theoretical foundations of all the techniques utilised in this thesis, the detail of which is informed by the extent to which each technique was used subsequently in my research.

Chapter 3 provides an account of the synthesis and average-structure solution of all obtained crystalline Zn-1,3-bdc MOFs: namely 'TRUMOF-1', 'MOX-2', 'MOX-3', 'MOX-4', and 'MOX-5'. The chapter includes an outline of the topology of each sample, allowing for literature searches to assess their novelty. Additionally, notable structural features that may contribute to interesting properties are discussed and analysed in detail.

Chapter 4 explores structure-property relationships for MOX-2 and MOX-4, two MOFs with structures exhibiting wine-rack and helix motifs *i.e.* structural features that have been associated with the emergence of both NTE and NLC. Accordingly, the flexibility of these MOFs was probed by means of variable-temperature and variable-pressure single-crystal and powder X-ray diffraction measurements. These experiments aim to provide insights into how changes in temperature and pressure affect the structural properties of MOX-2 and MOX-4, shedding light on their potential NTE and NLC behaviours.

In Chapter 5, the origin of diffuse scattering observed in the diffraction patterns of MOX-3 is investigated. The analysis includes comparison of experimental and simulated total scattering data as well as the generation of 3D-ΔPDFs. The chapter presents the results of these analyses and discusses how the observed diffuse scattering patterns in MOX-3 arise from dynamical contributions.

Our focus then shifts to disordered Zn-1,3-bdc MOFs. To introduce this topic, Chapter 6 serves as a literature review on correlated disorder in MOFs. This literature review outlines three primary types of correlated disorder and thus complexity

observed in MOFs: (i) correlated vacancies, (ii) compositional disorder, and (iii) orientational disorder. These types of disorder are discussed within the context of selected canonical systems, highlighting their nature and characteristics. The chapter concludes with a forward-looking discussion that highlights the future challenges and opportunities in the field of correlated disorder in MOFs, ultimately providing the necessary scientific background to understand the unique structural features and properties of TRUMOF-1 in relation to the broader field of MOFs with correlated disorder.

Chapter 7 represents the main body of work carried out during my DPhil project, focusing on the characterisation of the aperiodic topology of TRUMOF-1 and exploring its chemical and physical properties. My approach has included generation of a 3D Truchet-tiling model and subsequent validation through comparison to experimental data, including diffuse scattering. A particular emphasis is placed on understanding how the aperiodic connectivity of TRUMOF-1 influences its properties. This aspect was investigated through various experimental techniques, including gas adsorption measurements, thermogravimetric analysis, and high-pressure single crystal X-ray diffraction. Moreover, because TRUMOF-1 has a related chemical composition to that of MOF-5, the significance of its aperiodic connectivity could be probed by performing and comparing measurements for both MOFs. This comprehensive examination ultimately provides valuable insights into the structure-property relationships in TRUMOF-1 as well as highlights the unique characteristics and potential applications of such aperiodic 'TRUMOFs'.

Finally, Chapter 8 summarises the results presented throughout the thesis and aims to tie all findings together by discussing the overall Zn-1,3-bdc phase space. This summary includes an analysis of the significance of the linker's flexibility in torsion angle, by performing structure searches and extracting linker torsion angles for both 1,3-bdc- and 1,4-bdc-Zn MOFs for comparison. Findings from these structure searches provide an explanation for the observations made, being that specific synthetic parameters are required to obtain the disparate MOF structures as well

as the inability to systematically apply reticular chemistry. Ultimately, by elucidating the relationship between the linker's bent configuration and flexibility, synthetic parameters, and the resulting MOF structures, this chapter contributes to a deeper understanding of the design and synthesis of complex MOF phases with tailored properties.

Chapter 2

Methods

2.1 Summary

This chapter provides an overview of the theory behind analytical techniques employed in this thesis to characterise the structure, topology, and physical and chemical properties of MOFs.

The first section focuses on techniques used for structural characterisation and topology determination. These include single-crystal and powder X-ray crystallography, which provide information about the average atomic arrangement in crystals; diffuse scattering and 3D difference pair distribution function, which report on the local crystal structure; and extended X-ray absorption fine structure (EXAFS), which allows for the determination of element-specific local environments. Computational tools used to simulate the local structure of samples (*i.e.* Monte Carlo and density functional theory) are also discussed in this section. Infrared and Raman spectroscopy are introduced as vibrational spectroscopic techniques to further provide information on the chemical bonding. Additionally, nuclear magnetic resonance (NMR) was used to determine the composition of organic linkers from decomposed MOFs. This section concludes with a brief discussion on topology determination approaches, which are used to identify and classify the underlying network topology of MOFs.

The second section of this chapter highlights techniques used to probe chemical and physical properties of MOFs, such as surface area and mechanical stability. This includes variable temperature and high-pressure crystallography, which are described as methods to probe the structural behaviour and flexibility of MOFs under different conditions. A brief background on gas adsorption is also provided as a means of determining the surface area and porosity. And finally, thermogravimetric analysis (TGA) is introduced as a technique to study the thermal stability and decomposition behaviour.

2.2 X-ray crystallography

The structures of all MOFs described in this thesis were characterised using X-ray diffraction techniques. To understand how the scattering of X-rays can lead to the determination of the atomic structure, I will provide a brief overview of crystallography and scattering theory, as drawn in large parts from Refs. 33, 217, and 218.

2.2.1 Crystals and symmetry

To understand the theory of diffraction, it is important to define a crystal and recognise the significance of symmetry. The latter is reflected by the information needed to solve the crystal structure: the (i) lattice parameters; (ii) space group symbol, and (iii) atomic positions in the asymmetric unit.

According to the International Union of Crystallography (IUCr), the currently accepted definition of a crystal is that of 'a material which exhibits essentially a sharp diffraction pattern' [219]. However, I will describe this theory in the context of crystals as translationally periodic solids *i.e.* excluding aperiodic crystals such as quasicrystals.

Crystal lattice

The periodicity of a crystal is described by a periodic array of lattice points, which corresponds to the underlying crystal lattice. The lattice vectors $\mathbf{R} = U\mathbf{a} + V\mathbf{b} + W\mathbf{c}$ define this lattice, where $\mathbf{a}$, $\mathbf{b}$, and $\mathbf{c}$ are vectors that specify the crystallographic axes given by $|\mathbf{a}| = a, |\mathbf{b}| = b, |\mathbf{c}| = c$, respectively. The values of U, V, and W are integers. The angles between the vectors $\mathbf{b}$ and $\mathbf{c}$, $\mathbf{c}$ and $\mathbf{a}$, and $\mathbf{a}$ and $\mathbf{b}$ are represented by the parameters α, β, and γ, respectively. Thus, these angles define the orientation of the crystallographic axes with respect to each other. The set of a, b, c, α, β and γ are called the lattice parameters of the unit cell.

The three-dimensional translational periodicity of crystals is described by seven crystal classes based on the relationship between the lattice vectors: triclinic, monoclinic, orthorhombic, tetragonal, trigonal, hexagonal, and cubic (Fig. 2.1). Each

class exhibits different levels of symmetry. For example, in the cubic lattice, the lattice parameters are equal ($a = b = c$) and the angles between the lattice vectors are 90° ($\alpha = \beta = \gamma = 90°$). This results in a highly symmetric lattice. In contrast, the triclinic lattice has lower symmetry; its lattice parameters are not equal ($a \neq b \neq c$), and the angles between the lattice vectors are neither equal nor 90° ($\alpha \neq \beta \neq \gamma \neq 90°$).

Finally, the 14 distinct Bravais lattices are obtained by considering the centering of the cell. These include:

- P (primitive): No additional lattice points beyond the corners.
- F (face-centred): Additional lattice points at the centres of the faces.
- I (body-centred): Additional lattice points at the centre of the cell.
- C (c-centred): Additional lattice point at the centres of the faces parallel to the c-axis.

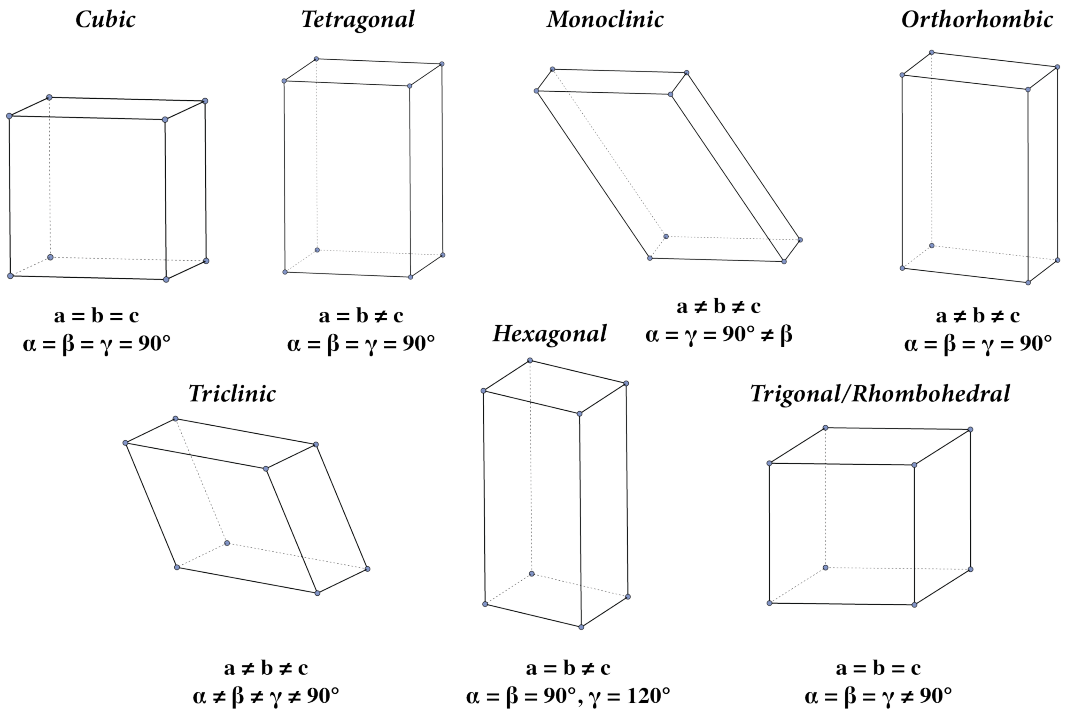

Figure 2.1: The seven crystal classes (from left to right): cubic, trigonal, monoclinic, orthorhombic, triclinic, hexagonal and trigonal/rhombohedral.

Space group

The unit cell of a crystal is the smallest repeating unit of the crystal structure that respects the crystal symmetry. Accordingly, there is no unique unit cell. In addition to the translational symmetry imposed by the lattice, a crystal structure may possess the following symmetry elements: (i) the identity operation, denoted as '1', which is (trivially) possessed by all structures; (ii) rotations, which are represented by integers *e.g.* '2' to indicate a 2-fold rotation; (iii) reflections, denoted as 'm', which involve reflecting the crystal structure through a plane; and (iv) inversion, represented as '$\bar{1}$', which involves inverting the crystal through a point (*i.e.* an inversion centre).

The combination of these symmetry elements gives rise to the 32 crystallographic point groups. Point- and translational- symmetry elements can combine in crystals to generate additional operations: (v) screw axes, denoted as *e.g.* '2_1', which involve a rotation followed by a translation along the same axis; and (vi) glide planes, denoted as *e.g.* 'a-glide', which involve a reflection followed by a translation along a direction normal to the reflection plane.

Combining these symmetry elements with the 14 Bravais lattices results in 230 space groups, all of which are fully tabulated in the International Tables of Crystallography [220]. The symmetry of a crystal is described fully by exactly one of these space groups. This formalism is therefore key to solving crystal structures.

The asymmetric unit

The asymmetric unit refers to the smallest number of atoms that can generate the complete unit cell by applying the symmetry elements of the relevant space group. In the asymmetric unit, each atom can occupy either a general or a special position. The former is characterised by having only the identity operation as its point symmetry. In contrast, a special position refers to any other position that exhibits a nontrivial point symmetry. Such special positions are labelled by a Wyckoff position. To illustrate this with an example, let us consider MOF-5, which crystallises in the space-group $Fm\bar{3}m$. The oxygen atom of each Zn_4O tetrahedron is positioned

on the $8c$ Wyckoff site corresponding to a multiplicity of 8 and a point symmetry of $\bar{4}3m$ *i.e.* $\mathrm{T_d}$. The Wyckoff letter (in this case 'c') is assigned based on the order of increasing multiplicity for each special and general position within the given space group (*i.e.* a, b, c,... etc.). For MOF-5, the $Fm\bar{3}m$ space group symmetry will generate the remaining oxygen atoms of the tetrahedron outside of the asymmetric unit.

2.2.2 Scattering theory

When exposed to a beam of radiation, the atoms in a crystal scatter the incident waves elastically to produce an interference pattern of discrete spots, known as the Bragg peaks. This diffraction pattern provides information about the underlying arrangement of atoms.

Scattering of waves by two atoms

The theory of wave-particle duality allows for the formulation of radiation in terms of waves using the wavefunction $\psi = A\exp(i\mathbf{k}\cdot\mathbf{x})$, where A represents the amplitude of the wave; $\mathbf{k}$ is the wave vector, in turn describing the direction of the wave; and $\mathbf{x}$ represents a point in space. As illustrated in Fig. 2.2a, the sum of two waves depends on both their amplitude and phase shift. The latter can be either linear (Δ) or angular ($\delta\phi$), and they are related by the formula $\delta\phi = \frac{2\pi}{\lambda}\Delta$.

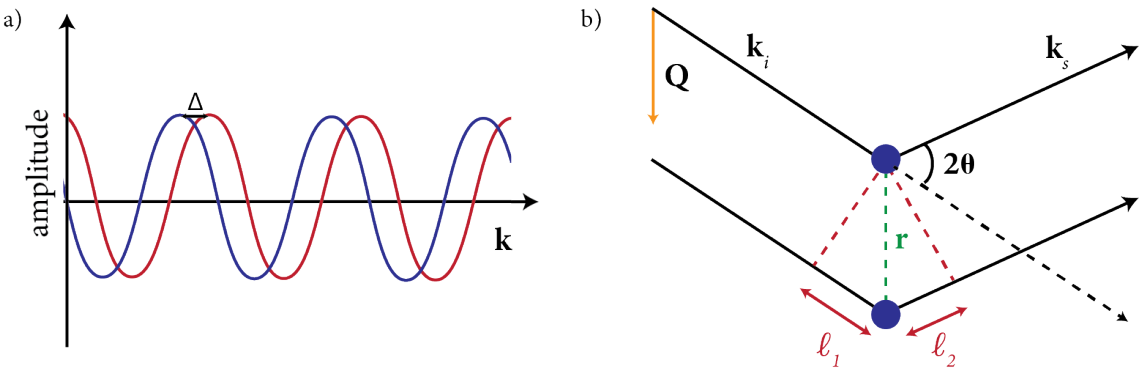

Figure 2.2: (a) Two waves scattering out of phase, with the phase difference Δ, or $\delta\phi = \frac{2\pi}{\lambda}\Delta$. (b) The scattering of an incident wave, $\mathbf{k}_i$, from two atoms separated by the vector $\mathbf{r}$, resulting in the scattered beam, $\mathbf{k}_s$. The phase difference, $\ell_1 + \ell_2 = \Delta$, can be described as $\Delta = \mathbf{Q}\cdot\mathbf{r}$, where $\mathbf{Q} = \mathbf{k}_i - \mathbf{k}_s$. The angle between $\mathbf{k}_i$ and $\mathbf{k}_s$ is 2θ.

Accordingly, the scattering of a beam of radiation from two particles can be described in terms of a phase shift (Fig. 2.2b). In this case, the phase shift (Δ) is expressed in terms of the scattering vector, $\mathbf{Q}$, and the vector that separates the two atoms (*i.e.* $\mathbf{x}_2 - \mathbf{x}_1$), $\mathbf{r}$: $\Delta = \mathbf{Q} \cdot \mathbf{r}$. In turn, $\mathbf{Q}$ depends on the difference between the incoming and scattered beams, $\mathbf{k}_i$ and $\mathbf{k}_s$, respectively:

$$\mathbf{Q} = \mathbf{k}_i - \mathbf{k}_s. \tag{2.1}$$

This is a particularly useful equation because it shows that the overall phase change depends on the change in wave vector $\mathbf{Q}$, and not on either the initial and final wave vectors, $\mathbf{k}_i$ and $\mathbf{k}_s$, separately.

Noting that the angle between $\mathbf{k}_i$ and $\mathbf{k}_s$ is the 2θ Bragg-Brentano geometry, and the magnitudes of the incoming and scattered wave vectors are $2\pi/\lambda$, we obtain:

$$Q = |\mathbf{Q}| = \frac{4\pi}{\lambda} \sin\theta, \tag{2.2}$$

where θ is the Bragg angle. By combining this equation with Bragg's law ($\lambda = 2d \sin\theta$), we can express the magnitude of $\mathbf{Q}$ in terms of the interatomic distance, d; $\mathbf{Q} = \frac{2\pi}{d}$.

Scattering of waves by a collection of atoms

The theory outlined above can easily be generalised for a collection of atoms. Namely, by summing up the phase shifts from each atom with their positions, $\mathbf{r}_j$, defined relative to a fixed origin, the structure factor, $F(\mathbf{Q})$, is obtained:

$$F(\mathbf{Q}) = \sum_j f_j \exp(\mathrm{i}\mathbf{Q} \cdot \mathbf{r}_j). \tag{2.3}$$

Here, the amplitudes are weighted by a scattering factor, f_j, which is determined by the identity of the atom. The intensity of the scattering is then given by:

$$|F(\mathbf{Q})|^2 = \left| \sum_j f_j \exp(i\mathbf{Q} \cdot \mathbf{r}_j) \right|^2 = \sum_{i,j} f_j \exp\left[i\mathbf{Q} \cdot (\mathbf{r}_i - \mathbf{r}_j)\right]. \tag{2.4}$$

This relationship demonstrates the phase problem: by measuring $|F(\mathbf{Q})|^2$, which is a real positive value, rather than $F(\mathbf{Q})$, which is a complex number, all information about the phase is lost. In other words, one loses information on the absolute positions of the atoms, but sensitivity to their relative positions is retained.

Scattering of waves by a continuous distribution of electrons

In the case of X-ray diffraction, the electron density around an atom, $\rho_{\text{el}}(\mathbf{r})$, at position $\mathbf{r}$, is responsible for the scattering of a beam. The X-ray atomic scattering factor is therefore given as:

$$f(\mathbf{Q}) = \int \rho_{\text{el}}(\mathbf{r}) \exp(i\mathbf{Q} \cdot \mathbf{r}) \mathrm{d}\mathbf{r}. \tag{2.5}$$

Consequently, the scattering power falls off with $\mathbf{Q}$, and $f(\mathbf{Q}) \to Z$ as $\mathbf{Q} \to 0$, where Z is the total number of electrons in an atom or ion. In other words, the maximum scattering power of an atom scales linearly with its atomic number, Z.

Now, we understand how waves are scattered by the atoms in a crystal, but how do we use this information to ultimately solve the average structure? To answer this question, we need to define a crystal as the convolution of the lattice and the unit cell:

$$\text{Crystal} = \text{lattice} \otimes \text{unit cell}. \tag{2.6}$$

Knowing that the convolution of two functions in one space corresponds to the product in Fourier space, we obtain:

$$F_{\text{Crystal}}(\mathbf{Q}) = F_{\text{lattice}}(\mathbf{Q}) \times F_{\text{unit cell}}(\mathbf{Q}). \tag{2.7}$$

In other words, to solve the structure of a crystal from scattering data, we need

the Fourier transforms of the lattice and the unit cell. The latter is given by the structure factor, $F(\mathbf{Q})$, whilst the former is known as the reciprocal lattice.

The reciprocal lattice

To obtain the reciprocal lattice, we first describe the crystal lattice as a series of delta functions centred on each lattice point:

$$\mathcal{L}(\mathbf{r}) = \sum_{U,V,W} \delta[\mathbf{r} - (U\mathbf{a} + V\mathbf{b} + W\mathbf{c})]. \tag{2.8}$$

Here, U, V, and W are integers that define the lattice vectors. The Fourier transformation results in the reciprocal lattice:

$$\mathcal{R}(\mathbf{Q}) = \sum_{h,k,l} \delta[\mathbf{Q} - (h\mathbf{a^*} + k\mathbf{b^*} + l\mathbf{c^*})], \tag{2.9}$$

where h, k, and l are integers. The reciprocal lattice vectors, $\mathbf{a^*}$, $\mathbf{b^*}$, and $\mathbf{c^*}$, are related to the real-space lattice vectors as follows:

$$\mathbf{a^*} = \frac{2\pi}{V}\mathbf{b^*} \times \mathbf{c^*}, \tag{2.10}$$

$$\mathbf{b^*} = \frac{2\pi}{V}\mathbf{c^*} \times \mathbf{a^*}, \tag{2.11}$$

$$\mathbf{c^*} = \frac{2\pi}{V}\mathbf{a^*} \times \mathbf{b^*}, \tag{2.12}$$

where V is the volume of the unit cell. These relations ensure that $\mathbf{a^*} \cdot \mathbf{a} = 2\pi$ and $\mathbf{a^*} \cdot \mathbf{b} = 0$, and so on.

Thus, the Fourier transform of a lattice is another lattice. In turn, $F_{\text{Crystal}}(\mathbf{Q})$ is non-zero only when $\mathbf{Q} = h\mathbf{a^*} + k\mathbf{b^*} + l\mathbf{c^*}$

Thermal motion

All atoms in a crystal will undergo thermal motion. To account for the atomic displacements, a Fourier transform is incorporated as a multiplicative factor in Equation 2.7. If the distribution of atom displacements from the average position is written as $\rho(\mathbf{r})$, the distribution of the electrons within the atom in the crystal can be represented by $\rho_j(\mathbf{r}) \otimes \delta(\mathbf{r}-\mathbf{r}_j) \otimes \rho(\mathbf{r})$. Assuming that the thermal motion is both isotropic and harmonic, $\rho(\mathbf{r})$ will be a Gaussian function with a width characterised by the mean-squared atomic displacement, $\langle u_j^2 \rangle$, also known as the atomic displacement parameter. The Fourier transform of the spread of distributions will also be a Gaussian distribution, which can be represented by the shorthand notation:

$$T_j(\mathbf{Q}) = \exp(-B_j \sin^2\theta/\lambda^2), \tag{2.13}$$

in which

$$B_j = 8\pi^2 \langle u_j^2 \rangle. \tag{2.14}$$

The Fourier transform of the crystal

Finally, we can perform the Fourier transformation of the crystal. By writing the positions of an atom in the unit cell as $\mathbf{r}_j = x_j\mathbf{a} + y_j\mathbf{b} + z_j\mathbf{c}$, we obtain the product:

$$\mathbf{Q} \cdot \mathbf{r}_j = (h\mathbf{a^*} + k\mathbf{b^*} + l\mathbf{c^*}) \cdot (x_j\mathbf{a} + y_j\mathbf{b} + z_j\mathbf{c}) = 2\pi(hx_j + ky_j + lz_j). \tag{2.15}$$

Thus, the overall structure factor for a crystal can now be written in its usual form:

$$F(hkl) = \sum_j f_j(Q_{hkl}) \exp(2\pi \mathrm{i}(hx_j + kyx_j + lz_j)) \times \exp(-B_j \sin^2\theta_{hkl}/\lambda^2), \tag{2.16}$$

where scattering is observed for integer values of h, k, and l.

To summarise, the pattern of Bragg peaks measured in X-ray scattering experiments is determined by the geometry of the lattice, with the corresponding intensities determined by the unit cell symmetry and atomic species therein. Notably, a diffraction experiment only measures the intensity of the Bragg peaks, leading to the loss of the relative phases *i.e.* the phase problem. However, various approaches are employed to overcome this loss of information, such as the Patterson method [221] and direct methods [222]. Modern dual-space methods such as charge flipping [223] are routinely used to solve crystal structures, as is the case in this thesis.

2.2.3 Single-crystal diffraction and refinement

To collect a single-crystal diffraction dataset, a crystal is mounted onto a loop, which is then centred in the beam. The crystal is first screened to assess its quality and determine the data collection method. This involves collecting a small number of frames while orientating the crystal at different angles. If the crystal diffracts well, this provides an estimate of the space group, which may be used to decide the collection strategy. If a crystal has low symmetry, for example, it may be necessary to collect a full sphere, which in turn takes longer than the collection of a high-symmetry crystal, for which a small section of reciprocal space may be sufficient to reconstruct the data for completeness [218].

In a typical single-crystal refinement procedure, an algorithm (*e.g.* charge flipping) is used to process the reflection data, resulting in a starting solution that is partially influenced by the input of an expected molecular formula. The initial model, also known as the trial structure, is then refined, as implemented in various software packages including CRYSTALS [224] and OLEX [225]. The refinement process involves the iterative adjustments of numerical parameters that describe the structural model, in order to optimise the agreement between the calculated and observed diffraction patterns. The quality of this agreement can be quantitatively assessed using the R-factor, which compares the calculated and measured structure factors:

$$R = 100 \times \frac{\sum_{hkl} ||F_{\text{obs}}(hkl)| - |F_{\text{calc}}(hkl)||}{\sum_{hkl} |F_{\text{obs}}(hkl)|}\%. \tag{2.17}$$

In this equation, the moduli of the structure factors are compared, eliminating any concerns related to the phases of the structure factors. The comparison is directly between the calculated and experimental magnitudes. Typically, the refinement process continues until an R-factor between 2% and 7% is achieved, indicating a good agreement between the calculated and observed data [33, 218].

During the initial stages of a single-crystal refinement, the focus is on refining the three positional coordinates (x, y, z) and the atomic displacement parameter for individual atoms. At this stage, the assumption is that the vibrations are isotropic and have the same magnitude in all directions. If the crystal structure is found to be stable and the data quality allows for it, the refinement can be extended to include anisotropic displacement parameters — usually six per atom — to account for the vibration of each atom in different directions and at different magnitudes. Hydrogen atoms are typically not included up until this point because their electron density is significantly lower than that of heavier atoms. However, after incorporating the anisotropic displacement parameters into the refinement, the presence of hydrogen atoms may become apparent in the electron density map, in turn allowing for their inclusion and subsequent refinement.

In some cases, the use of constraints or restraints can greatly enhance the refinement process. Constraints impose rigid mathematical relationships that must be obeyed throughout the refinement, effectively reducing the number of refined parameters whilst keeping the data unchanged. Restraints, on the other hand, are applied in conjunction with the diffraction data and do not alter the number or type of refined parameters. Accordingly, constraints are often employed when there are known relationships between certain parameters or groups of atoms in the crystal structure. For instance, if a framework structure contains an organic aromatic linker, a constraint can be applied to ensure that the benzene ring remains planar throughout the refinement. In contrast, restraints are typically derived from prior knowledge or assumptions about the system. For example, a restraint can be applied

to maintain bond lengths or bond angles within reasonable ranges.

Once the hydrogen atoms have been added to the model and it appears sensible (as indicated by a low R-factor), the details of the crystal structure, along with information on the diffraction experiment and refinement, can be stored in a crystallographic information file (CIF) [226]. CIFs are particularly useful as they allow for structure validation using the platform CheckCIF, as provided by the IUCr [227]. Thus, including a CIF is an important step in the publication and dissemination of crystallographic research, as it promotes transparency, reproducibility, and advancement of scientific knowledge.

A wide variety of single crystal X-ray diffraction (SCXRD) experiments were performed in this thesis. Therefore, the conditions of each experiment will be highlighted before presenting the relevant results. In all cases, a structure solution was obtained using intrinsic phasing methods from ShelXT [228], followed with refinements using a full-matrix least-squares approach on all unique F^2 values. The refinements were performed using ShelXL [229] as implemented within Olex2-1.5 [225].

2.2.4 Powder diffraction and refinement

MOF synthesis often yields powder samples; such is the case for many Fe-1,4-bdc MOFs and UiO-66. Due to the small size of the powder crystallites, the structure cannot be solved using single-crystal methods. Instead, powder diffraction may aid in doing so.

In a typical powder diffraction experiment, a slide is coated with a thin layer of powder, which is then exposed to the beam. Thus, rather than a rotating single crystal, several single crystals of the same material are simultaneously irradiated as they lie in different orientations. Each of these crystals produces its own diffraction pattern, which are superimposed. If a flat detector is positioned perpendicular to the beam on the opposite side of the sample — as is the case for single-crystal diffraction experiments — one would therefore observe a circular pattern composed of many spots.

As such, the radial distribution of diffraction intensity is averaged to generate a 1D powder diffraction pattern. Powder diffraction data thus contain less structural information than single-crystal diffraction data, in turn making structure determination more challenging. However, powder diffraction offers advantages such as faster and easier data collection, hence allowing for applied methods such as multi-phase analysis. Furthermore, lattice parameters determined from powder diffraction data analysis often have smaller uncertainties compared to those obtained from single crystal methods. This increased precision is particularly valuable for studying physical properties such as thermal expansion [230].

To extract structural information from powder diffraction data, it is first indexed. This involves assigning Miller indices (hkl) to the observed peaks, and thus gives information on the peak positions and systematic absences. As a result, the unit cell parameters as well as space group can be determined and subsequently refined. The unit cell contents and atomic positions, on the other hand, are determined by the relative intensities of the peaks. However, these can also be affected by atomic displacements arising from thermal motion and lattice strain. Preferred orientation may also impact peak intensities, although this only occurs when crystallites are anisotropic (*e.g.* needle-shaped) and therefore have a tendency to align themselves in a specific orientation.

To perform the indexing and refinement of a powder diffraction dataset, a crystallographer typically starts with a Pawley refinement [231]. This involves the refining of lattice parameters against the experimental data, assuming a particular space group symmetry. Thus, no information regarding the cell contents is needed: the peak intensities are refined freely to give the best fit. If a structural model is available, the more detailed Rietveld refinement can be performed [232]. In this method, not only the lattice parameters but also the atomic positions and their displacement parameters — both isotropic and anisotropic — are refined. In both the Pawley and Rietveld refinement, the parameters are refined *via* least-squares minimisation of the weighted square difference between the calculated and observed powder patterns, given by:

$$\chi^2 = \sum_{i=1} \frac{w_i(y_{i,\text{obs}} - y_{i,\text{calc}})^2}{N - P}, \tag{2.18}$$

where N refers to the number of data points and P to the number of parameters. Similarly to single-crystal refinements, the quality of fit is usually assessed *via* the R-factor, albeit in this case weighted and thus given by:

$$R_{\text{wp}} = \sqrt{\frac{N - P}{\sum_{i=1} w_i y_{i,\text{obs}}^2}}. \tag{2.19}$$

Likewise, a low value of R_{wp} is usually indicative of a good fit, however care must be taken to ensure the resulting structural model is chemically sensible.

Unless specified, all powder X-ray diffraction (PXRD) data reported in this thesis were collected at ambient conditions using a high-intensity Bruker D8 Advance Eco diffractometer equipped with a Cu-Kα source (λ = 1.54 Å) and a fluorescence-filtering LYNXEYE XE-T detector. Powder samples were prepared by grinding single crystals and allowing the resulting powder to dry in air. Thin layers of the powder sample were deposited on the sample holder using a minimum amount of vacuum grease. To verify the phase purity of the samples, Pawley refinements were performed using the TOPAS-Academic software [233].

2.2.5 Radiation sources

All diffraction experiments conducted in this thesis use X-ray radiation, as provided by both in-house diffractometers and synchrotrons. Whilst both sources emit X-rays, there are significant differences in the quality of radiation they provide. This section highlights the characteristics and advantages of each.

In-house

For both single crystal and powder X-ray diffractometers, the standard source of X-rays is an X-ray tube (Fig. 2.3a) [217]. This is usually an evacuated enclosure made of glass or ceramic, in which accelerated electrons are generated by passing an electron current through a wire filament. These accelerated electrons then collide

with a water-cooled metal block known as the metal target. The majority of these collisions result in the conversion of kinetic energy into heat, yet a small fraction of the electrons interact with the atoms of the metal target, leading to the emission of X-rays. This radiation then passes through a monochromator crystal to ensure the final beam is of the desired wavelength.

Copper (Cu), molybdenum (Mo, or Moly, as it is often referred to by crystallographers), and increasingly silver (Ag), are commonly used as metal targets in X-ray tubes [217]. The choice of metal target is particularly important as it determines the wavelengths of the emitted X-rays. In this thesis, both Cu and Mo radiation were used for in-house experiments, corresponding to wavelengths of 1.542 and 0.711 Å, respectively. The use of a Cu source is particularly advantageous for crystals with long unit cell dimensions, as it can help mitigate the issue of Bragg reflections being close together or potentially overlapping. Additionally, Cu X-ray tubes produce a higher flux of incident photons, making them useful for analysing small or weakly diffracting crystals. However, Cu radiation is readily absorbed by heavier elements in crystal samples. For such systems, a Mo source becomes essential to obtain data of good quality. Furthermore, the shorter wavelength of Mo radiation allows for data collection to a higher resolution.

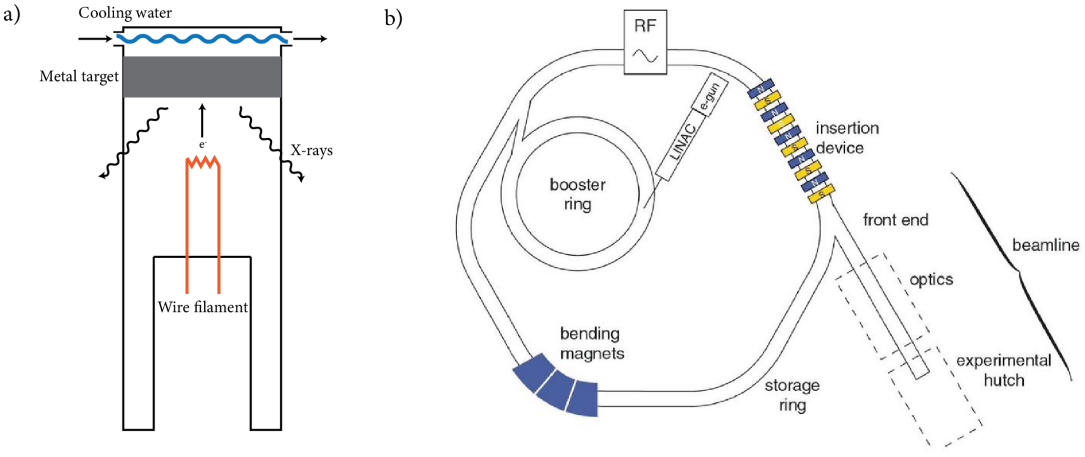

Figure 2.3: Graphical representations of the two X-ray sources used in this thesis: (a) X-ray tube, which gives rise to wavelengths governed by the metal target (commonly Cu, $\lambda = 1.542$ Å and Mo, $\lambda = 0.771$ Å); and (b) synchrotron, at which the wavelength of the high-energy X-rays can be tuned. Figure (a) adapted from Ref. 218 with permission from Oxford University Press and figure (b) from Ref. 234 with permission from Wiley-VCH.

Notably, both Mo and Ag wavelengths are typically too short for powder diffraction in the laboratory, as shorter wavelengths scatter weakly and result in the loss of resolution due to contraction of the diffraction pattern towards lower angles.

Synchrotron

In cases where a crystal diffracts too weakly on a laboratory source, researchers may opt to apply for beamtime at a synchrotron light-source facility. This is in essence a particle accelerator. Yet despite the first accelerators being built in the 1930s, it was not until the 1960s that the electromagnetic radiation emitted by electrons as they change direction was exploited for highly brilliant and collimated X-ray radiation [234].

Synchrotrons offer several advantages over in-house diffractometers: (i) the resolution between reflections is generally better; (ii) the wavelength of the X-ray beam can be tuned to specific values; and (iii) the intensity of the beam is typically significantly higher than that of a laboratory source, often representing a 100-fold gain or more. The mechanism of generating a beam in a synchrotron involves several components [234]. Electrons are accelerated through a linear accelerator, followed by a booster ring, and finally the largest storage ring (Fig. 2.3b). Although referred to as a ring, the latter is comprised of alternating straight sections that contain either undulators or insertion devices, connected by bending magnets at the vertices. This design ensures that the electrons maintain a polygonal orbit as they circulate around the ring. The undulators consist of a periodic array of magnets, which generates the intense radiation. The spacing between the magnets can be adjusted to control the wavelength of the X-ray beam. As the electrons are deflected by the bending magnets, they emit high-energy X-rays tangentially. These X-rays are subsequently monochromated and collimated in the optics hutch before being directed to the beamline, which houses the samples and detectors for data collection.

2.2.6 Diffuse scattering

The scattering theory outlined above is based on long-range translation periodicity, which results in a diffraction pattern consisting solely of discrete Bragg reflections

from which the average structure can be solved. However, there may be additional measured intensity running through, along, and between the Bragg peaks. In some cases, there may be no observable Bragg peaks at all; only broad, weak scattering. As mentioned in the introduction, this is known as diffuse scattering, and it arises from structural deviations away from the average crystallographic structure [235]. Depending on the underlying mechanism responsible for these deviations, the diffuse scattering is classified as either thermal or disorder diffuse scattering [236].

The origin of disorder diffuse scattering may be one of the following:

- Displacive disorder
- Occupational disorder
- Size-effect

In turn, each origin has a different experimental scattering signature [236, 237]. I will discuss these different signatures in the following section, in large parts drawn from Ref. 238. In all cases, the model used to calculate the diffuse scattering is based on a 2D chess-board like arrangement of atoms A and B, where atom B has a scattering power twice as large as atom A. The average composition of this model is therefore AB, with the symmetry plane (rather than space) group $c4mm$.

Displacive disorder refers to the displacement of an atom away from its crystallographic average position (Fig. 2.4a). To encapsulate this disorder in the simple structural model described above, the positions of atoms A and B were kept ordered,

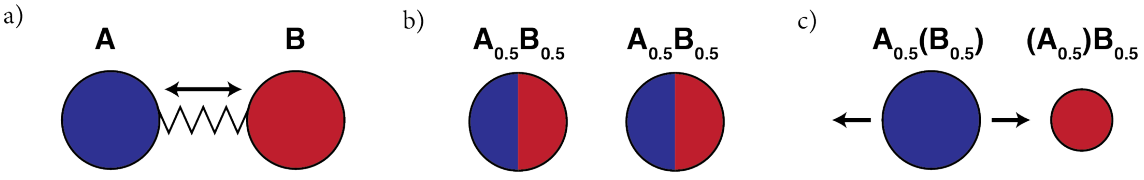

Figure 2.4: Schematic showing the different types of disorder based on atoms 'A' and 'B'. (a) Displacive disorder. One might imagine a spring between the two atoms, which contracts, expands, or translates. (b) Substitutional disorder, showing how each crystallographic site is occupied by A or B, each with a probability of 0.5. (c) The size effect, showing how the smaller atom, A, may displace as a function of the size of B. Note that each crystallographic site is occupied by A or B, each with a probability of 0.5.

with the displacements defined as harmonic and isotropic. The calculated diffuse scattering as a function of correlations between the displacements is presented in Fig. 2.5a. These patterns show that in the absence of interactions (*i.e.* the atoms displace independently of each other), an intensity of zero is expected at the origin of reciprocal space, with a continuous increase in intensity with increasing distance followed by a final decrease of intensities at large vectors, caused by the atomic form factor. In the case of negative correlations between the displacements (*i.e.* next neighbouring atoms tend to move along anti-parallel directions), the diffuse scattering condenses around the Bragg positions, with the features of strong diffuse maxima being very similar to the diffuse scattering from the uncorrelated model. When positive correlations apply to the displacements (*i.e.* next neighbouring atoms tend to move along parallel directions), a similar diffuse scattering pattern is observed, albeit with the weak/strong diffuse peaks inverted.

Occupational disorder applies to systems where different atoms and/or vacancies occupy the same crystallographic site (Fig. 2.4b). The simple structural model is

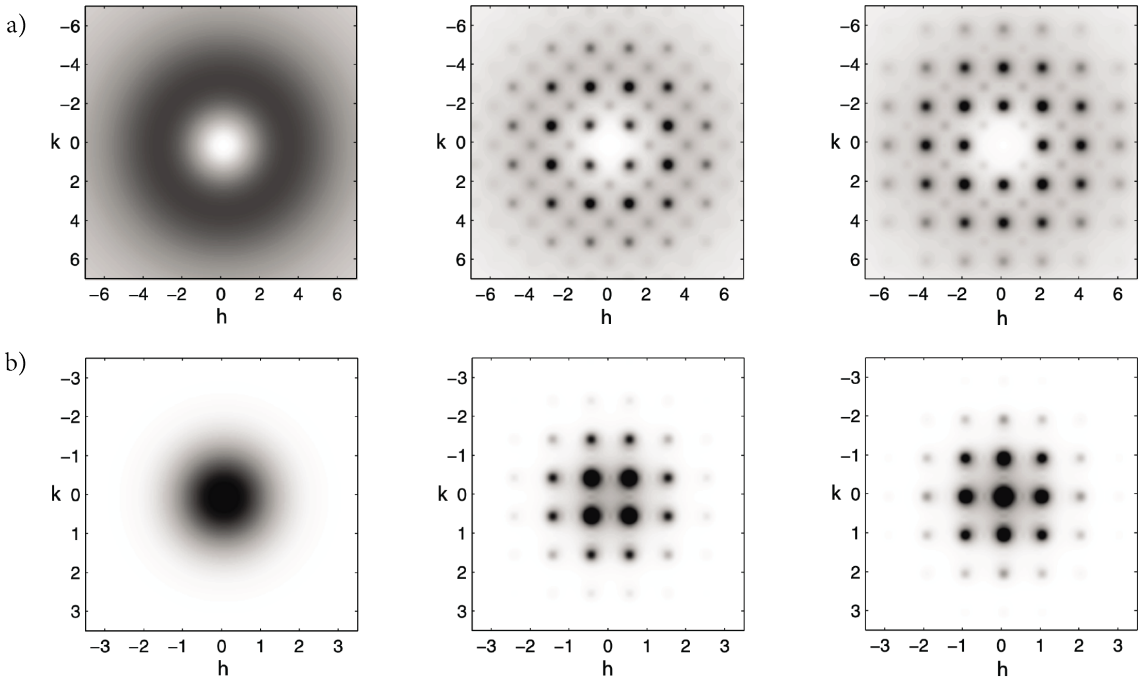

Figure 2.5: Diffuse scattering patterns calculated from (a) displacive and (b) occupational disorder 2D *AB* models, with (from left to right) no correlations, negative correlations, and positive correlations. In both (a) and (b), the Bragg reflections are omitted. Figures adapted from Ref. 238.

therefore adapted to have a mixed site occupancy of $0.5A$ and $0.5B$ atoms, in turn resulting in the symmetry plane group $p4mm$. The calculated diffuse scattering, as a function of correlations between the displacements, is presented in Fig. 2.5b. In the absence of interactions (*i.e.* A and B are randomly distributed), one would observe strong diffuse scattering at the origin of reciprocal space, of which the intensity decreases continuously with increasing distance. However, if there are negative occupational correlations (*i.e.* there is a preference for hetero-atomic pairs AB or BA), then one would expect diffuse scattering of broad maxima centred at positions $h, k = n/2$ (n = odd) *i.e.* where the Bragg reflections are extinct due to transformation of the c-centred lattice — of the displacive disorder model discussed above — to the p-lattice. This behaviour is best understood by considering the structure consists of domains with a local chess-board structure. Similarly, if the system is governed by positive occupational correlations (*i.e.* all atoms prefer being next to the same element), the diffuse peaks will be located at the Bragg positions, as the translation vector is now the same as the average periodicity.

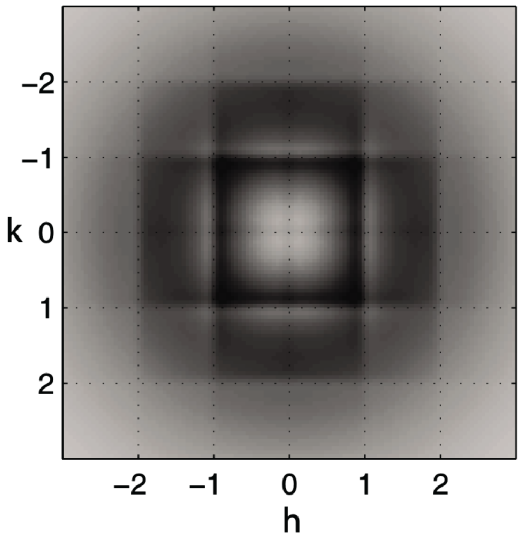

Figure 2.6: Diffuse scattering pattern calculated from the size effect 2D *AB* model. The Bragg reflections are omitted, but would be visible at integer *h,k* positions according to the p-lattice. The dotted grid in the diffuse scattering pattern is at integer *h* and *k* values to demonstrate the asymmetry of the diffuse intensities with respect to the integer Bragg positions. Figure adapted from Ref. 238.

Finally, when displacive disorder is caused by occupational disorder, this is referred to as the size effect (Fig. 2.4c). In this case, the displacements of the disordered components are governed by the interactions between them, and thus correlated to their distribution. These interactions may arise from a difference in size between the components, hence the term 'size effect'. The corresponding structural model has A and B atoms randomly distributed, with the average displacements equivalent to the displacive model defined above. The local interatomic distances now depend on the neighbouring elements: AB distances are the same as in the average structure, while AA distances are shorter and BB pairs are further apart. The resulting diffuse scattering shows asymmetries with respect to integer h,k values (Fig. 2.6), which is a typical feature for size-effect distortions [239].

Data collection

There are several important factors to consider when attempting to measure diffuse scattering. One key aspect is that the intensity is much weaker than that of the Bragg reflections, typically on the order of $\sim 10^{-4}$. As a result, the diffuse scattering is often of similar intensity to the background scattering arising from *e.g.* air and fluorescence [235, 240]. Therefore, special considerations and adaptations are necessary to optimise data collection for diffuse signatures [237].

A common strategy — also the one employed in this thesis — is to collect two datasets: the first optimised for Bragg scattering and the second for the collection of diffuse scattering. The second dataset is obtained by using longer exposure times per frame. This leads to higher intensity diffraction patterns and typically oversaturation of the Bragg peaks. The Bragg dataset is used to solve and refine the average crystal structure, whilst the diffuse scattering dataset can be used to characterise static disorder or dynamic contributions [236]. The recent development of single-photon pixel detectors has significantly contributed to addressing this challenge by enabling precise and quantitative measurements of weaker diffuse scattering [236].

A further complication to the weak intensity of diffuse scattering, is that diffraction patterns typically contain thermal diffuse scattering, regardless of the structure being disordered or not [236]. It is important to establish whether dynamic scatter-

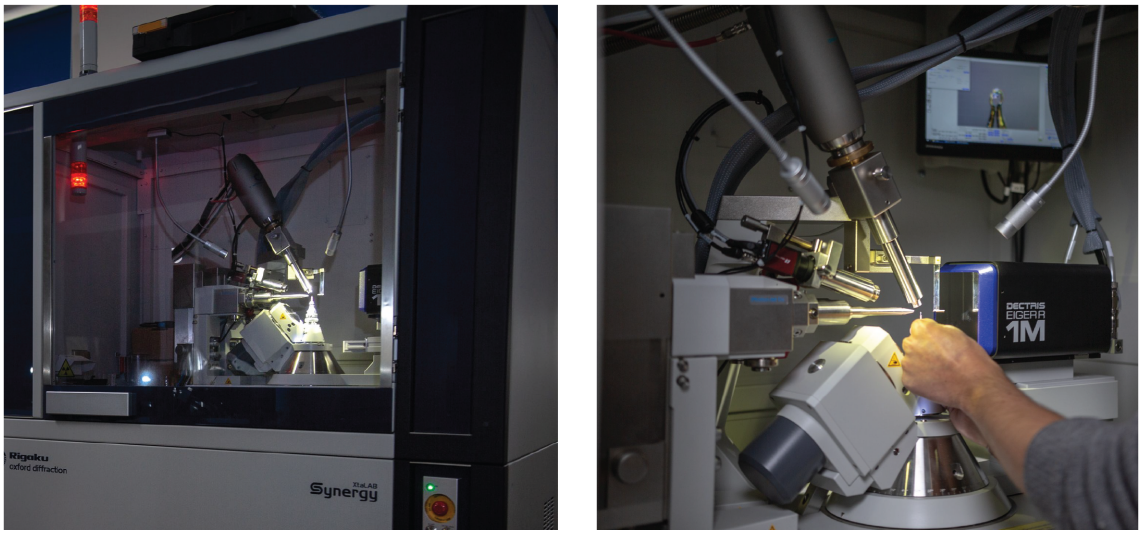

Figure 2.7: Pictures of our in-house diffractometer, which was used to perform most of the diffuse scattering diffraction experiments presented in this thesis.

ing is present in order to avoid misinterpreting it as static disorder. One approach to address this is to collect data at lower temperatures.

The majority of diffuse scattering data presented in this thesis were collected on our in-house Rigaku Synergy S diffractometer fitted with the photon-counting Dectris EIGER2 R 1M detector (Fig. 2.7). All data sets were collected under Cu radiation ($\lambda = 1.5406$ Å) and an exposure time of 200 seconds. Each measurement involved a full ϕ-scan carried out in a single run. CrysAlisPro was used for indexing, determination, and refinement of the orientation matrix [241].

Characterisation

Whilst the analysis of Bragg scattering is routine in the field of crystallography, the interpretation of diffuse scattering is rather complicated. Yet, a number of approaches have been developed over the past few decades to overcome this problem, both computationally *e.g.* Monte Carlo modelling and experimentally *e.g.* 3D difference pair distribution function.

Monte Carlo modelling

Monte Carlo (MC) modelling as used in my research includes the simulation of a structural model of disorder based on *a priori* knowledge of the chemical or physical

interactions from which disorder arises [242]. It typically involves generating a large box of atoms in which the degrees of freedom are made adjustable parameters. The energy of the system is minimised against an energy function *via* simulated annealing — an adaptation of the Metropolis-Hastings algorithm [243]. This approach typically leads to a sensible model for the system under investigation.

More specifically, MC modelling is based on expressing the total energy of a crystal as a function of random variables such as site occupancies or atomic displacements from the average structure [237]. During the simulation, a site within the crystal is chosen at random before the associated variable is altered by some random amount, which in turn alters the overall energy of the crystal. The corresponding energy difference of the configuration (ΔE) is computed to ultimately determine whether the new configuration should be accepted. The acceptance criteria is based on the transition probability (P) being greater than a random number chosen uniformly in the range [0,1]:

$$P = \frac{\exp(-\Delta E/kT)}{[1 + \exp(-\Delta E/kT)]}. \tag{2.20}$$

Here, T is the temperature and k the Boltzmann's constant. The value of T as part of this simulated annealing approach is particularly important as it controls the proportion of accepted modifications that lead to a larger total energy. During this process, a move is always accepted if the new energy is less than the old energy value; however it may also be accepted if the energy is greater albeit only with probability $P = \exp(-\Delta E/kT)$. This process is repeated until the system reaches its equilibrium.

When running a MC simulation one may consider the local rules governing the connectivity of *e.g.* a framework by taking into account atomic occupancies. Alternatively, an MC model may be dictated by atomic displacements. Hence, MC modelling is an extremely versatile method; it has been successfully applied to characterise disorder in materials such as paracetamol polymorphs [244], functional oxides, and even proteins [16]. However, one limitation of this method is that it requires prior knowledge or assumptions about the relevant interactions of the system [16].

This prerequisite can introduce bias towards specific assumptions and potentially overlook other important structural features. Additionally, the iterative process of exploring different models and adjusting parameters can be time-consuming, and implementation typically involves the use of custom written code.

Whilst not used in this thesis, the method of reverse Monte Carlo (RMC) provides an alternative approach to overcome these limitations by reversing the workflow [245]. Instead of starting with a suggested disordered model, a large box of atoms is generated as a starting configuration — typically the average structure. The atoms are then allowed to move by small amounts. These moves are accepted or rejected according to the same Metropolis-Hastings algorithm [243], and the fit is driven by minimising the difference between the model and the data. Thus, RMC offers an advantage by allowing the data to drive the fit and thus avoiding the need for preconceived assumptions. On the other hand, there is a risk of overfitting and achieving unrealistic structural features that are not representative of the true system.

Density functional theory

Density functional theory (DFT) is a computational approach used to determine the structure and properties of many-electron systems using functionals that depend on the electron density [246]. This widely employed method is commonly used to calculate the electronic — and therefore atomic — structure of a system at 0 K (*i.e.* the ground-state), making it suitable for optimising the geometry of models derived from MC simulations, as was done in this thesis.

Various functionals are available for calculating the exchange-correlation energy within DFT. These functionals can be incorporated into different DFT suites, either with or without dispersion interactions, and additional interactions can also be considered. Each combination of functionals has its own set of advantages and limitations. It is important to note that different functionals exhibit varying performance for different materials, and there is currently no systematic method to determine the most suitable functional. Therefore, it is customary to compare results obtained from multiple calculation methods for a given system.

Several significant limitations of DFT should be taken into account within the context of this thesis [247]. First, the calculated structure is applicable specifically at 0 K and may not accurately represent the structure at room temperature. Additionally, conventional functionals have limitations in capturing dispersion interactions, such as intermolecular or metallophilic interactions. The computational cost associated with DFT imposes restrictions on the number of atoms that can be studied within a reasonable timeframe. Moreover, periodic boundary conditions, which are necessary for DFT calculations, introduce a certain level of periodicity that may not be present in the actual material. This presents a challenge when dealing with disordered materials [248].

In this thesis, full cell optimisations were performed using the QUICKSTEP module of the CP2K package [249]. The DZVP MOLOPT basis sets were employed for all atoms, along with the PBE functional [250] and the "D3" van der Waals correction scheme [251]. To ensure smooth optimisation of the cell parameters and atomic coordinates, an 800 Ry cutoff was applied in conjunction with a reference cell until the forces on the atoms were reduced to less than 0.6 kJ mol^{-1} $Å^{-1}$. No atomic constraints were applied during the relaxation and no symmetry was imposed upon the cell parameters or coordinates (*i.e.* relaxing in $P1$).

3D diffference pair distribution function

The emerging method of 3D difference pair distribution function (3D-ΔPDF) allows for the direct refinement of single-crystal diffuse scattering by performing a Fourier transform on the diffuse scattering alone. The typical workflow begins with symmetry averaging the single-crystal total scattering data to enhance the diffuse features. Next, the Bragg peaks are removed from the symmetry-averaged diffraction pattern (using *e.g.* the punch-and-fill method) [252]. All that remains is the diffuse scattering, which can then be Fourier transformed to visualise only the interatomic distances that differ between the real and average structure in real-space [238]. The software MEERKAT2 was developed to facilitate these calculations, which requires the individual frames and the crystal's Laue symmetry as input. The output of this Fourier transformation is referred to as the 3D-ΔPDF. The term '3D' signifies that

the dataset corresponds to single-crystals and is therefore three-dimensional, whilst the symbol 'Δ' denotes that only the diffuse scattering is considered, capturing deviations from the average structure.

Similar to diffuse scattering, the features observed in 3D-ΔPDFs are often diagnostic of the type of disorder. This relationship is demonstrated by calculating the (in this case) 2D-ΔPDFs from the diffuse scattering patterns presented in Figs. 2.5 and 2.6, as calculated from the chess-board AB models described above [238]. The 2D-ΔPDFs obtained from the displacive and occupational disorder structural models are presented in Fig. 2.8, whilst the 2D-ΔPDF corresponding to the size-effect is shown in Fig. 2.9.

A notable feature of the 2D-ΔPDFs corresponding to the displacive disorder

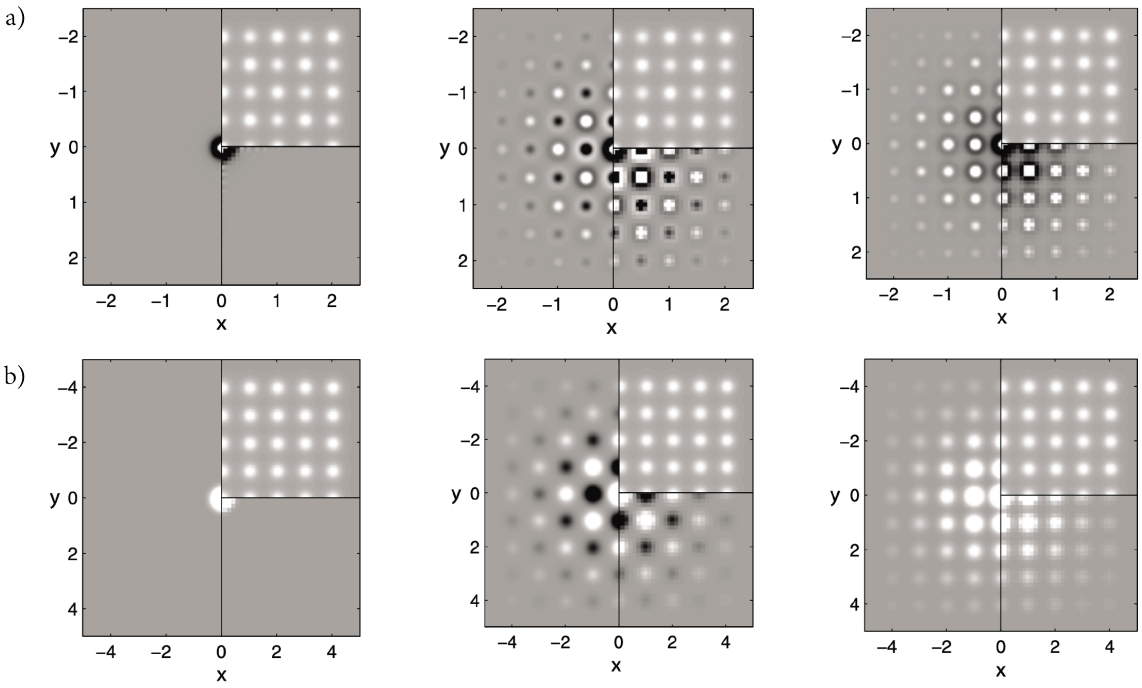

Figure 2.8: 2D-ΔPDFs calculated from displacive (a) and occupational (b) disorder 2D AB models, with (from left to right) no correlations, negative correlations, and positive correlations. Positive correlations are shown in white and negative correlations in black. In all panels, the map on the left-hand side is shown in very high resolution, whilst the lower right quarter shows the 2D-ΔPDF in a resolution corresponding to the visible diffuse scattering presented in Fig. 2.4. The upper right inset shows the total 2D-PDF pattern (*i.e.* the Fourier transform of both the Bragg and diffuse scattering). Note that the colour schemes of the total 2D-PDF and 2D-ΔPDF are on different scales; the intensities in the former are by far stronger than in the latter. Figures adapted from Ref. 238.

model is the so-called 'Mexican hat shape', where high/low densities at the origin of the scattering are enclosed by a ring with a density of the opposite sign (Fig. 2.8a). Considering the model which lacks correlations, this Mexican hat profile can be explained by the fact that the distance of an atom to itself is always zero. Therefore, a distance of zero is more likely to be observed in the real than in the average structure. On the other hand, the distance of an atom to itself will never be larger than zero, thus giving rise to negative intensities around the positive origin. This Mexican hat profile remains at the origin when correlations are present in the system — both negative and positive — with additional peaks found at positions corresponding to the average interatomic vectors. In the case of negative displacive correlations, the sign of the Mexican hat profiles changes at each increasing interatomic vector, due to different elements avoiding the average atomic distances. With positive displacive correlations, however, all Mexican hat profiles have the same sign, since all atomic pairs with shorter distances than the correlation length tend to move in phase.

In the case of occupational disorder, the 2D-ΔPDF contains a single peak at the origin, which is simply the autocorrelation function of the different electron densities of atoms A and B (Fig. 2.8b). Interpretation of the correlated models is straightforward: in the case of negative correlations, positive peaks are visible

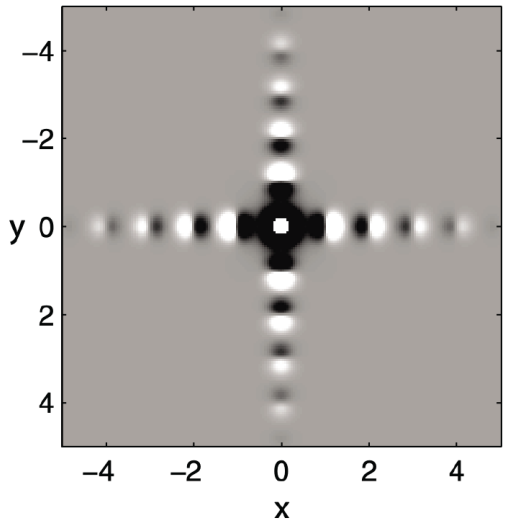

Figure 2.9: 2D-ΔPDF calculated from the size effect disorder model. Positive correlations are shown in white and negative correlations in black. Figure adapted from Ref. 238.

at positions $x + y$ = even, whilst peaks are negative at $x + y$ = odd. In the case of positive correlations, all peaks are positive. In other words, the likelihood of finding neighbouring elements in the negatively correlated model is lower than in the average structure, whilst in the positively correlated model, it is higher.

Finally, the 2D-ΔPDF model obtained from the size effect disorder model shows clearly correlations along the main axes only (Fig. 2.9). Therefore, similarly to the diffuse scattering, the size effect results in strong asymmetries along radial directions. The positions of the positive and negative peaks indicate that atoms separated by an interatomic vector corresponding to a distance larger than the average distance, are more likely to be found in the real structure than in the average structure, and less likely at shorter distances.

In all cases, the correlations decrease with increasing vector and hence the intensities of the 2D-ΔPDF peaks decrease accordingly.

As such, one can often gain significant information on the disorder by inspecting the 3D-ΔPDF by eye alone. However, in favourable cases, the calculated 3D-ΔPDF can also be refined using the software YELL [253].

Thus, in contrast to the qualitative nature of matching Monte Carlo models with diffuse scattering, the 3D-ΔPDF method offers a quantitative approach. The main challenges with this method, however, is the treatment of raw data; the background scattering needs to be accounted for, and the removal of the Bragg peaks is difficult to perform accurately, yet crucial. Using the punch-and-fill method, for example, any thermal diffuse scattering underneath the Bragg peaks is lost, and if the Bragg peak width is not precisely known, too much or little data may be discarded [252].

2.3 Spectroscopy techniques

Spectroscopy is a particular useful technique to study the chemical environment of samples, based on the absorption and emission of radiation by the material [254]. In this thesis, the spectroscopy techniques used to probe the local environments of MOF samples include extended X-ray absorption fine structure (EXAFS), nuclear magnetic resonance (NMR), infrared (IR), and Raman spectroscopy, of which the

underlying theory will be discussed in this section.

2.3.1 Extended X-ray Absorption Fine Structure

Whilst the previously described methods are based on the scattering of X-rays, EXAFS involves the absorption of X-rays by atoms *i.e.* X-ray absorption spectroscopy (XAS) [255, 256]. This absorption causes the excitation or ejection of a core electron, and can be quantified with the absorption coefficient, μ. Its value is determined by comparing the intensity of the incoming and transmitted beam, mathematically derived as the negative logarithmic derivative of the intensity with respect to the absorption path length:

$$\mu = -\frac{d \ln I}{dx}, \tag{2.21}$$

where I represents the intensity and x corresponds to a given thickness of the material *i.e.* the absorption path length.

To obtain the XAS spectrum, μ is measured for a range of incident X-ray energies. Characteristic of such a spectrum is the absorption edge, which is a sharp increase in absorption that occurs when the X-ray energy surpasses the threshold required to excite electrons from a specific orbital, dependent on the type of metal being studied. X-ray absorption studies often mention the 'K-edge', which refers to the excitation of an electron in the 1s orbital.

The gradual oscillations above the absorption edge correspond to the EXAFS. By analysing this region, valuable local structural information can be extracted for the atom under investigation; examples include the coordination number and identity of its first neighbours, which function as backscattering atoms.

To analyse the data, the EXAFS region is first represented as a function of $\chi(E)$:

$$\chi(E) = \frac{\mu(E) - \mu_0(E)}{\Delta\mu_0}. \tag{2.22}$$

Here, the subtraction of $\mu_0(E)$ accounts for the removal of the background, whilst the

division by $\Delta\mu_0$ represents the normalisation of the function. However in practice, it is common to express χ as a function of momentum, rather than energy, using the photoelectron wave vector, k:

$$k = \frac{2\pi}{\lambda} = \frac{2\pi m_e v}{h} = \left[\frac{8\pi^2 m_e (E - E_0)}{h^2}\right]^{\frac{1}{2}}, \tag{2.23}$$

where E represents the photon energy, E_0 is the threshold energy, m_e is the mass of an electron, v is the velocity, and h is Planck's constant. It is important to note that, for this expression to be valid, $E > E_0$.

The final 'EXAFS equation', derived using Fermi's golden rule, relates the X-ray absorption spectrum to the structural parameters of the system:

$$\chi(k) = \sum_j \frac{N_j f_j(k) \exp[-2k^2\sigma_j^2] \exp[-2R_j/\lambda]}{kR_j^2} \sin[2kR_j + \delta_j(k)]. \tag{2.24}$$

In this equation, the terms N_j and R_j represent the coordination number and radius of the scattering atom, respectively, σ_j is the measure of disorder in neighbouring atoms, $f_j(k)$ represents the amplitude, and $\delta_j(k)$ is the phase shift. By calculating the values of $f_j(k)$ and $\delta_j(k)$ for a given value of k, the unknown values of N_j, R_j, and σ_j can be obtained.

Since the amplitude of the oscillation falls off with k, $\chi(k)$ is often multiplied by k^2 or k^3; a process known as k-weighting. This approach allows for a more effective visualisation and interpretation of the oscillations.

To complete the data extraction, a Fourier transform is often performed on $\chi(k)$. This transformation results in a radial distribution function, thus describing the variety in electron density as a function of the radial distance from the nucleus. This function is not be confused with the 1D PDF, in which each peak corresponds to an interatomic distance.

Various methods and software packages have been developed to analyse EXAFS data. The FEFF code, for example, is a real-space multiple-scattering function code

which allows fitting of EXAFS data against a structural model [257]. In this thesis, however, EXAFS is solely used as a fingerprinting method *i.e.* comparison of functions. Although rather than comparing the EXAFS data by eye, an approach involving calculation of the Pearson correlation coefficient for each dataset was adapted, in turn enabling the quantitative comparison of functions [258, 259]. The value of the Pearson correlation coefficient is always between –1 and 1; –1 indicating an inverse linear relationship between functions, and 1 referring to a direct linear relationship. A correlation coefficient of 0 means there is no linear relationship.

X-ray absorption experiments are typically performed at synchrotrons to ensure the high-intensity of X-rays. Moreover, the tunability of the wavelength enables any element of interest in the sample to be probed. Samples tend to be prepared in powder form and may be diluted with a substance such as cellulite in order to minimise absorption. Another factor to take into consideration is the thickness of the sample. If too thick, there is a risk of absorbing all of the X-ray photons. Conversely, if the sample is too thin, it may absorb too few photons for accurate quantification.

In this thesis, all XAS experiments were performed at the LISA beamline (BM-08) [260] at the European Synchrotron Radiation Facility (ESRF, Grenoble, France) using the Zn K-edge (9658.6 eV). Samples were measured using a pair of Si(311) flat monochromator crystals, providing an energy resolution of $\sim 4 \times 10^{-5}$ ($\Delta E/E$). Si-coated focusing mirrors ($E_{\mathrm{cut-off}}$ ~16 keV) were used for harmonic rejection. In order to prevent beam-damage on samples, data were collected with a wide beam (approximately 2 × 2 mm^2) and low flux (approximately 2 ×10/69 ph s^{-1}). Measurements were performed in transmission mode at room temperature. The step size for the X-ray near edge structure (XANES) region was 0.5 eV; the post-edge EXAFS region of the spectrum was acquired with a fixed k-step width of 0.025 $\mathrm{Å}^{-1}$.

All samples were prepared as pellets using a manual hydraulic press. To prevent the crystal samples from collapsing, they were gently ground to a fine powder using a pestle and mortar. The required weight of each sample was calculated using the Viper XAFS mass software/widget [261], taking into account the energy required at the Zn K edge (9659 ± 50 eV) and the surface area of the pellets (1.237 cm^2).

Approximately 100 mg of cellulose was added to all samples. The two components were then mixed and ground together using a pestle and mortar, before gently depositing onto a macro-micro KBr pellet die. After fitting, the die was placed on the hydraulic press, which was used to increase the pressure to no higher than 2 bar, creating the pellet (the pressure was intentionally kept at a low value to prevent the porous samples from collapsing). The pellets were removed from the die and pressed between kapton (polyimide) tape, which in turn was fitted onto the sample holder to be kept in the beam.

Standard procedures outlined above (*i.e.* background removal, edge step normalisation and energy calibration) [255] were followed to extract the structural EXAFS signal using the software ATHENA [262].

2.3.2 Nuclear magnetic resonance

Nuclear magnetic resonance (NMR) spectroscopy is a powerful tool to probe local environments of atoms, routinely used to determine the structure of organic molecules in solution [263, 264]. It is based on the interaction ot atomic nuclei with a magnetic field, resulting in resonance at frequencies that are characteristic of the atoms. This phenomenon makes NMR element specific and provides information about the coordinating atoms and coordination number. It is also quantitative and can determine the relative populations of different atomic environments.

In this thesis, both ^{1}H and ^{13}C NMR spectroscopy were performed to confirm the structure and presence of 1,3-bdc in MOF crystals. To perform these experiments, the MOFs were dissolved using an acid-digestion approach, which involved adding a minimum amount of DCl/D_2O solution (33%) to the crystals.

All NMR measurements were carried out on a 2-channel Bruker AVIII 400 nanobay instrument (VIII HD 400) running TOPSPIN 3 equipped with a 5-mm z-gradient broadband multinuclear probe with variable temperature accessories, and a 24-position SampleCase robotic sample changer. Data analysis was performed using the software MESTRENOVA [259].

2.3.3 Infrared and Raman Spectroscopy

In this thesis, both infrared (IR) and Raman spectroscopy were used to characterise the vibrational spectrum of samples. These techniques operate on different principles of energy transfer to the molecules [265]. In IR spectroscopy, electric-dipole mediated transitions occur between molecular vibrational energy levels as a result of mid-IR radiation (4000 – 670 cm^{-1}) absorption, whereas Raman spectroscopy is a two-photon inelastic light scattering event involving the Raman polarisability of the molecule; the incident photon is of much greater energy than the vibrational quantum energy, and therefore transfers some of its energy to the molecular vibration, with the remaining energy scattered as a photon with reduced frequency.

Although both techniques can be used for molecular structure identification, in this thesis, they were employed primarily as fingerprinting methods to compare the chemical environments of different samples.

IR absorbance specta were recorded by placing dried samples onto a Shimadzu IRAffinity-1. A background scan was taken before each measurement in order to ensure the previous sample had been completely removed. The acquired data were processed using the LabSolutions IR software [266].

Raman scattering spectra were obtained using a Renishaw InVia Qontor confocal spectrometer. Samples were excited with a Renishaw plc RL785 red diode laser outputting an excitation wavelength of 785 nm (25% laser power, 40–50 mW) and were referenced internally with respect to silicon at 520.5 $\pm$ 0.1 cm^{-1}. Single crystalline samples were loaded onto an aluminium plate, and a Leica long 50$\times$ objective was used to focus the laser beam perpendicularly onto the sample. The spectra were recorded on a Renishaw Centrus 2957N7 CCD detector using 10-second exposure times averaged over three accumulations. Data were processed using Renishaw's WiRE software [267], with baseline subtractions and cosmic ray removal as required.

2.4 Topology determination

As stated in the introduction, MOF structures need to be simplified in order to characterise their topology. This task is facilitated by the ToposPro software, which allows for the determination of MOF topologies through deconstruction of crystal structures using either the standard, or cluster representation [268]. In both approaches, atoms and parts of the structure are compressed to their centers of mass. Either representation is appropriate to use, however the standard representation specifically shows how metal atoms are connected, whereas the cluster representation reports on the connectivity of polynuclear complex groups. In this thesis, the standard representation was used to characterise all MOF structures obtained.

2.5 Mechanical and thermal stability

To realise MOFs for (industrial) applications such as catalysis and gas separation, it is crucial that they exhibit thermal and mechanical stability. This property is often probed by means of exposure to high temperature and pressure. The combination of such extreme conditions and crystallography forms a particularly powerful tool to understand structure-property relationships of MOFs [269].

2.5.1 Variable temperature X-ray diffraction

Variable-temperature crystallographic measurements are straightforward: one performs a diffraction experiment as normal whilst varying the temperature. This variation of temperature is typically regulated by data collection software (*e.g.* CrysAlisPro [241]), which starts a new experiment at set temperature increments.

One may gain significant information on the material's mechanical behaviour from indexing the variable-temperature diffraction data alone. Namely, the change in lattice parameters, ℓ, as a function of temperature, T, can be directly related to the bulk expansivity, also known as the thermal expansion coefficient α_ℓ [270]:

$$\alpha_\ell = +\frac{1}{\ell}\left(\frac{\partial \ell}{\partial T}\right)_p . \tag{2.25}$$

Thus, α_ℓ is a measure of both the direction of the expansion (*i.e.* positive or negative) and the magnitude.

In this thesis, the value of α_ℓ was derived from experimental data using the software PASCAL [270], which uses a straightforward linear relationship for this purpose: $\ell(T) = \ell_0(1 + \alpha_i T)$. The use of more intricate fitting approaches would require another fitting software, and is beyond the scope of this thesis.

Finally, it is important to note that Equation 2.25 only applies to unit cell parameters from crystal systems with orthorhombic or higher symmetry. For lower symmetry classes, the principal axes do not necessarily relate to the unit-cell axes and therefore must be determined as the eigenvector of the full strain tensor. This process is also fully implemented in PASCAL [270].

2.5.2 High-pressure X-ray diffraction

In contrast to variable-temperature crystallography, high-pressure diffraction experiments are more involved. This shift arises from the change in apparatus, consequently requiring special settings and additional corrections during data collection and refinement. In fact, depending on the experimental set-up, one may gain valuable information concerning mechanical properties such as the elasticity, stiffness, hardness and fracture toughness of a material [271].

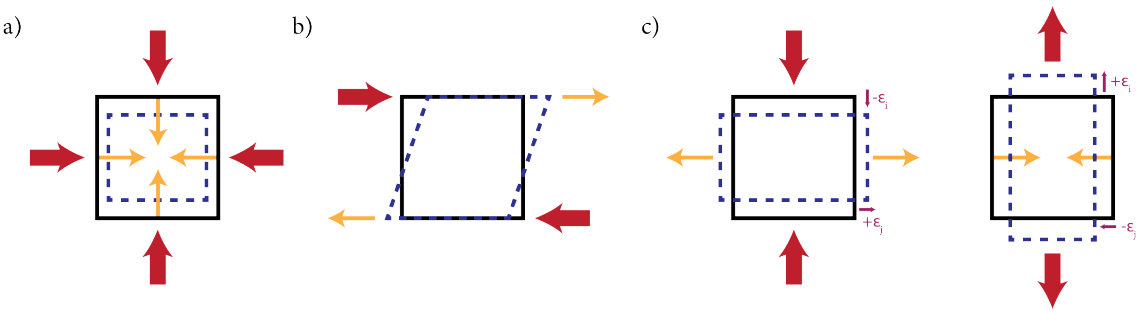

Figure 2.10: Schematic of directional elastic properties of materials: (a) hydrostatic compression represented with the bulk modulus, *B*, (b) shear, represented with the shear modulus, *G*, (c) uniaxial compression (left) and tension (right). The terms ϵ_i and ϵ_j denote the axial and lateral strain, respectively. Dark blue dotted lines indicate the distorted geometries, with red arrows representing the direction of stress exerted and orange arrows the axis along which the response is measured.

The terms bulk (B), shear (G) and Young's (E) moduli (as well as the Poisson's ratio) are often mentioned in high-pressure studies [271]. The former applies to experiments where pressure is applied hydrostatically (*i.e.* isotropically), whilst the other two involve the anisotropic application of pressure (Fig. 2.10). In this thesis, all high-pressure experiments were performed under hydrostatic pressure. Therefore the bulk modulus is determined in our data analysis. There is also some discussion of the Young's modulus, however this was not measured experimentally. I will discuss the origin of these terms, but not before I have described the details of a high-pressure diffraction experiment.

Set-up: the diamond anvil cell

The first attempts at high-pressure X-ray diffraction experiments date back to 1933 [272], therefore not long after the discovery of X-ray crystallography in 1912 [273, 274]. The experimental set-up involved a powder-containing steel bomb fitted with two beryllium windows on opposite ends to allow the incident and diffracted beams to pass through. Pressure was applied through the compression of gas. However this arrangement presented two main challenges. Firstly, the windows only allowed diffraction at certain angles, preventing the collection of a full dataset. Secondly, the cell contributed significantly to the background, in turn interfering with weakly scattered radiation. As a result, data quality was poor. Moreover, the pressures achieved in this cell were rather modest, reaching up to 0.1 GPa. For context, guacamole is currently produced industrially at 0.8 GPa [275].

Significant progress in the field was made with the introduction of the diamond anvil cell (DAC) in 1959 [277]. Initially developed for Raman spectroscopy measurements, crystallographers quickly recognised the potential of DACs for high-pressure crystallography due to the compact size of the cell and 180° optical transmission capabilities [278]. Slight modifications to the original cell resulted in the so-called "Merril-Bassett" DAC, now consistently used in high-pressure single-crystal diffraction experiments (Fig. 2.11a) [279]. This cell is composed of two steel plates with a conical hole at their centres, each having a half opening angle of 40°. Tungsten carbide backing seats are located within the plates to hold the opposing diamond

anvils in place. Between the flat-faced diamond anvils, a metal gasket is positioned. Prior to assembling the cell, this gasket is created by drilling a cylindrical hole of 200–300 μm in diameter through a thin plate, typically made of tungsten or Inconel. By placing the gasket in between the diamonds, a cylindrical sample chamber is created. The pressure inside this chamber is increased by tightening the three Allen screws attached to the steel plates, which brings the diamond faces closer together.

The sample chamber usually contains a single crystal surrounded by a small amount of pressure transmitting medium (PTM). The PTM is an important component of the set-up, as it ensures that pressure is applied hydrostatically. It is often a liquid, but can also be a gas or soft solid. In this thesis, only liquid PTM was used, which is simply pipetted into the chamber. It is crucial to carefully consider the type of PTM for two different reasons. Firstly, different PTM's have different hydrostatic limits *i.e.* a pressure threshold above which the PTM no longer applies pressure hydrostatically. Once the limit is breached, it may lead to inaccuracies in

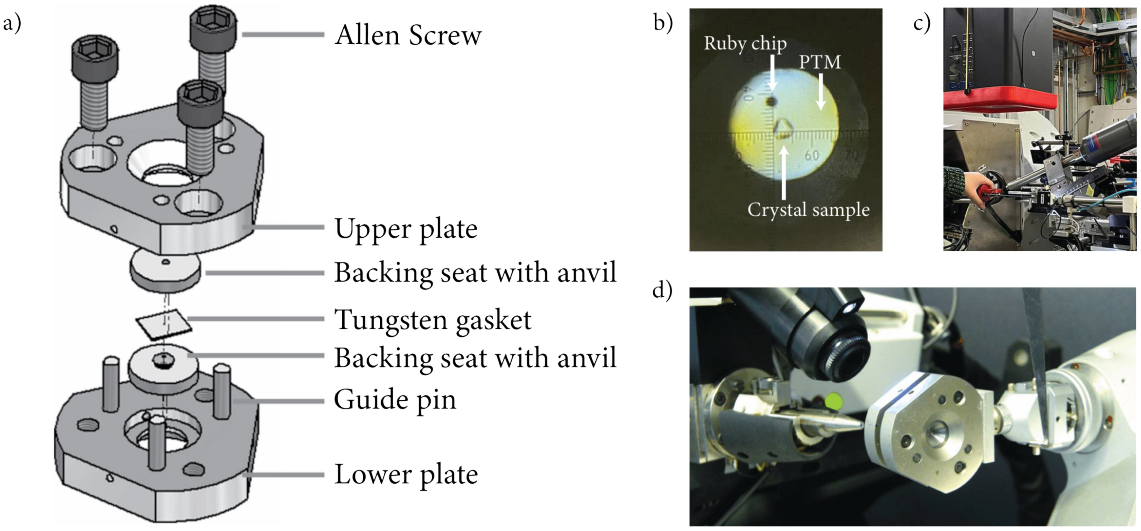

Figure 2.11: Experimental DAC set-up: (a) Deconstructed view of a Merril-Basset DAC, with the name of each component displayed on the right.(b) View of sample chamber containing a single crystal sample, ruby chip, and PTM. (c) Picture of a DAC mounted on the i19 beamline of the diamond source, which is the set-up used in this thesis. The DAC is placed in a sample holder (coloured red in the image) to be positioned on the goniometer head in front of the beam. The detector is positioned at 90° during the mounting of the sample (as is shown in the image); it moves into position at the start of each measurement. (d) Picture of a DAC mounted on a diffractometer to show the position of the beamline with regards to the half opening angle. Figures (a) and (d) adapted from Ref. 276 with permission from the IUCr.

data analysis. Secondly, due to the high porosity of MOFs, one needs to consider the molecular size of the PTM *i.e.* whether it is desired for the PTM to enter the pores and interfere with the mechanical stability of the framework by supporting it from the inside.

In this thesis, all high-pressure experiments were carried out in a Merrill-Bassett diamond-anvil cell using DAPHNE oil 7373 as PTM. This PTM applies hydrostatic pressure up to 2.2 GPa and is also sufficiently bulky to prevent it from entering the pores [280]. Due to the low viscosity of DAPHNE oil, the crystal samples had to be glued onto the diamond faces to prevent them from moving during the experiment.

Finally, along with the sample and PTM, a ruby chip is placed inside the chamber (Fig. 2.11b). This ruby crystal serves as a pressure calibrant using the well-established ruby fluorescence method, since the fluorescence transition of ruby is correlated to the applied pressure [281]. To obtain an accurate estimation of the experimental error, the pressure should be measured both before and after data collection, ensuring reliable pressure calibration throughout the experiment.

Data collection and refinement

As for the data collection, one needs to take into account the shading of the body of the cell. In other words, modified collection strategies are needed. A typical data collection, based on Ref. [282], is outlined in Table 2.1. This includes eight runs of 0.3° ω scans performed at different values of ϕ and 2θ, ensuring the angle between the incident beam and the cell axis is less than 40° and less than 80% of the detector is shaded.

In this thesis, all high-pressure X-ray diffraction data were collected on the I19 beamline (hutch 2) at the Diamond Light Source using an Eiger2 4M CdTe detector. Because of the large size of this detector, only two runs were needed to collect all data, which involved starting at a high value for 2θ and then scanning across the face of the DAC.

The processing of high-pressure SCXRD data is also non-standard compared to routine SCXRD experiments. In order to index the data, the harvested reflections

Table 2.1: A typical data collection strategy of a high-pressure diffraction experiment, as outlined in Ref. 282.

Run	2θ / °	ϕ / °	ω_{max} / °	ω_{min} / °
1	–28	90	–10	–40
1	28	90	40	–25
1	–28	90	–155	–220
1	28	90	–140	–170
1	–28	270	–155	–220
1	28	270	–140	–170
1	–28	270	–10	–40
1	28	270	40	–25

need to be filtered from all that do not arise from the sample. This includes powder rings from the tungsten carbide backing seats as well as intense reflections from the diamonds. Once indexed, the data must be integrated with dynamic masks that allow for shaded areas in the frames to be excluded. Finally, integrated reflections that are poorly measured due to partial shading of the cell or overlap with diamond reflections, must be omitted. These corrections are implemented in single crystal refinement software such as CrysAlis Pro [241] and APEX II [283]. From the resulting reflection data, structure refinement proceeds as usual.

Bulk modulus

The bulk modulus (denoted by B in this thesis, albeit often given the symbol K [269, 270]) characterises the variation of the volume of a material with increasing hydrostatic pressure, at constant temperature:

$$B = -V \left(\frac{\partial p}{\partial V} \right)_T , \tag{2.26}$$

where V reflects the volume, p is the pressure, and T is the temperature. It is therefore a measure of the resistance (*i.e.* compressibility) of a material to hydrostatic pressure. Its dimensionless pressure derivative, $B' = (\partial B/\partial p)_T$, can be an indicator of unusual mechanical behaviour. For example, a large B' is often indicative of a rapid stiffening, in turn characteristic of layered materials, for example [284], whilst

a negative B' can indicate the presence of a dynamic instability [285].

The value of B can be determined by fitting an ideal equation of state (EoS) to pressure-volume data [286]. Several forms of EoS exist, though in this thesis the Birch-Murnaghan (BM) EoS [287] has been utilised as it is implemented by the software PASCal [270].

The BM theory is based on a Taylor expansion series, whereby adding increasing derivative truncation order terms allows more complex behaviour to be modelled [287]. Usually, only 2nd or 3rd order BM EoS are used. Defining the parameter

$$\eta \equiv -V \left(V_0/V\right)^{1/3}, \tag{2.27}$$

where V_0 represents the zero-pressure unit-cell volume, the 2nd and 3rd order BM fits correspond to the following equations of state, respectively:

$$p(V) = \frac{3B}{2}\left(\eta^7 - \eta^5\right), \tag{2.28}$$

$$p(V) = \frac{3B_0}{2}\left(\eta^7 - \eta^5\right)\left[1 + \frac{3}{4}(B' - 4)(\eta^2 - 1)\right]. \tag{2.29}$$

Here, B_0 can be interpreted as the value of B at zero pressure. Thus, the 2nd and 3rd order BM EoS refine 2 and 3 parameters, respectively. One may choose which EoS gives a more accurate estimate of B, based on the fit. There is no thermodynamic requirement that the experimental equation of state, $p(V)$, follows the BM form.

Linear compressibility

The change in lattice parameters, ℓ, as a function of pressure, p, can be directly related to the bulk, linear compressibility, K_ℓ [288, 289]:

$$K_\ell = -\frac{1}{\ell}\left(\frac{\partial \ell}{\partial p}\right)_T. \tag{2.30}$$

Here, K_ℓ describes the relative rate of contraction of a material's linear dimensions

with increasing pressure whilst keeping the temperature constant. In other words, K_ℓ is the (anisotropic) inverse of the bulk modulus. Unlike the thermal coefficient discussed above, the compressibility coefficient has a minus sign in front of the inverse of ℓ, which simply indicates that a positive compressibility corresponds to a reduction in length under increasing pressure.

The magnitude of the compressibility usually reflects the bond strengths: the softer the material, the larger the value of K_ℓ.

Young's modulus and Poisson's ratio

The Young's or elastic modulus, E, provides a measure of the stiffness of a material under the effects of unidirectional loading (Figs. 2.10c). Accordingly, the reciprocal of the stiffness, $1/E$, defines the compliance of the framework. When a material is deformed elastically and axially (*i.e.* along the loading direction), it is accompanied by a lateral dimensional change. The ratio of the lateral strain, ε_j, to the axial strain, ε_i, is defined by the Poisson's ratio ($\nu_{ij} = -\varepsilon_j/\varepsilon_i$) (Fig. 2.10d).

Experimentally, one typically obtains the Young's modulus of a MOF by nanoindentation. This technique consists of pressing a tip made of a very hard material — usually a diamond of a few hundred nanometers in diameter — onto a single crystal [290, 291]. The Young's modulus and Poisson's ratio are then usually extracted using the Oliver and Pharr method [292].

Computational tools

As mentioned previously, the software PASCal was used to analyse the behaviour of MOF samples both at variable-temperature and under high-pressure [270]. In addition to PASCal, the General Utility Lattice program (GULP) [293, 294] and ELATE code [295] were utilised for calculating elastic constants and determining the orientational dependence of various elastic moduli, respectively.

GULP is a lattice dynamics program specifically designed for simulating material properties, such as elastic constants, phonon frequencies, and NMR shifts [293, 294]. It employs force field methods to compute the energies and associated properties of materials based on force field parameters specific to a given configuration. These

parameters can include bond strength, atomic charges, and potentials for bond stretching or bending. By utilising GULP to calculate the elastic stiffness matrix of a system, the resulting data can subsequently be fed into the ELATE software for the analysis and visualisation of second-order elastic tensors [295].

2.6 Gas adsorption

In this thesis, the porosity of MOF samples was investigated using a combination of experimental techniques and simulations involving geometry-optimised MC models. Therefore, this section provides an overview of both gas adsorption measurements and the principles of grand canonical Monte Carlo simulations as relevant background information.

2.6.1 Gas adsorption measurements

Due to the highly porous nature of MOFs, their surface area is routinely probed through high-pressure gas adsorption experiments. Sample preparation is crucial in this regard: to obtain accurate results, the sample needs to be activated or degassed (*i.e.* all solvent needs to be removed) without irreversible alteration or collapse of the framework [296]. In this thesis, sample evacuation was achieved by exchanging high-boiling solvents for those with a low boiling point, before heating under dynamic vacuum; a process known as thermal treatment [297]. Glass cells were used to hold the samples during evacuation. After completion, glass rods were placed within the glass cells to minimise dead space, before transferring to a BET machine to perform the adsorption experiment.

There are a range of adsorptives to select for gas adsorption experiments. Most common are N_2 measurements carried out at 77 K, however this is less suited to calculation of the surface area of MOFs with polar surface area functionality [298]. Other common gases used in adsorption experiments are Ar, CO_2, CH_4, and H_2. In this thesis, experiments were performed with N_2, CO_2, CH_4, and H_2 gas. Notably, experiments with CO_2 and CH_4 gas are performed at 273 K, rather than 77 K.

The surface area may be extracted from measured adsorption isotherms using the Brunauer-Emmett-Teller (BET) equation:

$$\frac{p/p^\circ}{n(1-p/p^\circ)} = \frac{1}{Cn_\mathrm{m}} + \frac{C-1}{Cn_\mathrm{m}}(p/p^\circ), \tag{2.31}$$

where p is the pressure, p° is the saturated pressure of the adsorbate at the indicated temperature, n is the specific quantity adsorbed at the relative pressure (p/p°), n_m is the monolayer capacity, and C is a constant obtained from the linear fit of the isotherm. The value of C should be at least 10 to ensure meaningful results [299].

It is important to note that this BET surface area is apparent, and therefore must not be treated as a realistic probe-accessible surface area. To evaluate its accuracy, it is common to compare the BET surface area with values calculated from crystallographic models using computational methods such as DFT and grand canonical Monte Carlo (GCMC) simulations [300].

Gas adsorption measurements may also give information regarding the strength of the interactions between the gas and host material — *i.e.*, the heat or enthalpy of adsorption [296]. Although calorimetry can be used to directly measure the enthalpies of adsorption *in situ*, the isosteric method was used in this thesis, which includes the comparison of isotherms obtained at ∼10 °C temperature intervals [301–303]. Here, the Clausius-Clapeyron equation is used to calculate the isosteric energy, E_iso [304]:

$$\left[\frac{\mathrm{d}\,\ln(p)}{\mathrm{d}T}\right] = \frac{E_\mathrm{iso}}{RT^2}. \tag{2.32}$$

This equation may be simplified for two data points:

$$\ln\left[\frac{p_1}{p_2}\right] = \frac{E_\mathrm{iso}}{R}\left[\frac{1}{T_2} - \frac{1}{T_1}\right]. \tag{2.33}$$

Notably, this approach assumes that the adsorption is reversible and that the responsible mechanism does not change in the considered temperature range.

In this thesis, all gas adsorption experiments were performed using ultra-high

purity N_2, CO_2, CH_4, and H_2 gas from BOC gas Australia (Grade 5.0), recording gas adsorption isotherms at low pressure (0–1.2 bar) by a volumetric method using a Micromeritics 3Flex instrument. All samples were prepared by exchanging solvents for chloroform and leaving to dry in air, before weighing in a pre-dried and weighed BET tube. The crystal samples were then activated at 150 °C under dynamic vacuum at 10^{-4} mbar for 120 h to remove any solvent. The mass of degassed samples was measured prior to the analysis.

All analysis of adsorption data was performed using the MicroActive 3Flex software [305], which implements the BET and Clausias-Clapeyron equation to calculate the surface area and heat of adsorption, respectively.

2.6.2 Grand canonical Monte Carlo

Grand Canonical Monte Carlo (GCMC) simulations enable the investigation of systems under fixed volume and temperature conditions [306]. In a typical GCMC simulation, particles are inserted, deleted, or moved within the system whilst maintaining the desired chemical potential. The objective is to sample system configurations that align with the specified chemical potential and other thermodynamic parameters.

In the context of this thesis, GCMC simulations were employed to study the adsorption behaviour of porous materials. Specifically, single-component adsorption isotherms of geometry-optimised MC models were determined for CH_4 and CO_2 gases at temperatures of 273 K and 293 K. The pressure range for the isotherms was selected as 0 to 1 bar, with a step size of 0.01 bar. The Lennard-Jones (LJ) parameters for the framework were assigned based on the Universal Force Field (UFF) [307], and the charge parameterisation was performed using the DDEC6 method [308]. In the CO_2 simulations, electrostatic interactions were computed using the Ewald summation method. The TraPPE force field was utilised for both CH_4 and CO_2 adsorbates. CH_4 was represented as a single united atom site [309], whilst CO_2 was modelled using three LJ sites [310]. Lorentz–Berthelot mixing rules were employed to calculate the interactions between the adsorbate and the framework. All Monte Carlo simulations were conducted using the RASPA software [311].

2.6.3 Thermogravimetric analysis

Thermogravimetric analysis (TGA) is routinely used to probe the thermal stability of MOFs. In a typical experiment, the mass of a sample ($\sim$ 1 mg) is recorded while the temperature is increased to $\sim$700 °C at a steady rate in a controlled atmosphere [312]. The mass loss usually occurs in a number of distinct steps: (i) desolvation; followed by a (ii) plateau region — *i.e.*, where the evacuated MOF is stable; and a (iii) a secondary mass loss event, which corresponds to the decomposition of the MOF.

In this thesis, all TGA measurements were carried out using a Mettler Toledo TGA/DSC 1 system operated under flowing N_2 gas with a ramp rate of 5 °C min^{-1} from 25 to 700 °C. Prior to the experiment, samples were prepared by soaking in dichloromethane (DCM) for two consecutive days. The samples were left to dry at room temperature under vacuum.

Chapter 3

Synthesis and average structure analysis

3.1 Summary and acknowledgements

By performing a range of solvothermal syntheses with 1,3-bdc (derived) linkers and $Zn(NO_3)_2 \cdot 6\ H_2O$, five MOFs of different topologies were obtained: TRUMOF-1, MOX-2, MOX-3, MOX-4, and MOX-5. Of these, TRUMOF-1, MOX-2 and MOX-5 had not yet been reported in the literature. This chapter will present the synthesis of each sample as well as a detailed description of their structure and topology, as derived from single-crystal and powder X-ray diffraction measurements.

Initial synthetic efforts focused on combining 1,3-bdc with $Zn(NO_3)_2 \cdot 6\ H_2O$ salt in a range of different solvents. Reactions were only successful with N,N-dimethyl formamide (DMF) and ethyl acetate (EA), resulting in TRUMOF-1 and MOX-2, respectively. Despite having the same building blocks, their structures are significantly different. The average structure of TRUMOF-1 includes partially occupied atoms, indicating it to be disordered. MOX-2, on the other hand, is ordered. Its network is described by the **3,5T25** net, and includes a wine-rack and helical motif.

To investigate the impact of reticular chemistry, the syntheses of TRUMOF-1 and MOX-2 were repeated for 1,3-bdc linkers with functional groups attached to the 4,5-, and/or 6-position(s) of the benzene ring. For the 5- substituted 1,3-bdc linker analogue, products were only obtained for reactions performed in EA. The resulting phase, called MOX-3, adopts the **ptr** topology and is characterised by large hexagonal channels that are lined by the functional groups. In contrast, products were only obtained for 4,6-substituted 1,3-bdc analogues when performing syntheses in DMF, resulting in the phases of MOX-5α and MOX-5. The former is the metastable, stacking faulted phase of MOX-5, which consists of layers held together by non-covalent interactions between the functional groups.

Finally, the significance of the 120° angle of 1,3-bdc was investigated by repeating the synthesis of TRUMOF-1 and MOX-2 with other bent linkers such as *cis*-4,4'-stilbene and 2,5-thiophene dicarboxylic acid. The reaction was only successful for the latter, resulting in MOX-4, which, despite having a **tcj-3,5-Pnma** topology, shares structural features with MOX-2.

I am grateful to Lisa Cameron, Hunter Windsor, David Dharma, and Cameron J. Kepert for their help with solving the average structure of TRUMOF-1, and Davide M. Proserpio for his help in determining the topologies of MOX-2 and MOX-4.

3.2 TRUMOF-1

3.2.1 Synthesis

TRUMOF-1 was synthesised by combining solutions of $Zn(NO_3)_2 \cdot 6\ H_2O$ (0.33 mmol) and 1,3-bdc (0.33 mmol) in DMF (5 mL). The resulting mixture was placed in a teflon-lined solvothermal vial and sealed. The vial was placed in an oven and heated to 110 °C. After 14 h at this temperature, the system was slowly cooled to room temperature to afford TRUMOF-1 as colourless truncated tetrahedra (Fig. 3.1). The crystals were isolated by filtration and washed three times with chloroform ($CHCl_3$). Each washing cycle involved soaking TRUMOF-1 crystals in fresh $CHCl_3$ for 24 h, followed by filtration.

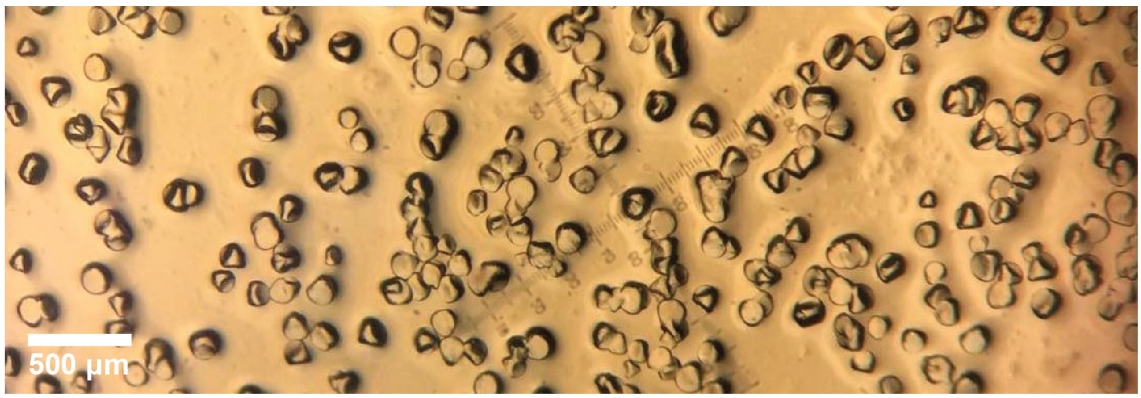

Figure 3.1: Batch of TRUMOF-1 crystals. Scale bar given in the bottom left corner for reference (500 µm).

3.2.2 Average Structure Determination and Refinement

Single crystal X-ray diffraction

The single crystal diffraction pattern of TRUMOF-1 was measured using a Bruker FR591-D85-Apex-II diffractometer equipped with an Incoatec IμS 2.5 rotating anode source, D85 four-circle kappa goniometer, and Incoatec Quazar multilayer optics. The instrument outputted mirror-monochromated Mo-Kα ($\lambda = 0.71073$ Å) radiation and was fitted with a Bruker Apex-II CCD area detector which was equipped with an Oxford Cryosystems Cryostream 700 for temperature control.

A washed crystal of TRUMOF-1 was isolated directly with $CHCl_3$, evacuated, and then mounted onto a 0.2 mm diameter MiTeGen loop using Paratone-N oil as a cryoprotectant. The crystal was then attached to the instrument goniometer and cooled to the desired initial temperature (100 K) before data were collected about ϕ and ω rotations.

Unit cell determination, data integration, frame scaling, and absorption corrections (multi-scan implemented in SADABS with beam profile correction) were performed within APEX4 [283].

An initial solution in the non-centrosymmetric cubic space group $F\bar{4}3m$ with a = 15.392(2) Å showed clearly the presence of OZn_4 tetrahedra centred on the $4a$ Wyckoff position. The remaining electron density extended between neighbouring tetrahedra, forming molecular arrangements that resembled the trigonally symmetric molecule 1,3,5-btc. The centre of this molecular scattering was the $16e$ site, which has $3m$ point symmetry.

To assess whether the structure of TRUMOF-1 actually contains the organic linker 1,3,5-btc rather than 1,3-bdc, both ^{1}H (Fig. 3.2a) and ^{13}C (Fig. 3.2b) NMR measurements were performed on acid-digested crystals as well as separate solutions containing 1,3-bdc and 1,3,5-btc. Our results show that there are no 1,3,5-btc linkers incorporated within the structure of TRUMOF-1, as the corresponding peaks are not present in the spectra of digested TRUMOF-1 samples. Instead, all peaks —

except for one that corresponds to the remnant of DMF retained within the pores — correspond to 1,3-bdc.

Accordingly, we proceeded to test whether this 3-fold symmetry ligand-site scattering density is consistent with partial occupancies arising from different orientations of the 1,3-bdc units. In this case, the occupancies of the carboxylate carbon and oxygen atoms should be linked (these are labelled C1 and O2, respectively), Likewise, the occupancies of the benzene carbon atoms should all be identical (these appear as two crystallographically-distinct sites and are labelled C2 and C3). A simplified refinement model in which site occupancies were allowed to vary subject to these constraints gave the occupancies listed in Table A1.3 in the appendix. In order to avoid strong covariance between site occupancies and atomic displacement parameters, we used a single common U_{iso} value for all linker atoms. The key result is that the occupancies of C1 and O2 refine to values close to 0.5 (46(3)), and those of C2 and C3 close to 0.75 (0.70(4)); these values would correspond to a crystal

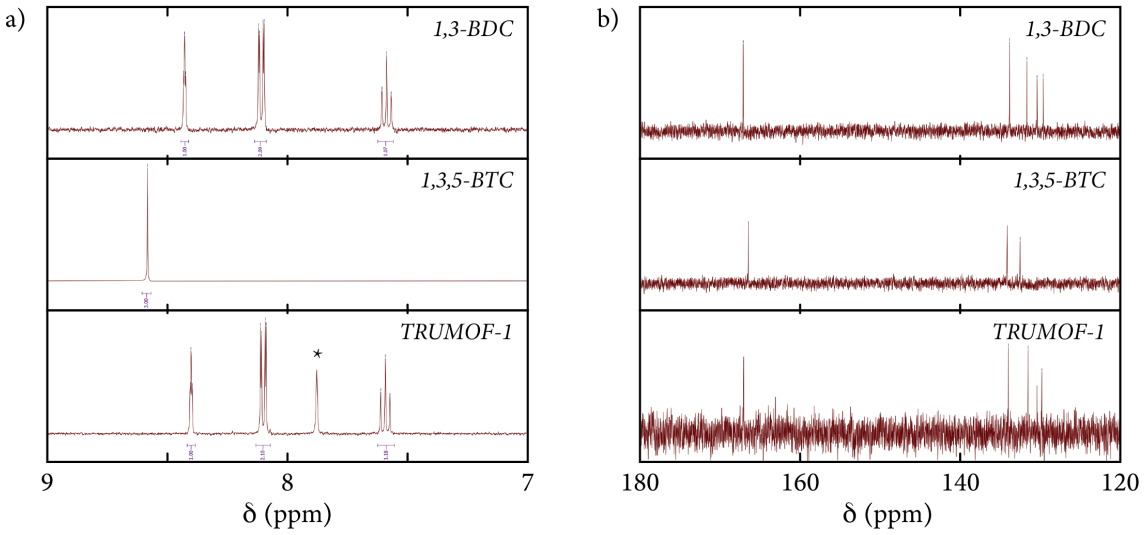

Figure 3.2: (a) ^{1}H and (b) ^{13}C NMR spectra of acid-digested TRUMOF-1 crystals and comparison to 1,3-bdc and 1,3,5-btc, all measured in deuterated DMSO. The regions shown cover the shifts associated with all C and H atoms, together with those of the carboxylic acid C environments. The only signals not included in these regions arise from DMF solvent. Detected signals are as follows. 1,3-bdc: ^{1}H δ 8.43 (t, J = 1.7 Hz, 1H), 8.11 (dd, J = 7.7, 1.8 Hz, 2H), 7.59 (t, J = 7.7 Hz, 1H); ^{13}C δ 167.08 (s), 133.86 (s), 131.70 (s), 130.41 (s), 129.65 (s). 1,3,5-btc: ^{1}H δ 8.60 (s, 3H); ^{13}C: δ 166.36 (s), 134.05 (s), 132.43 (s). Digested TRUMOF-1: ^{1}H δ 8.40 (t,J = 1.7 Hz, 1H), 8.09 (dd,, J = 7.8, 1.8 Hz, 2H), 7.58 (t,J = 7.8 Hz, 1H), and a solvent peak originating from DMF (indicated by and asterisk); ^{13}C δ 166.98 (s), 133.94 (s), 131.49 (s), 130.36 (s), 129.77 (s).

stoichiometry of $[OZn_4][1,3\text{-bdc}]_3$.

Having established that the linker site reflects a configurational average over three orientations of 1,3-bdc units, we developed a full structural model for refinement against the single-crystal diffraction data. The asymmetric unit of this model is shown in Figure 3.3a. In this model, C2 is split into two atoms (C2A and C2B) with identical coordinates and displacement parameters. These split sites reflect the (1,3)- and 5-positions of the 1,3-bdc molecule, respectively. Accordingly, the H atom bound to the 5-site is given the label H2B. The C3 site corresponds to the (2,4-)positions of the 1,3-bdc molecule, and is connected to the corresponding H3 atom.

All non-hydrogen atoms could be treated by an unrestrained anisotropic refinement unless otherwise stated. The position of H2B could not be located from the Fourier difference map and so had to be added in its calculated position and refined using riding thermal parameters. The second hydrogen site H3 could not be located from the Fourier difference map either, but also could not be added in its calculated position due to the symmetry imposed by the selected space group. Thus, the H3 site had to be added manually and refined with considerably strong geometric restraints to achieve a physically realistic C–H distance. The DFIX command was employed for this purpose, generating a length fixing restraint of 0.95 Å to achieve

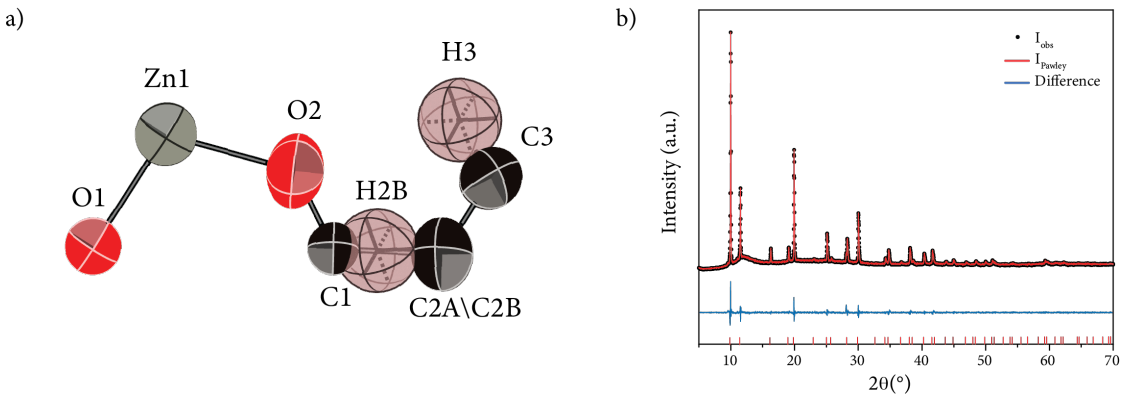

Figure 3.3: (a) Asymmetric unit of TRUMOF-1 at 100 K. Ellipsoids are drawn at 50% probability. Colour scheme is as follows: C = black spheres, O = red spheres, Zn = grey spheres and H = pink spheres. (b) Pawley refinement of the experimental TRUMOF-1 PXRD pattern, resulting in a = 15.5094(3) Å for $F\bar{4}3m$.

a similar bond length as for the constrained H2B site. The thermal parameter U_{iso} for H3 was also fixed to be the same as H2B. The 1,3- distance between H3 and its ortho carbon sites C2A and C2B was unrestrained, but to achieve an overall flat geometry of the 1,3-bdc linker, a FLAT command was applied to C2A, C2B, C3, and all of the other symmetry generated positions that make up the central C6 ring.

As imposed by the symmetry of the $F\bar{4}3m$ space group, the 1,3-bdc linker is equally disordered over three different orientations. However, because of the chemistry of the TRUMOF-1 system, each carbon site in the C6 ring is only 75% occupied. The occupancies of C2A and C2B (which share a common position) where therefore fixed at 50% and 25%, respectively, in order to achieve a 75% overall occupancy and to reflect the extent of there being a 25% vacancy of the 1,3-bdc unit. Accordingly, C2A and C2B had their atomic coordinates and thermal parameters fixed using the EXYZ and EADP constraints.

Finally, a refineable inversion-twin fraction was included.

Crystal data and refinement statistics for the 100 K data set, which is representative of all temperature points, are given in Table A1.4 in the appendix. An entirely equivalent approach was used to obtain structural models for six further temperature points; namely, 140, 180, 220, 260, 300, and 340 K. The corresponding CIFs and checkCIFs as well as selected variable-temperature structural parameters are provided as electronic data files (Folder 'Ch3-TRUMOF-1'), and the crystallographic details are presented in Table A1.4 (Appendix). All structures have been deposited with the Cambridge crystallographic data centre (CCDC) and have reference numbers 2203467–2203473.

Powder X-ray diffraction

To verify the phase purity of the TRUMOF-1 sample, a Pawley refinement was performed on PXRD data collected on the in-house diffractometer (Fig. 3.3b). This resulted in an excellent fit-to-data ($R_{wp} = 5.6\%$), using a refinement model containing a single phase with $F\bar{4}3m$ space-group symmetry. The refined lattice parameter obtained was $a = 15.5094(3)$ Å.

The Rietveld refinement of TRUMOF-1 was not included in the analysis since the absence of solvent molecules in the pores of the crystallographic model complicates the fitting of peaks at lower angles.

3.2.3 Structural features and topology

To understand the average structure of TRUMOF-1, it helps to use the OZn_4 tetrahedra as a starting point (Fig. 3.4a). The central O atom is coordinated by four Zn centres, arranged in a tetrahedra (Fig. 3.4b). Each Zn binds six additional O atoms — each with 50% occupancy — such that on average the coordination environment is ZnO_4. The partially-occupied O sites correspond to the carboxylates of 1,3-bdc linkers (Fig. 3.4c). A total of 12 linkers are arranged around each OZn_4; each carboxylate linker is occupied with 50% probability.

Assuming full occupancies of all atoms, the topology of TRUMOF-1 was found to be **ttt**. However it is important to note that this net characterises the average structure of TRUMOF-1 and not the topology of its real structure, which will be disordered as indicated by the observed partial occupancies.

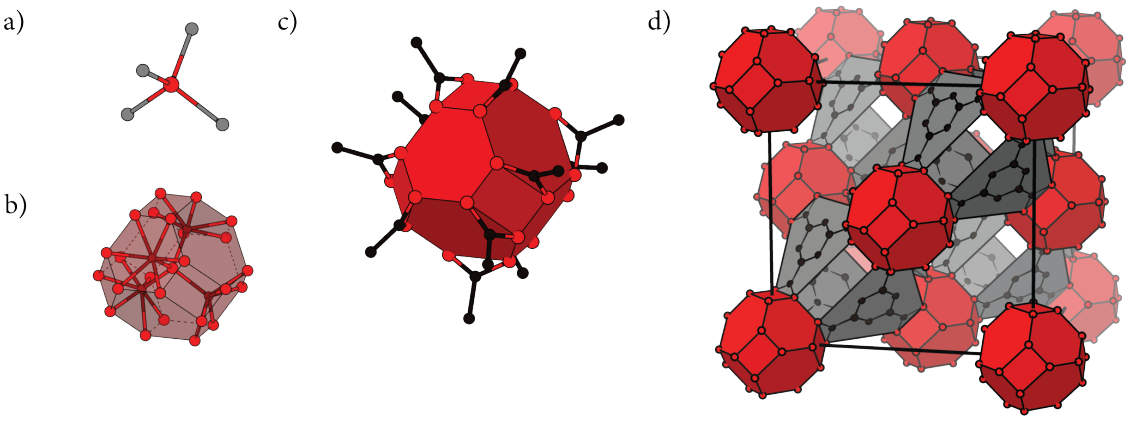

Figure 3.4: Structural features and topology of TRUMOF-1: (a) The OZn_4 tetrahedra including the linker (b) carboxylate oxygen atoms (*i.e.* the SBU) and (c) carbon atoms. (d) Single unit cell of TRUMOF-1 showing the SBUs as red, opaque units connected by the 3-fold orientationally disordered linkers. Colour scheme is as follows: C = black, spheres, O = red spheres, Zn = grey spheres and red polyhedra. H atoms are omitted for clarity.

3.3 MOX-2

3.3.1 Synthesis

MOX-2 was synthesised by combining solutions of $Zn(NO_3)_2 \cdot 6\ H_2O$ (0.33 mmol) and 1,3-bdc (0.33 mmol) in EA (5 mL). The resulting mixture was placed in a Teflon chamber and sealed, which in turn was fitted in an autoclave. The Teflon lined autoclave was placed in an oven and heated to 110 °C. After 14 h at this temperature, the system was slowly cooled to room temperature to afford MOX-2 as colourless, single-crystal rods amidst intergrown clusters (Fig. 3.5). The crystals were isolated by filtration and washed three times with EA. Each washing cycle involved soaking MOX-2 crystals in fresh EA for 24 h, followed by filtration.

3.3.2 Average Structure Determination and Refinement

Single crystal X-ray diffraction

The single crystal diffraction pattern of MOX-2 was measured using a Rigaku Synergy S diffractometer fitted with a Dectris EIGER2 R 1M detector. The instrument outputted mirror-monochromated Cu-Kα (λ = 1.5406 Å) and was equipped with an Oxford Cryosystems Cryostream 700 for temperature control.

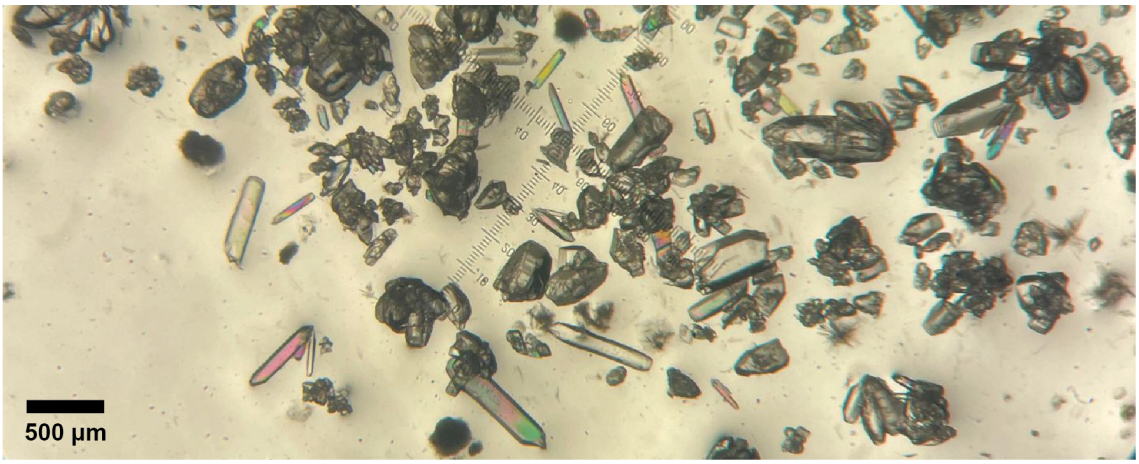

Figure 3.5: Batch of MOX-2 crystals. Scale bar given in the bottom left corner for reference (500 µm).

A washed crystal of MOX-2 was isolated directly with EA, dried in air, and then mounted onto a 0.2 mm diameter MiTeGen loop using Paratone-N oil as a cryoprotectant. The crystal was then attached to the instrument goniometer before data were collected about ϕ and ω rotations.

Unit cell determination, data integration, frame scaling, and absorption corrections (multi-scan implemented in ABSPACK) with beam profile correction) were performed in CrysAlisPro [241].

An initial solution in the non-centrosymmetric orthorhombic space group $P2_12_12_1$ with $a = 11.0562(2)$ Å, $b = 12.6155(2)$ Å, and $c = 15.2102(2)$ Å showed clearly the presence of two Zn atoms directly connected to 1,3-bdc, forming distorted ZnO_4 tetrahedra. The remaining electron density was found to originate from ordered solvent in the pores. All non-hydrogen atoms could be treated by an unrestrained anisotropic refinement unless otherwise stated. The H-atom positions were added in their calculated position and refined using riding thermal parameters.

The resulting molecular formula of MOX-2 was determined to be Zn(1,3-bdc)(EA). The asymmetric unit of this model is shown in Figure 3.6a. The corresponding CIF and checkCIF are provided as electronic data files (Folder 'Ch3-MOX-2') and the

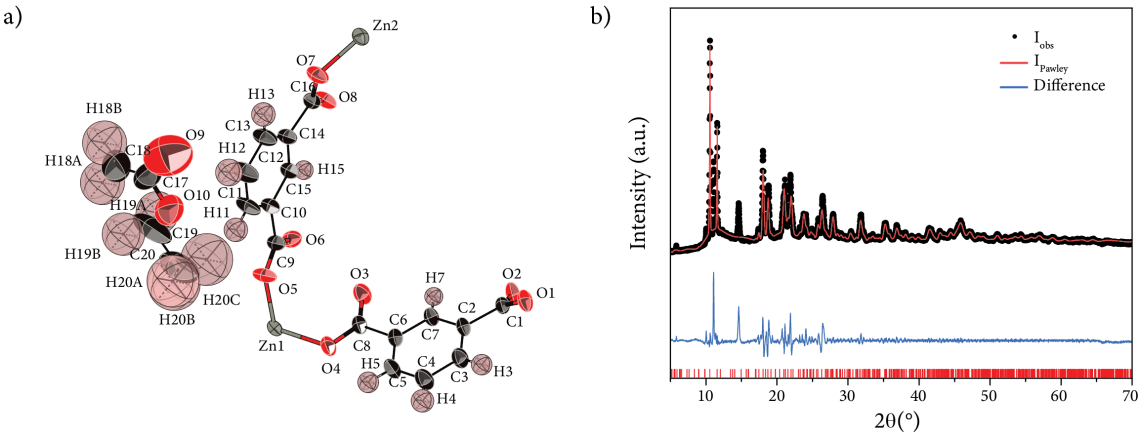

Figure 3.6: MOX-2 single crystal and powder refinement: (a) Asymmetric unit of MOX-2 at 298 K. Ellipsoids are drawn at 50% probability. Colour scheme: C atoms are shown in black, O atoms in red, Zn atoms in grey and H atoms in pink.(b) Pawley refinement of the experimental MOX-2 PXRD pattern, resulting in $a = 11.068(9)$ Å, $b = 12.835(4)$ Å and $c = 15.281(8)$ Å for $P2_12_12_1$.

crystallographic details are presented in Table A2.5 (Appendix).

Powder X-ray diffraction

To verify the phase purity of the MOX-2 sample, a Pawley refinement was performed on the PXRD data collected on the in-house diffractometer (Fig. 3.6b). This resulted in a reasonable fit ($R_{wp} = 12.9\%$) using a refinement model containing a single phase with $P2_12_12_1$ space-group symmetry; the refined lattice parameter obtained was a = 11.068(9) Å, b = 12.835(4) Å, and c = 15.281(8) Å.

This fit possibly indicates the presence of an additional phase. In fact, this second phase may arise from unreacted starting material; both the $Zn(NO_3)_2 \cdot H_2O$ salt and 1,3-bdc linker did not dissolve in the EA solvent at room temperature. Whilst heating in the oven, the solution may become saturated, in turn leaving some of the starting material undissolved, which therefore does not react. This hypothesis is reflected by the heterogeneity in crystal shapes when viewing the sample under a microscope (Fig. 3.4a): on top of the large MOX-2 crystals, there are many intergrown clusters which may belong to a different phase or starting material.

3.3.3 Structural features and topology

The structure of MOX-2 is best described as distorted ZnO_4 tetrahedra (Fig. 3.7a) connected in pairs through three carboxylates, of which each O atom belongs to a different ZnO_4 unit, with the fourth O atom belonging to a fourth 1,3-bdc linker, of which one carboxylate O remains uncoordinated (Fig. 3.7b).

The first striking structural feature of MOX-2 is its resemblance to a wine-rack when viewed down the *b*-axis (Fig. 3.7c). This motif is similar to that of MIL-53 [187], which, as was highlighted in the introduction, gives rise to the breathing effect. However, MIL-53 is a 2D MOF *i.e.* the SBUs and linkers are all located within the same plane, whereas in MOX-2, both the SBUs and linkers are staggered along the *b*-axis. Hence, MOX-2 may only be compared to 2D wine-rack MOFs such as MIL-53 with caution.

In addition to the wine-rack motif, MOX-2 contains a helical component. This

helix is found when considering the basic building block of MOX-2 *i.e.* two ZnO_4 tetrahedra connected through three pairs of 1,3-bdc linker carboxylates (Fig. 3.7b). When tracing the two linkers that face each other at an angle close to 180° down the *c*-axis, one detects the helical motif (Fig. 3.7d). Of course, such helical motifs are to be expected within the $P2_12_12_1$ space group. Yet this helical feature is noteworthy since it is composed from covalently bound ZnO_4 tetrahedra *via* the 1,3-bdc linkers. Accordingly, the combination of this helical and wine-rack motif may result in interesting dynamic behaviour similar to that observed for $Zn[Au(CN)_2]_2$, in which the helical aurophilic chains amplifies the NLC effect arising from the

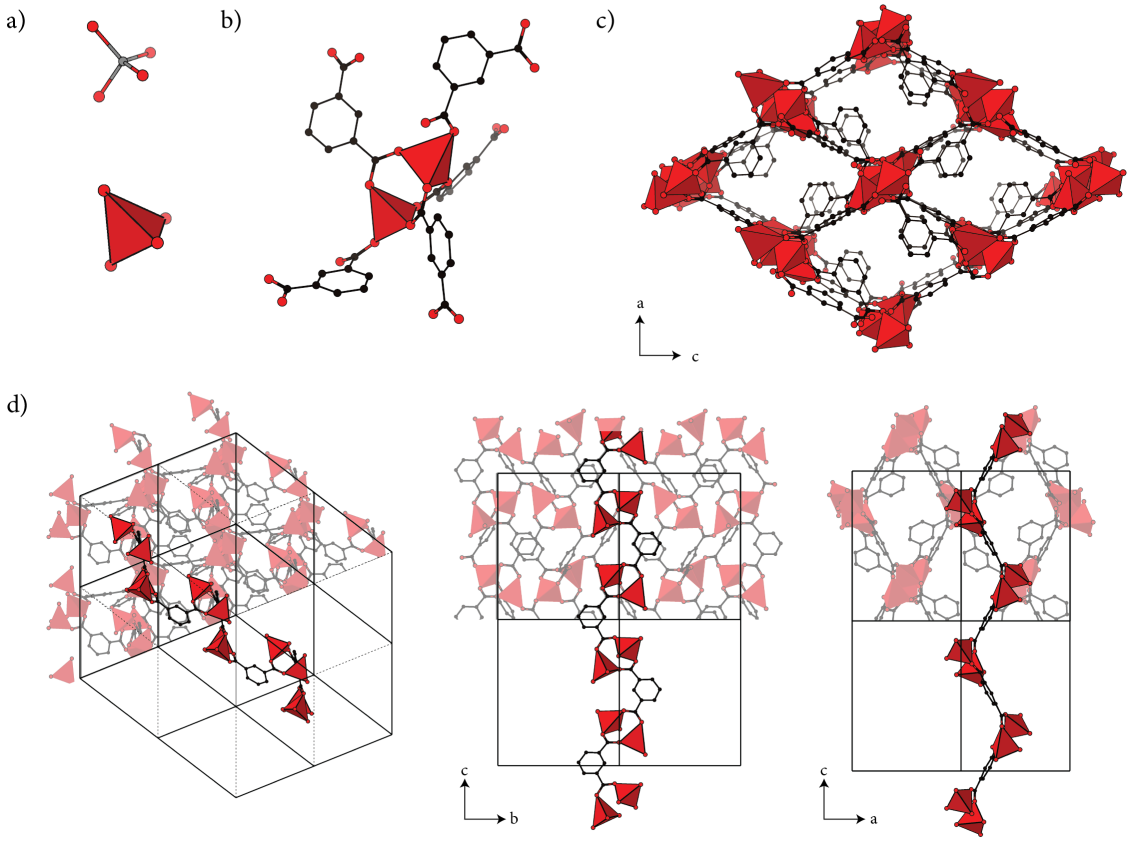

Figure 3.7: Structural features and topology of MOX-2: (a) The distorted ZnO_4 SBU (b) extended with five linkers to show the basic building block and (c) its arrangement into a single network along the *b*-axis to emphasise the wine-rack morphology. Solvent molecules are removed for clarity. (d) The helix motif along the *c*-axis highlighted (from left to right) along the [111]-direction, *a*-, and *b*-axis. Colour scheme is as follows: C = black spheres, O = red spheres, Zn = grey spheres and red polyhedra. H atoms are omitted for clarity.

honeycomb structure [162].

The topology of MOX-2 was determined to be **3,5T25**. This topology further emphasises the 3D nature of the wine-rack motif. The **3,5T25** net is observed in 14 other structures — 8 of which are MOFs — of which none correspond to the structure of MOX-2 [313]. Thus, to the best of my knowledge, there is no record of MOX-2 in the literature.

3.4 MOX-3

3.4.1 Synthesis

MOX-3 was synthesised by combining solutions of $Zn(NO_3)_2 \cdot 6\ H_2O$ (0.33 mmol) and 5-X-1,3-bdc (0.33 mmol) in EA (5 mL) for X = Br, Cl, I, F, NO_2, CH_3, OH, Br/Cl (1:1) and Br/H (1:1). The resulting mixture was placed in a Teflon chamber and sealed, which in turn was fitted in an autoclave. The Teflon lined autoclave was placed in an oven and heated to 110 °C. After 14 h at this temperature, the system was cooled to room temperature to afford MOX-3 as colourless crystals, most of which intergrown clusters, though some single crystals (Fig. 3.8a). The crystals were isolated by filtration and washed three times with EA. Each washing cycle involved soaking MOX-3 crystals in fresh EA for 24 h, followed by filtration.

Single crystals were obtained for X = Br, Cl, I, and Br/Cl, powders were obtained for X = F, NO_2, CH_3 and Br/H. For X = OH, no product was obtained.

3.4.2 Average Structure Determination and Refinement

Single crystal X-ray diffraction

All MOX-3 single crystal diffraction patterns were measured using a Rigaku Synergy S diffractometer fitted with a Dectris EIGER2 R 1M detector. The instrument produced mirror-monochromated Cu-Kα (λ = 1.5406 Å) and was equipped with an Oxford Cryosystems Cryostream 700 for temperature control.

A washed crystal of MOX-3 was isolated directly with EA, dried in air, and

a) b)

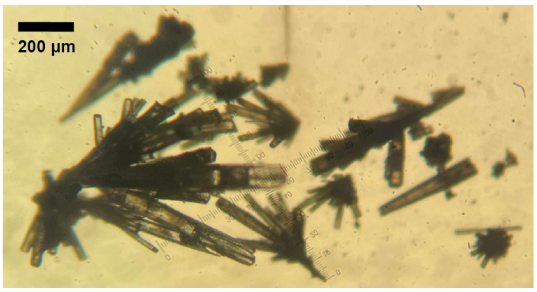

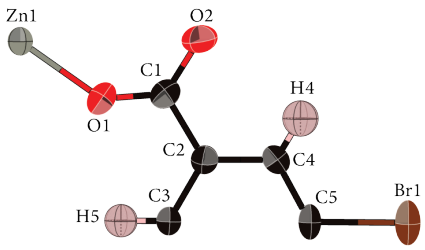

Figure 3.8: MOX-3 single crystal refinement: (a) Batch of MOX-3 crystals with X = Br. Scale bar given in the top left corner for reference (200 µm). (b) Asymmetric unit of MOX-3 at 298 K. Ellipsoids are drawn at 50% probability. Colour scheme is as follows: C = black spheres, O = red spheres, Zn = grey spheres and H = pink spheres.

then mounted onto a 0.2 mm diameter MiTeGen loop using Paratone-N oil as a cryoprotectant. The crystal was then attached to the instrument goniometer before data were collected about ϕ and ω rotations, using an exposure time of 0.1 s.

Unit cell determination, data integration, frame scaling, and absorption corrections (multi-scan implemented in ABSPACK) were performed in CrysAlisPro [241].

An initial solution in the non-centrosymmetric rhombohedral space group $R\bar{3}m$ (lattice parameters given in Table 3.1) showed clearly the presence of distorted ZnO_4 tetrahedra centred on the 18f Wyckoff position, connected by 5-X-1,3-bdc linkers. The remaining electron density was determined to originate from disordered EA solvent molecules in the pores. Their exact positions and orientation was not able to be solved. Since the remaining electron density was quite low, no solvent masking was used to account for this.

Table 3.1: MOX-3 unit cell parameters for MOX-3 single crystals with X = Br, Cl, I, and Br/Cl.

Lattice parameter	Br	Cl	I	Br/Cl
a (Å)	28.4852(3)	28.4445(5)	28.5799(4)	28.4902(4)
c (Å)	7.9052(1)	7.82240(10)	8.09130(10)	7.90730(10)

All non-hydrogen atoms could be treated by an unrestrained anisotropic refinement unless otherwise stated. The H-atom positions were added in their calculated position and refined using riding thermal parameters.

The resulting molecular formula of MOX-3 was determined to be Zn(5-X-1,3-bdc). For the MOX-3 sample with X = Cl/Br, Cl1 and Br1 had their atomic coordinates and thermal parameters fixed using the EXYZ and EADP constraints. Their occupation was set to refine freely starting from 50%, resulting in a final distribution of $Br_{0.3}Cl_{0.7}$. The asymmetric unit of this model is shown in Figure 3.8b. The corresponding CIFs and checkCIFs are provided as electronic data files (Folder 'Ch3-MOX-3') and the crystallographic details are presented in Tables A3.6–A3.9 (Appendix).

3.4.3 Diffuse scattering

Upon close inspection of the total scattering data, diffuse scattering was observed for MOX-3 with X = Br. To explore this observation, additional SCXRD data was collected for all single-crystal samples on the in-house diffractometer about ϕ rotations, using an exposure time of 30 s per frame. This resulted in diffuse scattering of significant intensity between the Bragg peaks. These diffuse features were particularly intense for the MOX-3 samples with X = Br and Cl/Br, yet very low in intensity for the samples with X = I. Thus, there is an apparent correlation between the size of the X functional group and the intensity of the diffuse scattering.

As mentioned in the previous chapter, diffuse scattering may arise from either

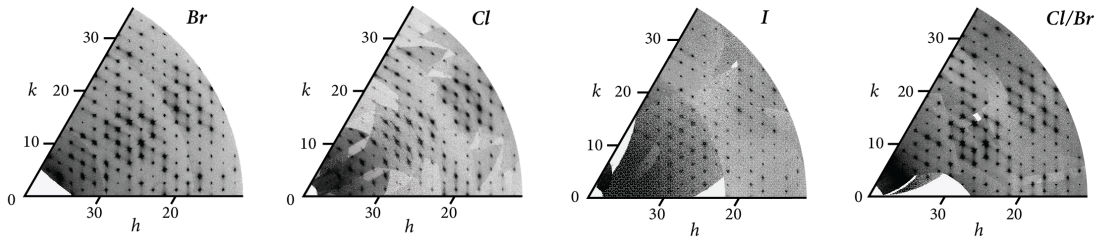

Figure 3.9: Diffuse scattering observed in the *hk*0 layer for MOX-3 samples with (from left to right) X = Br, Cl, I and Cl/Br.

static disorder or dynamic contributions. Since there was no indication of disorder in the average structure refinement, the latter seems more probable. Further analysis is needed to confirm this hypothesis, which will be discussed later in this thesis.

3.4.4 Structural features and topology

The structure of MOX-3 can be best described as distorted ZnO_4 tetrahedra (Fig. 3.10a), where each O atom belongs to a different 5-X-1,3-bdc linker (Fig. 3.10b). The ZnO_4 clusters spiral down the *c*-axis in a 3-fold rotational symmetry, forming hexagonal channels of 11.1 Å in diameter perpendicular to the *c*-axis (Fig. 3.10c). These hexagonal channels are particularly striking as their shape and size is comparable to that of the channels found in MIL-88B (*viz.* ∼11.0 Å) [104] and MOF-74 (*viz.* ∼15.2 Å) [94]. It is these hexagonal pores that make MIL-88B and MOF-74 well-suited for applications such as gas sorption and catalysis [314, 315]. Similar to MOF-74, the presence of a functional group attached to the linker benzene ring forces the framework to be rigid, rather than flexible like MIL-88B.

In fact, the interactions between these functional groups appear to be antipolar,

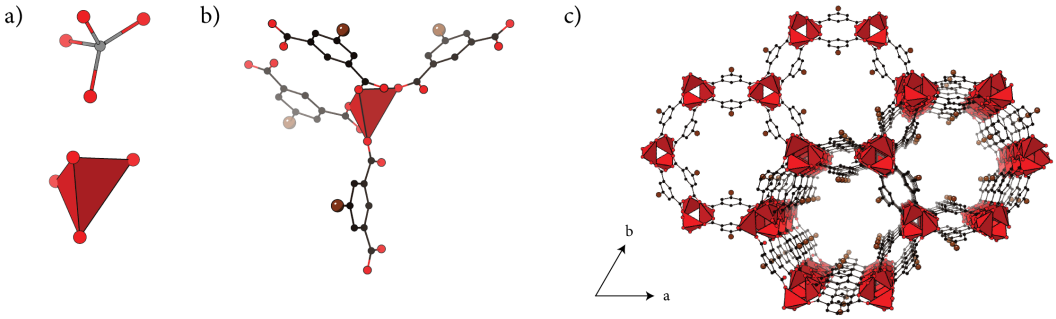

Figure 3.10: Structural features and topology of MOX-3: (a) The distorted ZnO_4 SBU (b) extended with four linkers to show the basic building block and (c) its arrangement into a single network, shown along the c-axis to show the hexagonal channels. Two channels are presented to lie in the plane of this thesis whilst the other two channels are shown with perspective. This is to show the configuration of the linkers along the columns. Colour scheme is as follows: C = black spheres, O = red spheres, Zn = grey spheres, functional group 'X' = brown spheres and H atoms are omitted for clarity.

being that for each pore lined by 6 linkers, 3 are pointing up along the channel, and 3 are pointing down. For each linker that points up, its two neighbours point down. These configurations are consistent along the same columns *i.e.* all linkers stacked along the *c*-axis point up/down along the channel. Since the distance between neighbouring linkers within the same layer is $\sim$ 6.8 Å, it is likely these antipolar interactions are governed by steric hindrance.

Additionally, each linker interacts with another from a neighbouring channel in a stacked configuration. Again, these interactions are antipolar: if one linker in the pair points down, the other will point up. With a distance of 3.5 Å, the stacked linkers are even closer together than the 6 linkers lining the channel. Therefore, steric hindrance appears to steer the observed arrangement. Since the lattice of MOX-3 can accommodate for these interactions *i.e.* is not frustrated, its structure is ordered. Therefore, the functional groups appear to play an important role in directing the structure of MOX-3, likely governed by steric interactions.

The topology of MOX-3 was determined to be the **ptr** net. This topology is rather uncommon — only 18 entries on the Cambridge Structural Database (CSD) exhibit this net [313]. Among these are structures identical to MOX-3, albeit with X = Bu^t [316, 317], Ph [318, 319], Ph-OH [320, 321], Ph-NHC_4H_8 [322] and Ph-NH_2 [323]. These MOX-3 analogues were subjected to studies predominately focusing on the application of luminescence [318, 321] and selective gas adsorption/separation [316, 319, 320, 322].

3.5 MOX-4

3.5.1 Synthesis

MOX-4 was synthesised by combining solutions of $Zn(NO_3)_2 \cdot 6\ H_2O$ (0.33 mmol) and thiopene 2,5-dicarboxylic acid (2,5-tdc) (0.33 mmol) in EA (5 mL). The resulting mixture was placed in a Teflon chamber and sealed, which in turn was fitted in an autoclave. The Teflon lined autoclave was placed in an oven and heated to 110 °C. After 14 h at this temperature, the system was slowly cooled to room temperature to

afford MOX-4 as large, colourless tablets amidst intergrown clusters (Fig. 3.11). The crystals were isolated by filtration and washed three times with EA. Each washing cycle involved soaking MOX-4 crystals in fresh EA for 24 h, followed by filtration.

3.5.2 Average Structure Determination and Refinement

Single crystal X-ray diffraction

The single crystal diffraction pattern of MOX-4 was measured using a Rigaku Synergy S diffractometer fitted with a Dectris EIGER2 R 1M detector. The instrument produced mirror-monochromated Cu-Kα ($\lambda = 1.5406$ Å) and was equipped with an Oxford Cryosystems Cryostream 700 for temperature control.

A washed crystal of MOX-4 was isolated directly with EA, dried in air, and then mounted onto a 0.2 mm diameter MiTeGen loop using Paratone-N oil as a cryoprotectant. The crystal was then attached to the instrument goniometer before data were collected about ϕ and ω rotations.

Unit cell determination, data integration, frame scaling, and absorption corrections (multi-scan implemented in ABSPACK) were performed in CrysAlisPro [241].

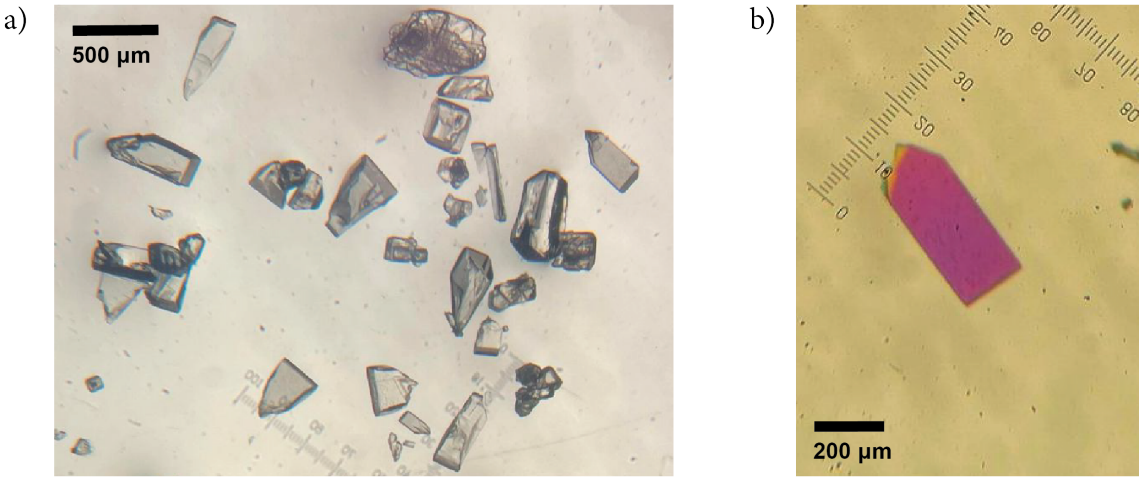

Figure 3.11: Batch of (a) and single (b) MOX-4 crystal(s), which appeared pink at certain angles as a result of light polarisation. Scale bars given in the top (500 µm) and bottom (200 µm) left corner for reference in (a) and (b), respectively.

An initial solution in the non-centrosymmetric orthorhombic space group $P2_12_12_1$ with $a = 10.0887(1)$ Å, $b = 13.1854(2)$ Å, and $c = 15.0775(2)$ Å showed clearly the presence of Zn atoms directly connected to 2,5-tdc linkers, forming distorted ZnO_4 tetrahedra. The remaining electron density was found to originate from ordered solvent in the pores. All non-hydrogen atoms could be treated by an unrestrained anisotropic refinement unless otherwise stated. The H-atom positions were added in their calculated position and refined using riding thermal parameters.

The resulting molecular formula of MOX-4 was determined to be Zn(2,5-tdc)(EA). The asymmetric unit of this model is shown in Figure 3.12a. The corresponding CIF and checkCIF are provided as electronic data files (Folder 'Ch3-MOX-4') and the crystallographic details are presented in Table A4.10 (Appendix).

Powder X-ray diffraction

To verify the phase purity of the MOX-4 sample, a Pawley refinement was performed on PXRD data collected on the in-house diffractometer (Fig. 3.12b). This resulted in a reasonable fit ($R_{wp} = 17.1\%$) using a refinement model containing a single phase

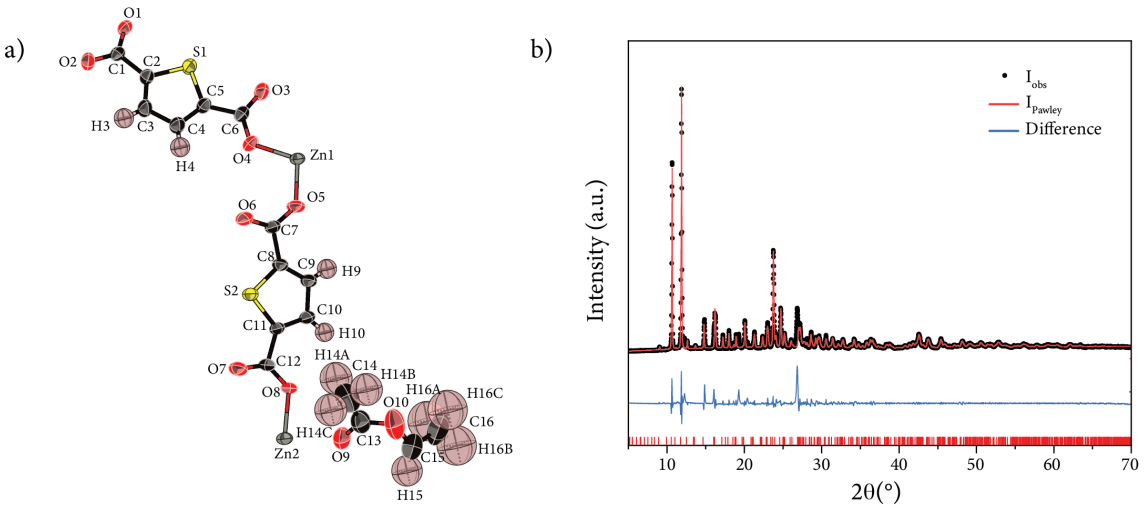

Figure 3.12: MOX-4 single crystal and powder refinement: (a) Asymmetric unit of MOX-4 at 298 K. Ellipsoids are drawn at 50% probability. Colour scheme is as follows: C = black spheres, O = red spheres, Zn = grey spheres, S = yellow spheres and H = pink spheres. (b) Pawley refinement of the PXRD pattern measured for MOX-4, giving lattice parameters $a = 10.105(2)$ Å, $b = 13.187(1)$ Å and $c = 15.059(1)$ Å for $P2_12_12_1$.

with $P2_12_12_1$ space-group symmetry; the refined lattice parameter obtained was a = 10.105(2) Å, b = 13.187(1) Å, and c = 15.059(1) Å.

The bulk sample does not entirely correspond to the single crystal phase. As was the case for MOX-2, this most likely arises from unreacted starting material; both the $Zn(NO_3)_2 \cdot 6\ H_2O$ salt and 2,5-tdc linker did not dissolve in EA at room temperature. Whilst heating in the oven, a small residue may remain undissolved and hence does not react. This is reflected by the heterogeneity in crystal shape when viewing the sample under the microscope (Fig. 3.11). Comparison of the reflections not accounted for by the Pawley fit of MOX-2 and MOX-4 neither confirms nor rejects this hypothesis: there is some agreement in reflections which may arise from the metal starting material (Fig. A4.4)

3.5.3 Structural features and topology

There are many similarities between the structures of MOX-4 and MOX-2. This similarity may arise due to the identical synthetic parameters, the type of incorporated linker being the only difference. Accordingly, MOX-4 has a 3D wine-rack morphology when viewed down the *b*-axis (Fig. 3.13c). However in contrast to MOX-2, the linkers do not only run along the diagonal, but also vertically *i.e.* along the *a*-axis. Yet similarly to MOX-2, there is a helical motif that runs along the *c*-axis, consisting out of SBU pairs that are covalently bound to the same linker (Fig. 3.13d). This helix has more curvature than the one observed in MOX-2, perhaps due to the larger angle between the carboxylates of the 2,5-tdc linker.

Again, the question arises whether this combination of helical and wine-rack motifs may result in interesting dynamic behaviour. Seeing the subtle difference between the structures of MOX-4 and MOX-2 as a function of angle between linker carboxylates, it will be particularly interesting to probe this behaviour by means of variable temperature and high-pressure crystallography.

The topology of MOX-4 was determined to be **tcj-3,5-Pnma**, which has the maximal symmetry of *Pnma*. This topology has been reported before in a structure identical to MOX-4 [313], albeit with ordered isopropanol coordinated in the pores

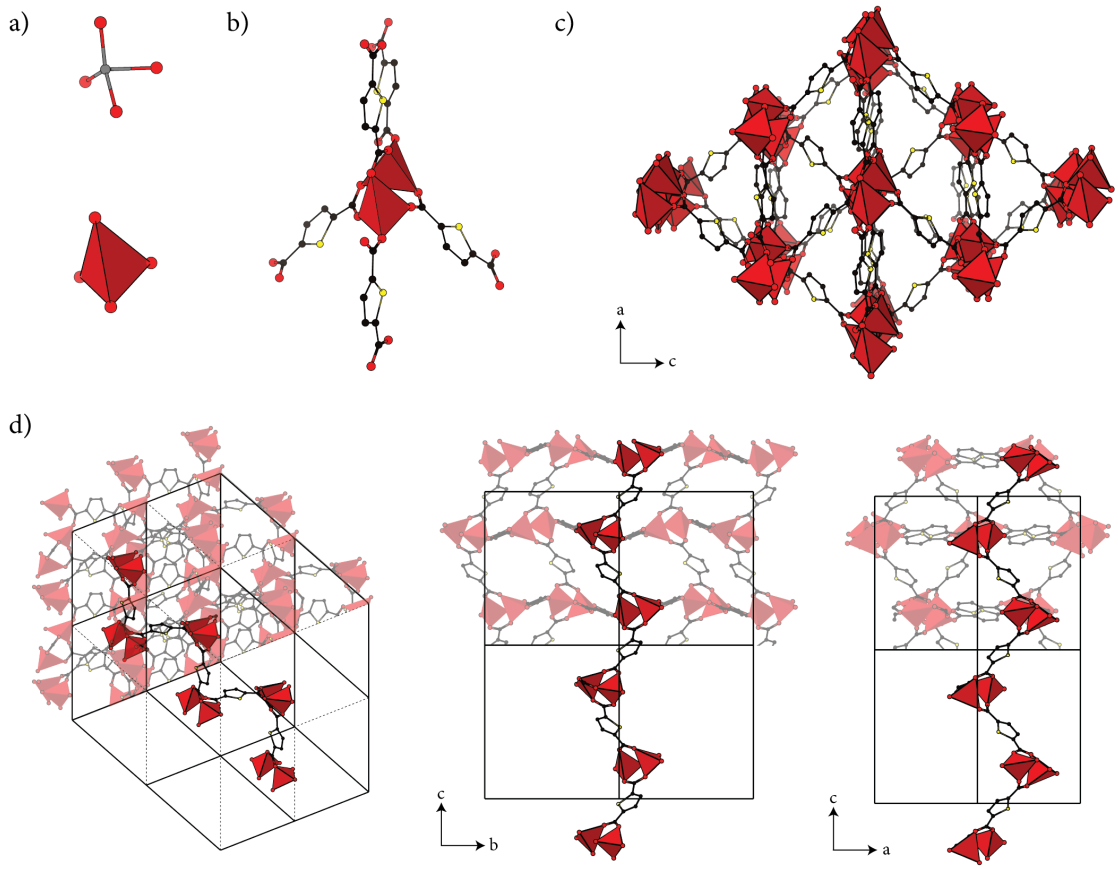

Figure 3.13: Structural features and topology of MOX-4: (a) The distorted ZnO_4 SBU (b) extended with five linkers to show the basic building block and (c) its arrangement into a single network, shown along the b-axis to emphasis the wine-rack morphology. Colour scheme is as follows: C = black spheres, O = red spheres, Zn = grey spheres. The H atoms and solvent molecules are omitted for clarity. (d) The helix motif along the c-axis highlighted (from left to right) along the 111-direction, a-axis, and b-axis.

of the framework, rather than EA [324]. Other than the structure, this previous publication does not report on the chemical or physical properties of the framework.

3.6 MOX-5

3.6.1 Synthesis

MOX-5 was synthesised by dissolving 0.33 mmol (97.7 mg) $Zn(NO_3)_2 \cdot 6\ H_2O$ and 0.33 mmol (106.9 mg) 4,6-dibromo isophthalic acid (4,6-Br_2-1,3-bdc) in DMF (5 mL). The resulting solution was then heated to 110 °C in a sealed vial for 14 h

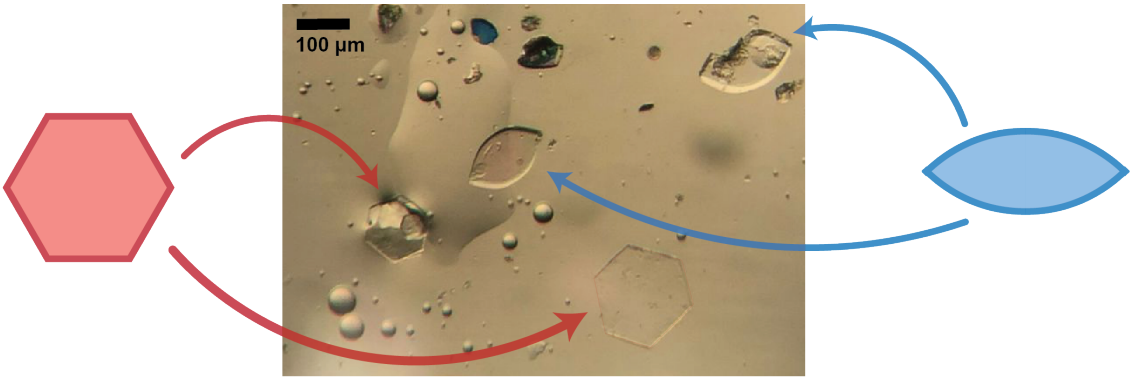

Figure 3.14: Batch of MOX-5 crystals, indicating both oval- and hexagonal-shaped crystals with blue and red arrows, respectively. Scale bar given in the top left corner for reference (100 µm)

resulting in clear, colourless, hexagonal shaped disks (Fig. 3.14). These crystals are referred to as MOX-5α.

By placing the disks in paratone-n oil and leaving them for *ca.* 2 h, the hexagonal disks turned into oval-shaped crystals (Fig. 3.14). These crystals belong to the phase of MOX-5. They were kept in oil and therefore not washed nor treated with other solvents for analysis.

3.6.2 Average Structure Determination and Refinement

Single Crystal X-ray diffraction

As mentioned in the synthetic procedure, two types of crystals were obtained: the hexagonal- (MOX-5α) and oval-shaped disks (MOX-5). The SCXRD patterns of both crystals were measured using a Rigaku Synergy S diffractometer fitted with a Dectris EIGER2 R 1M detector. The instrument outputted mirror-monochromated Cu-Kα ($\lambda = 1.5406$ $\AA$) and was equipped with an Oxford Cryosystems Cryostream 700 for temperature control. Crystals of both MOX-5α and MOX-5 were isolated directly with DMF and mounted onto a 0.2 mm diameter MiTeGen loop using Paratone-N oil as a cryoprotectant. The crystals were then attached to the instrument goniometer before data were collected about ϕ and ω rotations. Unit cell determination, data integration, frame scaling, and absorption corrections (multi-scan implemented in ABSPACK) were performed in CrysAlisPro [241].

MOX-5

An initial solution in the centrosymmetric monoclinic space group $P2_1/n$ (no. 14) with a = 12.7970(2) Å, b = 9.5085(1) Å, c = 16.9103(2) Å, and β = 111.969(2)° showed clearly the presence of a Zn atom on the 4e Wyckoff position directly connected to a 4,6-Br_2-1,3-bdc linker, forming distorted ZnO_4 tetrahedra. The remaining electron density was found to originate from ordered DMF solvent, of which the O atom is coordinated to the Zn atom. All non-H atoms could be treated by an unrestrained anisotropic refinement unless otherwise stated. The H-atom positions were added in their calculated position and refined using riding thermal parameters.

The resulting molecular formula of MOX-5 was determined to be Zn(4,6-Br-1,3-bdc)(DMF). The asymmetric unit of this model is shown in Figure 3.15. The corresponding CIF and checkCIF are provided as electronic data files (Folder 'Ch3-MOX-5') and the crystallographic details are presented in Table A5.11 (Appendix).

MOX-5α

The MOX-5α crystals diffracted very poorly; rather than Bragg reflections, diffuse "streaks" were observed in reciprocal space (Fig. 3.16). Hence it was not possible to automatically assign a lattice to the system using the CrysAlisPro software.

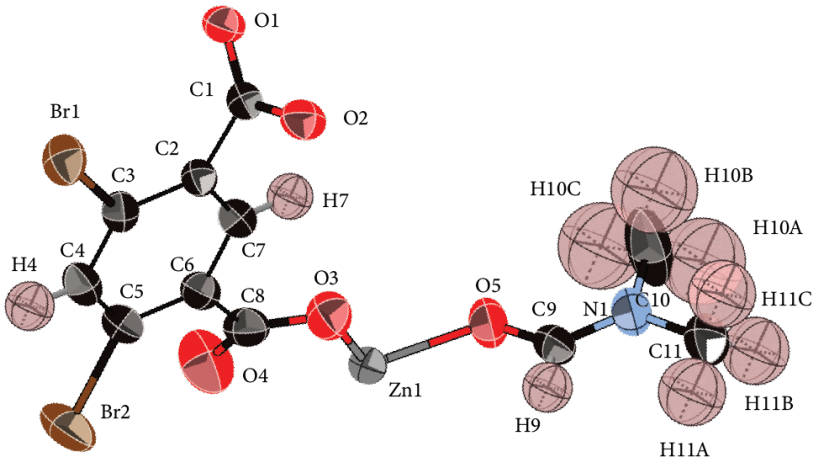

Figure 3.15: Asymmetric unit of MOX-5 at 298 K. Ellipsoids are drawn at 50% probability. Colour scheme is as follows: C = black spheres, O = red spheres, N = blue spheres, Zn = grey spheres, Br = brown spheres and H = pink spheres.

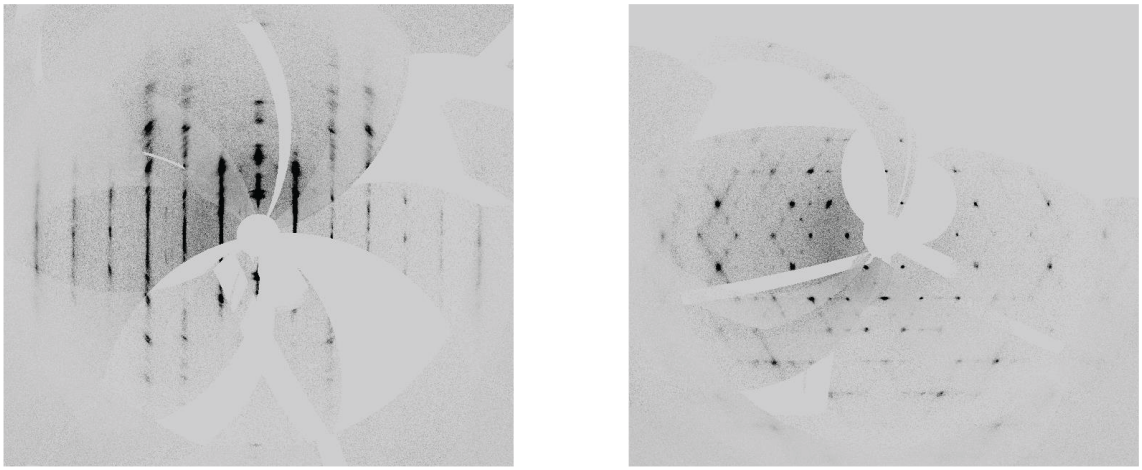

Figure 3.16: Reconstructed "0*kl*" (left) and "*hk*0" (right) layers of MOX-5α.

Instead, a lattice was manually selected in reciprocal space by indexing the peaks that appeared to reside on a hexagonal lattice. This plane was assigned the $hk0$ plane, subsequently implying that the diffuse streaks run along l.

There are several ways to interpret these features. A possible cause is mosaicity, which refers to a spread of crystal plane orientations resulting from a variety of imperfections in the packing of contents [325, 326]. This typically results in diffracted rays being emitted as cones rather than perfectly linear beams. Thus, mosaicity can have the effect of broadening, (radial) smearing, and overlap of Bragg reflections, which is observed in the data (Fig. 3.16): each spot in the "0kl" plane seems to be smeared out in a circular manner, agreeing with the characteristics of mosaic spread. Otherwise, MOX-5α may be a plastic crystal, thus exhibiting a heterogeneity in packing contents as caused by orientational degrees of freedom [49]. A final hypothesis is that MOX-5α exhibits stacking faults [327]. These features introduce disorder along the stacking axis of close-packed layers, as characterised by continuous diffuse scattering superimposed on the Bragg reflections.

3.6.3 Structural features and topology

The structure of MOX-5 consists out of distorted ZnO_4 tetrahedra (Fig. 3.17a), of which the O atoms belong to three linkers and one DMF solvent molecule (Fig. 3.17b). These units assemble to form a network with two striking features. First,

there are channels running along the a-axis that strike a resemblance to the hexagonal channels observed in MOF-74, MIL-88B, and MOX-3, for example [94, 104]. Secondly, when viewed down the b-axis, it can be seen that MOX-5 consists out of layers which are coordinated through non-covalent halogen-halogen bond interactions between the Br groups (Fig. 3.17d). These features are particularly striking because they may explain our observations for MOX-5α, the metastable phase of MOX-5. We anticipate that the structure of MOX-5α consists of similar layers that are not yet arranged in the ordered, lowest energy configuration. Instead, the layers slip over one another, resulting in stacking faults.

The topology of MOX-5 was determined to be the **sql** net. This 2D net is not

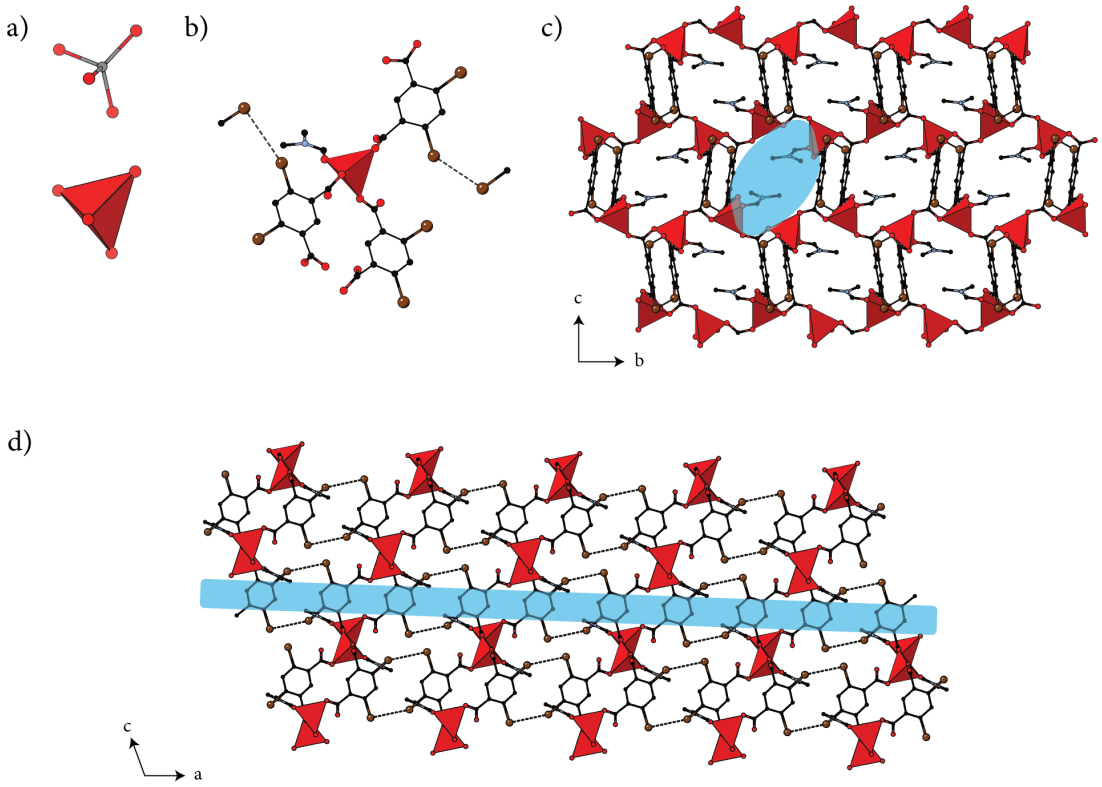

Figure 3.17: Structural features and topology of MOX-5. (a) The distorted ZnO_4 SBU (b) extended with three linkers and one DMF molecule to show the basic building block and (c) its arrangement into a single network, shown along the a-axis to show the pseudo-hexagonal channels and (d) along the b-axis, showing the layers held in place through interactions between the bromine functional groups. Colour scheme is as follows: C = black spheres, O = red spheres, N = blue spheres, Zn = grey spheres and red polyhedra, Br = brown spheres and H atoms are omitted for clarity.

uncommon for MOF structures. Quite the opposite — the **sql** lattice accounts for 45% of over 10,000 reported 2D polymer structures [328]. Generally, there are three approaches of achieving the **sql** net topology. The one that applies here is the combination of tetrahedral metal centers with bent linkers. This method is considered non-trivial and therefore least often used to do so [329]. There is no account of MOX-5 in the literature, nor **sql** topology structures with 4,6-substituted 1,3-bdc.

3.7 Conclusion and Outlook

This chapter outlined the successful attempts at synthesising a series of new Zn-1,3-MOFs: namely, TRUMOF-1, MOX-2, MOX-3, MOX-4 and MOX-5 (Fig. 3.18). Notably, these reactions were performed using the solvents DMF and EA. Whilst DMF is often used in MOF synthesis due to its high polarity – facilitating the solubility of reagents – and high boiling point, the role of EA is less clear in obtaining a crystalline phase as it is less polar and rather volatile [330]. Yet, the EA solvent molecule is positioned within the unit cell of both MOX-2 and MOX-4, indicating

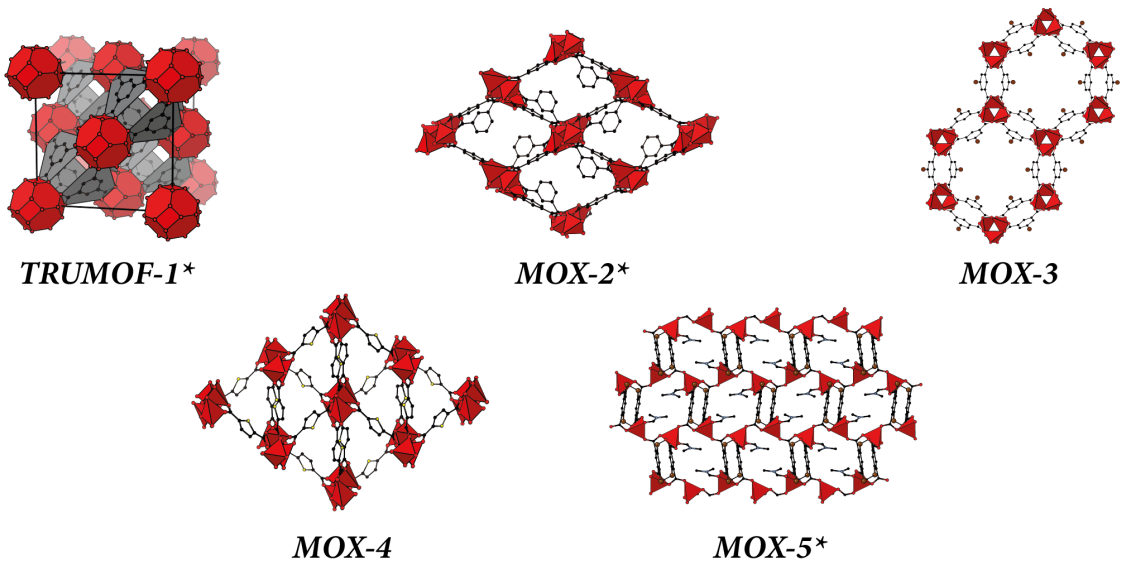

Figure 3.18: Summary of the Zn-1,3-bdc MOF structures obtained in this thesis (from left to right, top to bottom): TRUMOF-1, MOX-2, MOX-3, MOX-4, and MOX-5. The structures that have never been reported are highlighted with an asterisk. Colour scheme is as follows: Zn = red tetrahedra, O = red spheres, C = black spheres, N = blue spheres, S = yellow spheres, Br = brown spheres. H atoms are omitted for clarity.

it interacts with the framework and therefore may have a structure directing role.

For each phase, we were able to determine their crystal structure and assign a network topology.

The case of TRUMOF-1 is intriguing and we will come to show particularly complex. Despite the sharp Bragg peaks observed in the total scattering data — indicating TRUMOF-1 to be crystalline — some atoms had to be refined with partial occupancies. This requirement indicates that TRUMOF-1 is disordered. Since this disorder is related to the orientation as well as the presence of the 1,3-bdc linkers, it affects the connectivity of the framework. In turn, the disorder may be correlated if the configuration of each linker affects that of the neighbouring linkers *i.e.* those attached to the same SBU. Chapter 7 describes the work performed to solve the local structure of TRUMOF-1 as well as measure and understand some of its physical properties.

Despite having different topologies, the structures of MOX-2 and MOX-4 both exhibit wine-rack and helical motifs. As both structural features are known to give rise to NTE and NLC phenomena in framework materials, it will be interesting to probe the dynamic behaviour of both MOFs by means of variable temperature and high-pressure crystallography. Chapter 3 describes precisely these experiments. The structural differences between MOX-2 and MOX-4 arise due to the difference in angle between the linker dicarboxylates. Hence, any differences in mechanical behaviour may be related to this feature.

The structure of MOX-3 is characterised by large hexagonal channels, which are maintained by repulsive interactions between the linker functional groups. Notably, there are two linker configurations in the structure; one where they point up along the *c*-axis, and the other where they point down. The interactions between the linkers is antipolar, being that for each 'up' linker, its neighbours will be 'down'. These interactions are satisfied on the lattice, and hence the structure of MOX-3 is ordered. Despite this, its diffraction patterns contain significant diffuse scattering, of which the intensity changes as a function of the size of the functional group. The origin of this diffuse scattering will be further explored in Chapter 4.

Finally, the phase of MOX-5 forms from crystals of its metastable phase, MOX-5α, after being submerged in oil. We expect that this ageing process allows the disordered layers to rearrange themselves as governed by non-covalent halogen ($Br^{\delta-} \ldots Br^{\delta-}$) interactions to form an ordered structure. This ordering is accompanied with a change in crystal shape; the pseudo-hexagonal disks of the MOX-5α phase slowly change into oval-shaped disks, which correspond to the crystalline MOX-5. Detailed structural investigation of this transformation process (using *e.g.* DFT to simulate stacking faults) was beyond the scope of this thesis, but our qualitative observations will be relevant to the general discussion of Zn/1,3-bdc MOFs presented in Chapter 8.

Chapter 4

Flexibility of MOX-2 and MOX-4

4.1 Summary and acknowledgements

Both MOX-2 and MOX-4 exhibit a wine-rack-like structure, in which a helical motif runs along the *c*-axis. Similar features have been known to give rise to NTE and NLC in framework materials. However, both MOFs have additional linkers arranged to those making up the wine-rack, resulting in a propeller and reinforced configuration for MOX-2 and MOX-4, respectively. These structural differences arise from the different angle between the linker carboxylates. Hence, any differences in mechanical behaviour may be attributed to this property, which was probed by means of variable-temperature and high-pressure X-ray crystallography. Our results, reported in this chapter, show that both frameworks exhibit NTE, and MOX-4 also shows NLC. The compliance of the underlying framework increases with decreasing angle between the carboxylates.

I am grateful to Claire Hobday, Joshua Levinsky, and Phillippa Partridge for assistance with data collection on beamtime at I19, and Simon Cassidy for measuring my samples at I11. I am also grateful to the I19 beamline scientists Rebecca Scatena and Mark Warren for kindly and patiently guiding me through both the data collection and processing.

4.2 Background

As highlighted in the previous chapter, the structures of MOX-2 and MOX-4 exhibit both a wine-rack and helical motif. Wine-rack frameworks such as MIL-53 [178] are known to exhibit both NTE and NLC, as permitted by the flexibility arising from the 2D SBU 'hinges' and the rigid linker 'struts'. And in the case of $Zn[Au(CN)_2]_2$, the presence of helical aurophilic ($Au^+ \ldots Au^+$) chains amplifies the perpendicular uniaxial expansion of its honeycomb structure [162].

However, as was also stated in the previous chapter, there are a couple of important things to note about the wine-rack motif in MOX-2 and MOX-4 (Fig. 4.1). First, the SBU 'hinges' are 3D, rather than 2D *i.e* the configuration of the MIL-53 wine-rack [187]. Second, both structures have an extra linker arrangement on top of the one that functions as the 'strut' of the wine-rack. In the case of MOX-2, the extra 1,3-bdc linker lies in the plane of the wine-rack, keeping two SBUs apart along the diagonal. Since each SBU has four such bent linkers surrounding it when collapsed in 2D, I refer to this arrangement as a 'propeller wine-rack'. In MOX-4, by contrast, the extra linker is positioned between stacked SBU 'hinges' along the *c*-axis *i.e.* the vertical direction of the wine-rack. So I refer to this arrangement as a 'reinforced wine-rack' due to the added stability of the vertical struts affecting the ability of the hinges to open. This reinforced wine-rack also characterises the structure of MIL-140 (albeit in 2D), which compresses uniformly in all directions when heated or subjected to hydrostatic pressure [331].

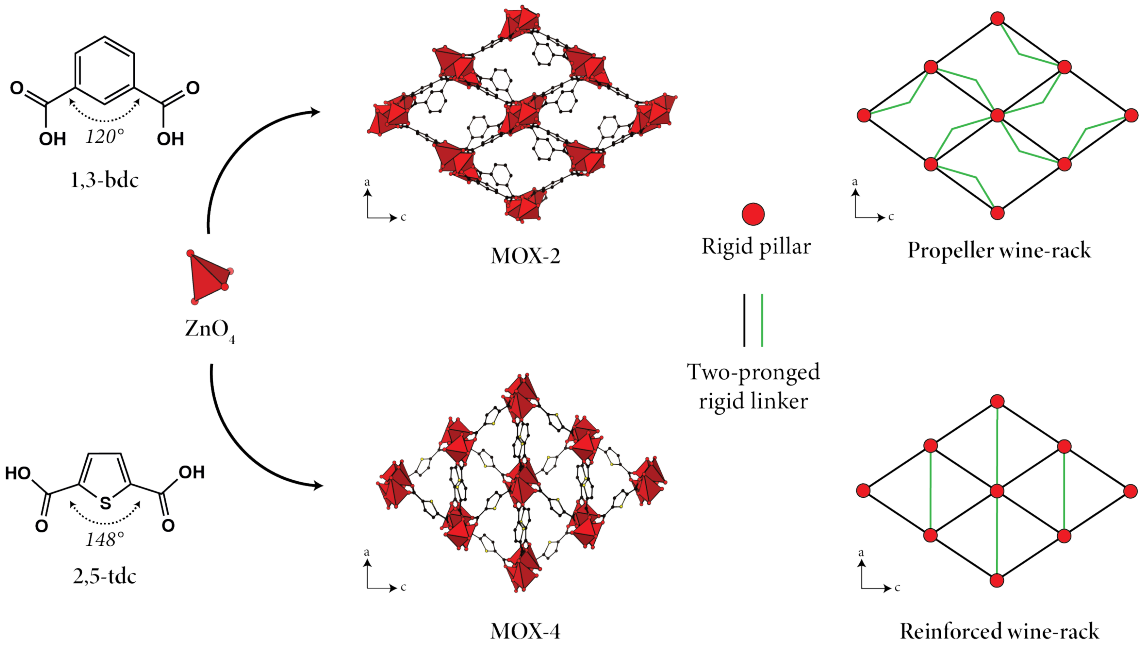

Figure 4.1: Comparison of wine-rack compositions MOX-2 and MOX-4. Both MOX-2 and MOX-4 are built from the same ZnO_4 cluster, connected by 1,3-bdc and 2,5-tdc linkers, respectively. Coarse-grained representations of the wine-rack motif viewed down the *b*-axis demonstrate how that of MOX-2 resembles a propeller wine-rack, whilst that of MOX-4 resembles a reinforced wine-rack. Colour scheme is as follows: C = black spheres, O = red spheres, Zn = red polyhedra. H atoms and solvent molecules are omitted for clarity.

These different structural features must arise from the difference in angle between the linker carboxylates, *viz.* 120° and 148° for 1,3-bdc (*i.e.* MOX-2) and 2,5-tdc (*i.e.* MOX-4), respectively. Since the angle of 1,3-bdc is smaller, the linker can position itself in the plane of the wine-rack, whilst the large angle of 2,5-tdc enables it to connect nodes stacked along the *a*-axis. In turn, the positions of these linkers may impose additional stability along a specific direction, in turn interfering with the behaviour typically observed for a wine-rack framework: to expand along the longer (*c*-) axis of the wine-rack upon cooling or exposure to pressure, whilst contracting in all other dimensions [163, 269, 332]. Additionally, the helical motif running along the *c*-axis in both MOX-2 and MOX-4 may further interfere with the wine-rack mechanical behaviour by enhancing compression or expansion along the *c*-axis by functioning as springs.

Therefore, MOX-2 and MOX-4 may exhibit interesting (*e.g.* NTE and NLC) yet different dynamic behaviour as a function of the angle between the linker carboxylates. This behaviour was probed by means of variable temperature and high-pressure X-ray crystallography, including both SCXRD and PXRD.

4.3 Variable Temperature X-ray diffraction

4.3.1 Experimental details

The variable temperature single crystal X-ray diffraction patterns of both MOX-2 and MOX-4 were measured in-house, using a Rigaku Synergy S diffractometer fitted with a Dectris EIGER2 R 1M detector. The instrument produced mirror-monochromated Cu-Kα ($\lambda = 1.5406$ $\mathring{A}$) and was equipped with an Oxford Cryosystems Cryostream 700 for temperature control. For both samples, a washed crystal was isolated directly with EA and then mounted onto a 0.2 mm diameter MiTeGen loop using Paratone-N oil as a cryoprotectant. The crystal was then attached to the instrument goniometer before data were collected about ϕ and ω rotations, starting from room temperature and cooling to 100 K with 50 K increments per experiment. Unit cell determination, data integration, frame scaling, and absorption corrections (multi-scan implemented in ABSPACK) were performed in CrysAl-

isPro [241]. Structure solutions for all SCXRD datasets were obtained in the non-centrosymmetric orthorhombic space group $P2_12_12_1$ as described in Chapter 3. The corresponding CIFs, checkCIFs and PXRD parameters are provided as electronic data files (Folder 'Ch4-VT') and the crystallographic details are presented in Appendix B1.

The powder X-ray diffraction patterns of both MOX-2 and MOX-4 were measured on the I11 beamline at the Diamond Light Source with an X-ray wavelength of 0.826872 Å. The position-sensitive detector was used to collect diffraction patterns over the temperature range 100 – 300 K with an Oxford Cryosystems Cryostream 700. Both samples were prepared by directly isolating washed crystals with EA and leaving to dry in air. After evaporation of the solvent, the single crystals were ground with a pestle and mortar until a fine powder was obtained. The powder was then deposited in 0.2 mm glass capillaries. The PXRD data were analysed through sequential Pawley refinements using the TOPAS software [233].

The dynamic behaviour of MOX-2 and MOX-4 at variable temperature was analysed using the PASCal software [270].

4.3.2 Results and discussion

Both the PXRD and SCXRD data measured for MOX-2 show that the framework exhibits NTE along the c-axis and positive thermal expansion (PTE) along the a- and b-axes (Fig. 4.2). Thus, the wine-rack motif expands along the longer axis upon cooling, indicating MOX-2 behaves as an conventional wine-rack framework. There are some discrepancies between the thermal expansion coefficients, α, calculated for each unit cell parameter from the SCXRD and PXRD data (Table 4.1). These differences most likely arise from different guest loadings in the pores, as indicated by different absolute unit cell volumes. The most important aspect, however, is the direction of the NTE, which remains the same for both datasets.

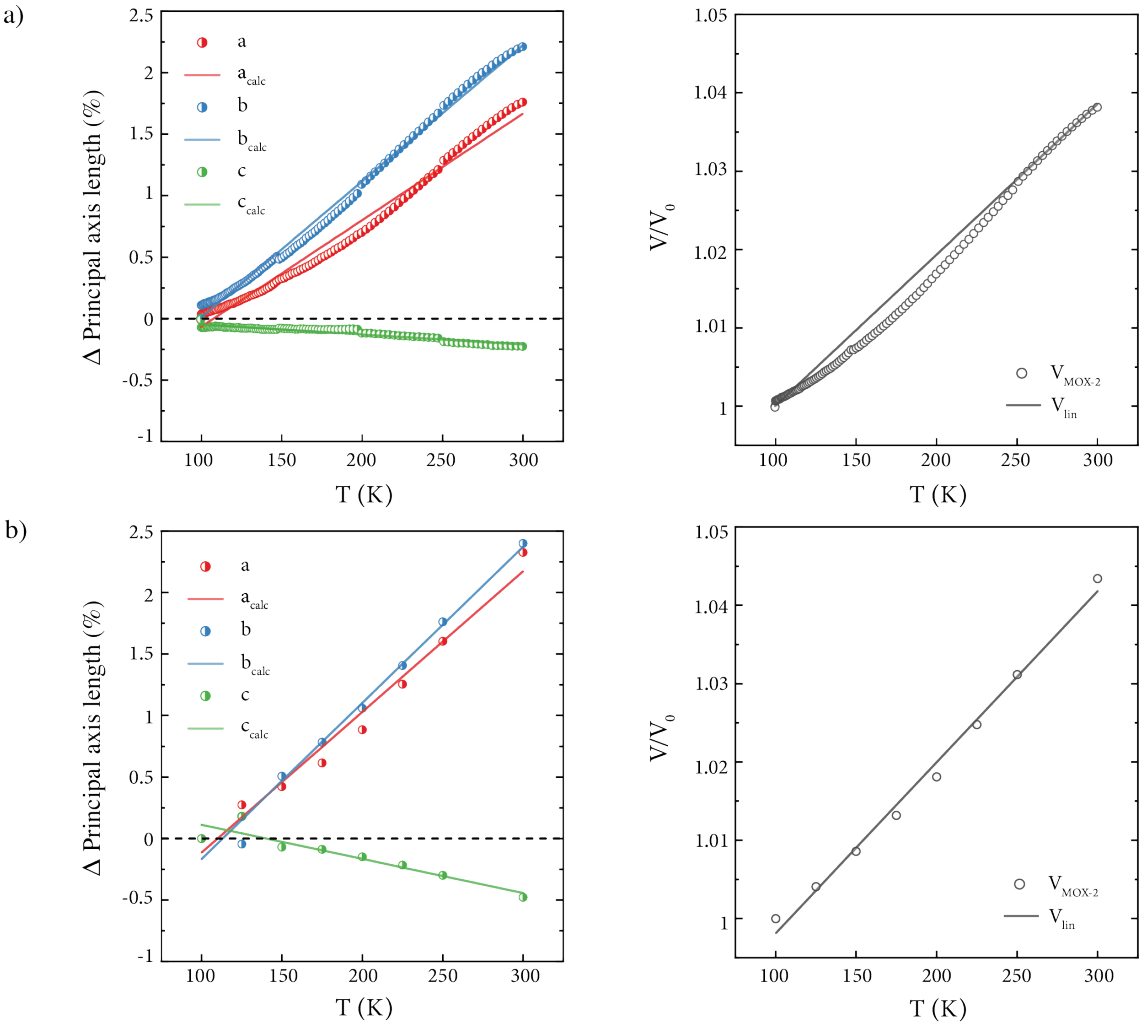

Figure 4.2: Change in unit cell parameters and volume as a function of temperature for MOX-2 as determined from (a) PXRD and (b) SCXRD variable-temperature measurements. Note that the discontinuities at 150, 200 and 250 K in (a) are likely a result of artefacts introduced during the fitting process in the TOPAS software.

Table 4.1: Thermal expansion coefficients, α (MK^{-1}), of MOX-2 calculated from both PXRD and SCXRD variable-temperature data.

Cell parameter	α (MK^{-1}), PXRD	α (MK^{-1}), SCXRD
a	87.3(1)	114(7)
b	111.8(8)	127(7)
c	–8.07(3)	–28(5)

For MOX-4, both the PXRD and SCXRD data indicate the framework exhibits NTE along the a-axis and PTE along the b- and c-axes (Fig. 4.3). Thus, the wine-rack motif expands along the shorter axis upon cooling. Similar to the case of MOX-2, there are some discrepancies between the thermal expansion coefficients, α, calculated for each unit cell parameter from the SCXRD and PXRD data (Table 4.2), most likely caused by different guest loadings in the pores. However the direction of the NTE remains the same for both datasets.

Thus, results show that for both samples, the thermal coefficients α_a and α_c

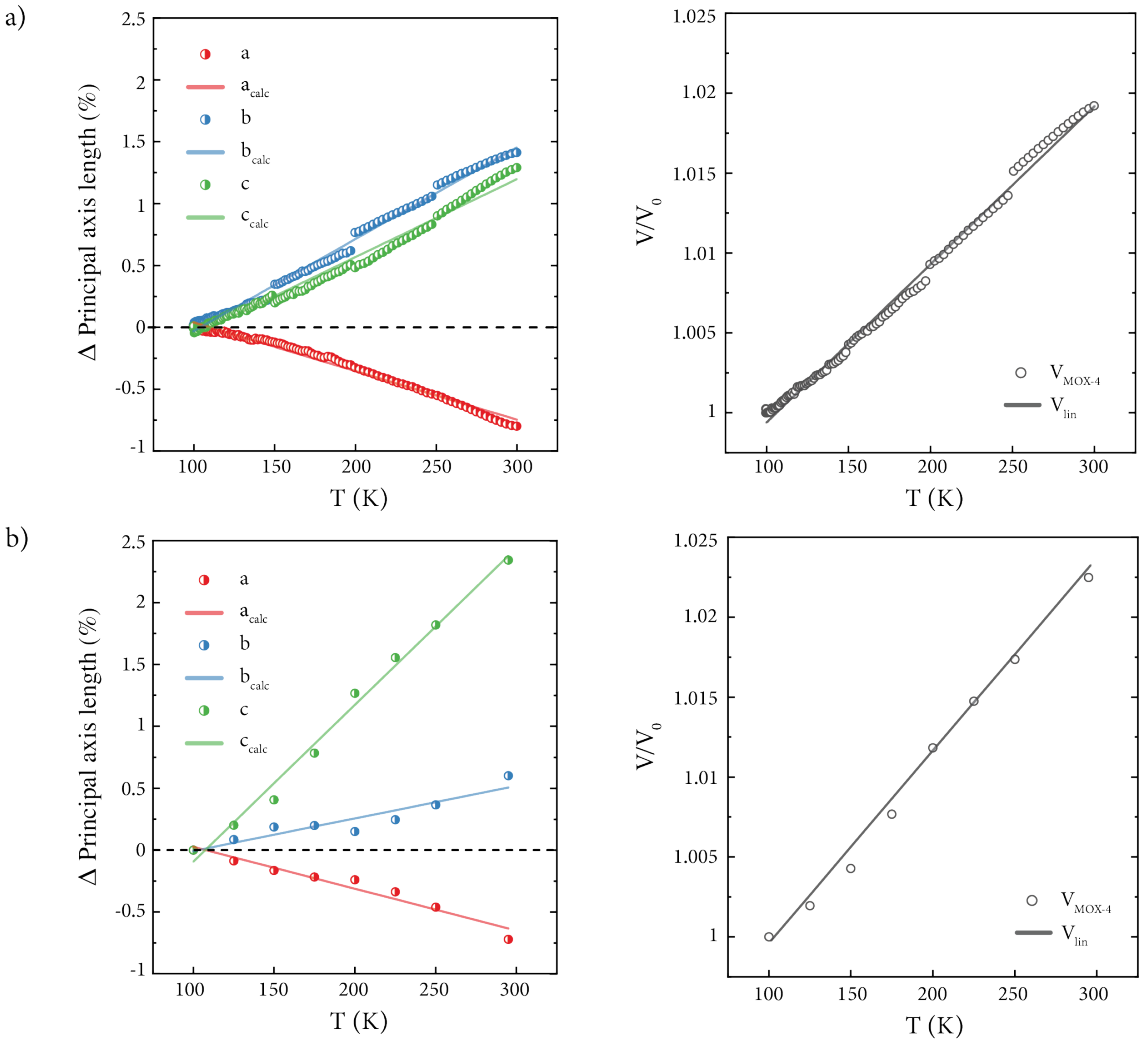

Figure 4.3: Change in unit cell parameters and volume as a function of temperature for MOX-4 as determined from (a) PXRD and (b) SCXRD variable-temperature measurements. Note that the discontinuities at 150, 200 and 250 K in (a) are likely a result of artefacts introduced during the fitting process in the TOPAS software.

Table 4.2: Thermal expansion coefficients, α (MK^{-1}), of MOX-4 calculated from both PXRD and SCXRD variable-temperature data.

Cell parameter	α (MK^{-1}), PXRD	α (MK^{-1}), SCXRD
a	–39.3(6)	–34(3)
b	74.3(6)	26(4)
c	63.1(9)	127(4)

have the opposite sign. As stated previously, this inverse relationship is expected for wine-rack frameworks [163, 269, 332]. Yet the direction of the NTE inverts from MOX-2 (c-axis) to MOX-4 (a-axis), for which the reason is unknown. Conventionally, wine-rack frameworks exhibit NTE along the direction that corresponds to the smallest angle between the hinges of the framework *i.e.* the c-axis. Whilst this correlation applies to MOX-2, MOX-4 exhibits anomalous behaviour by expanding in the direction perpendicular to the smallest angle between hinges upon cooling.

To further investigate the impact of the wine-rack geometry on the behaviour of MOX-2 and MOX-4 at variable temperature, the difference in both distance, r, between metal nodes and angle, θ, between the hinges of the wine-rack motif were extracted by course-graining crystallographic models of MOX-2 and MOX-4 solved from the SCXRD data (Fig. 4.4). The corresponding thermal expansion coefficients α_r and α_θ (Table 4.4) were calculated using the following relationships:

$$\alpha_r = \frac{1}{r}\frac{\mathrm{d}r}{\mathrm{d}T}, \tag{4.1}$$

$$\alpha_\theta = \frac{1}{\theta}\frac{\mathrm{d}\theta}{\mathrm{d}T}. \tag{4.2}$$

If the behaviour of MOX-2 and MOX-4 can solely be attributed to their wine-rack geometry *i.e.* the hinging of the SBUs as permitted by rigid linker struts, it would be expected that r remains constant whilst θ changes as a function of temperature [332].

Results show that, as expected, the angle θ increases in MOX-2 and decreases in

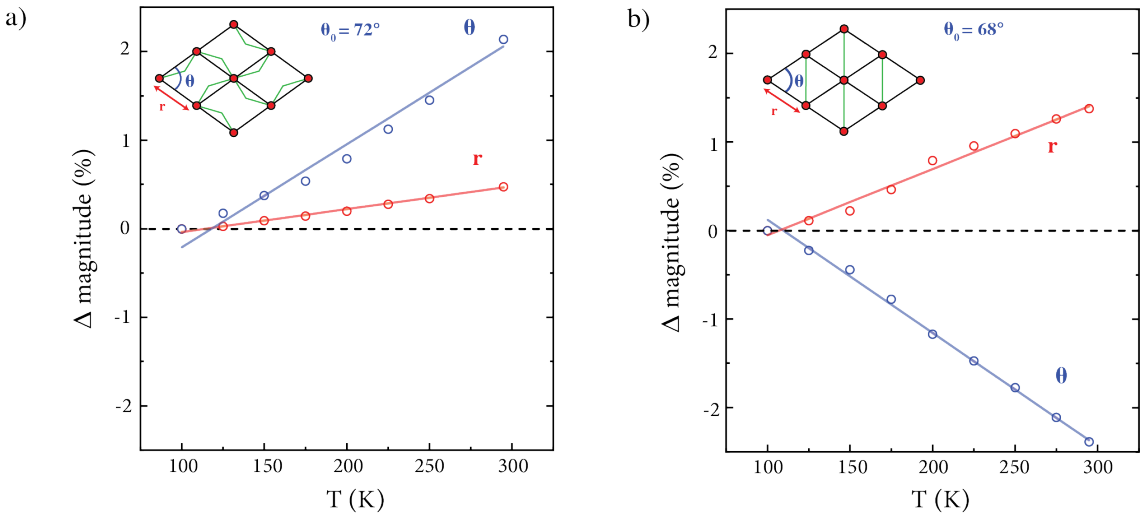

Figure 4.4: Thermal variation in the (a) MOX-2 and (b) MOX-4 M–ligand–M linker distance r (green) and corresponding framework angle θ (blue) as a function of temperature. The inset figure demonstrates the location of r and θ within the framework structure.

Table 4.3: Thermal expansion coefficients, α (MK^{-1}), of MOX-2 and MOX-4 as a function of θ and r.

α (MK^{-1})	MOX-2	MOX-4
α_θ	116(6)	–128(3)
α_r	26(1)	75(2)

MOX-4 upon heating. The value of r expands positively upon heating in both cases. For MOX-2, the contribution of r to the structural changes appears less significant than that of θ, as the magnitude of the change in r is much smaller (Fig. 4.4a). This insignificance of r indicates that the behaviour of MOX-2 at variable temperature is dominated by the change in θ and thus the wine-rack motif. For MOX-4, on the other hand, the value of r changes significantly as a function of temperature (Fig. 4.4b). This observation indicates that the structural changes in MOX-4 are not solely dominated by the wine-rack motif.

Therefore, MOX-2 behaves as an conventional wine-rack framework whilst MOX-4 shows anomalous behaviour which cannot be solely attributed to the geometry of the wine-rack motif. Instead, it appears that in MOX-4 the angle of θ moves towards the value of 60° as a function of temperature. This value for θ corresponds

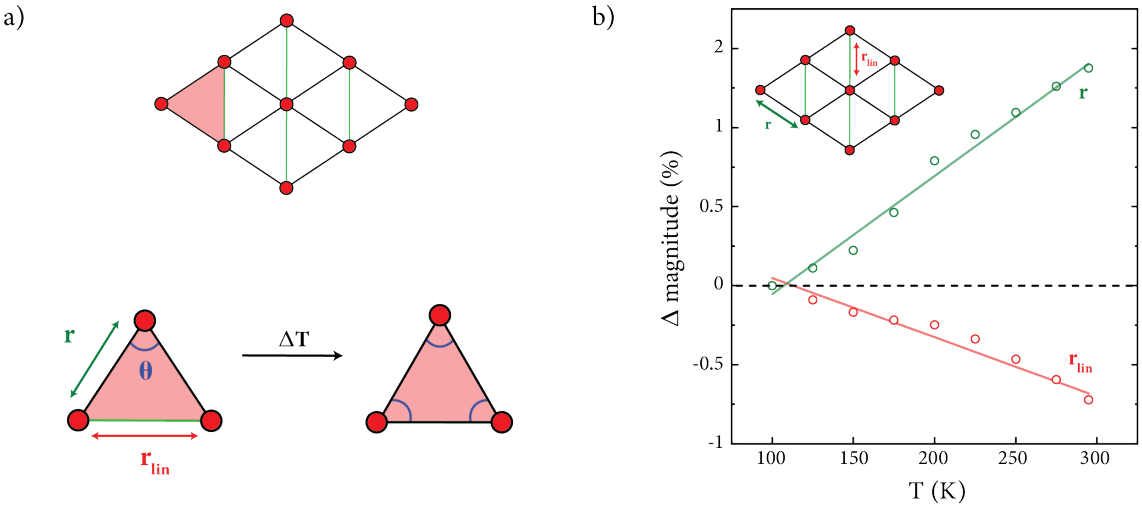

Figure 4.5: Maximum Zn column separation in MOX-4 as a function of temperature. (a) Change in the angle θ and distances r and r_{lin} as a function of temperature to ultimately obtain a pore environment of an equilateral triangular configuration. (b) Change in distance between diagonally and vertically separated Zn columns, r and r_{lin}, respectively, as a function of temperature.

to the configuration of maximum separation between Zn columns *i.e.* where each pore environment corresponds to an equilateral triangle (Fig. 4.5a). Indeed, the significant increase in r upon heating is correlated to a decrease in the value of the M–ligand–M linker distance between linearly stacked columns (*i.e.* along the a-axis), r_{lin}, in turn confirming the preference for a configuration with maximum separation between Zn columns, where $r = r_{\mathrm{lin}}$ (Fig. 4.5b). In turn, the presence of the additional 2,5-tdc linker arranged along the a-axis — characteristic of the reinforced wine-rack configuration — is key in this observation for MOX-4.

Finally, there is no notable effect of the helical motif enhancing the NTE behaviour in either MOX-2 or MOX-4.

4.4 High-pressure X-ray diffraction

4.4.1 Experimental details

MOX-2 and MOX-4 crystals were prepared as outlined in Chapter 3 and left to soak in fresh $CHCl_3$ before loading onto a Merrill-Bassett DAC. All high-pressure X-ray diffraction data were collected on the I19 beamline (hutch 2) at the Diamond

Light Source on a Eiger2 4M CdTe detector at pressures between 0.10(1)–2.00(7) GPa for MOX-2 and 0.15(1)–2.09(1) GPa for MOX-4. Data collection included a step size, transmission and exposure time of 1, 3% and 0.3 seconds, respectively. Unit-cell determination, data integration, frame scaling, and absorption corrections were performed using the Diamond Light Source customised software XIA2 [333].

Structure solutions for all datasets were obtained in the non-centrosymmetric orthorhombic space group $P2_12_12_1$ as described in Chapter 3. The corresponding CIFs and checkCIFs are provided as electronic data files (Folder 'Ch4-hp') and the crystallographic details are presented in Appendix B2.

The dynamic behaviour of MOX-2 and MOX-4 at high-pressure was analysed using the PASCAL software [270].

4.4.2 Results and discussion

A first observation from the high-pressure SCXRD data is that both MOX-2 and MOX-4 remained crystalline up to 2 GPa, in turn enabling both unit cell indexing and structural refinement of all datasets. Graphs depicting the change in unit cell parameters and volume as a function of pressure, together with the fits of the 2nd and 3rd order Birch-Murnaghan (BM) equations of state (EoS), are shown in Fig. 4.6.

In MOX-2, all axes compress upon the application of pressure. However the compressibility of the a- and b-axes is much larger than that of the c-axis (Table 4.4), in turn indicating that the latter is rather in comparison to the other directions. Notably, this direction of stiffness corresponds to the NTE axis. Based on the better fit of the 3rd order BM EoS, the bulk modulus of MOX-2 was determined to

Table 4.4: Compressibility, K (TPa^{-1}), of MOX-2 and MOX-4, extracted from SCXRD data.

Cell parameter	MOX-2	MOX-4
a	30.0(6)	–5.4(1)
b	45.7(7)	24.6(3)
c	7.2(2)	33.8(6)

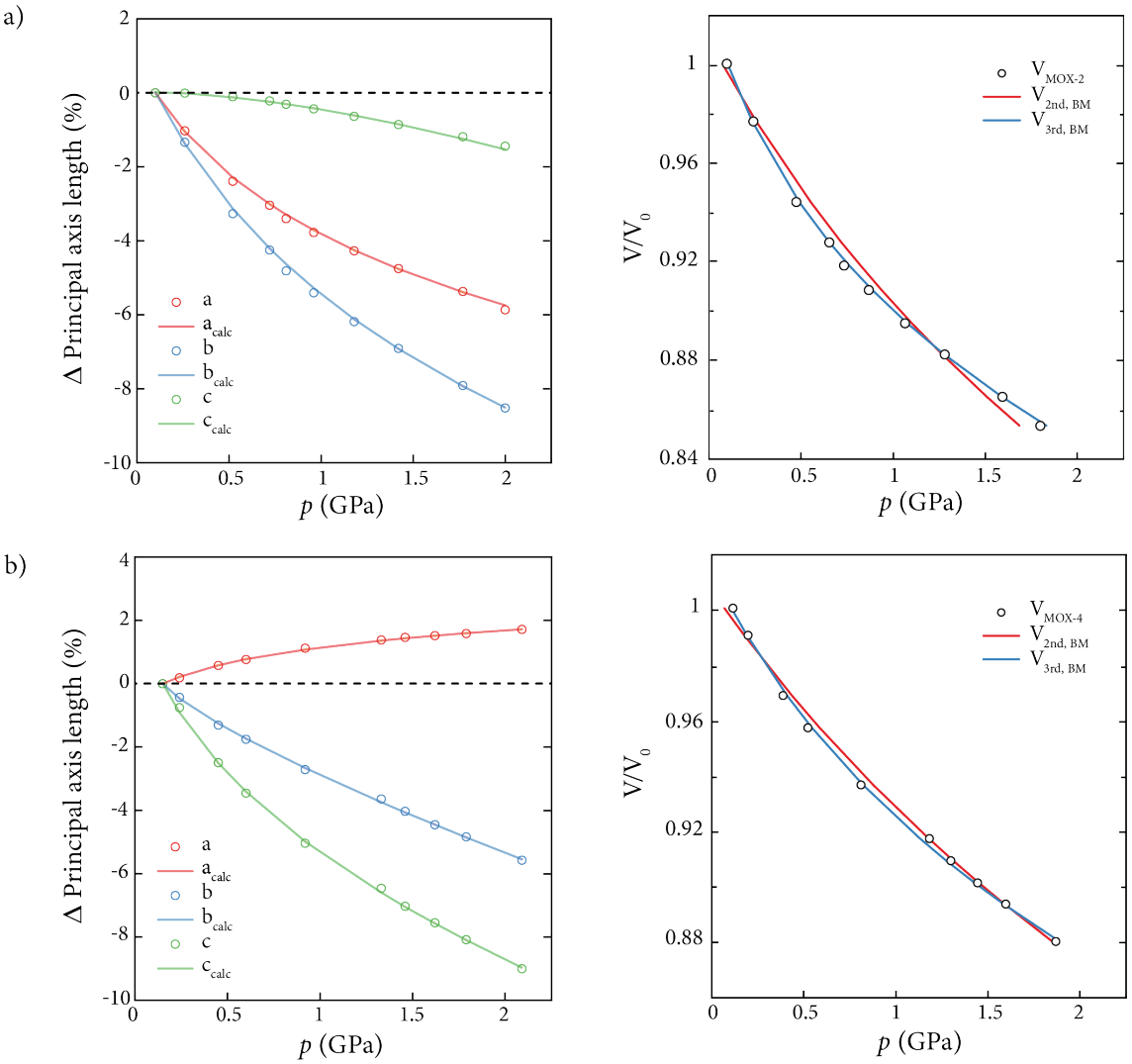

Figure 4.6: Change in unit cell parameters (left) and volume (right) as a function of pressure for (a) MOX-2 and (b) MOX-4. The change in volume as a function of pressure is fitted with both a 2nd and 3rd Birch-Murnaghan equation of state.

Table 4.5: EoS parameters of MOX-2 and MOX-4 as calculated from the BM fits presented in Fig. 4.6.

Order of BM EoS	MOX-2, B_0 (GPa)	B'	MOX-4, B_0 (GPa)	B'
2	8.0(2)	(4)	11.5(3)	(4)
3	4.3(4)	13(2)	7.9(8)	9(2)

be 4.3 with $B' = 12.8$ (Table 4.5). Accordingly, MOX-2 is very soft but becomes significantly harder as it is compressed.

In MOX-4, on the other hand, the a-axis has a compressibility of $K = -5.4$

TPa^{-1} (Table 4.4); thus MOX-4 expresses NLC. Based on the better fit of the 3rd order BM EoS, it has a larger bulk modulus than MOX-2 ($B = 7.9$ GPa, $B' = 9.0$) and is therefore more resistant to the applied hydrostatic pressure. Similarly, the resistance of the framework increases as it is compressed.

Thus, the behaviour of MOX-2 and MOX-4 is again related by an inverse relationship between the a- and c-axis. However in this case, MOX-2 compresses positively along all directions with increasing pressure whilst MOX-4 exhibits NLC along the a-axis. Again, the significance of the wine-rack geometry for these observations could be probed by tracking the changes in both the distance r between metal nodes and the angle θ between the hinges of the wine-rack framework (Fig. 4.7). In this case, the corresponding values of compressibility K_r and K_θ were calculated by adapting Equations 4.1 and 4.2 to account for the changes as a function of pressure (Table 4.6).

The results show similar trends that were observed for the behaviour of MOX-2 and MOX-4 at variable temperature. Namely, θ increases positively as a function of pressure for MOX-4 and negatively for MOX-2. However a difference is that the change in magnitude of r, which in both cases decreases as a function of pressure, is now significant in both MOX-2 and MOX-4. Namely, in the case of MOX-2,

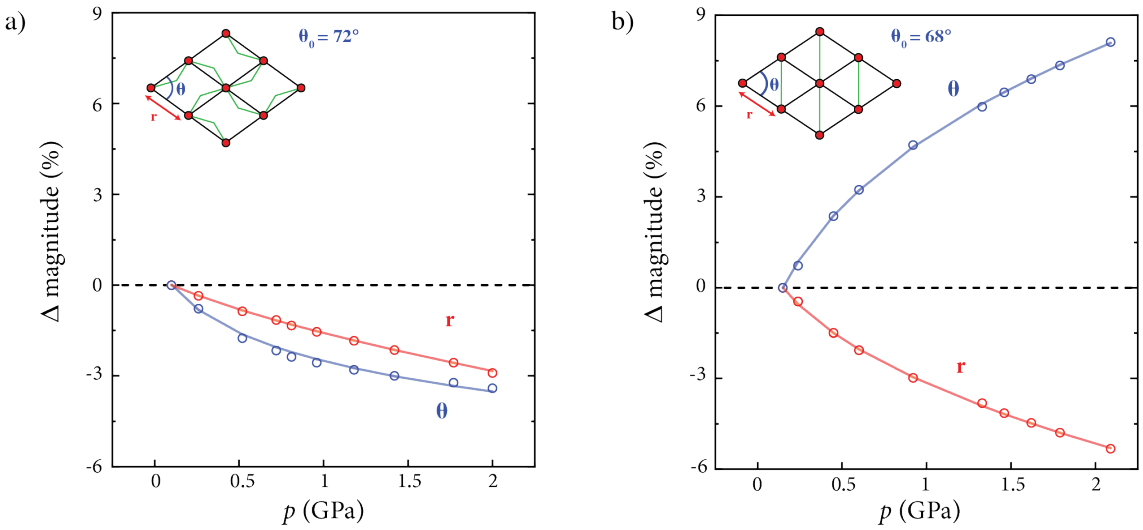

Figure 4.7: Compressibility of the (a) MOX-2 and (b) MOX-4 M–ligand–M linker distance r (red) and corresponding framework angle θ (blue) as a function of pressure. The inset figure shows the location of the angle θ within the framework structure.

Table 4.6: Compressibility, K (TPa^{-1}), of MOX-2 and MOX-4 as a function of θ and r.

Compressibility	MOX-2	MOX-4
K_θ (TPa^{-1})	16.9(5)	–39.4(6)
K_r (TPa^{-1})	15.2(1)	25.8(4)

the compressibility of r was calculated as 15.2 TPa^{-1}; only ∼2 TPa^{-1} less than the compressibility of θ. Accordingly, the behaviour of MOX-2 can not be solely attributed to the geometry of the wine-rack motif. This is in agreement with the observation that a conventional wine-rack would be expected to exhibit NLC along the c- axis[163, 269], yet MOX-2 compresses positively upon exposure to high-pressure. For MOX-4, the change in magnitude of r possibly indicates that the mechanism of maximum Zn column distance highlighted above reverses as a function of pressure.

Again, there is no notable effect that arises from the helix motif on the behaviour of MOX-2 and MOX-4 under pressure.

4.5 Summary and conclusion

In conclusion, both MOX-2 and MOX-4 exhibit unusual dynamical behaviour, albeit not in agreement with typical observations made for wine-rack frameworks; being the expression of both NTE and NLC along the same, longer axis of the wine-rack [178, 269]. Namely, MOX-2 exhibits NTE along the longer axis of the wine-rack motif but compresses positively in all directions upon the application of pressure. MOX-4, on the other hand, does show both NTE and NLC along the same direction, albeit along the shorter axis of the wine-rack.

Yet, all these observations can be understood by considering the contributions of solely the wine-rack geometry in opposition to other interfering mechanisms, for example caused by the added linker positions characteristic of the propeller and reinforced wine-rack motif of MOX-2 and MOX-4, respectively. This contribution was analysed by considering the change in both the distance and angle between the metal cluster hinges of the wine-rack framework. For mechanisms dominated by the

wine-rack framework geometry, a minimum change in magnitude of the distance, r, would be expected. Such a small change was only observed for MOX-2 during variable temperature experiments, in turn confirming that its behaviour under these conditions is governed by a change in hinge angles of the wine-rack geometry. In all other cases, however, the change in the angle θ as a function of temperature or pressure was accompanied by a significant change in r, indicating the contribution of other mechanisms responsible for the observed behaviour.

In the case of MOX-4, the additional linker positioned along the a-axis appears to constrain the Zn columns so that the framework prefers a configuration that minimises the distances between the columns through realisation of equilateral triangular-shaped pore environments. The framework shifts towards this configuration upon heating whilst the application of pressure reverses this effect.

Likewise, the anomalous behaviour of MOX-2 under pressure might be attributed to the significant change in r, although the exact mechanism responsible remains unknown.

However, it is noteworthy that the parameter r is susceptible to significant alterations. Indeed, the value of r is correlated to the length of the linker. Since the linkers in MOX-2 and MOX-4 are bent, there is potential for stretching or contraction by increasing or decreasing the bend angle, respectively, in turn leading to an increase or decrease in r in each case. This assertion is supported by the observation that well-studied, compliant wine-rack MOFs contain linear linkers such as isonicotinate and 1,4-bdc [331, 332].

Ultimately, ignoring the occurrence of NTE and NLC, there is something to be said about the difference in bulk modulus of MOX-2 and MOX-4. Namely, MOX-2 is much softer than MOX-4, demonstrating the softening effect of the propeller wine-rack motif.

This difference in softness may be traced back to the different densities of the framework, being 1.71 g cm^{-3} and 1.85 g cm^{-3} for MOX-2 and MOX-4, respectively. However, it is noteworthy that the heavier 2,5-tdc linker likely contributes to the higher density of MOX-4. Moreover, this difference in density alone does not seem

sufficient to account for the twofold increase in bulk modulus observed in MOX-4 compared to MOX-2.

Instead, the distinction in softness may be traced back to the different angle between the linker carboxylates, as was discussed in the introduction of this chapter. Namely, the smaller angle associated with 1,3-bdc allows for the additional linker to align along the wine-rack configuration, as opposed to the vertical arrangement seen in MOX-4 with 2,5-tdc. This alignment of 2,5-tdc is in turn made possible by the greater angle between the carboxylates, which creates the necessary distance between the stacked metal cluster pillars along the a-axis. As a result of this configuration, MOX-4 is stabilised, or "reinforced", to a greater extent, providing increased stability against applied mechanical forces. This is consistent with work done on the reinforced wine-rack MIL-140A, where the linker 1,4-bdc — thus with the maximum angle of 180° — is arranged between stacked SBUs along the a-axis, in turn leading to the abscence of a "soft" direction [331].

Accordingly, the mechanical behaviour of MOX-2 and MOX-4 outlined in this chapter nicely demonstrates the impact of the angle between linker carboxylates on MOF structures and ultimately, properties.

Chapter 5

MOX-3 thermal diffuse scattering

5.1 Summary and acknowledgements

As discussed in Chapter 3, MOX-3 exhibits significant diffuse scattering in its total scattering diffraction patterns. Yet the corresponding average structure of MOX-3 shows no signs of disorder. Rather, it indicates that the antipolar 'up' and 'down' configuration of the functionalised 1,3-bdc linkers along the hexagonal channels is satisfied by the hexagonal lattice. This then also rules out the possibility of frustration between neighbouring channels, of which the configuration maps onto the triangular lattice [17]. What is more, diffraction experiments show that the total scattering signatures change as a function of the size of the functional group attached to the 1,3-bdc ring.

All these observations indicate that the diffuse scattering observed for MOX-3 may arise from dynamic contributions *i.e.* thermal diffuse scattering (TDS). This chapter aims to confirm this hypothesis by studying the diffuse scattering in more depth by collecting diffraction data at a synchrotron beamline as well as generating the corresponding 3D-ΔPDF. Additionally, TDS was calculated using a simple MC simulation based on the hexagonal lattice, in turn showing features similar to those observed in the experimental data.

I am grateful to Arianna Minelli and Johnathan Bulled for collecting total scattering data of MOX-3 on beamtime at the ID28 beamline at the European Synchrotron Radiation Facility (ESRF).

5.2 Methods

All SCXRD data presented in this chapter was collected at the ID28 beamline of the ESRF [334] on MOX-3 crystals with X = Br. For the data collection, a monochromatic beam of $\lambda = 0.697$ Å was used, collecting data on a pilatus 1M Dectris detector

with a pixel size of 172×172 μm^2 in single photon counting mode. Each measurement was performed at room temperature and involved a full ϕ-scan carried out in a single run, with 0.25° increments and an exposure time of 0.25 s per frame.

The 3D-ΔPDF was calculated using the FFT algorithm as implemented in MEERKAT2 [335]. The correct input was provided by removing the Bragg peaks *via* the punch-and-fill feature, similarly facilitated by MEERKAT2 [335].

5.3 Results and discussion

The reconstructed layers of total scattering for MOX-3 (Fig. 5.1) show that in the *hkn* planes (n = an integer), the diffuse features are sharp and intense, appearing between Bragg peaks to resemble "bow-ties" arranged in a six-fold rotational symmetry. Between the bow-tie features, the intensity of the diffuse scattering is much lower. In all directions other than *hkn*, the diffuse features are more broad and

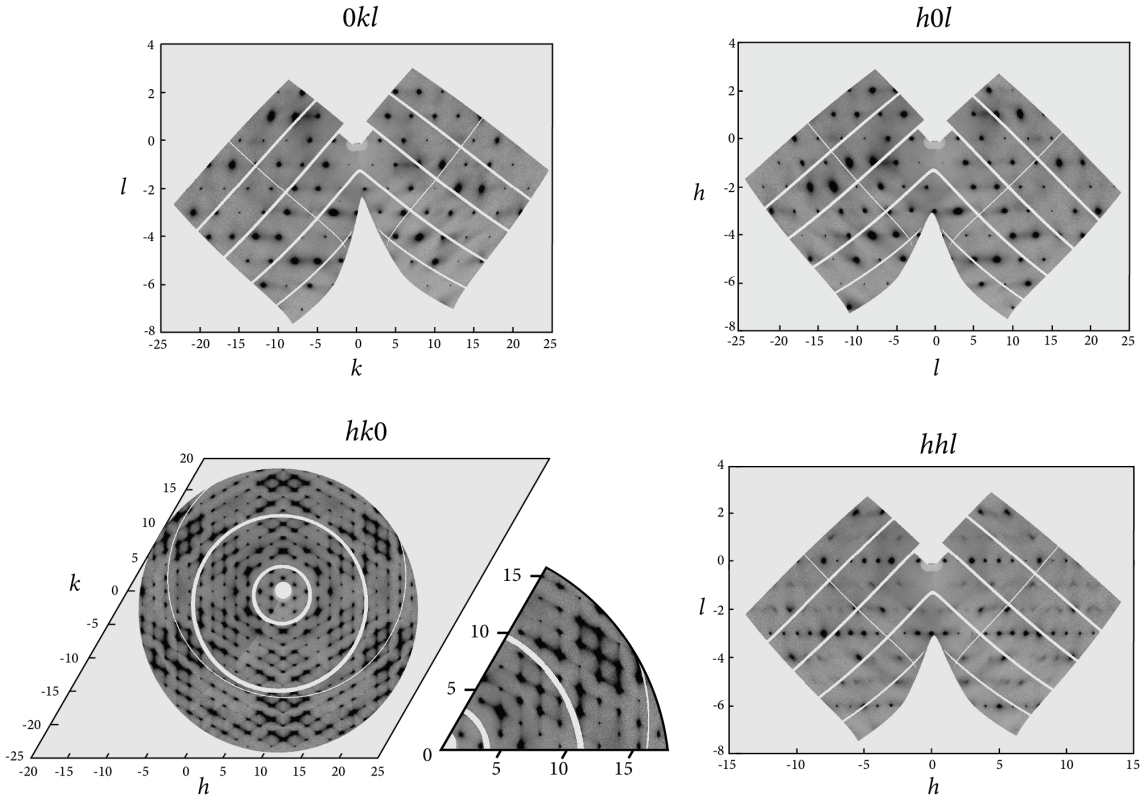

Figure 5.1: Reconstructed (top, left to right) 0*kl*, *h*0*l*, (bottom, left to right) *hk*0, and *hhl* layers collected for MOX-3 with X = Br, showing the diffuse scattering features.

appear as diffuse clouds.

The corresponding 3D-ΔPDF is noisy and does not show significant or sharp features, other than those at the [1,0,0] and [1,1,0] vectors (Fig. 5.2). These signatures are both blue and red, indicating positive and negative correlations at these positions. This is commonly indicative of displacements caused by the size effect [236]. This cannot apply to this system — except for X = Cl/Br — since there are no substitutions. Instead, these features are an indication of dynamic contributions. However it is important to consider the signatures observed in this 3D-ΔPDF with a pinch of salt regarding the limitations of this technique, as highlighted previously in Chapter 2.

As mentioned in Chapter 3, the intensity of the diffuse scattering of MOX-3 is affected by the identity of X: the diffuse features are most prominent for X = Br and Cl, whilst for X = I, the diffuse scattering is significantly weaker. This observation is another indication that the diffuse scattering observed for MOX-3 is TDS, as it costs more energy for the framework to undergo dynamic displacements if the X functional group is heavy [33]. In turn, the TDS may arise from the flipping or swinging of the 1,3-bdc benzene ring, which can be in an up or down configuration. Alternatively, the observed diffuse scattering may arise from the collective movement

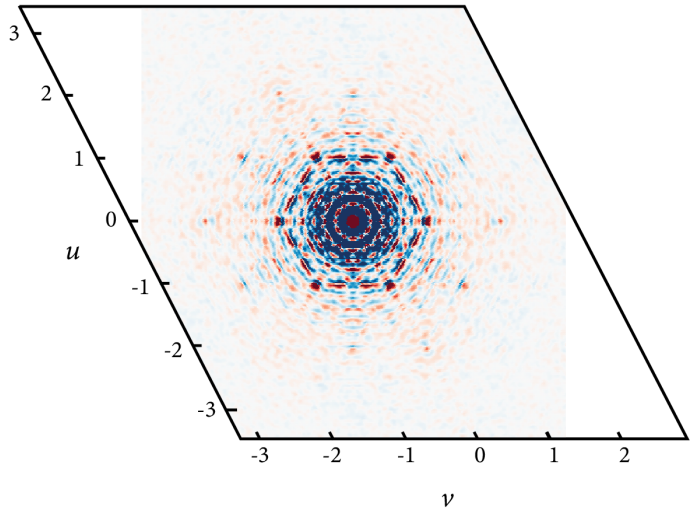

Figure 5.2: *uv*0 cut of the 3D-ΔPDF calculated for MOX-3 with X = Br, generated from the diffuse scattering. Positive correlations are shown in red and negative correlations in blue.

of the hexagonal lattice, rather than the individual molecular components that make up the structure of MOX-3. The latter hypothesis is supported by the observation that the diffuse scattering observed in the $hk0$ plane of MOX-3 is rather similar to the TDS observed for β-quartz [45], which was described in Chapter 1 (Fig. 1.7b), and similarly resides on a hexagonal lattice.

As a final test of this hypothesis, a MC simulation was used to calculate the TDS for a layer of atoms residing on a hexagonal lattice (Fig. 5.3a). In this model, the atoms were separated by springs with a given force constant, k. During the simulation, the atoms are allowed to displace in two dimensions *i.e.* within the same layer for a given temperature, calculating the energy using Hooke's law ($E = \frac{1}{2}k(r - r_0)^2$). The parameters used to calculate the TDS shown in Fig. 5.3 were $k = 4$ eVÅ^{-2} and $T = 100$ K.

Comparing the simulated $hk0$ layer to the experimental data shows a good agreement; the bow-tie features are encapsulated by the simple model, in turn confirming that the observed diffuse scattering in MOX-3 is indeed TDS mostly arising from displacements of the hexagonal lattice. The intensities of the scattering do not

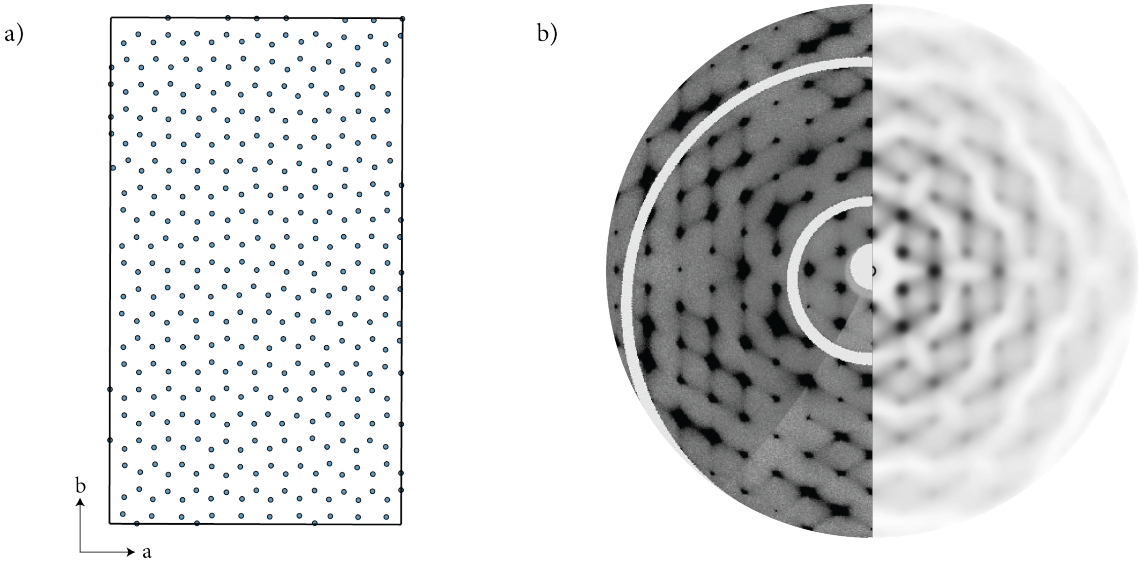

Figure 5.3: Calculation of TDS of a simple hexagonal model: (a) coarse grained lattice used to calcute the TDS. (b) Comparison of the experimental total scattering data (left) with the calculated TDS (right), showing the reconstructed $hk0$ layer.

match entirely, however this disagreement is to be expected as the simulated total scattering does not include real atoms and therefore lacks an atomic form factor.

5.4 Conclusion

In conclusion, the observed diffuse scattering observed for MOX-3 is in fact TDS, as confirmed by the 3D-ΔPDF generated from experimental data and TDS calculated from a MC simulation based on the hexagonal lattice. Accordingly, this brief chapter effectively demonstrates that diffuse scattering observed in the total scattering data of MOFs does not always indicate the presence of static correlated disorder. Instead, the flexibility of frameworks may result in dynamic displacements, which in the case of MOX-3 could be efficiently accounted for by solely considering the collective movement of the hexagonal lattice that it decorates. A more accurate analysis may involve decorating the simple model with the appropriate atoms, or a simulation of TDS as a result of the collective movement of rigid units (*i.e.* the Zn tetrahedra and rigid linkers), to mimic the approach adapted for the characterisation of the TDS observed for β-quartz as reported in Ref. 45.

Chapter 6

Correlated disorder in MOFs

6.1 Introduction

As described in Chapter 3, the structure of TRUMOF-1 is disordered. We will come to show, in the next chapter, that this disorder is in fact strongly correlated. Such correlated disorder is not uncommon in MOF chemistry; a vacancy at one linker site in an otherwise crystalline MOF, for example, may affect the likelihood for neighbouring linkers also to be vacant. Such vacancy correlations can propagate throughout a structure, collectively determining a variety of bulk properties — including porosity [336, 337]. Likewise, mixed-metal and/or mixed-linker MOFs can have non-statistical distributions that determine their corresponding chemistry; such is the basis, after all, of the MTV-MOF approach which, as mentioned in Chapter 1, exploits compositional heterogeneity to improve functionality [120]. And in orientationally-disordered MOFs, correlations in linker orientations can also affect mechanical and host/guest responses [338]. These various distinctions are illustrated schematically in Fig. 6.1, and accordingly demonstrate how the presence and nature of disorder in MOFs can be used as an important design tool with which to tune their physical and chemical properties [339, 340].

Exploiting such complexity in MOFs is a relatively young branch of the field because it was for long assumed that MOFs are perfectly crystalline [341, 342]. The discovery of disordered [343], defective [336, 344], amorphous [345], and even liquid [346, 347] MOFs has therefore forced a paradigm shift in the collective understanding of MOF structural chemistry [348]. However, as highlighted in Chapter 1 and 2, distinguishing correlated from random disorder is often a nontrivial experimental and computational challenge. Conventional crystallography probes only the average crystal structure; it is demonstrably insensitive to correlations within disordered states [17]. Yet a number of developments have now converged to equip the community with the tools needed to probe correlated disorder in MOFs. Experimentally,

recent advances in solid-state NMR, X-ray diffuse scattering, PDF, and electron microscopy measurements are providing valuable empirical insight into MOF defect structures [337, 349–351]. At the same time, *ab initio* DFT calculations of a sufficient scale to interrogate non-crystalline MOF architectures are becoming increasingly tractable [347, 352]. The development of efficient high-quality MOF force-field methodologies extend these approaches beyond the nanometre scale [353, 354].

In this chapter, I review the concept of correlated disorder in MOFs. Three primary types of (correlated) disorder in MOFs are described: (i) correlated vacancies; (ii) compositional disorder; and (iii) orientational disorder. These are in turn discussed in the context of the behaviour of a small selection of canonical systems. The emphasis in these sections is also threefold: (i) the nature of correlated disorder

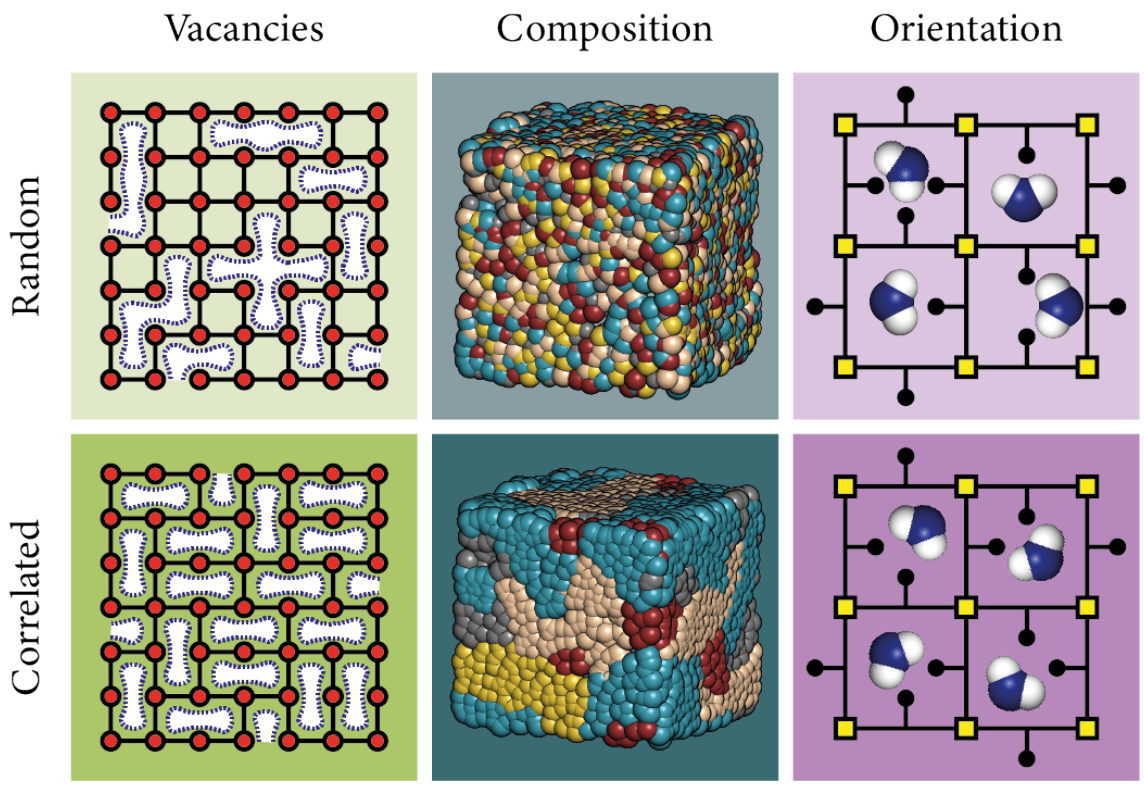

Figure 6.1: Schematic illustration of the conceptual distinction between random and correlated disorder in MOFs. (left) Linker vacancies can lead to heterogeneous or homogeneous pore size distributions depending on the presence or absence of correlations. The two panels have the same number of missing linkers but exactly one linker is missing from each node in the bottom panel. (centre) The degree of clustering or anticlustering in mixed-metal or mixed-linker MOFs can give rise to uniform or domain-like structures. (right) Here the orientations of substituted linkers control the nature and diversity of host–guest interactions. Note that in the bottom panel each pore has the same interactions, despite the disorder of linker orientations.

in these MOFs; (ii) the use of experimental and computational tools to characterise correlations; and (iii) the implications for physical and chemical properties. The chapter concludes with a forward-looking discussion of the future challenges and opportunities in the field. Ultimately, these cases provide the scientific context necessary to understand the significance of TRUMOF-1.

6.2 Vacancy correlations

UiO-66 and its variants are the canonical example of MOFs in which vacancy defects occur in a correlated — rather than random — manner [93, 355, 356]. As highlighted in Chapter 1, the parent compound UiO-66 adopts a face-centred cubic structure based on the 12-connected **fcu** net [93]. Not only does the high connectivity confer thermal, chemical and mechanical stability [208], but it also renders the framework tolerant to both missing-linker and missing-cluster defects [357].

The first signs of correlations in vacancy arrangements came from the appearance of structured diffuse scattering in the PXRD patterns of UiO-66(Hf) samples

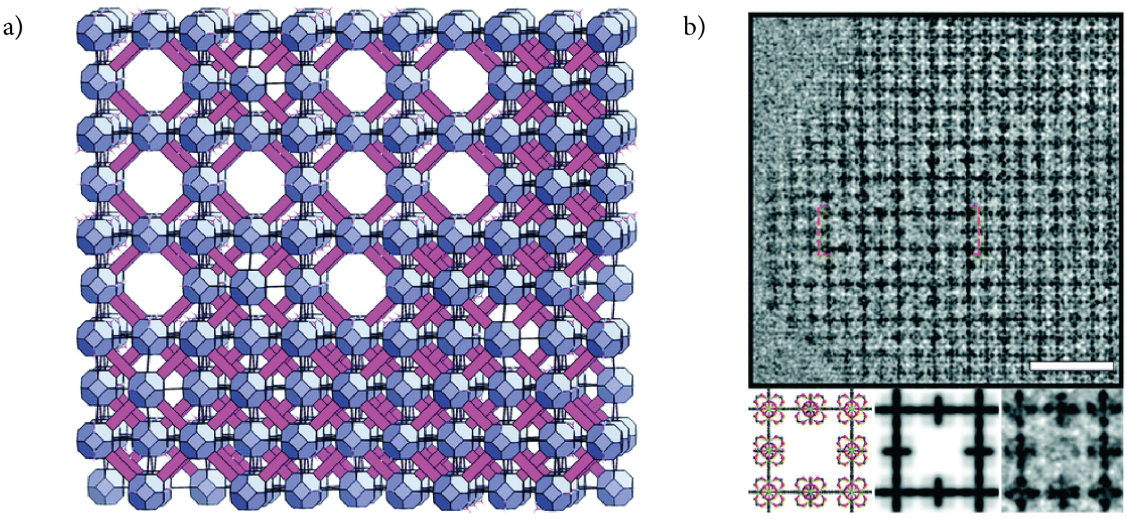

Figure 6.2: Correlated vacancies in UiO-66. (a) Nanodomain model for UiO-66(Hf): cluster vacancies are correlated to give domains of the **reo** topology embedded within the parent **fcu** framework. (b) High-resolution transmission electron microscopy images of missing-cluster/missing-linker nanodomains in UiO-66. The scale bar measures 5 nm. The lower panels denote (from left to right) the atomistic model, the calculated potential map, and the observed potential map. Figure (a) adapted from Ref. 355 with permission from Springer Nature and figure (b) from Ref. 351 with permission from ACS.

synthesised under high modulator concentrations [358]. Diffuse scattering is featureless in the case of random disorder [17, 240], and so its modulation in these patterns is characteristic of correlations in cluster vacancies — the specific form indicating nanodomains with the 8-connected **reo** topology (Fig. 6.2a) [355]. With the advent of low-dose high-resolution transmission electron microscopy (HRTEM), it has since been possible to image these nanodomains directly, which are found to coexist with related missing-linker variants (Fig. 6.2b) [359]. More recently, scanning electron diffraction (SED) was used to image **reo** nanodomain distributions within individual crystallites at a spatial resolution of about 5 nm [351].

The driving force for correlated disorder in the UiO-66 family is thought to be the mechanical stability of **reo**-type connectivity within the **fcu** net [360]. Other, lower symmetry, vacancy distributions are mechanically unstable with respect to shear and so do not survive during crystal growth; this biases the system away from purely statistical vacancy arrangements. An additional consideration is the structure-directing interaction between the UiO-66 framework and both counterions and solvent in the reaction mixture [361]. The picture that emerges is one in which vacancy incorporation in UiO-66 is a kinetic effect — and hence why defect density can be controlled by *e.g.* synthesis temperature [362], solvent [363], or modulator concentration *i.e.* pK_a [364].

From a functional perspective, there are a number of implications of random *vs.* correlated vacancy defects in this family. Perhaps the most obvious is the effect on sorption behaviour, because this depends on the nature of the pore network generated by connected vacancies [364]. Related is the dramatic increase in proton conductivity observed for UiO-66 samples with high linker-vacancy concentrations — although the specific link between missing-linker arrangements and efficiency of proton transport in this system remains to be explored in detail [365]. Correlated cluster absences affect mechanical properties, such as thermal expansivity [366] and compressibility [339, 367]. And DFT calculations show the distribution of both linker and cluster vacancies control the spatial localisation of frontier orbitals, in turn affecting both electronic and catalytic behaviour [361, 368].

The importance of vacancy correlations in other MOF systems is also increasingly apparent. In the aluminium carboxylate MOF AlTz-53-DEF, for example, correlated linker vacancies facilitate a remarkable reversible switching between **sql** and **kgm** network topologies during desolvation/resolvation cycles (Fig. 6.3a) [369].

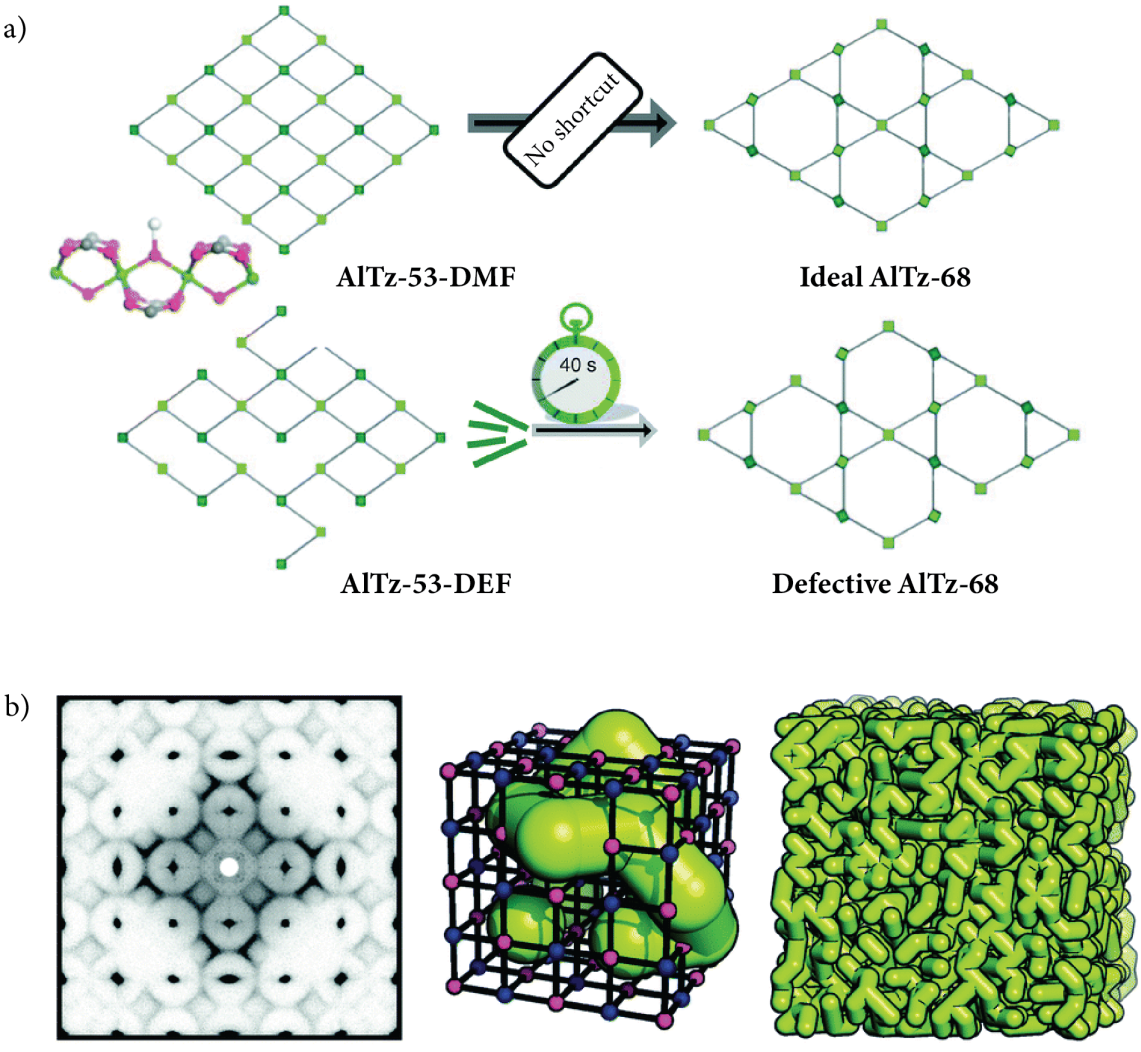

Figure 6.3: Correlated vacancies in other MOFs. (a) Comparison of **sql–kgm** transformation mechanisms (from left to right) in non-defective AlTz-53-DMF (top) and defective AlTz-53-DEF (bottom); the coordinating strength of included solvent plays a key role in facilitating network rearrangement [369]. The green nodes denote aluminium hydroxide/carboxylate columns (illustrated on the left). (b) The single-crystal X-ray diffuse scattering pattern of the $Zn_3[Co(CN)_6]_2$ PBA is characteristic of non-random correlations in the underlying pore network structure (green tubes) that permeates the cubic transition-metal cyanide framework. Figure in (a) adapted from Ref. 369 with permission from Springer Nature and figure (b) from Ref. 337 with permission from Springer Nature.

Even for MOF-5, adsorption isotherms are sensitive to the distribution of linker vacancies — a result demonstrated using grand canonical Monte Carlo (GCMC) simulations [370]. A similar link between linker vacancy arrangements and water adsorption behaviour has been made particularly clear in the case of MOF-801 — a fumarate-containing relative of UiO-66 [371]. And in DUT-49, correlations between cluster vacancies in its **fcu** network are thought to play a key role in the quenching of the NGA effect [372].

Dense coordination networks can also harbour disordered correlated vacancy distributions, the form and origin of which we expect may prove relevant in due course to the behaviour of MOFs. For example, Prussian blue analogues (PBAs) are heavily defective cyanide frameworks with the **pcu** topology [373, 374]. SCXRD measurements of PBAs reveal highly structured diffuse scattering [337, 375, 376], which has recently been interpreted using the 3D-ΔPDF approach (Fig. 6.3b) [337]. The scattering arises from correlated hexacyanometallate vacancies, which avoid occupying neighbouring sites. A key point is that the precise correlations — which control the sorption and transport characteristics of the resulting pore network — can be tuned by variation in PBA composition and synthesis route [337]. Conceptually similar vacancy patterns are found in the thiocyanate analogues, albeit with long-range order [377]. And in formate perovskites, cation vacancies again interact by avoiding neighbouring sites; this leads to a disorder/order transition in [GUA] $Mn^{2+}_{1-x}Fe^{3+}_{2x/3}\square_{x/3}(HCOO)_3$ (GUA^+ = guanidinium cation) at $x_{ord} \simeq 0.6$ [378].

6.3 Compositional disorder

As was also highlighted in Chapter 1, MOF architectures are tolerant to the incorporation of multiple different metals and/or linkers within the one material [340, 348, 379, 380]. In such cases an obvious consideration is whether the composition is homogeneously distributed or varies in some nonstatistical way *e.g.* domain formation or core-shell architectures [381]. The MTV-MOF paradigm [114], and strategies such as sequential linker installation (SLI) [382], have at their heart the concept that the spatial arrangement of different linkers or metals within a given MOF architecture is key to function, in some way comparable to the sequence of

nucleotides in DNA [383].

The sense one gets is that, other than for very dilute mixtures, truly-random compositional distributions are conspicuously rare in MOFs. Clearly, kinetics of crystallisation play an important role here; for example, the different nucleation rates of Zn- and Co-containing imidazolate frameworks allow the one-pot formation of mixed-metal frameworks with core–shell architectures [385]. Likewise, precursors with different kinetic stabilities can be chosen cleverly to control the degree of mixing during synthesis of mixed-metal coordination polymers [384]. But there

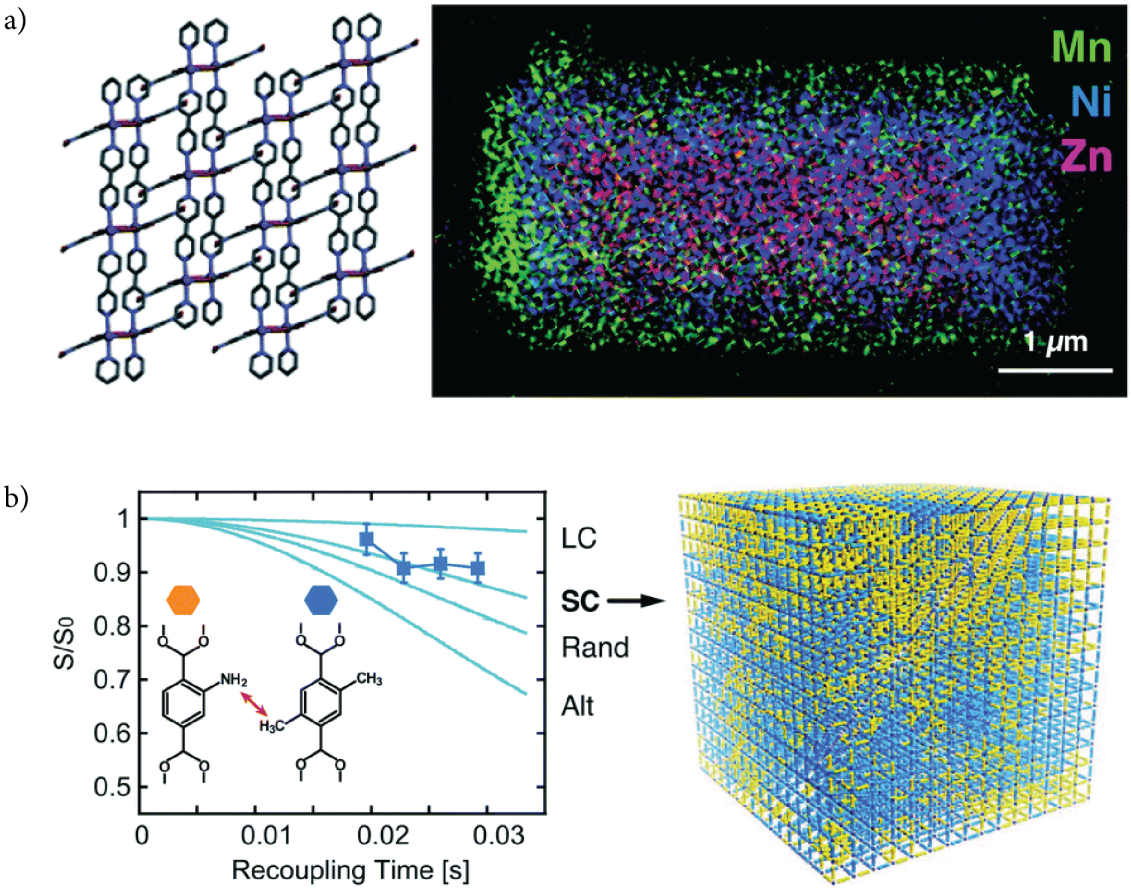

Figure 6.4: Determining compositional correlations in compositionally disordered MOFs Pt. I. (a) Scanning transmission electron microscopy–energy dispersive X-ray (STEM-EDX) images of transition-metal segregation in the mixed-metal Zn/Ni/MnCID-5 ⊃ G MOF (CID = a coordination polymer with an interdigitated structure). (b) REDOR-NMR decay curves are sensitive to the degree of clustering/anticlustering of individual linkers in mixed-linker MOFs (LC = large clusters, SC = small clusters, Alt = alternating). Figure in (a) adapted from Ref. 384 with permission from ACS and figure (b) from Ref. 381 with permission from AAAS.

are thermodynamic considerations at play too; a comprehensive DFT study has highlighted the dual roles of charge distribution and size-mismatch in determining the balance between mixing and segregation [386, 387]. Such considerations may rationalise the preferential formation of $CeZr_5$ clusters in mixed-Ce/Zr UiO-66 samples, as evidenced by EXAFS measurements and as implicated in their catalytic behaviour [388].

In addition to DFT calculations and EXAFS measurements, a variety of techniques offer sensitivity to the spatial distribution of components in compositionally disordered MOFs. Electron microscopy allows direct visualisation of compositional gradients on the micron scale (Fig. 6.4a); so too does fluorescence imaging microscopy [389]. Even peak asymmetry in synchrotron PXRD measurements has some indirect sensitivity to this microstructure [390]. Rotational-echo double-resonance (REDOR) NMR measurements are sensitive to the through-space distance between nuclear spins; by selective labelling of different linkers it is possible to differentiate random, clustered and anti-clustered mixed-linker arrangements on the unit-cell lengthscale. A particularly elegant REDOR-NMR study of the MTV MOF-5 family showed how different linker mixtures favoured different substitutional correlation types (Fig. 6.4b) [381]. Very recently, atom probe tomography (APT) has even been used to 'sequence' metals in mixed-metal MOF-74 rods (Fig. 6.5a), demonstrating that both random and correlated sequence types emerge naturally from different metal combinations and synthesis temperatures [391]. While both REDOR-NMR and APT provide very detailed information, they are nonetheless demanding techniques. By contrast, Sapnik *et. al* have found that humble infrared spectroscopy can offer a surprisingly straightforward measure of cation distributions in mixed-metal MOFs and coordination polymers (Fig. 6.5b) [392].

Just as enzymes derive their function from the precise spatial arrangement of different components — *e.g.* through the amino-acids of their protein backbone — the vision with compositionally complex MOFs has always been one of controlling heterogeneity to optimise a particular chemical or physical property [340]. A simple but effective example is the recent demonstration of correlation-dependent photocatalysis in a mixed-linker UiO-68 derivative [393]. As demonstrated in Chapter 1,

this vision is not unique to the MOF field: indeed, conventional solid-state chemistry has long exploited the use of solid solutions and inhomogeneity in this general way. The example of relaxor ferroelectrics such as PMN demonstrate this point where the structural complexity responsible for their useful dielectric properties emerges naturally from an interplay between composition and lattice geometry [11]. The design rules developed to control complexity in these inorganic materials may yet have a role to play in MOF science [7].

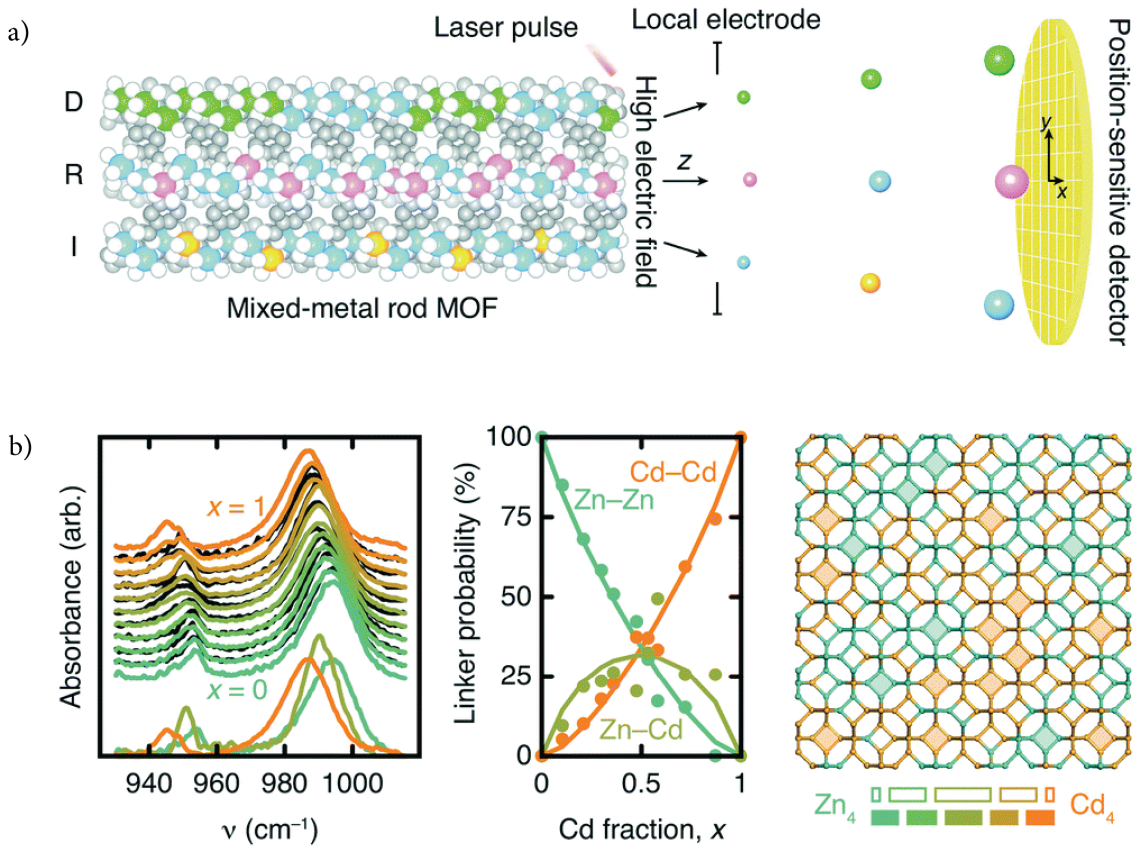

Figure 6.5: Determining compositional correlations in compositionally disordered MOFs Pt. II. (a) APT allows the sequencing of metal-oxide rods in multivariate MOF-74 [391]. Here the method is shown to differentiate 'duplicate' (D), random (R), and 'insertion' (I) sequences. (b) The in-plane mIm stretching region of the IR spectra of mixed-metal (Zn/Cd) ZIF-8 derivatives is sensitive to the relative populations of Zn–mIm–Zn, Zn–mIm–Cd and Cd–mIm–Cd linkages. These populations can be extracted using non-negative matrix factorisation and used to derive models of the Zn/Cd distribution, which is found to involve clustering [392]. Note the greater-than-statistical population of Zn_4/Cd_4 four-rings (experimental Zn_nCd_{4-n} populations as solid bars; statistical populations as open bars). Figure in (a) adapted from Ref. 391 with permission from AAAS and figure (b) from 392 with permission from the RSC.

6.4 Orientational disorder

Whenever the nodes or linkers of a MOF have lower point symmetry than that of the corresponding site in the MOF lattice, the issue of orientational disorder arises [7, 393]. A longstanding example is that of the IRMOF series, where orientational disorder follows from asymmetric substitution of terephthalate linkers [112]. Because the pores of MOFs are surrounded by multiple neighbouring linkers, the chemical and physical pore environments are affected by the presence or absence of correlations in linker orientations. Hence the distinction between random and correlated disorder in such systems may be crucial for interpreting a variety of host/guest phenomena. Such is the case in the CAU-1 (CAU = Christian-Albrechts University) family, for example, for which hyperpolarised ^{129}Xe NMR spectroscopy has been used to identify correlations in side-chain orientations, in turn reflected in the experimental Ar sorption isotherms [394]. So too in the IRMOF-3-AMPh system (AMPh = a phenylamide substituent), where linker orientations can be ordered or disordered according to a clever choice of synthesis approach; the two polymorphs have profoundly different H_2 sorption profiles (Fig. 6.6a) [395].

Just as linker orientations influence pore chemistry, so is it that guest adsorption can affect the correlations in linker orientations. Perhaps the clearest example in a disordered MOF is found in DUT-8(Ni), a pillared paddle-wheel MOF with 2,6-ndc linkers [396]. The origin of disorder in this system is the existence of two degenerate 2,6-ndc orientations [397]. Each orientation introduces an offset — either up or down — in the positions of the neighbouring paddlewheel pillars. Since the lozenge-shaped pores of DUT-8(Ni) are flanked by four 2,6-ndc linkers, there is a natural constraint that two must step up and two step down — after all, the total offset on traversing a loop around the pore must vanish to zero [393]. The six possible 2,6-ndc arrangements satisfying this rule partition into a set of four with a C_{2v}-symmetric pore structure, and a set of two with a D_{2d} pores. Neighbouring pores share edges, such that a large and complex configurational landscape emerges, characterised by different spatial arrangements of pore geometries [338]. Remarkably, the adsorption and desorption of different solvent molecules drives the system reversibly across

this landscape — the strength of host/guest interactions overcoming the $\sim$ 20 kJ mol^{-1} barrier to 2,6-ndc 'flips' (Fig. 6.6b). The recent development of efficient and accurate MOF force fields [353, 354] may allow computational insight into the mechanism for this unusual disorder–disorder switching.

The extent to which orientational disorder is static or dynamic depends on the reorientation barrier height, and if this barrier is commensurate with the available thermal energy then one expects to observe an order/disorder transition [7]. There are plenty of examples in the literature, but we focus here on the case of the hybrid perovskite $[NPr_4][Mn(N(CN)_2)_3]$ — not technically a MOF but relevant nonetheless because its MOF-like framework structure exhibits a particularly useful barocaloric effect exploitable in solid-state cooling [398]. The conformations of the flexible $[NPr_4]^+$ extra-framework cations and orientations of the dicyanamide linkers couple:

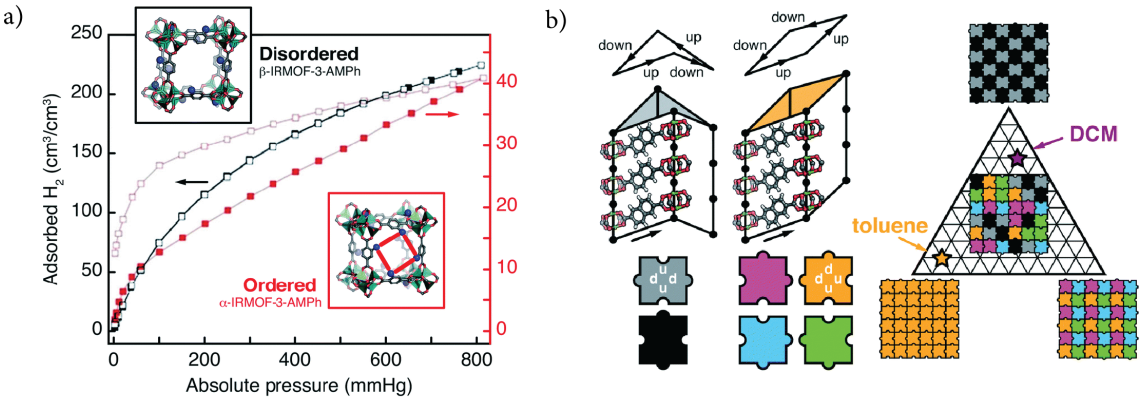

Figure 6.6: Orientational disorder in MOFs. (a) The α- and β-polymorphs of the substituted MOF-5 derivative IRMOF-3-AMPh have different linker orientation correlations and H_2 (de)sorption profiles. Using the fully substituted AMPh-terephthalate linker during MOF synthesis gives the ordered α phase, with reduced and hysteretic H_2 uptake is sorption profile. By contrast, post-synthetic modification of an aminoterephthalate MOF-5 derivative gives the disordered β phase, which has a greater accessible pore volume. (b) In the pillared MOF DUT-8(Ni), naphthalenedicarboxylate linkers introduce a 'step-up'/'step-down' between neighbouring columns (exaggerated for effect here). There are six feasible 2,6-ndc arrangements — *i.e.* two steps up and two steps down — around the lozenge-shaped pores. These arrangements give pores with either D_{2d} or C_{2v} point symmetry (greyscale and coloured tiles, respectively) that propagate according to a set of simple rules (jigsaw pairings shown here). Different guest molecules have different affinities for these two pore geometries, which allows a guest-induced transition between complex phases; for example, toluene and DCM favour configurations with C_{2v}- and D_{2d}-rich pore geometries, respectively. Figure (a) adapted from Ref. 395 with permission from the RSC and figure (b) from Ref. 338 with permission from Springer Nature.

they are disordered at temperatures above 331 K and ordered below. The transition between the two states is accompanied by a large change in both entropy and volume. The latter confers sensitivity to pressure — the disordered state can be re-ordered by squeezing, which is the basis for a barocaloric heating/cooling cycle (Fig. 6.7) [399]. Correlations within the disordered state, although still poorly understood, influence the barocaloric entropy change and reduce the critical pressure needed for each cooling cycle [7, 398]. In the parallel field of magnetocalorics — based on the order and disorder of magnetic spins—correlated disorder and the geometric frustration from which it arises are well-known to increase cooling efficiency [400–402]. We therefore anticipate that similar design principles will prove valuable in exploiting orientational disorder in hybrid frameworks and MOFs alike.

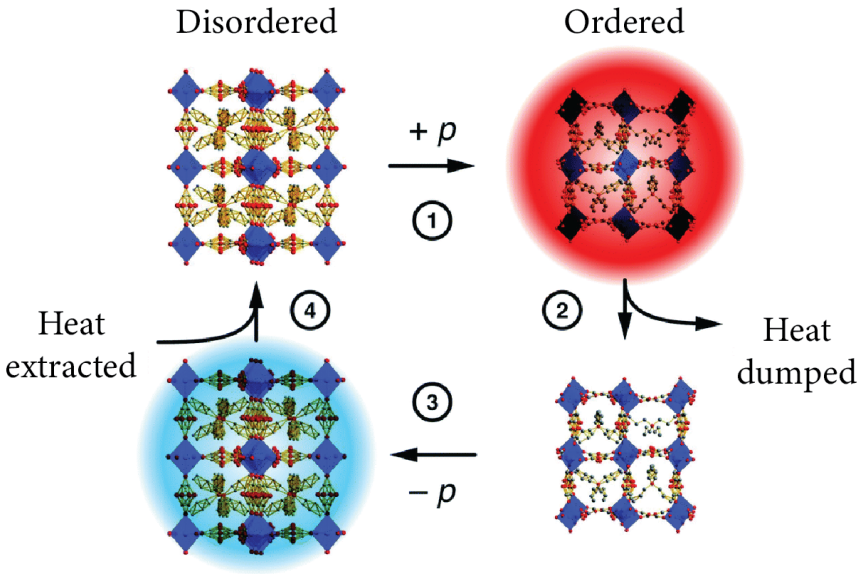

Figure 6.7: A simple barocaloric cooling strategy that exploits the pressure-dependence of the order/disorder transition in $[NPr_4][Mn(N(CN)_2)_3]$. Starting at ambient conditions where the system is orientationally disordered (top left), ordering is induced by (1) application of pressure (note the change in unit cell dimensions is exaggerated here for effect). The loss of configurational entropy results in heating, and this excess heat (2) is dumped to the environment. (3) Removing the applied pressure forces the system to disorder; the concomitant increase in entropy now requires the system to cool. The cold solid (4) extracts heat from its environment. Figure adapted from Ref. 398 with permission from Springer Nature.

6.5 Conclusions and outlook

As such, MOFs are fundamentally predisposed to correlated disorder. On the one hand, they have many compositional and configurational degrees of freedom [403] — so there will always be a strong entropic driving force for disordered states [404]. And, on the other hand, interactions between neighbouring nodes, or neighbouring linkers, or between host and guest are rarely negligible, such that disorder is unlikely to be random. Sometimes this distinction between random and correlated disorder will be unimportant; however, as highlighted in this chapter, in some cases MOFs exhibit physical and chemical properties for which the distinction is crucial.

An historical barrier to studying and exploiting correlated disorder in MOFs has been the apparent insensitivity of experimental techniques to its presence and nature: conventional crystallography is the obvious culprit here. But there are now many different experimental and computational tools available with the relevant capabilities. The hurdle that unquestionably remains is that of developing rigorous strategies for exercising synthetic control over correlated disorder. The interplay between composition and network geometry is a potential mechanism for driving very specific types of correlated disordered states, as well as local-symmetry lowering, which is the approach adapted in this thesis. The balance of kinetic and thermodynamic control during synthesis is clearly also to be decisive in many cases.

Looking forward, the field shares much of its aims with those of MTV-MOF chemistry [120, 383]. Ultimately, correlated disorder is a form of structural complexity that might be exploited in *e.g.* catalysis, information storage or selective host/guest chemistry [340, 393]. An intriguing recent development along similar lines is the concept of using correlated disordered states as intermediates in materials synthesis to target low-dimensional phases [405]. Notably, there is possible additional importance of different types of correlated disorder in MOFs to those outlined here — involving *e.g.* frustrated magnetism [402], local charge ordering [406], or cooperative spin-state transitions [407]. Clearly, there is enormous potential in combining the unconventional physics of correlated disordered states with the scope for exquisite control over geometry for which MOFs are renowned.

Chapter 7

TRUMOF-1: an atomic-scale realisation of a Truchet-tiling

7.1 Summary and acknowledgements

As indicated by partial occupancies of the 1,3-bdc linker atoms, the average structure of TRUMOF-1 — as described in Chapter 3 — does not represent its real, local structure. In this chapter we will come to show that the local structure of TRUMOF-1 is correlated disordered, as derived from sensible chemical rules and drawing an analogy to MOF-5. We will also highlight some of the physical and chemical properties of TRUMOF-1, such as gas adsorption and behaviour under high-pressure.

The first section of this chapter focuses on solving the pore structure of TRUMOF-1. This was achieved by building a model based on Truchet tiles, which, as highlighted in Chapter 1, is a valuable approach in understanding complex, aperiodic structures. This model was successfully validated by comparing experimental data — diffuse scattering, 3D-ΔPDF, and atomic displacement parameters — to those calculated from geometry optimised approximants.

This Truchet-tile model confirms the complex, maze-like pore network of TRUMOF-1. To further investigate the impact of the aperiodic connectivity of TRUMOF-1 on its physical properties, high-pressure crystallography experiments were performed. Results are highlighted in the final section of this chapter, and indicate TRUMOF-1 to be remarkably soft yet stable. This unusual relationship is caused by the irregular connectivity enabling heterogeneous internal reorganisations.

Ultimately, TRUMOF-1 is the first atomic realisation of a Truchet tiling to be reported. However there is no reason to expect it is the only one; suitable symmetry lowering of inorganic or organic building blocks should allow for other TRUMOFs

to be obtained.

I am grateful to Lisa Cameron, Hunter Windsor, David Dharma, and Cameron J. Kepert for their help with solving the average structure of TRUMOF-1, Ella M. Schmidt and Arianna Minelli for their help in measuring and interpreting the X-ray diffuse scattering data, Ella M. Schmidt for her help in developing the Truchet-tile model, Lisa J. Cameron, A. Dave Dharma, and Cameron J. Kepert for their help in performing and analysing gas adsorption measurements, Giovanni O. Lepore for his in help in performing and analysing the EXAFS measurements, and finally Tom Pope and Ben Slater for performing DFT and GCMC calculations.

7.2 Chemical and physical properties

As described in Chapter 3, the average structure of TRUMOF-1 is disordered. Crystallising in $F\bar{4}3m$, its unit cell includes OZn_4 clusters positioned both at the corners and face centres of the cell, which in turn are connected by (apparently) trigonally-symmetric linker molecules, of which the benzene C and carboxylate C/O atoms are only partly occupied at 0.70(4) and 0.46(3), respectively (Fig. 3.3). These partial occupancies, together with NMR data confirming the presence of 1,3-bdc rather than 1,3,5-btc, imply a crystal composition of $[OZn_4][1,3\text{-bdc}]_{2.8(2)}$, which is near the idealised composition of $[OZn_4][1,3\text{-bdc}]_3$.

Hence, TRUMOF-1 appears to have an identical chemical composition to that of MOF-5 *i.e.* $[OZn_4][1,4\text{-bdc}]_3$. As further evidence in support of this assertion, the chemical environments of both TRUMOF-1 and MOF-5 were probed by means of IR- and Raman spectroscopy, as well as Zn K-edge EXAFS. Results are presented in Fig. 7.1a-c. For all techniques, similar features were observed in data from the two crystal samples. Most striking is the agreement of the EXAFS data; Pearson correlation coefficients [258] were calculated as 0.996 (Table C2.50), thus confirming very high similarities. Hence, the EXAFS data measured for MOF-5 and TRUMOF-1 are essentially indistinguishable, indicating that in these two materials, the Zn atoms are in the same local environments. This is in agreement with the average unit cell of TRUMOF-1, being that the OZn_4 cluster appears ordered and fully occupied, in

turn surrounded by 12 carboxylate anion sites, each occupied with 50% probability, thus indicating a connectivity of 6. This is in agreement with the octahedral Zn SBU of MOF-5.

To further investigate this similarity in chemical environment, the thermal stability of both TRUMOF-1 and MOF-5 was probed by TGA (Fig. 7.1d). The data obtained for both samples reflect four distinct temperature regimes. First, up to about 100 °C, there is a small degree of mass loss associated with loss of

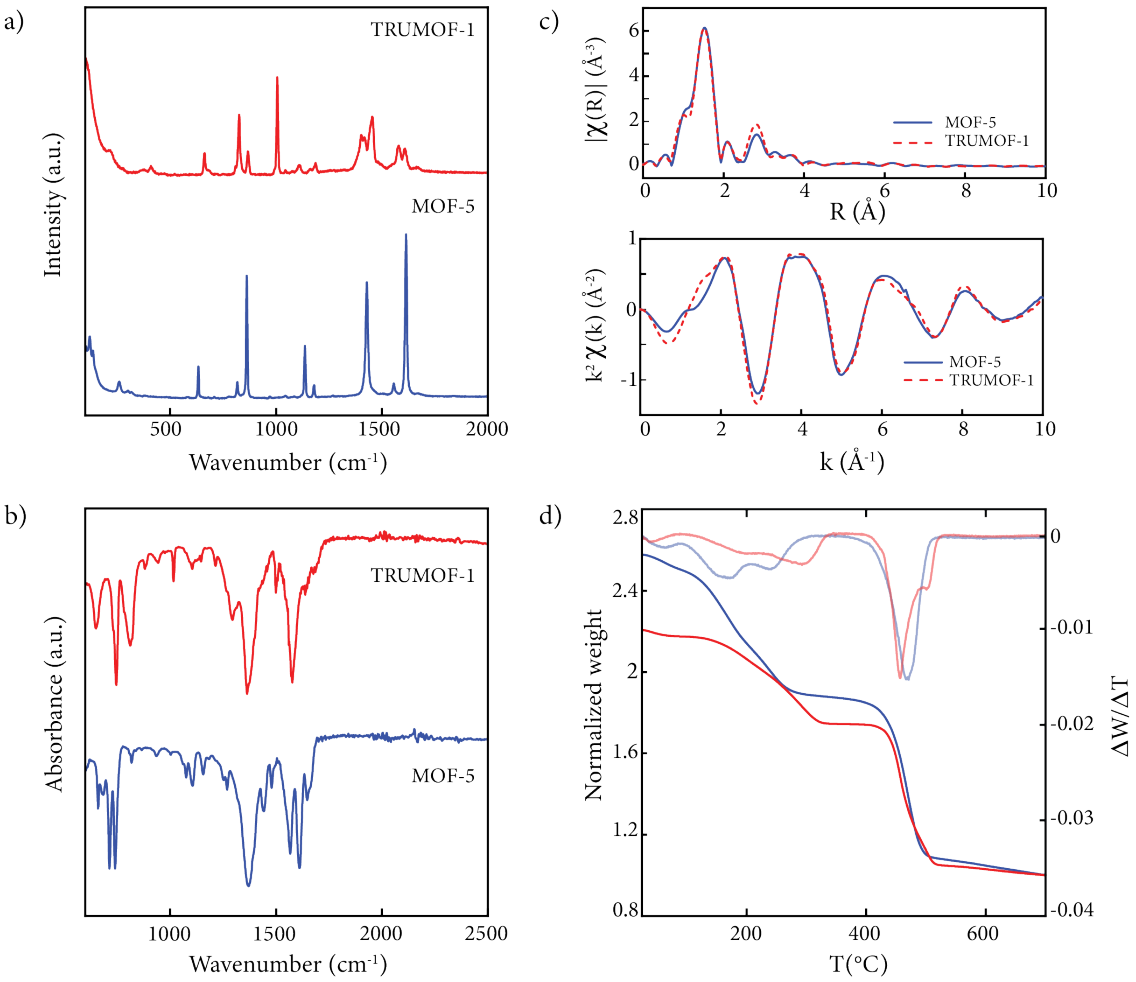

Figure 7.1: Characterisation of chemical properties of TRUMOF-1. (a) Raman spectra of TRUMOF-1 (red) and MOF-5 (blue). (b) IR spectra of TRUMOF-1 (red) and MOF-5 (blue). (c) Zn K-edge EXAFS measurements and derived functions: (top) The real component of the EXAFS Fourier transform, which shows similar features for both MOF-5 and TRUMOF-1. (bottom) The original EXAFS signal from which these Fourier transforms were obtained. (d) TGA measurements of TRUMOF-1 (red) and MOF-5 (blue). The upper traces give the thermal derivative of the relative mass changes, which help identify the temperatures at which desorption/decomposition mechanisms switch.

surface-bound solvent. Subsequently, over the temperature range 100–300 °C, there is a gradual loss of adsorbed solvent to give the evacuated MOF. This regime is followed by a plateau that extends up until about 400 °C corresponding to the stability window of the evacuated frameworks. Thereafter, the organic components of the frameworks decompose. The decomposition temperatures for TRUMOF-1 and MOF-5 are similar, thus further supporting the similarity in chemical environments.

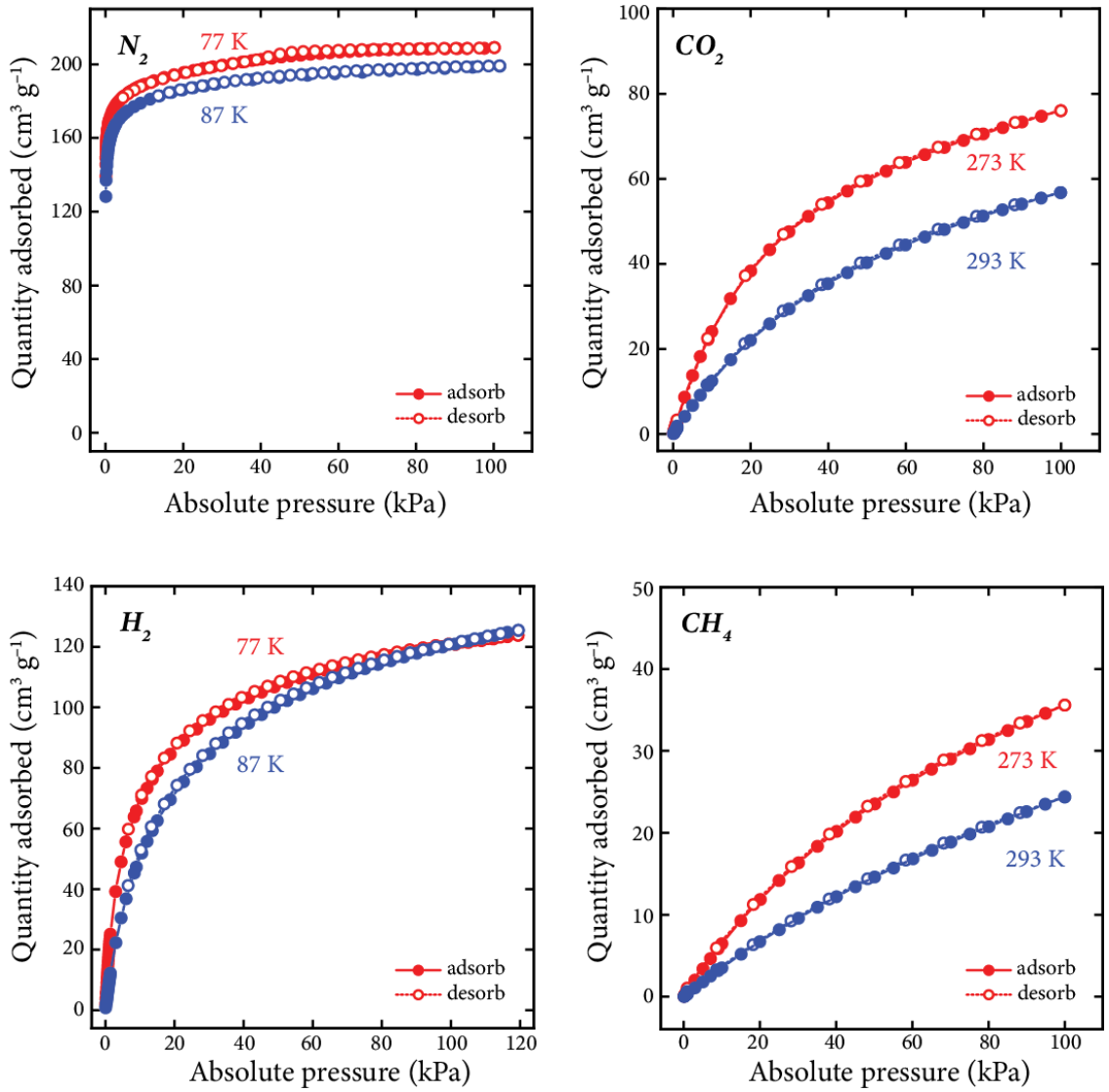

Figure 7.2: Adsorption and desorption isotherms of TRUMOF-1 with N_2, CO_2, H_2 and CH_4 gases at two different temperatures. Quantities represent $cm^3\ g^{-1}$ uptake of each gas at standard temperature and pressure. The higher and lower temperature data are presented in blue and red, respectively.

Of course, an important property of MOFs is their high porosity, as characterised by a high surface area. MOF-5 is no exception to this trend, exhibiting a surface area of ∼2900 m^2g^{-1} [88]. Notably, this property is more related to the pore network (*i.e.* structure) of a MOF, rather than to its chemical composition. Therefore if the connectivity of TRUMOF-1 is significantly different to that of MOF-5, this should be reflected by its sorption behaviour. As such, TRUMOF-1 was exposed to N_2, CO_2, H_2, and CH_4 gas at a range of different temperatures (Fig. 7.2). Based on the adsorption of N_2 gas, the BET surface area was calculated at 765 m^2 g^{-1}. Thus, TRUMOF-1 is porous — therefore officially categorised as a MOF [408] — and has a significantly lower surface area than MOF-5. Furthermore, its adsorption enthalpies are about twice as large (Table 7.1, Fig. C3.9), indicating it is harder to remove adsorbed gas from TRUMOF-1. Based on both observations, it is anticipated that, compared to MOF-5, the network of TRUMOF-1 consists of smaller pores or possesses a higher curvature; possibly a combination of both.

Our results so far establish that TRUMOF-1 behaves as a conventional MOF [408]. Yet, its average structure is rather unusual, being that the partial occupancies of linker atoms indicate that its connectivity is disordered. Adsorption data provides further information on its structure: the relatively high adsorption enthalpy suggests that it is more difficult to remove guests from its network compared to MOF-5. In turn, since TRUMOF-1 has an identical chemical composition to that of MOF-5, this suggests that the pore network of TRUMOF-1 is less open, possibly due to smaller cavities or a higher tortuosity.

Table 7.1: Heat of adsorption (kJ mol^{-1}) of various gases in TRUMOF-1 (experimental) and MOF-5 (literature)

MOF	H_2	CO_2	CH_4
TRUMOF-1	7.2	26.7	21.8
MOF-5	3.8 [409]	–	12.6 [410]

7.3 Building the structural model

7.3.1 Truchet tile mapping

Of course, the question arises: how do we approach this, exactly? Let us start with a breakdown of what we know about the local structure. The [OZn_4] cluster positions are ordered, and thus translate periodically. Their connectivity through 1,3-bdc, however, is disordered, as permitted through the lower symmetry of the linker introducing orientational degrees of freedom. As a consequence, the connectivity of TRUMOF-1 ought to be aperiodic. As highlighted in Chapter 1, such complexity may be better understood by relating the system to aperiodic tilings, as is the case of quasicrystals and Penrose tilings [62, 63]. Of course, neither Penrose nor Einstein

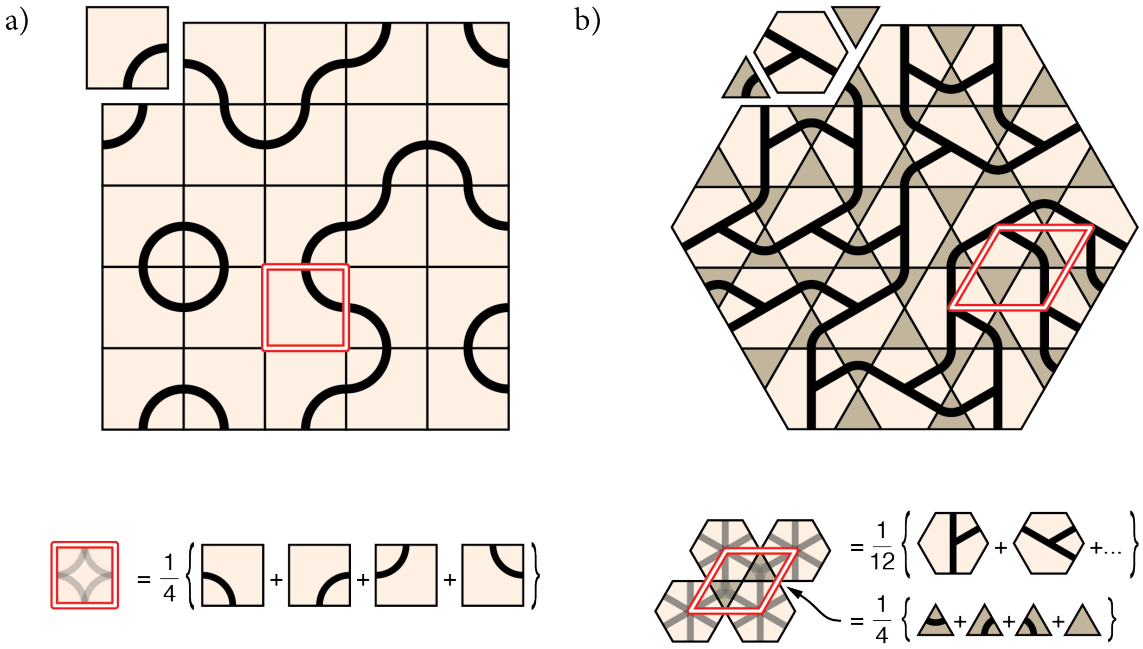

Figure 7.3: Representative Truchet tilings. (a) Decorating square tiles with a single arc can generate Truchet tilings with curved paths. The positions of the square tiles are translationally periodic, but the continuous pattern produced by the arc decorations is aperiodic. Projecting any such tiling onto the underlying unit cell (shown in red) gives an average structure with partial occupancies. For large systems, one expects equal occupancies of each of the four possible arc orientations. (b) More-complex Truchet tilings can be generated using a combination of different decorated and undecorated tiles. In this particular example, based on the hexagonal tiling of the plane, the connected path of line decorations forms a single percolating network that spans the entire system.

tilings apply here, as the system does not exhibit 5- or 10-fold symmetry nor can be described by just one low-symmetry tile. Instead, the natural chemical connectivity of the cluster (*i.e.* 6) and 1,3-bdc linker (*i.e.* 2) describe matching rules of the kind found in Truchet tilings. Moreover, the cluster and linker sites are periodic, as are the tile positions in Truchet tilings. To help illustrate the mapping, we consider two sets of 2D correlated disordered Truchet tilings, which can be described with an average 'unit cell', as derived from projecting all orientations onto the same tile (Fig. 7.3).

For the first example, square tiles were decorated with a single arc, giving rise to four different orientations (Fig. 7.3a). By arranging these tiles so that the arc decoration continues to the next tile, a Truchet tiling with curved paths was created. As such, the translation of the tile orientations is aperiodic, yet each is influenced by the orientation of its neighbour. Note that the tiling, although aperiodic, generates a uniformly 2-connected set of paths.

The second example is more complicated. Here we use two tile shapes — hexagons and triangles — and decorate these in a way that lowers their symmetry. We also leave one triangle entirely undecorated. In this context of a MOF, the two tiles might be associated with node and linker SBUs. Again the natural matching rules result in an aperiodic network that is uniform on the local scale.

Yet of course, the structure of TRUMOF-1 propagates in space and therefore does not map onto the 2D Truchet tiling in Fig. 7.3b. Therefore, in order to solve its local structure, a 3D Truchet tile needs to be realised. To do so, the average structure of TRUMOF-1 was redefined in terms of 3D space-filling tiles by performing a Voronoi decomposition using the average cluster and ligand positions as mid-points (Fig. 7.4a). The two tile shapes so produced — a cube and a trigonal bipyramid — fill 3D-space when placed on the TRUMOF-1 cluster and ligand sites, respectively. Note that the trigonal bipyramids pack such that any four combine to form a cube. Any MOF can be similarly decomposed using this approach — the Voronoi decomposition of MOF-5 is given in Fig. 7.4b as an example.

Now the shapes of the 3D-tiles are established, their decorations have to be determined through the interpretation of the average crystal structure. The decoration of the trigonal bipyramid, which corresponds to volume surrounding the ligand site, has already been nicely described by the 2D example in Fig. 7.3b. Namely, the crystallographic model represents an average over three equally-populated orientations of the 1,3-bdc linker (Fig. 7.4c). The emergence of an apparently threefold-symmetric

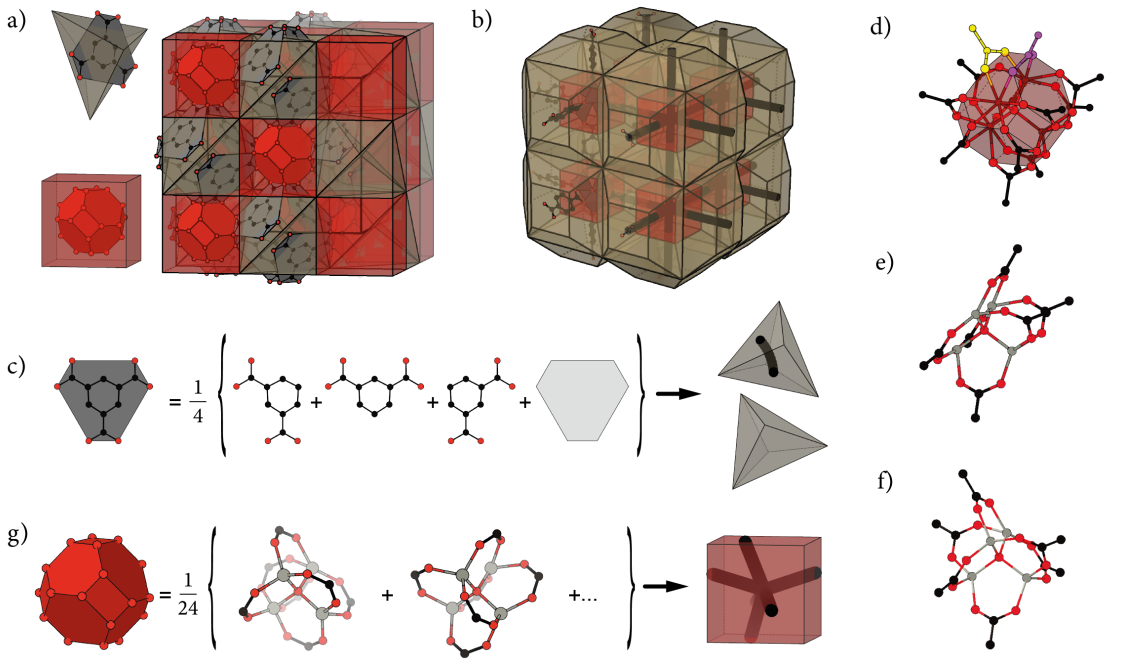

Figure 7.4: Building a 3D Truchet tiling that maps onto the structure of TRUMOF-1. (a) Representation of the average structure of TRUMOF-1 in terms of its underlying tiling. There are two different tiles: one decorated with the OZn_4-centered clusters (red cubes), and the other with the trigonally symmetric ligand (grey trigonal bipyramids). Note that the trigonal bipyramids pack such that any four combine to form a cube of the same dimensions as the red cluster cube. (b) Representation of the structure of MOF-5 in terms of its underlying tiling for comparison against TRUMOF-1. (c) Interpretation of the crystallographic model at the ligand site in terms of a configurational average over three 1,3-bdc orientations and 25% linker vacancies. The corresponding 3D Truchet tiles are given on the right. (d) Inorganic cluster surrounded by 12 partially-occupied carboxylate sites that partition into six pairs. These pairs are too close to one another to be occupied simultaneously; *e.g.* only one of the yellow- and purple-coloured sites might be occupied at any one time. (e) Even within this constraint, some carboxylate decorations give unfeasibly distorted cluster geometries and so are excluded. (f) The cluster decoration that disposes carboxylates as uniformly as possible. (g) Final interpretation of the inorganic cluster as an average over 24 octahedral cluster orientations. The corresponding 3D Truchet tile is given on the right. Colour scheme is as follows: C = black spheres, O = red spheres, Zn = grey spheres and H atoms are omitted for clarity.

ligand results from the crystallographic site having higher point symmetry than the linker itself. To give the chemically sensible stoichiometry $[OZn_4][1,3\text{-bdc}]_3$, the site must also be vacant with 25% probability; note that this value is consistent with the observed site occupancies. Accordingly, three quarters of the trigonal bipyramids are decorated by an arc that reflects the bent linking geometry of a 1,3-bdc molecule. The remaining quarter of the trigonal bipyramidal tiles are left undecorated.

For the cluster site, from both the atom occupancies and the EXAFS measurements, it was established that each OZn_4 unit must coordinate exactly six dicarboxylates. In principle, there are $C(12,6) = 924$ ways of occupying six of the 12 dicarboxylate sites around each cluster. However, many of these possibilities involve unphysically close O–O contacts and need not be considered. For example, the 12 sites divide into 6 pairs disposed along the $\langle 100 \rangle$ directions (Fig. 7.4d). The O–O distances within pairs are so small that only one of each pair might be occupied at any one time, reducing the number of possibilities to $2^6 = 64$. Even amongst these 64 local configurations there are cases with unfeasible geometries (Fig. 7.4e), which are therefore excluded. The decoration that maximises the O–O contact distances is approximately, but not exactly, octahedral *i.e.* 'pseudo-octahedral' (Fig. 7.4f). This maximally-distributed configuration has trivial point symmetry and so there are 24 equivalent carboxylate decorations with this same local geometry (this being the ratio of the orders of the crystallographic $\bar{4}3m$ point symmetry at the cluster site and the cluster point symmetry) (Fig. 7.4g). Accordingly, the cubic tiles are decorated with a pseudo-octahedral arrangement of rods that capture the arrangement of carboxylate substituents around each OZn_4 cluster.

Now, a local representation of TRUMOF-1 can be realised by arranging the low-symmetry decorated tiles such that a continuous network result. This shows that, as expected purely on geometric grounds, the various partial site occupancies are strongly correlated because the orientation of a given cluster decoration places strong constraints on which neighbouring 1,3-bdc linkers are present and in which possible orientations they could lie [7, 338]. The next section will describe how such models were realised using a custom MC code, followed by geometry optimisation using DFT.

7.3.2 Monte Carlo algorithm

In agreement with the 24 cubic tile decorations, the MC algorithm assigned cluster geometry orientations as a 24-states Potts variable [411]; these are the fundamental degrees of freedom. Initially, each cluster site in an appropriately-chosen supercell (*e.g.* 2×2×2) was assigned randomly one of the 24 equivalent states, with the corresponding carboxylate sites occupied accordingly. The initial MC energy was determined by cycling through the 1,3-bdc linker sites and counting the number of occupied carboxylate ligands converging on that site. If this number were 0 or 2, then the corresponding energy term was zero: the former case allows for a linker vacancy, and the latter can always be accommodated by a 1,3-bdc linker in a suitable orientation. By contrast, if either 1 or all 3 carboxylate sites were occupied, then the energy was incremented by 1 — there being no way of arranging 1,3-bdc linkers to give this carboxylate occupancy. Defined in this way, the total MC energy is zero if and only if the cluster decorations are consistent with 75% occupancy of the linker sites by 1,3-bdc molecules. The system was driven towards this ground state by repeatedly choosing different cluster orientations as the MC move, and by using simulated annealing to gradually tighten the MC acceptance criterion until the system energy converged to zero.

The final stage in the approximant generation was to allow the configuration to relax into a state with idealised $[OZn_4][OOCR]_6$ node geometries. Starting from one of our MC configurations, the 1,3-bdc molecules and $[OZn_4]$ clusters were treated as rigid bodies with translational and rotational degrees of freedom. A new MC energy could now be defined based on the squared distance between carboxylate oxygen positions and the 'ideal' positions for the corresponding OZn_4 cluster. Again, a simulated annealing approach was used to relax the configuration, proposing and rejecting small rigid-body translations and rotations of both 1,3-bdc and OZn_4 units in each MC loop. An additional closest-approach constraint was used to ensure that no atom positions overlapped. Note that the framework connectivity remained hardwired from the initial MC process.

7.3.3 Geometry optimisation

Next, to test whether our MC model and thus Truchet-tile description of TRUMOF-1 is physically reasonable, a series of *ab initio* DFT calculations were performed on the MC generated representations described above. The approach was to calculate the geometry and cell optimised 0 K energies of periodic realisations ("approximants") [412] of the MC simulated system with increasingly large unit cells so as to understand the underlying energetic landscape. There were only three symmetry-distinct 1×1×1 approximants — that is, with unit cells commensurate with the ∼15 Å^3 cell of the average structure. Each relaxed to give a sensible structure, with ten distinct realisations giving equilibrium energies within a few kilojoules per mole of Zn of one another (Fig. 7.5a).

The number of possible configurations grew very quickly with system size. For the 2×2×2 case (32 formula units; 1696 atoms), there were too many possibilities to enumerate; hence we focused on 20 representative realisations, one of which is shown in Fig. 7.5b. These larger configurations span a wider range of energies and have more open structures (Fig. 7.5a); the range of observed unit-cell volumes

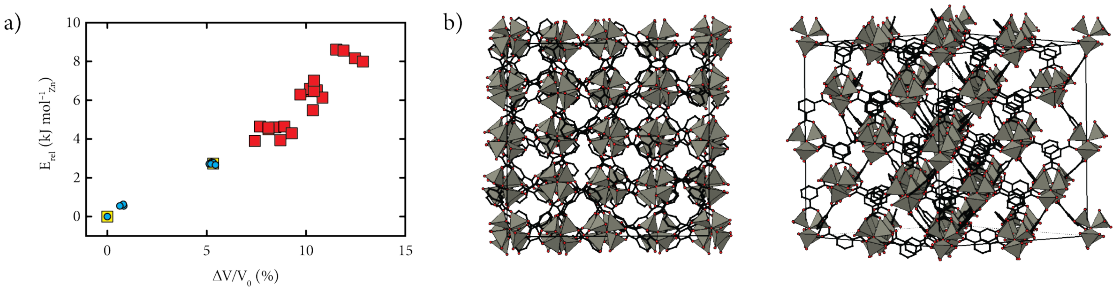

Figure 7.5: Results from DFT geometry optimisation of the MC representations of TRUMOF-1. (a) The relative lattice energies of different 1×1×1 (blue circles) and 2×2×2 (red squares) approximants are within a few kJ mol^{-1} of one another. Also included are the energies for geometry-optimized 2×2×2 supercells of two representative 1×1×1 approximants (yellow squares). The more disordered configurations are those at higher energy, for which the molar volume is largest. (b) Representations of the geometry-optimised structure of one 2×2×2 TRUMOF-1 approximant, viewed down [100] (left panel) and approximately [110] (right panel) crystal axes. Colour scheme is as follows: Zn = grey tetrahedra, O = black spheres, and C = red spheres and H atoms are omitted for clarity.

is characteristic of flexible MOF structures [194]. Since the enthalpic differences amongst these periodic TRUMOF-1 approximants is commensurate with solvent binding enthalpies in zinc carboxylate MOFs (*e.g.* MOF-5) [413, 414], guest inclusion may reduce the spread of energies in practice, because loading would be higher in the less dense realisations. Hence, it can be concluded that the configurational landscape accessible to TRUMOF-1 spanning different Truchet-tile arrangements involves many thermally accessible minima.

7.3.4 The final model

Now, we can visualise the local structure of TRUMOF-1 both as a 3D Truchet tile and a 1×1×1 approximant cell. This shows that any combination of orientations of the two Truchet tiles — alternating on their respective sites — that produces a connected network, relates to a model of 1,3-bdc-linked OZn_4 clusters in which each cluster is octahedrally coordinated by six 1,3-bdc linkers and each 1,3-bdc linker connects exactly two clusters. There are infinitely many such networks; one simple example is shown in Fig. 7.6.

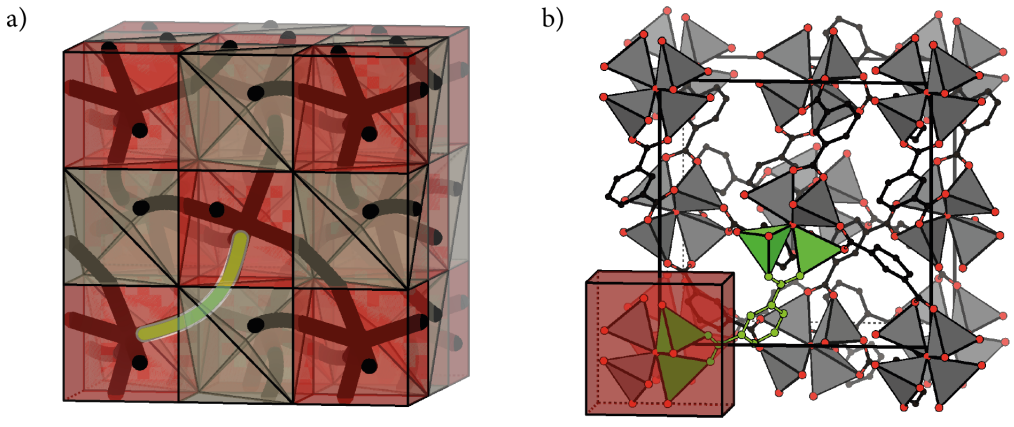

Figure 7.6: The local crystal structure of TRUMOF-1 represented as a (a) 3D Truchet tiling and a (b) 1×1×1 cell with atoms. The relation between the SBU and the cubic Truchet tile is emphasised for one metal cluster; likewise, the connectivity between two clusters in the foreground and the corresponding link in the related Truchet tiling are highlighted in green. Colour scheme is as follows: C = black spheres, O = red spheres, Zn = grey polyhedra and H atoms are omitted for clarity.

7.4 Model validation

Whilst DFT confirms the models to be physically reasonable, it needs to be validated whether they accurately represent the real, local structure of TRUMOF-1. This is the final step of solving the crystal structure of TRUMOF-1, as realised by comparing simulated to experimental data.

7.4.1 Single crystal diffuse scattering

As mentioned throughout this thesis, the experimental measurement with greatest sensitivity to structural disorder and its correlation in crystalline materials, is single-crystal diffuse scattering [240]. Accordingly, single-crystal X-ray diffuse scattering measurements of evacuated TRUMOF-1 crystals were collected as outlined in Chapter 2.

Datasets collected at short exposure times did not show any diffuse scattering at all (Fig. 7.7, panel I). Hence, an exposure time of 200 s was necessary to observe

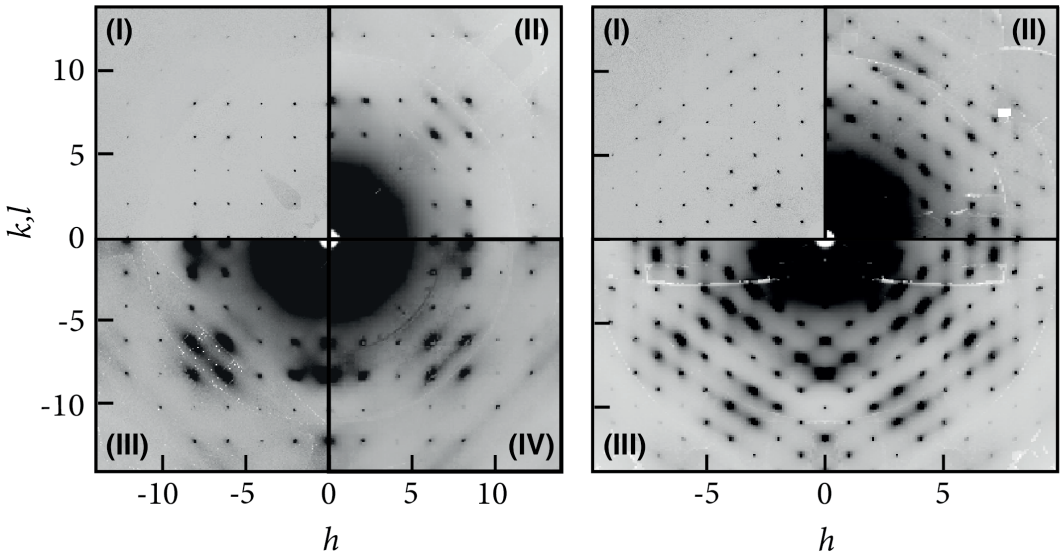

Figure 7.7: Reconstructed and symmetry averaged *hk*0 (left) and *hhl* (right) layers collected from TRUMOF-1 under Cu radiation (I) at 300 K, collecting frames at an exposure time ranging from 0.45 to 2.82 seconds, (II) 300 K, collecting frames at an exposure time of 200 s, (III) soaked with iodine-soaked at 300 K, collecting frames at an exposure time of 200 s, and (IV) soaked with iodine-soaked at 120 K, collecting frames at an exposure time of 200 s. The diffuse ring around the origin in (IV) arises from icing.

the diffuse features presented in Figure 7.7, panel II. The observed diffuse scattering patterns are dominated by transverse-polarised diagonal features. These strike a resemblance to the diffuse scattering observed for the plastic crystal CBr_4 [56–58]; in turn corresponding to correlated displacements of the relaxed metal clusters. Furthermore, the intensity of these features could be increased by soaking the crystals in an iodine–cyclohexane solution (Fig. 7.7, panel III). Performing an identical data collection on the same iodine-soaked crystal at a temperature of 120 K, resulted in a decrease in intensity of the diffuse scattering on the Bragg peaks (Fig. 7.7, panel IV). Yet, the diffuse streaks running through the Bragg peaks on the diagonals, keep their intensity. This lack of a strong temperature-dependence to the scattering confirms this contribution to be attributed predominantly to static displacements, rather than to thermal effects.

The non-iodine incorporated dataset was selected for comparison with the simulated data, as this would most accurately correspond to the non-solvent containing models. To facilitate this comparison, a number of additional steps were performed in the reconstruction of this experimental dataset. Firstly, the crystal orientation as refined with CrysAlisPro [241] was converted using a customised python code to serve as input for the Meerkat2 program [335], with which the dataset was symmetry averaged for $m\bar{3}m$ Laue symmetry and reconstructed on a 3D grid defined by $-20 \leq h,k,l \leq +20$. Secondly, the background caused by scattering from air and/or Paratone-N oil was estimated as a smooth, radially symmetric background function, which in turn was subtracted from the data.

As for the models, total scattering data were calculated by importing the 20 DFT-relaxed 2×2×2 supercell configurations into the DISCUS program [415]. The X-ray scattering was calculated on the Bragg positions of the supercells, with a reciprocal space coverage matching the experiment (*i.e.* $-20 \leq h,k,l \leq +20$). Notably, the DFT-relaxed cells are limited to a size of 2×2×2 unit cells. Hence to mimic the distribution of configurations in a crystal, the 20 calculated diffraction patterns were averaged. The output was subsequently averaged again for $m\bar{3}m$ Laue symmetry, using Meerkat2 [335]. Finally, the calculated diffuse scattering was resampled to a finer reciprocal space grid using the Lanczos resampling approach as described in

Ref. 416.

The results from these calculations and corrections are presented in Fig. 7.8a. Taking into consideration that none of the calculated data is refined or fitted to the experimental data, there is an excellent match; the transverse-polarised diagonal features are particularly well-capsulated by the modelled dataset. The subtle difference in sharpness of the features can be attributed to the finite size of the DFT models.

To further compare the experimental to computational data based on diffuse scattering, the 3D-ΔPDF was calculated for both datasets using the FFT algorithm as implemented in MEERKAT2 (Fig. 7.8b) [238, 335]. As mentioned before, this requires the removal of the Bragg peaks from the total scattering data. For the experimental dataset, this was achieved using the KAREN algorithm [47], which is based on an outlier rejection. This works because, in the 3D reconstruction, the Bragg peaks only extend over a few voxels on well-defined positions. The intensity of these voxels is much larger than the intensity of the diffuse scattering, and therefore recognised as outliers. As for the computational dataset, the missing intensity from the removed Bragg peaks was interpolated from the surrounding voxels using a custom script with the SciPy interpolate package [417]. Additionally, to reduce the effect of Fourier ripples, the (background-subtracted and Bragg-peak removed) data

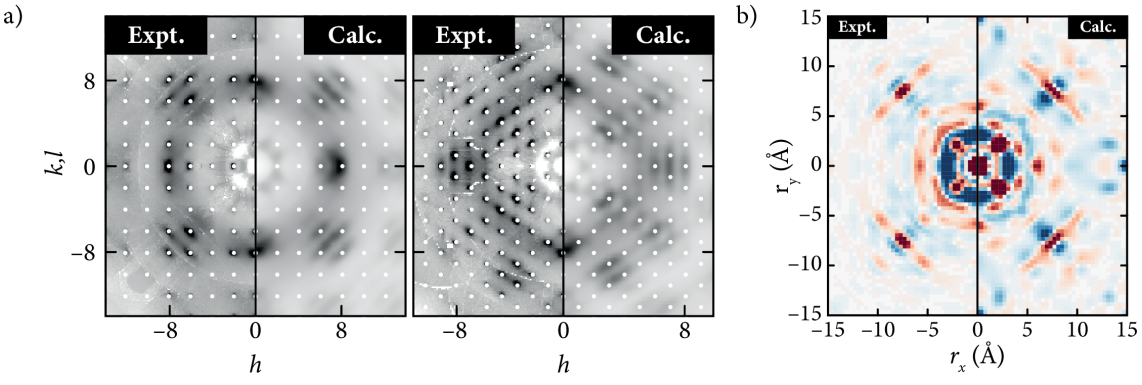

Figure 7.8: Computational and experimental validation of the TRUMOF-1 structure. (a) Comparison of experimental and calculated single-crystal X-ray diffuse scattering in the (left) (*hk*0) and (right) (*hhl*) planes. The Bragg reflection positions are masked by white circles. (b) Comparison between experimental and calculated $r_x r_y 0$ cuts of the 3D-ΔPDF. Positive correlations are shown in red and negative correlations in blue.

were multiplied with a Gaussian fall-off, which smooths the edges of the measured reciprocal space section [47]. The resulting datasets could then be used as input to MEERKAT2 [335]. Results are given in Fig. 7.8b.

As expected, the experimental and calculated data have a good agreement. There are some subtle differences, especially at low-$|\mathbf{r}|$, however these can be attributed to dynamical effects, which mostly affect features in this region. Therefore, taking this aspect into account, the match between the simulated and experiment 3D-ΔPDF is of very high quality, which in turn is indicative of the model being fundamentally correct. I will confirm the uniqueness of the presented model later in this section to further support this conclusion.

Finally, it is important to note that the 3D-ΔPDF data are only used as a finger-printing method to compare the experimental to computational data. As to which feature corresponds to which interatomic distance, this cannot be stated with certainty. The reason for this is the high number of atoms that make up the structure of TRUMOF-1 complicate this assignment.

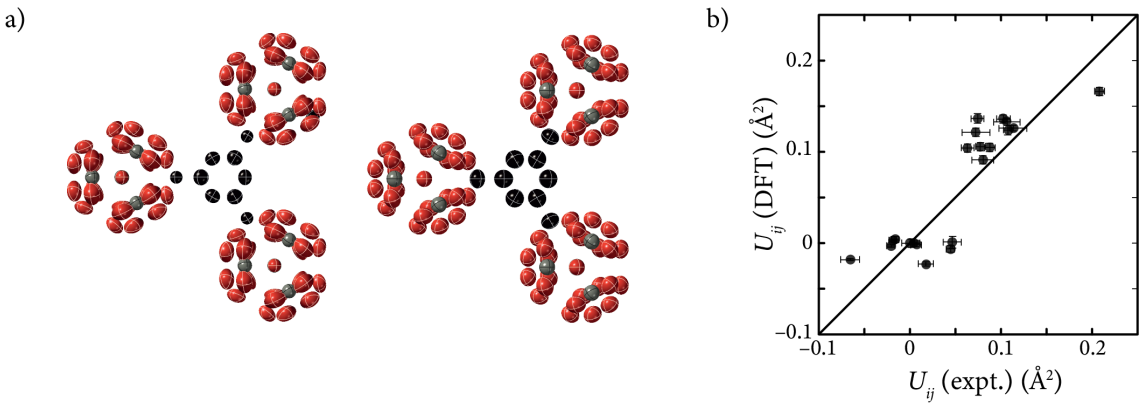

Figure 7.9: Computational and experimental validation of the TRUMOF-1 structure based on anisotropic displacement parameters. (a) Comparison between the experimentally derived crystallographic model for scattering density at the ligand site at 100 K (left) and that obtained by projection of DFT-relaxed structures onto the same site (right). Ellipsoids are shown at 50% probability. (b) Contribution of static disorder to the anisotropic displacement parameters of TRUMOF-1 as determined using DFT, on the one hand, and estimated from linear fits to the experimental U_{ij}(T) values (Fig. C.4.10), on the other hand. The observed values cluster around the diagonal.

7.4.2 Atomic displacement parameters

As a further check against experiment, the distribution of atomic positions determined from configurational averaging over the DFT configurations was compared with the anisotropic displacement parameters determined in the SCXRD refinements (Figs. 7.9a). As anticipated, the values are consistent. Furthermore, the models indicate that the static disorder contributes ∼0.1 Å^2 to atomic mean-squared displacements in the $F\bar{4}3m$ average structure model. A similar value was obtained by extrapolating the experimental displacement parameters measured between 100 K and 350 K to 0 K (Figs. 7.9b, C4.10). Hence, the Truchet-tile model rationalises at once both average and local structure measurements of TRUMOF-1.

7.4.3 Uniqueness

In conclusion, both the calculated diffuse scattering and 3D-ΔPDF data closely matches experimental results. This would indicate that the model represents the real structure of TRUMOF-1. However, to a certain extent, the scattering is composed of a mostly crystalline pattern which in turn is part of the original MOF structure. Accordingly, the observed diffuse scattering may be expected from the addition of any type of disorder to the original crystalline system, and not specifically the way it is described with the Truchet-tile model.

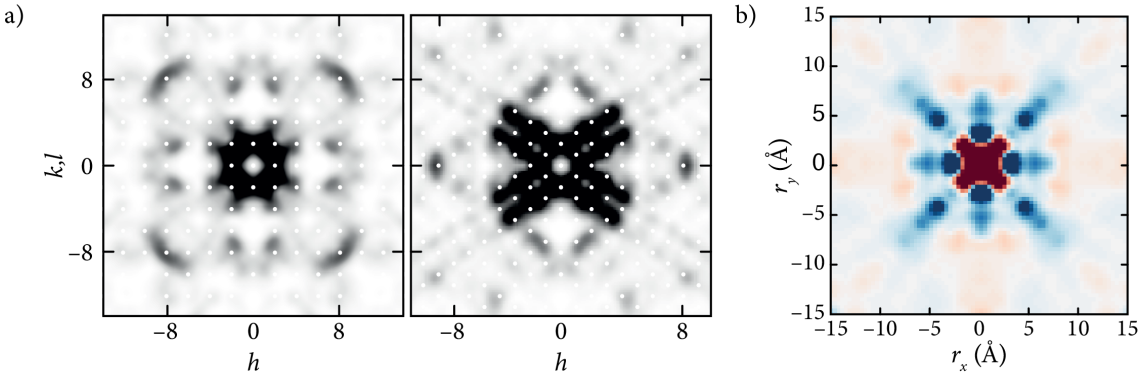

Figure 7.10: Further validation of the TRUMOF-1 Truchet tile model. (a) Single-crystal diffuse scattering, in which the Bragg reflection positions are masked by white circles, and (b) 3D-ΔPDF function (positive correlations are shown in red and negative correlations in blue) as calculated for the Truchet tile TRUMOF-1 models prior to relaxation.

To test whether this is the case, the total scattering and corresponding 3D-ΔPDFs were calculated from models that had not yet been relaxed *i.e.* represent only the correct connectivity of TRUMOF-1 (Fig. 7.10). Clearly, the agreement has got significantly less; the transverse-polarised diffuse scattering along the diagonal are less well-defined, and the sharp features observed in the experimental 3D-ΔPDF are no longer present. This both shows that the DFT models are indeed a very accurate representation of the structure of TRUMOF-1 and the sensitivity of the two functions to the precise structural relaxations driven by the aperiodic framework connectivity.

7.5 Intermezzo

Let us summarise what we have learnt so far about the structure of TRUMOF-1 by considering it a 3D Truchet tiling. Its network consists of a fully 6-connected net, with nodes arranged on a periodic lattice *i.e.* as in MOF-5. However its connectivity is aperiodic *i.e.* unlike MOF-5.

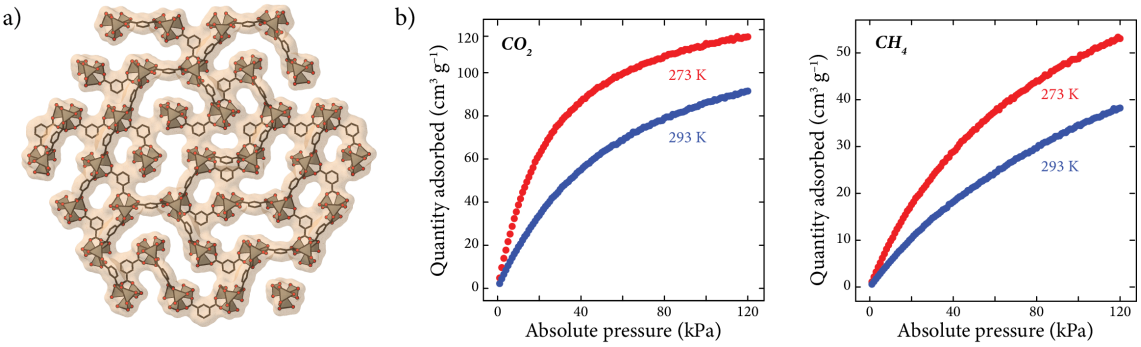

Figure 7.11: Pore structure of TRUMOF-1 and its properties. (a) Representative planar fragment of a TRUMOF-1 structure model, viewed down the ⟨111⟩ crystal axis to show the complexity of its pore network. Only those 1,3-bdc molecules that link clusters within this plane are shown. Each cluster is connected to six neighbouring clusters, some of which will be in planes above or below that shown here. The surface of the solvent-accessible pores is shown as a grey outline. Note that, despite the periodic arrangement of inorganic clusters, the pore network is disordered. There is a qualitative similarity to the Truchet tiling shown in Fig. 7.3b. (b) Adsorption isotherms of TRUMOF-1 for (left) CH_4 and (right) CO_2 calculated using GCMC simulations.

This topological aperiodicity may be important, because it translates into a disordered pore network with specific characteristics [418]. Evidently, guest molecules are sensitive to this aperiodicity, since loading TRUMOF-1 crystals with I_2 enhanced the X-ray diffuse scattering contrast (Fig. 7.7c). A representative of the pore structure, extracted from one of the DFT configurations, is illustrated in Fig. 7.11a. It is rather maze-like; the observed complex transport pathways are qualitatively similar to those in gels [419] and granular porous media [420], and so may be useful in separations. GCMC simulations enabled calculation of the corresponding adsorption behaviour (Fig. 7.11b), in turn demonstrating a good agreement with the experimental data (Fig. 7.2). As anticipated, the smaller pore dimensions relative to MOF-5 ($\sim$10 Å *vs* 13 Å, based on our models) as well as the higher curvature of the network, reflect the stronger adsorption enthalpies of TRUMOF-1.

In addition to guest uptake, the aperiodic pore network of TRUMOF-1 may have an impact on its elastic behaviour. In fact, it has been well appreciated that irregular, heterogeneous architectures can confer mechanical strength through frustration of collapse mechanisms [393, 421, 422]. An archetypal example is that of dry stone walls, which derive their mechanical strength from varying stone sizes and shapes (Fig. 7.12a) [423]. Another example is the complex disordered channel networks in termite nests (Fig. 7.12b) [424], which optimise structural stability and ventilation, in turn serving as inspiration for a new class of advanced metamaterials [422]. Accordingly, due to the different cluster configurations in the network of TRUMOF-1, there may be no uniform response to the application of pressure, which is typically the cause of framework collapse in crystalline materials. Instead, the presence of different local motifs could allow TRUMOF-1 to respond in different volume-reducing ways for loads applied in different directions [393].

Otherwise, as was highlighted in Chapter 6, correlated disorder in frameworks — albeit in this example cluster defects — may affect mechanical properties such as thermal expansivity [366] and compressibility [339, 367]. And in some cases, the application of pressure introduces an order/disorder transition in materials [398, 399]. As such, the next — and final — section of this chapter will discuss the

behaviour of TRUMOF-1 under hydrostatic pressure, based on high-pressure single-crystal X-ray diffraction measurements.

7.6 Elastic behaviour

7.6.1 Experimental details

TRUMOF-1 crystals were prepared as outlined in Chapter 3, left to soak in fresh $CHCl_3$, and evacuated under vacuum before loading onto a Merrill-Bassett DAC. All high-pressure X-ray diffraction data were collected on the i19 beamline at the Diamond Light Source, at pressures between 0.13(1)–1.81(2) GPa. Data collection included a step size, transmission and exposure time of 1, 3% and 0.3 seconds, respectively. Unit cell determination, data integration, frame scaling, and absorption corrections were performed using CrysAlisPro [241].

Structure refinements were carried out for the dataset collected at 0.13 GPa as outlined in Chapter 3, albeit without accounting for the disorder *via* the split carbon sites C2A and C2B, *i.e.* refining 'C2' with an occupancy of 0.75. This model was then used to refine models against all other measurements. All atoms were refined isotropically, and the FLAT, DFIX and SADI constraints were used on the C2 and C3 atoms to fix the geometry of the benzene-ring. H-atom positions were placed geometrically and constrained to ride on their host atoms. The corresponding

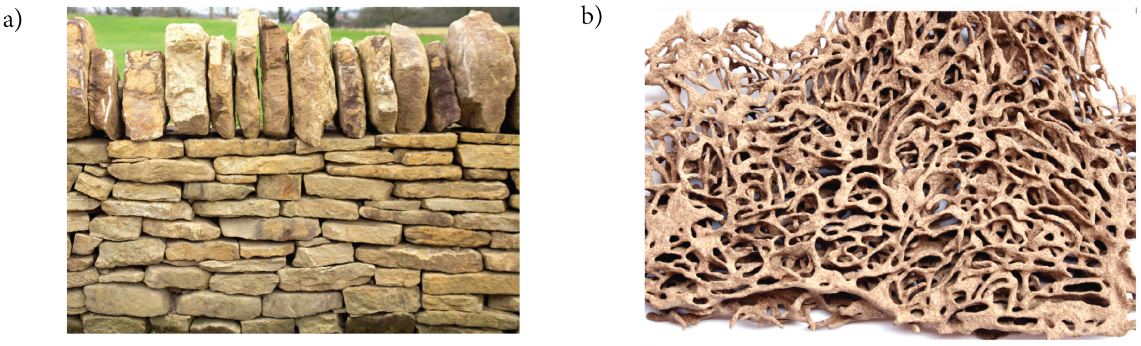

Figure 7.12: Examples of heterogeneous microstructures known to enhance elastic stability: (a) The irregular arrangement of heterogeneously shaped stones in dry stone walls and (b) the irregular internal structure of a termite nest and. Figure (b) adapted from Ref. [422] with permission from AAAS.

CIFs and checkCIFs are provided as electronic data files (Folder 'Ch7-hp') and the crystallographic details are presented in Appendix C5.1.

The bulk modulus was calculated from the change in volume as a function of pressure using the web-based tool PASCaL [270].

7.6.2 Results

On first inspection, the mechanical behaviour of TRUMOF-1 seems straightforward: TRUMOF-1 remains crystalline throughout the $0.13 - 1.81$ GPa pressure range (without undergoing any phase transitions) and its volume decreases with increasing pressure (Fig. 7.13a). The latter corresponds to the atoms of the asymmetric unit moving closer, as permitted through the decrease in the angle θ_1 (between C2–C1–O2). Notably, there are small non-linearities of the volume reduction at low and high pressures. These may be caused by remnants of DMF solvent in the pores, which was calculated to be 3–4 molecules per unit cell using the solvent mask algorithm [425] within Olex2 (Table C5.60).

The 3rd order BM equation of state resulted in the best fit (Fig. 7.12a), indicating a bulk modulus of $B_0 = 7.6(5)$ GPa with $B' = 5.8$ (Table 7.2). Accordingly,

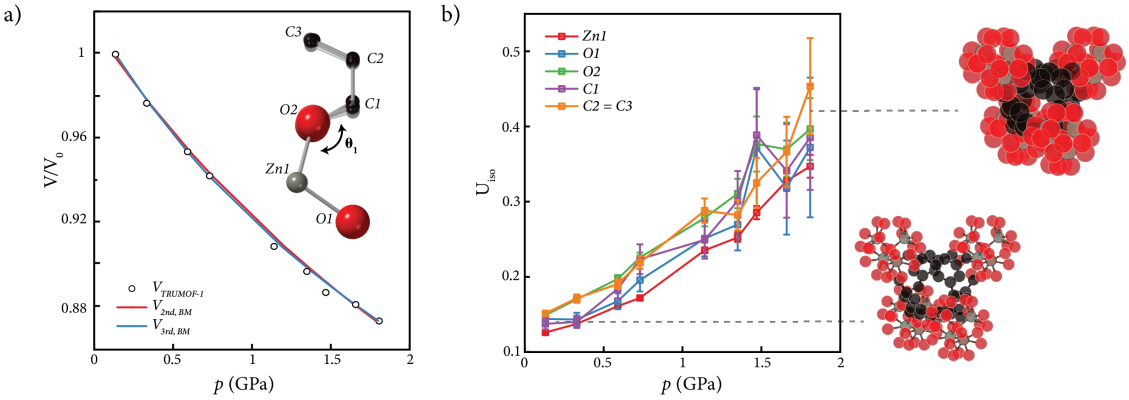

Figure 7.13: Changes in the average structure of TRUMOF-1 as a function of pressure. (a) Change in volume as a function of pressure fitted with the 2nd and 3rd BM EoS. The asymmetric unit of TRUMOF-1 for each pressure point dataset is given in the top right corner with increasing opacity as a function of pressure, showing the change in angle θ_1. (b) U_{iso} values of all atoms in the asymmetric unit as a function of pressure, shown with error bars. Two structures are given for the datasets collected at 0.13 and 1.81 GPa, to show the difference in U_{iso} quantitatively.

Table 7.2: Bulk moduli of TRUMOF-1 as calculated from the 2nd and 3rd BM fits show in Fig. 7.13a.

Order of BM EoS	B_0 (GPa)	B'
2	8.9(1)	4
3	7.6(5)	5.8(7)

TRUMOF-1 has a compressibility comparable to ZIF-8 [426–428], yet it is significantly more stable; ZIF-8 collapses at ∼1.4 GPa in the non-penetrating PTM FC-70 [426].

As the example of ZIF-8 demonstrates, the combination of softness and stability observed for TRUMOF-1 is rather rare for a cubic MOF. Accordingly, the aperiodic connectivity of TRUMOF-1 may be responsible for this unusual elastic behaviour. To test this hypothesis, U_{iso} values for all atoms were plotted as a function of pressure, assuming they represent the disorder in atomic translations rather than vibrations (Fig. 7.13b). The results demonstrate a direct — rather than an inverse — relationship between the magnitude of atomic displacements and pressure *i.e.* as the pressure is increased, the atoms move to a greater extent. This experimental signature of the atomic displacement parameters is an indication of pressure-induced internal reorganisation, which amplifies the degree of static disorder in node positions.

7.6.3 Mechanism

To understand more about the mechanism responsible for the elastic behaviour observed for TRUMOF-1, we developed a very simple empirical potential model based on the elastic behaviour of MOF-5 (as reported in the literature). This was then transferred to TRUMOF-1, in order to simulate its behaviour under hydrostatic pressure using the GULP software [293, 294].

MOF-5 parameterisation

In order to capture the key mechanical behaviour of MOF-5, a simple model based on the primitive cubic lattice was built, in which every atom represents the [OZn_4] cluster. These atoms are in turn connected by effective springs, that model the stiffness of cluster–linker–cluster linages. Likewise, angular harmonic interactions were included to capture the shear resistance of MOF-5. As implemented in GULP [293, 294], this resulted in the corresponding potential model:

$$E_{\text{latt}} = \frac{1}{2}k_r \sum_{\text{pairs}} (r - r_e)^2 + \frac{1}{2}k_\theta \sum_{\text{triplets}} (\theta - \theta_e)^2, \tag{7.1}$$

in which the equilibrium separation between neighbouring nodes, r_e, was set to be half the unit-cell parameter of MOF-5 (*i.e.* 12.946 Å [88]), and the equilibrium angles, θ_e, were assigned to the corresponding high-symmetry values.

Accordingly, the values of k_r and k_θ are the two variables to be determined in this parameterisation. These were obtained by calculating the bulk and shear moduli implied by Equation (7.1), and optimising these to best match the DFT values determined for MOF-5 (B_0 = 18.2 GPa and G = 1.8261 GPa, as reported in Ref. 196). These values were reproduced with the effective force constants k_r = 4.4118 eV Å^{-2} and k_θ = 3.811eV rad^{-2}.

Subjecting this model to hydrostatic pressure ($0 \leq p \leq 2$ GPa) resulted in a straightforward compression (Fig. 7.14). However notably, the pressure dependence of its Young's, bulk, and shear moduli revealed the onset of an elastic instability at 1.2 GPa (Fig. 7.14b). This behaviour is consistent with the facile amorphisation of MOF-5 under compression, despite the simplicity of this model *e.g.* compared to the finite-temperature MOF force-field analysis discussed in Ref. 429.

The corresponding elastic stiffness matrix could be used to calculate the orientational dependence of various elastic moduli using the ELATE code [295] (Appendix C5.4). Results further confirm the mechanical stability of the model by showing the elastic tensor is definite positive. Particularly striking is the Young's modulus (Fig. 7.14c), as it highlights the extreme anisotropy of the system; being that there is a

strong resistance only along the ⟨100⟩ axes *i.e.* the direction of the linkers. This anisotropy is again consistent with the results presented in Ref. 429.

Application to TRUMOF-1

This simple potential was then transferred to TRUMOF-1 in order to help interpret our experimental results. To do so, a couple of changes had to be made to the potential model in Equation (7.1). Firstly, the equilibrium separation, r_e, was modified to the relevant value for the TRUMOF-1 crystal structure (10.898 Å). Secondly, whereas in the MOF-5 parameterisation all neighbouring pairs at r_e were included in the pairwise sum, for TRUMOF-1 only those pairs that are topologically connected in a Truchet approximant were included. This topological connectivity was encoded in the GULP input file, informed by the same MC routine described pre-

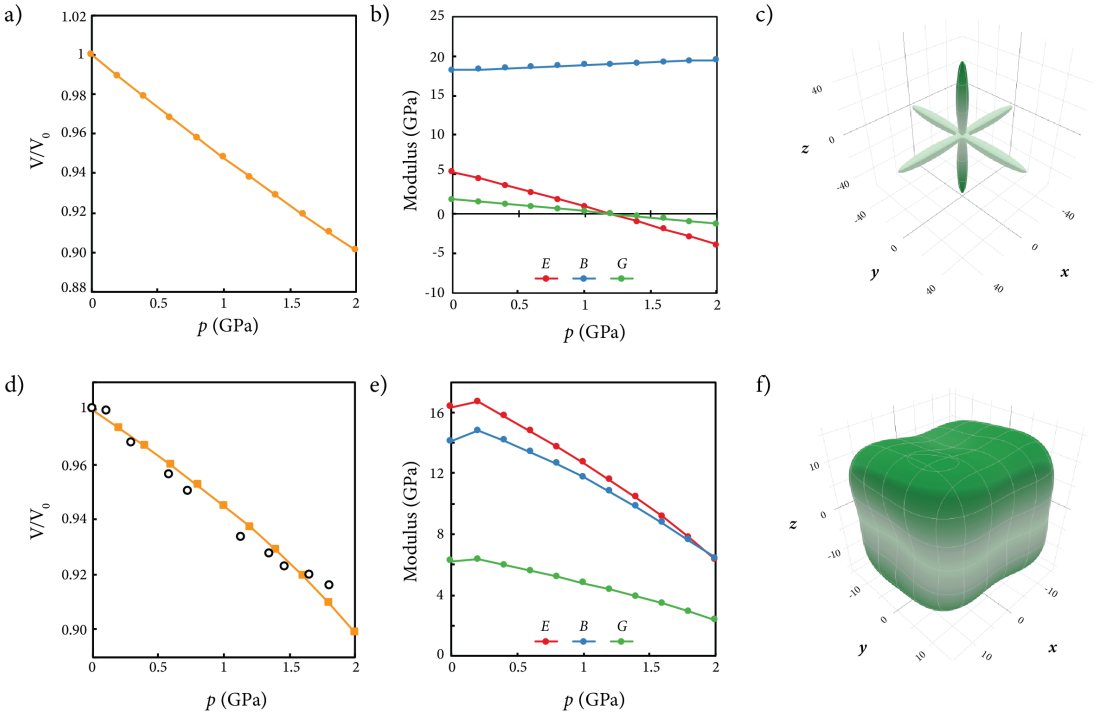

Figure 7.14: Mechanical stability of our simplified models for MOF-5 ((a) – (c)) and TRUMOF-1 ((d) – (f)) under hydrostatic pressure. (a) EoS of compressibility under hydrostatic pressure. (b) Pressure dependence of the Young's, bulk, and shear moduli. (c) Young's modulus as calculated using the code ELATE [295]. (d) EoS of compressibility (orange) under hydrostatic pressure compared to experimental data (white dots). (e) Pressure dependence of the Young's, bulk, and shear moduli. (f) Young's modulus as calculated using the code ELATE [295].

viously. Similarly, the triplet sum term for TRUMOF-1 included only those triplets in which the central atom was topologically connected to the peripheral atoms. Finally, the values of k_r and k_θ could be left unchanged, however the equilibrium angles, θ_e, were taken to be the corresponding angles when nodes are placed at the high-symmetry (face-centred) sites in the underlying $F\bar{4}3m$ cell. The final calculations used a 4×4×4 approximant of the TRUMOF-1 connectivity, with periodic boundary conditions applied.

The EoS was similarly calculated over the hydrostatic pressure range of $0 \leq p \leq 2$ GPa (Fig. 7.14d). Notably, the basic form of the experimental data is captured well. And in contrast to MOF-5, the simplified TRUMOF-1 model was elastically stable over this entire pressure range (Fig. 7.14e). This observation is particularly remarkable because both the simplified MOF-5 and TRUMOF-1 network are characterised by six-connected nets, with identical bond and angle stiffnesses. However, the former is elastically unstable, whilst the latter is stable over a wide pressure range. It is important to note that this observation for MOF-5 has been reported in computational studies — the only experimental high-pressure measurement of guest-free MOF-5 is an *ex situ* compression study [430], due to the large pores enabling bulky PTM to enter the framework [200].

Furthermore, the corresponding Young's modulus shows a very different degree of anisotropy compared to MOF-5; the shape of the tensor is rather isotropic, being much more similar to that of UiO-66 [429] — which shares a face-centred cubic arrangement of nodes. In turn, UiO-66 is very mechanically stable. As I highlighted before, this property is commonly attributed to its high connectivity, though these results may indicate that this is not necessarily the key factor.

Anisotropy may also be quantified by defining it in terms of the ratio of maximum and minimum values of any orientationally-dependent elastic quantity. This can take values from unity (100% isotropy) to infinity (∞ anisotropy). Accordingly, values obtained for the Young's and shear anisotropies for both models are presented in Table 7.3. These values show that, based on the simple models, the elastic tensor of TRUMOF-1 is about an order of magnitude less anisotropic than that of MOF-5.

Table 7.3: Quantified anisotropy calculated for the simple models of MOF-5 and TRUMOF-1

System	$E_{\max}/E_{\min}$	$G_{\max}/G_{\min}$
MOF-5	16.5	24.25
TRUMOF-1	1.59	1.77

Yet, this analysis does not give a microscopic mechanism for the low elastic anisotropy — and, in turn, the large elastic stability — of TRUMOF-1. To address this point, the deformation mechanism of this simple TRUMOF-1 model was interrogated. In agreement with the hypothesis mentioned above, it was anticipated that, whereas the high symmetry of the MOF-5 structure constrains the node positions to the same crystallographic site at all pressures, the complete absence of crystallographic symmetry in TRUMOF-1 (except in a statistical sense) allows internal reorganisation as a function of pressure. Indeed, a large collective of translations and rotations were found, as shown in Fig. 7.15a: some domains migrate to a greater degree with increasing pressure than others.

To provide the final piece of evidence that this model accurately describes the behaviour of TRUMOF-1 at hydrostatic pressure, a measure of the pressure-induced node displacements was extracted from the experimental U_{iso} values using the relation:

$$\delta(p) = \sqrt{\langle U_{\text{iso}}(p)\rangle - \langle U_{\text{iso}}(0)\rangle}, \tag{7.2}$$

where the averages are taken over all atom types. Defined in this way, $\delta(p)$ can be compared with the root-mean-squared displacements of node positions observed by collapsing the simplified GULP models onto its parent $Fm\bar{3}m$ structure (Fig. 7.15b).

Clearly, there is a very good correspondence between the experimental and model-derived $\delta(p)$ values, and therefore, despite the simplicity of the developed empirical potential model, it seems nonetheless to capture the key mechanical mechanisms at play in the high-pressure behaviour of TRUMOF-1. In contrast to what has

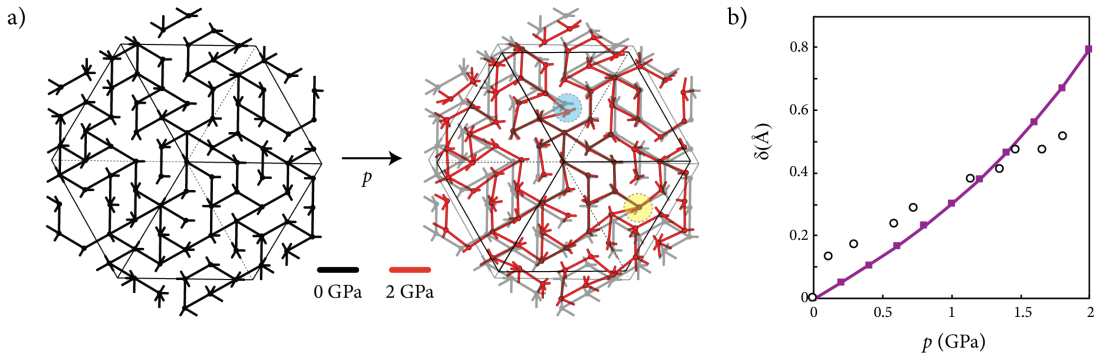

Figure 7.15: Microscopic mechanism of TRUMOF-1 under hydrostatic pressure. (a) Representation of simplified TRUMOF-1 model at 0.0 GPa (left) and 2.0 (right) GPa, in which the elastic connections between neighbour nodes are indicated by solid lines, and the view is taken of a slice of the 4×4×4 approximant normal to one of the ⟨111⟩ axes. Two nodes have been highlighted; one of which does not migrate with pressure (yellow), and one of which migrates significantly (blue). (b) Comparison of $\delta(p)$ calculated from the experimental (white dots) and simulated (purple) data, as a function of pressure.

been reported in the literature, we found that the high elastic stability of TRUMOF-1 (for a MOF) is not a function of particularly strong bonding or high connectivity, but rather conferred by the topological heterogeneity of its underlying network structure. Counter-intuitively, this heterogeneity actually leads to strong elastic isotropy.

7.7 Conclusion and Outlook

Evidently, TRUMOF-1 is unusual in a number of respects. This is attributed to its topology, in which each node has a connectivity of 6 and is arranged on a periodic lattice, though their connectivity is aperiodic. This makes TRUMOF-1 an intermediate to conventional crystalline MOFs and amorphous MOF derivatives with continuous random network structures [80, 345], in turn allowing for the experimental investigation of its impact on collective materials properties. Accordingly, its aperiodic pore network was found to be responsible for its high elastic stability, as governed by the internal reorganisation of different local motifs [393]. Furthermore, the smaller pores arising from this maze-like connectivity, results in strong

gas adsorption enthalpies.

However there is no reason to expect that TRUMOF-1 should be the unique MOF with a Truchet-tile structure. Because every conventional periodic tiling can be modified to give Truchet tilings, suitable symmetry-lowering of inorganic and organic building units should allow targeted synthesis of alternative 'TRUMOFs'. Indeed, the structures of some previously-described MOFs [431] and related systems [432] with partially-occupied and/or complex structures might be reinterpretable as Truchet tilings.

Ultimately, whilst TRUMOF-1 crystals share the same statistical properties, the aperiodic topology means no two crystals are the same. In other words, each crystal stores different information. As described in Chapter 1, Truchet tiles are currently used as (visual) data storage platforms and conceptually show how they could have data error-correcting abilities. Since TRUMOF-1 is an atomic realisation of a Truchet tiling, it may therefore function as a next generation, high-density data storage platform. As such, TRUMOF-1, and other to-be-discovered Truchet-tile-inspired systems, may provide a useful avenue for the design of a variety of (next-generation) functional systems.

Chapter 8

Summary and perspective

8.1 Summary and acknowledgements

This thesis explored whether complexity can be introduced to materials by incorporating low-symmetry components. Indeed, the combination of the low-symmetry linker 1,3-bdc with Zn metal resulted in the complex phase of TRUMOF-1 — the first topologically aperiodic material to be reported. However in addition to the complexity of TRUMOF-1, the Zn-1,3-bdc MOF phase space explored in this thesis appeared rather complex regarding both the specificity of reaction conditions required to obtain crystalline phases of different topologies and the inability of applying reticular chemistry. The final chapter aims to summarise all results obtained in this thesis as well as tie all these findings together through comparison of the variety in torsion angle observed for 1,3-bdc and 1,4-bdc in Zn-MOFs through a literature study. Our results indicate that the overall complexity observed for the Zn-1,3-bdc MOF phase space not only arises from the bent configuration of 1,3-bdc, but also from the flexibility in torsion angle between the carboxylates.

I am grateful to Thomas Nicholas, who wrote a code to extract all torsion angles from the TRUMOF-1 approximants.

8.2 The Zn-1,3-bdc MOF phase space

The broad aim of this thesis was to introduce complexity into materials through symmetry lowering of components. MOFs were chosen as the platform to do so, as they offer full control over the geometry of building units. Because it has the same chemical composition as the prevalent linker 1,4-bdc, the low-symmetry linker 1,3-bdc was selected and combined with Zn containing precursors, ultimately shaping the final objective of this thesis; to explore the Zn-1,3-bdc MOF phase space.

This exploration led to the synthesis and characterisation of five different phases,

three of which had not previously been reported (Fig. 8.1). Most striking is the phase of TRUMOF-1, which has an aperiodic topology and therefore is the first of its kind (Chapter 7). Yet other phases show interesting properties such as NTE and NLC (MOX-2 and MOX-4, Chapter 4) and thermal disorder (MOX-3, Chapter 5) including stacking faults (MOX-5α, Chapter 3).

Whilst each chapter so far has focused on describing how the corresponding framework structures are responsible for these properties, there is yet to be a conclusion on how the different phases relate to each other. However, this thesis is an exploration of the phase space overall, and hence I will provide a final perspective to tie all findings together.

There are two main observations to be made when inspecting the obtained phases in this thesis. First, one of them is disordered and therefore highly frustrated. This implies that the energy landscape of Zn-1,3-bdc is rather shallow. Second, the application of reticular chemistry — the extent of which it was explored limited to attaching a functional group to the benzene ring — was unsuccessful, being that for

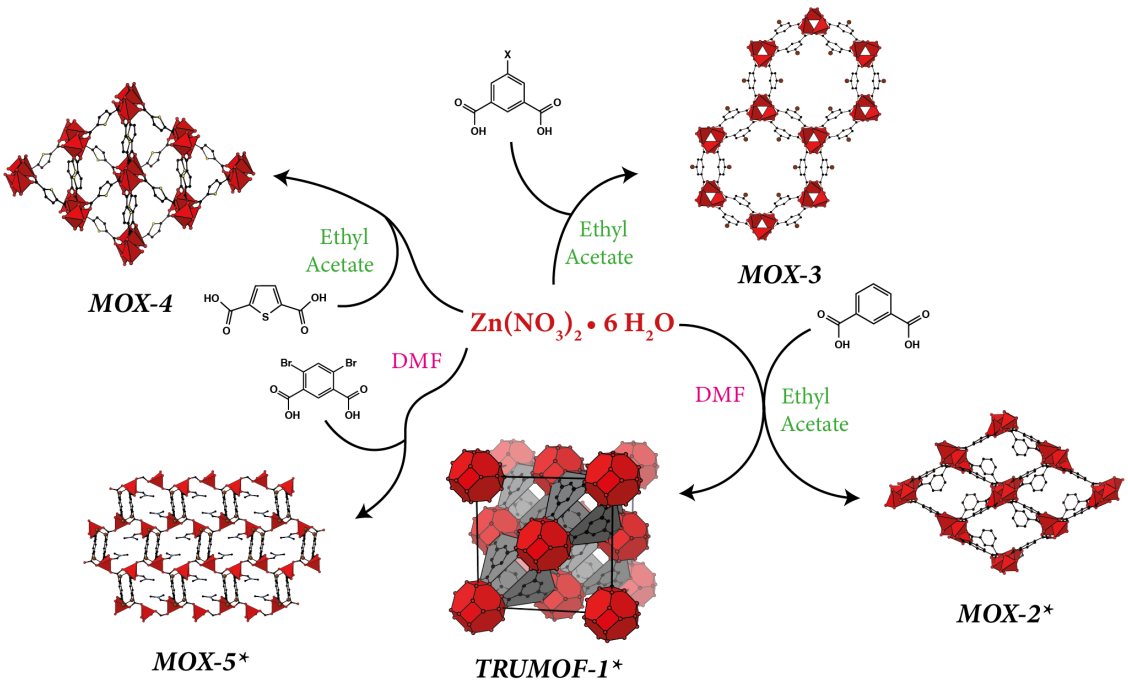

Figure 8.1: Summary of the crystal Zn-1,3-bdc MOF phases obtained in this thesis, together with the required starting material and reaction solvent. All MOF phases not yet reported before in the literature are indicated with an asterisk.

each (differently) substituted 1,3-bdc analogue, a different phase was obtained. Furthermore, changing the angle between the carboxylates also seemed to be significant in obtaining a different phase (*i.e.* MOX-2 *vs* MOX-4).

Not covered in the previous chapters, but worth mentioning for the discussion here, is that many synthetic attempts resulted in powders or no solid product at all (Tables E1.63, E1.64). These attempts include syntheses in different solvents and with elongated, bent linkers. This failure at obtaining single crystals under certain synthetic parameters further adds to the complexity of the Zn-1,3-bdc MOF phase space, as it demonstrates the specifity of synthetic conditions to obtain each (single-crystal) phase. Moreover, a slight change in temperature or reaction time in the synthesis for TRUMOF-1 resulted in smaller crystals stuck together, or no crystals at all. Again, this observation hints towards a shallow energy landscape, where the local minima are only found when the conditions are precisely met.

The question arises, from where does this complexity come? Of course, the approach of this thesis was to introduce such complexity through the low symmetry of 1,3-bdc. In the case of TRUMOF-1 it indeed appears that the bent configuration of the linker is the origin of its aperiodic topology. However there is no evidence that the bent shape of 1,3-bdc is the only property responsible for the observed complexity. In fact, as highlighted in Chapter 1, 1,3-bdc may exhibit a different behaviour with regards to the flexibility in torsion angle (*i.e.* the angular orientation of the carboxylate groups relative to the benzene ring) compared to 1,4-bdc due to having a different electronic structure (Figs. 1.26, 1.27). Accordingly, this flexibility may be key in the shallow energy landscape of Zn-1,3-bdc and, ultimately, crucial in obtaining a TRUMOF.

To test this hypothesis, the spread in 1,3-bdc torsion angles were extracted from all TRUMOF-1 2×2×2 DFT approximants, followed by a comparison in energy. To put these findings into perspective, our analysis was repeated for 1,3-bdc(-X) and 1,4-bdc(-X) Zn MOFs reported in the literature, which were found using the software ConQuest [433].

8.3 Torsion angle variations TRUMOF-1

In total, 2,134 linkers were extracted from 22 2×2×2 TRUMOF-1 approximants, each with the carboxylates C1 and C2 and therefore 4,268 torsion angles. In addition, the relationship between C1 and C2 regarding the direction of their twist was extracted for each linker: carboxylates moving in-phase (*i.e.* in the same direction) are labelled as *syn* and carboxylates moving out-of-phase (*i.e.* in the opposite direction) are labelled as *anti*.

Our results show a wide distribution of torsion angle; most lie between 0–15°, but some carboxylates achieve an angle up to 40° (Fig. 8.2). It is particularly evident from Fig. 8.2b that there is no correlation between average torsion angle

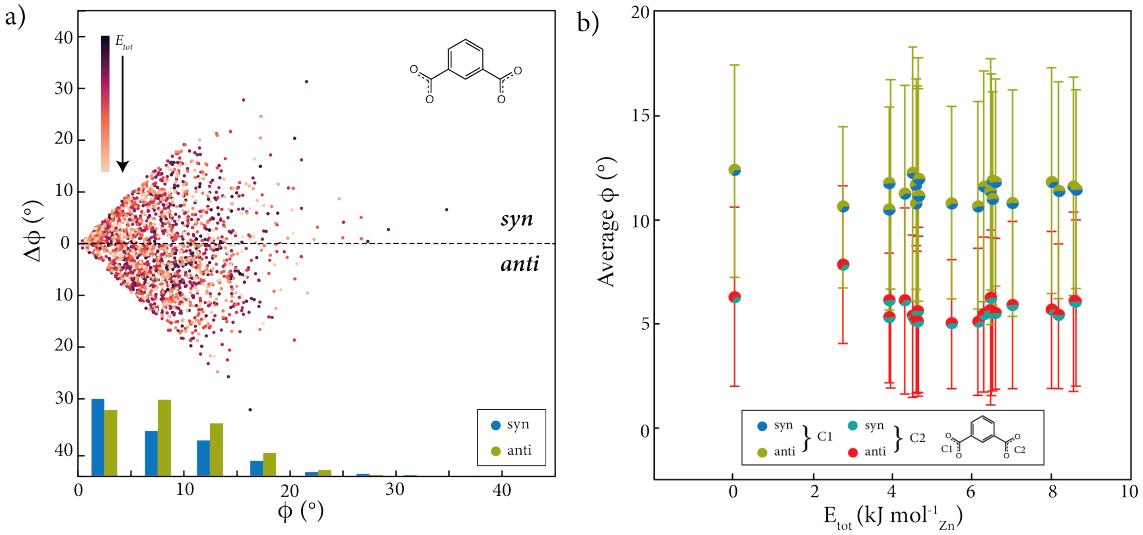

Figure 8.2: Distribution of 1,3-bdc torsion angle values in 22 2×2×2 TRUMOF-1 DFT supercell configurations: (a) Graph showing the average torsion angle value, ϕ, of each 1,3-bdc linker carboxylate extracted from all supercells. To demonstrate the independence of C1 and C2, the difference between the two values, $\Delta\phi$, is given for each torsion angle. All carboxylate twists with a *syn* and *anti* relationship are plotted above and below the dotted line, respectively. All torsion angle values are coloured according to a gradient depicting the energy state (kJ $\text{mol}_{\text{Zn}}^{-1}$) of the supercell. Histograms are given at the bottom of the graph to indicate the ratio of *syn*:*anti* C1 and C2 carboxylates (*i.e.* not the average) for each 5° interval. (b) Graph showing the average torsion angle values of C1 and C2 of each supercell as a function of energy (kJ $\text{mol}_{\text{Zn}}^{-1}$), as well as the ratio of *syn*:*anti* linkers represented as pie-charts for each data-point. Note that in order to calculate the average value of C1 and C2, the carboxylate with the largest torsion angle was assigned as C1, leaving the smaller torsion angle to be assigned as C2. The standard deviation in torsion angle is represented with error bars.

Table 8.1: Syn:anti ratio of 1,3-bdc in TRUMOF-1 approximants.

Linker	Syn(%)	Anti(%)	Total (100%)
1,3-bdc	44	56	2,134

and overall energy of the supercell configuration, as there is no (clear) linear trend between the C1 and C2 carboxylates. The large error bars further confirm the wide variety of the 1,3-bdc torsion angles in each supercell. This would in turn further hint towards a shallow energy landscape with regards to the linker torsion angle, for values between 0–15°.

The histograms plotted in Fig. 8.2a show that the number of *syn* linkers gradually decrease with increasing torsion angle, whilst the *anti* linkers increase from the 0–5° to 5–10° range, after which the number gradually decreases. With a distribution of 44% and 56% for the *syn* and *anti* linkers respectively, there is a slight preference for the latter (Table 8.1). However, there is no notable trend in supercell energy and overall *syn*:*anti* ratio (Fig. 8.2b).

8.4 Torsion angle variations 1,3-bdc *vs* 1,4-bdc in Zn-MOFs

To further interrogate these observations, the torsion angles for both (5-X-)1,3-bdc and (2-X-)1,4-bdc in Zn-MOFs (X = Br, Cl, I, F, CH_3, OCH_3, OH and NH_2) were extracted from the Cambridge structural database (CSD) using the software ConQuest [433]. The search criteria were set to single metal and single linker MOFs (*i.e.* Zn and 1,3-bdc, respectively). Hence, results include MOFs in which the carboxylates are not all coordinated and Zn has a non-tetrahedral environment. It was noted that, in contrast to 1,4-bdc, 1,3-bdc has 3 unique carbons onto which a functional group may be attached. However, results were only obtained for Zn-*n*-X-1,3-bdc with $n = 5$. Linker torsion angles from MOX-2 and MOX-3 were also added to the dataset. Results are presented in Fig. 8.3.

A first observation is the widespread distribution of torsion angles in the (5-X-)1,3-bdc phase space (Fig. 8.3a), matching the previous observations for TRUMOF-1 (Fig. 8.2a). There is a slight preference for the *syn* configuration for 1,3-bdc, whereas the *syn*:*anti* ratio for 5-X-1,3-bdc is close to 1:1 (Table 8.2). Evidently, 1,3-bdc linkers with the *anti* configuration prefer to have a torsion angle between 0–10° whilst those of the *syn* configuration do not seem to have a preference for small or larger torsion angles; an equal distribution of *syn* linkers is observed over the 0–40° range. As for 5-X-1,3-bdc, both linker configurations gradually decline with increasing torsion angle. Hence, the distribution of torsion angles in TRUMOF-1 is

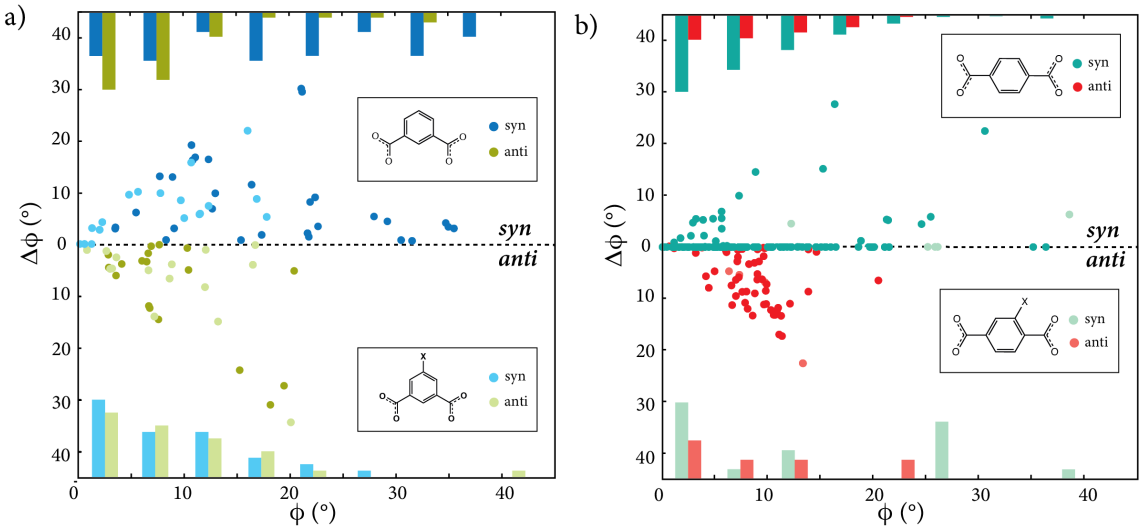

Figure 8.3: Distribution of (5-X-)1,3-bdc and (2-X-)1,4-bdc torsion angle values in the Zn-MOF phase space: (a) Graph showing the average torsion angle value, ϕ, of each (5-X-)1,3-bdc linker carboxylate extracted from all Zn-(5-X-)1,3-bdc MOFs found in the literature. To demonstrate the independence of C1 and C2, the difference between the two values, $\Delta\phi$, is given for each torsion angle. All carboxylate twists with a *syn* and *anti* relationship are plotted above and below the dotted line, respectively. All torsion angle values are coloured according to having a functional group attached to the ring (dark colours = 1,3-bdc, light colours = 5-X-1,3-bdc). Histograms are given at the top (1,3-bdc) and bottom (5-X-1,3-bdc) of the graph to demonstrate the ratio of *syn*:*anti* C1 and C2 carboxylates (*i.e.* not the average) for each 5° interval. (b) Graph showing the average torsion angle value, ϕ, of each (2-X-)1,4-bdc linker carboxylate extracted from all Zn-(2-X-)1,4-bdc MOFs found in the literature. To demonstrate the independence of C1 and C2, the difference between the two values, $\Delta\phi$, is given for each torsion angle. All carboxylate twists with a *syn* and *anti* relationship are plotted above and below the dotted line, respectively. All torsion angle values are coloured according to having a functional group attached to the ring (dark colours = 1,4-bdc, light colours = 5-X-1,4-bdc). Histograms are given at the top (1,4-bdc) and bottom (2-X-1,4-bdc) of the graph to demonstrate the ratio of *syn*:*anti* C1 and C2 carboxylates (*i.e.* not the average) for each 5° interval.

Table 8.2: *Syn*:*anti* ratio of (5-X-)1,3-bdc and (2-X-)1,4-bdc linkers found in Zn-MOFs.

Linker	Syn(%)	Anti(%)	Total (100%)
1,3-bdc	60	40	50
1,4-bdc	72	28	189
5-X-1,3-bdc	51.6	48.4	31
2-X-1,4-bdc	66.7	33.3	15

not fundamentally different to that found in crystalline analogues.

As for the (2-X-)Zn-1,4-bdc phase space, there is a significant preference for the *syn*-configuration, both with and without a functional group attached to the ring (Table 8.2). Notably, the database does not include many Zn-2-X-1,4-bdc MOFs (15 in total), hence conclusions can only be based on the Zn-1,4-bdc phase space. Results show that the bulk of the 1,4-bdc linkers prefer to have a low torsion angle. The majority of the *syn*-configured linkers lie on the dashed of the graph, indicating that the C1 and C2 dicarboxylates are planar whilst the benzene ring twists out of the plane. As such, its inversion symmetry is maintained. The spread of *anti* configured linkers is similar to the torsion angle distribution of 1,3-bdc and 5-X-1,3-bdc, though this corresponds to a relatively small proportion of the extracted 1,4-bdc linkers. Finally, both linker configurations gradually decline with increasing torsion angle.

8.5 Conclusion and discussion

What do these results tell us? Firstly, it appears that the torsion angle flexibility of 1,3-bdc is crucial in obtaining the aperiodic connectivity characteristic of TRUMOF-1, as reflected by the wide distribution of torsion angles between the values of 0 and 40°. This flexibility translates into both the magnitude of the twist and the relationship between the carboxylates (*i.e. syn vs anti*). Since there is no correlation between average torsion angle and overall configurational energy, this hints towards a shallow energetic landscape governing the torsion angle flexibility of 1,3-bdc between 0 and ∼40°.

This range of torsion angle values is not unique to 1,3-bdc, however — a similar distribution was observed for 1,4-bdc. In turn, this observation is in agreement with the torsion angle potential curves given in Fig. 1.27, which describes the behaviour of 1,3- and 1,4-bdc as rotors: both linkers have a shallow energy landscape in the range of 0–40°. What is unique to 1,3-bdc, however, is the independent behaviour of C1 and C2: whilst these carboxylates tend to lie in the same plane for 1,4-bdc, they achieve wide-spread distributions in 1,3-bdc without a preference for a *syn* nor *anti* relationship. This property can in turn be related to the lower symmetry of 1,3-bdc as compared to 1,4-bdc.

The independent torsion angle behaviour of C1 and C2 may also explain the difficulty of applying reticular chemistry within the Zn-1,3-bdc phase space. Namely, the introduction of a functional group onto 1,4-bdc may be compensated by a twist of the benzene ring, rather than the individual carboxylates. The 1,3-bdc ring cannot perform a full 180° rotation however, and therefore compensates for the added bulkiness through crystallising in a different topology as permitted by the independent torsional flexibility of the C1 and C2 carboxylates. This proposed mechanism is demonstrated with TRUMOF-1 and MOX-2, which are rather dense frameworks. Accordingly, it would be energetically unfavourable for their structures to host a functionalised 1,3-bdc linker analogue, as governed by steric hindrance. Instead, incorporating 1,3-bdc substituted at either the 5- or 4,6-positions of the ring result in MOX-3 and MOX-5, respectively. The former has very large pores lined by the functional groups, and the structure of the latter consists out of individual layers held together by non-covalent interactions between the separated functional groups. Thus, the functional group appears to have a significant structural directing role led by repulsive and/or interactive interactions.

In turn, the rather rigid 1,4-bdc facilitates crystallisation of Zn-MOFs as opposed to 1,3-bdc, which behaves more flexible. Hence, synthetic parameters have to be well-defined to find the energy minima required for crystallisation. This prerequisite is further reflected by the majority of my synthetic attempts resulting in no solid product (Tables E1.63, E1.64). Perhaps as a result, there is a lower number of reported Zn-1,3-bdc MOFs in the literature (50) compared to Zn-1,4-BDC (189).

To conclude, this thesis addresses the efficiency of introducing complexity through the introduction of low-symmetry components as probed by an exploration of the Zn-1,3-bdc MOF phase space. Results demonstrate various facets of complexity, being the disparate phase structures and topologies, difficulty in applying reticular chemistry, and, perhaps most striking, the synthesis and characterisation of a MOF with an aperiodic topology. This case of TRUMOF-1 particularly demonstrates how such structural complexity can ultimately give rise to unusual physical properties, which in turn is desired for real-life applications. And since it is the first atomic realisation of a Truchet tiling to be discovered, there are likely many other relevant applications yet to be discovered *e.g.* high-density and error-correcting memory storage.

Whilst this approach of incorporating low-symmetry components thus seems efficient in introducing complexity, there is yet to be a systematic way of doing so. The synthetic parameters required to obtain TRUMOF-1 are very specific — any alteration to the solvent or reaction time resulted in a different phase or crystals of lesser quality. This observation reflects the shallow energy landscape and thus indicates that, in order to obtain further TRUMOFs, a lot of trial-and-error may be required (at least for the time being). This difficulty in finding suitable synthetic parameters, together with the ultimate goal of controlling disorder and thus the aperiodic connectivity, are important aspects to focus on in future research. Ultimately, such symmetry-lowering approaches can be key in the realisation of future generation materials.

Bibliography

[1] D. Whitford, *Proteins: structure and function* (John Wiley & Sons, Ltd, Chichester, 2005), first edn.

[2] T. Alber, D. W. Banner, A. C. Bloomer, G. A. Petsko, D. C. Phillips, P. S. Rivers, I. A. Wilson, C. C. F. Blake, H. C. Watson, *Philos. Trans. R. Soc. B: Biol. Sci.* **293**, 159 (1981).

[3] J. Gim, N. Schnitzer, L. M. Otter, Y. Cui, S. Motreuil, F. Marin, S. E. Wolf, D. E. Jacob, A. Misra, R. Hovden, *Nat. Comm.* **10**, 4822 (2019).

[4] A. P. Jackson, J. F. V. Vincent, R. M. Turner, R. M. Alexander, *Proc. R. Soc. B: Biol. Sci.* **234**, 415 (1997).

[5] Z. Zhang, S. Ren, *ACS Appl. Polym. Mater.* **1**, 2197 (2019).

[6] A. Amini, A. Khavari, F. Barthelat, A. J. Ehrlicher, *Science* **373**, 1229 (2021).

[7] A. Simonov, A. L. Goodwin, *Nat. Rev. Chem.* **4**, 657 (2020).

[8] J. M. Rowe, J. J. Rush, E. Prince, *J. Chem. Phys.* **66**, 5147 (1977).

[9] C. S. Coates, H. J. Gray, J. M. Bulled, H. L. B. Boström, A. Simonov, A. L. Goodwin, *Philos. Transact. A Math. Phys. Eng. Sci.* **377**, 20180219 (2019).

[10] A. L. Goodwin, *Nat. Comm.* **10**, 4461 (2019).

[11] M. Paściak, T. R. Welberry, J. Kulda, M. Kempa, J. Hlinka, *Phys. Rev. B* **85**, 224109 (2012).

[12] M. Eremenko, V. Krayzman, A. Bosak, H. Y. Playford, K. W. Chapman, J. C. Woicik, B. Ravel, I. Levin, *Nat. Comm.* **10**, 2728 (2019).

[13] S. J. L. Billinge, I. Levin, *Science* **316**, 561 (2007).

[14] Z. Wang, X.-G. Zhao, R. Koch, S. J. L. Billinge, A. Zunger, *Phys. Rev. B* **102**, 235121 (2020).

[15] P. Juhás, D. M. Cherba, P. M. Duxbury, W. F. Punch, S. J. L. Billinge, *Nature* **440**, 655 (2006).

[16] T. R. Welberry, D. J. Goossens, *IUCrJ* **1**, 550 (2014).

[17] D. A. Keen, A. L. Goodwin, *Nature* **521**, 303 (2015).

[18] M. R. Ahmed, G. A. Gehring, *Phys. Rev. B* **74**, 014420 (2006).

[19] X. Qiu, T. Proffen, J. F. Mitchell, S. J. L. Billinge, *Phys. Rev. Lett.* **94**, 177203 (2005).

[20] A. Sartbaeva, S. A. Wells, M. F. Thorpe, E. S. Božin, S. J. L. Billinge, *Phys. Rev. Lett.* **99**, 155503 (2007).

[21] M. Pissas, I. Margiolaki, G. Papavassiliou, D. Stamopoulos, D. Argyriou, *Phys. Rev. B* **72**, 064425 (2005).

[22] C. N. R. Rao, A. K. Cheetham, *Science* **272**, 369 (1996).

[23] R. Comès, M. Lambert, A. Guinier, *Acta Cryst. A.* **26**, 244 (1970).

[24] W. Zhong, D. Vanderbilt, K. M. Rabe, *Phys. Rev. B* **52**, 6301 (1995).

[25] M. S. Senn, D. A. Keen, T. C. A. Lucas, J. A. Hriljac, A. L. Goodwin, *Phys. Rev. Lett.* **116**, 207602 (2016).

[26] E. H. Wolpert, A. R. Overy, P. M. M. Thygesen, A. Simonov, M. S. Senn, A. L. Goodwin, *Phys. Rev. B* **97**, 134106 (2018).

[27] J.-F. Sadoc, R. Mosseri, *Geometrical Frustration* (Cambridge University Press, 1999).

[28] G. H. Wannier, *Phys. Rev.* **79**, 357 (1950).

[29] A. Simonov, T. Weber, W. Steurer, *J. Appl. Cryst.* **47**, 2011 (2014).

[30] C. S. Zehe, J. A. Hill, N. P. Funnell, K. Kreger, K. P. van der Zwan, A. L. Goodwin, H.-W. Schmidt, J. Senker, *Angew. Chem. Int. Ed.* **56**, 4432 (2017).

[31] B. Rasche, A. Isaeva, M. Ruck, S. Borisenko, V. Zabolotnyy, B. Büchner, K. Koepernik, C. Ortix, M. Richter, J. van den Brink, *Nat. Mater.* **12**, 422 (2013).

[32] T. R. Welberry, A. P. Heerdegen, D. C. Goldstone, I. A. Taylor, *Acta Cryst. B* **67**, 516 (2011).

[33] M. T. Dove, *Structure and Dynamics: An Atomic View of Materials* (Oxford University Press, Oxford, 2003).

[34] O. Delaire, J. Ma, K. Marty, A. F. May, M. A. McGuire, M.-H. Du, D. J. Singh, A. Podlesnyak, G. Ehlers, M. D. Lumsden, B. C. Sales, *Nat. Mater.* **10**, 614 (2011).

[35] S. Christensen, N. Bindzus, M. Sist, M. Takata, B. B. Iversen, *Phys. Chem. Chem. Phys.* **18**, 15874 (2016).

[36] G. W. Watson, S. C. Parker, *J. Phys. Chem. B.* **103**, 1258 (1999).

[37] A. Walsh, D. J. Payne, R. G. Egdell, G. W. Watson, *Chem. Soc. Rev.* **40**, 4455 (2011).

[38] J. M. Skelton, S. C. Parker, A. Togo, I. Tanaka, A. Walsh, *Phys. Rev. B* **89**, 205203 (2014).

[39] Y. Liu, R. L. Withers, H. B. Nguyen, K. Elliott, Q. Ren, Z. Chen, *J. Sol. St. Chem.* **182**, 2748 (2009).

[40] J. R. Esquivel-Elizondo, B. B. Hinojosa, J. C. Nino, *Chem. Mater.* **23**, 4965 (2011).

[41] A. D. B. Woods, W. Cochran, B. N. Brockhouse, *Phys. Rev.* **119**, 980 (1960).

[42] M. Schwoerer-Böhning, A. T. Macrander, D. A. Arms, *Phys. Rev. Lett.* **80**, 5572 (1998).

[43] T. Ruf, J. Serrano, M. Cardona, P. Pavone, M. Pabst, M. Krisch, M. D'Astuto, T. Suski, I. Grzegory, M. Leszczynski, *Phys. Rev. Lett.* **86**, 906 (2001).

[44] M. T. Dove, *Eur. J. Miner.* **14**, 203 (2002).

[45] M. G. Tucker, D. A. Keen, M. T. Dove, *Mineral. Mag.* **65**, 489 (2001).

[46] M. T. Dove, K. O. Trachenko, M. G. Tucker, D. A. Keen, *Rev. Miner. Geo.* **39**, 1 (2000).

[47] J. Weng, E. D. Dill, J. D. Martin, R. Whitfield, C. Hoffmann, F. Ye, *J. Appl. Cryst.* **53**, 159 (2020).

[48] J. Timmermans, *J. Phys. Chem. Sol.* **18**, 1 (1961).

[49] K. Kobashi, R. D. Etters, *Mol. Phys.* **46**, 1077 (1982).

[50] R. W. Impey, M. L. Klein, I. R. McDonald, *J. Chem. Phys.* **82**, 4690 (1985).

[51] G. Coulon, M. Descamps, *J. Phys. Chem. C* **13**, 2847 (1980).

[52] G. Coulon, *J. Phys. Chem. C* **15**, 881 (1982).

[53] M. T. Dove, R. M. Lynden-Bell, *J. Phys. Chem. C* **19**, 3343 (1986).

[54] J. C. W. Folmer, R. L. Withers, T. R. Welberry, J. D. Martin, *Phys. Rev. B* **77**, 144205 (2008).

[55] M. T. Dove, *J. Phys. Chem. C* **19**, 3325 (1986).

[56] M. More, F. Baert, J. Lefebvre, *Acta Cryst. B* **33**, 3681 (1977).

[57] M. More, J. Lefebvre, B. Hennion, B. M. Powell, C. M. E. Zeyen, *J. Phys. C.* **13**, 2833 (1980).

[58] L. Temleitner, L. Pusztai, *Phys. Rev. B* **81**, 134101 (2010).

[59] V. A. Blatov, O. Delgado-Friedrichs, M. O'Keeffe, D. M. Proserpio, *Acta Cryst. A* **63**, 418 (2007).

[60] D. Shechtman, I. Blech, D. Gratias, J. W. Cahn, *Phys. Rev. Lett.* **53**, 1951 (1984).

[61] R. Van Noorden, *Nature* (2011).

[62] A. L. Mackay, *Phys. A: Stat. Mech.* **114**, 609 (1982).

[63] L. A. Bursill, P. Ju Lin, *Nature* **316**, 50 (1985).

[64] T. Yadav, N. Mukhopadhyay, *Curr. Opin. Chem. Eng.* **19**, 163 (2018).

[65] R. Penrose, *J. Math. Anal. Appl.* **10**, 266 (1974).

[66] D. Smith, J. S. Myers, C. S. Kaplan, C. Goodman-Strauss, An aperiodic monotile (2023). ArXiv:2303.10798.

[67] L. Bindi, P. J. Steinhardt, N. Yao, P. J. Lu, *Science* **324**, 1306 (2009).

[68] X. Zeng, G. Ungar, Y. Liu, V. Percec, A. E. Dulcey, J. K. Hobbs, *Nature* **428**, 157 (2004).

[69] T. Dotera, *Isr. J. Chem.* **51**, 1197 (2011).

[70] Z. M. Stadnik, *Physical Properties of Quasicrystals* (Springer Science & Business Media, 1998).

[71] E. G. Noya, C. K. Wong, P. Llombart, J. P. K. Doye, *Nature* **596**, 367 (2021).

[72] R. Veneziano, S. Ratanalert, K. Zhang, F. Zhang, H. Yan, W. Chiu, M. Bathe, *Science* **352**, 1534 (2016).

[73] C. Radin, *Proc. Am. Math. Soc.* **123**, 3543 (1995).

[74] J. E. S. Socolar, J. M. Taylor, *J. Comb. Theory Ser. A.* **118**, 2207 (2011).

[75] J. E. S. Socolar, J. M. Taylor, *Math. Intell.* **34**, 18 (2012).

[76] D. Smith, J. S. Myers, C. S. Kaplan, C. Goodman-Strauss, A chiral aperiodic monotile (2023). ArXiv:2305.17743.

[77] S. Truchet, *Mém. Acad. R. Sci.* pp. 363–372 (1704).

[78] C. S. Smith, P. Boucher, *Leonardo* **20**, 373 (1987).

[79] C. Browne, *Computers & Graphics* **32**, 268 (2008).

[80] A. R. Overy, A. B. Cairns, M. J. Cliffe, A. Simonov, M. G. Tucker, A. L. Goodwin, *Nat. Comm.* **7**, 10445 (2016).

[81] H. Li, M. Eddaoudi, T. L. Groy, O. M. Yaghi, *J. Am. Chem. Soc.* **120**, 8571 (1998).

[82] X. Zhang, Z. Chen, X. Liu, S. L. Hanna, X. Wang, R. Taheri-Ledari, A. Maleki, P. Li, O. K. Farha, *Chem. Soc. Rev.* **49**, 7406 (2020).

[83] A. J. Fletcher, K. M. Thomas, M. J. Rosseinsky, *J. Solid State Chem.* **178**, 2491 (2005).

[84] S. M. Moosavi, A. Nandy, K. M. Jablonka, D. Ongari, J. P. Janet, P. G. Boyd, Y. Lee, B. Smit, H. J. Kulik, *Nat. Comm.* **11**, 4068 (2020).

[85] D. Ongari, L. Talirz, B. Smit, *ACS Cent. Sci.* **6**, 1890 (2020).

[86] *Nat. Chem.* **8**, 987 (2016).

[87] J.-B. Lin, T. T. T. Nguyen, R. Vaidhyanathan, J. Burner, J. M. Taylor, H. Durekova, F. Akhtar, R. K. Mah, O. Ghaffari-Nik, S. Marx, N. Fylstra, S. S. Iremonger, K. W. Dawson, P. Sarkar, P. Hovington, A. Rajendran, T. K. Woo, G. K. H. Shimizu, *Science* **374**, 1464 (2021).

[88] H. Li, M. Eddaoudi, M. O'Keeffe, O. M. Yaghi, *Nature* **402**, 276 (1999).

[89] K. K. Gangu, S. Maddila, S. B. Jonnalagadda, *RSC Adv.* **12**, 14282 (2022).

[90] S. S. Kaye, A. Dailly, O. M. Yaghi, J. R. Long, *J. Am. Chem. Soc.* **129**, 14176 (2007).

[91] S. S. Y. Chui, S. M. F. Lo, J. P. H. Charmant, A. G. Orpen, I. D. Williams, *Science* **283**, 1148 (1999).

[92] K. S. Park, Z. Ni, A. P. Côté, J. Y. Choi, R. Huang, F. J. Uribe-Romo, H. K. Chae, M. O'Keeffe, O. M. Yaghi, *Proc. Natl. Acad. Sci.* **103**, 10186 (2006).

[93] J. H. Cavka, S. Jakobsen, U. Olsbye, N. Guillou, C. Lamberti, S. Bordiga, K. P. Lillerud, *J. Am. Chem. Soc.* **130**, 13850 (2008).

[94] N. L. Rosi, J. Kim, M. Eddaoudi, B. Chen, M. O'Keeffe, O. M. Yaghi, *J. Am. Chem. Soc.* **127**, 1504 (2005).

[95] R. Banerjee, A. Phan, B. Wang, C. Knobler, H. Furukawa, M. O'Keeffe, O. M. Yaghi, *Science* **319**, 939 (2008).

[96] D. Ruano, M. Díaz-García, A. Alfayate, M. Sánchez-Sánchez, *Chem. Cat. Chem.* **7**, 674 (2015).

[97] U. Böhme, B. Barth, C. Paula, A. Kuhnt, W. Schwieger, A. Mundstock, J. Caro, M. Hartmann, *Langmuir* **29**, 8592 (2013).

[98] F. Hoffmann, M. Fröba, *Network Topology* (2016), pp. 5–40.

[99] D. Bara, C. Wilson, M. Mörtel, M. M. Khusniyarov, S. Ling, B. Slater, S. Sproules, R. S. Forgan, *J. Am. Chem. Soc.* **141**, 8346 (2019).

[100] T. Devic, C. Serre, *Chem. Soc. Rev.* **43**, 6097 (2014).

[101] S. Bauer, C. Serre, T. Devic, P. Horcajada, J. Marrot, G. Férey, N. Stock, *Inorg. Chem.* **47**, 7568 (2008).

[102] G. Férey, C. Mellot-Draznieks, C. Serre, F. Millange, J. Dutour, S. Surblé, I. Margiolaki, *Science* **309**, 2040 (2005).

[103] C. Serre, F. Millange, S. Surblé, G. Férey, *Angew. Chem. Int. Ed.* **43**, 6285 (2004).

[104] S. Surblé, C. Serre, C. Mellot-Draznieks, F. Millange, G. Férey, *Chem. Commun.* pp. 284–286 (2006).

[105] P. Horcajada, F. Salles, S. Wuttke, T. Devic, D. Heurtaux, G. Maurin, A. Vimont, M. Daturi, O. David, E. Magnier, N. Stock, Y. Filinchuk, D. Popov, C. Riekel, G. Férey, C. Serre, *J. Am. Chem. Soc.* **133**, 17839 (2011).

[106] T. R. Whitfield, X. Wang, L. Liu, A. J. Jacobson, *Solid State Sci.* **7**, 1096 (2005).

[107] F. Millange, N. Guillou, R. I. Walton, J.-M. Grenèche, I. Margiolaki, G. Férey, *Chem. Commun.* pp. 4732–4734 (2008).

[108] X. Liu, T. Liang, R. Zhang, Q. Ding, S. Wu, C. Li, Y. Lin, Y. Ye, Z. Zhong, M. Zhou, *Amer. Chem. Soc. App. Mater. inter.* **13**, 9643 (2021).

[109] A. Fateeva, P. Horcajada, T. Devic, C. Serre, J. Marrot, J.-M. Grenèche, M. Morcrette, J.-M. Tarascon, G. Maurin, G. Férey, *Eur. J. Inorg. Chem.* **2010**, 3789 (2010).

[110] A. C. Sudik, A. P. Côté, O. M. Yaghi, *Inorg. Chem.* **44**, 2998 (2005).

[111] D. Bara, E. G. Meekel, I. Pakamorė, C. Wilson, S. Ling, R. S. Forgan, *Mater. Horiz.* **8**, 3377 (2021).

[112] M. Eddaoudi, J. Kim, N. Rosi, D. Vodak, J. Wachter, M. O'Keeffe, O. M. Yaghi, *Science* **295**, 469 (2002).

[113] H. Deng, S. Grunder, K. E. Cordova, C. Valente, H. Furukawa, M. Hmadeh, F. Gándara, A. C. Whalley, Z. Liu, S. Asahina, H. Kazumori, M. O'Keeffe, O. Terasaki, J. F. Stoddart, O. M. Yaghi, *Science* **336**, 1018 (2012).

[114] H. Deng, C. J. Doonan, H. Furukawa, R. B. Ferreira, J. Towne, C. B. Knobler, B. Wang, O. M. Yaghi, *Science* **327**, 846 (2010).

[115] L. J. Wang, H. Deng, H. Furukawa, F. Gándara, K. E. Cordova, D. Peri, O. M. Yaghi, *Inorg. Chem.* **53**, 5881 (2014).

[116] J. Gascon, U. Aktay, M. D. Hernandez-Alonso, G. P. M. van Klink, F. Kapteijn, *J. Cat.* **261**, 75 (2009).

[117] S. J. Garibay, S. M. Cohen, *Chem. Commun.* **46**, 7700 (2010).

[118] A. Schaate, P. Roy, T. Preuße, S. J. Lohmeier, A. Godt, P. Behrens, *Chem. Eur. J.* **17**, 9320 (2011).

[119] F. Millange, R. I. Walton, *Isr. J. Chem.* **58**, 1019 (2018).

[120] A. Helal, Z. H. Yamani, K. E. Cordova, O. M. Yaghi, *Nat. Sci. Rev.* **4**, 296 (2017).

[121] V. Guillerm, D. Maspoch, *J. Am. Chem. Soc.* **141**, 16517 (2019).

[122] M. Eddaoudi, J. Kim, M. O'Keeffe, O. M. Yaghi, *J. Am. Chem. Soc.* **124**, 376 (2002).

[123] V. Guillerm, T. Grancha, I. Imaz, J. Juanhuix, D. Maspoch, *J. Am. Chem. Soc.* **140**, 10153 (2018).

[124] M. Eddaoudi, J. Kim, J. B. Wachter, H. K. Chae, M. O'Keeffe, O. M. Yaghi, *J. Am. Chem. Soc.* **123**, 4368 (2001).

[125] J. J. Perry IV, J. A. Perman, M. J. Zaworotko, *Chem. Soc. Rev.* **38**, 1400 (2009).

[126] S. Krause, V. Bon, U. Stoeck, I. Senkovska, D. M. Többens, D. Wallacher, S. Kaskel, *Angew. Chem. Int. Ed.* **56**, 10676 (2017).

[127] V. Bon, V. Senkovskyy, I. Senkovska, S. Kaskel, *Chem. Commun.* **48**, 8407 (2012).

[128] J. Weitkamp, *Solid State Ion.* **131**, 175 (2000).

[129] B. F. Hoskins, R. Robson, *J. Am. Chem. Soc.* **111**, 5962 (1989).

[130] O. M. Yaghi, G. Li, H. Li, *Nature* **378**, 703 (1995).

[131] S. Kitagawa, M. Munakata, T. Tanimura, *Inorg. Chem.* **31**, 1714 (1992).

[132] I. M. Hönicke, I. Senkovska, V. Bon, I. A. Baburin, N. Bönisch, S. Raschke, J. D. Evans, S. Kaskel, *Angew. Chem. Int. Ed.* **57**, 13780 (2018).

[133] L. Sarkisov, *Adv. Mater.* **24**, 3130 (2012).

[134] A. A. Talin, A. Centrone, A. C. Ford, M. E. Foster, V. Stavila, P. Haney, R. A. Kinney, V. Szalai, F. El Gabaly, H. P. Yoon, F. Léonard, M. D. Allendorf, *Science* **343**, 66 (2014).

[135] L. J. Murray, M. Dincă, J. R. Long, *Chem. Soc. Rev.* **38**, 1294 (2009).

[136] D. Alezi, Y. Belmabkhout, M. Suyetin, P. M. Bhatt, Ł. J. Weseliński, V. Solovyeva, K. Adil, I. Spanopoulos, P. N. Trikalitis, A.-H. Emwas, M. Eddaoudi, *J. Am. Chem. Soc.* **137**, 13308 (2015).

[137] E. Adatoz, A. K. Avci, S. Keskin, *Sep. Purif. Technol.* **152**, 207 (2015).

[138] J.-R. Li, R. J. Kuppler, H.-C. Zhou, *Chem. Soc. Rev.* **38**, 1477 (2009).

[139] J. Lee, O. K. Farha, J. Roberts, K. A. Scheidt, S. T. Nguyen, J. T. Hupp, *Chem. Soc. Rev.* **38**, 1450 (2009).

[140] D. Britt, H. Furukawa, B. Wang, T. G. Glover, O. M. Yaghi, *Proc. Natl. Acad. Sci.* **106**, 20637 (2009).

[141] T. M. McDonald, J. A. Mason, X. Kong, E. D. Bloch, D. Gygi, A. Dani, V. Crocellà, F. Giordanino, S. O. Odoh, W. S. Drisdell, B. Vlaisavljevich, A. L. Dzubak, R. Poloni, S. K. Schnell, N. Planas, K. Lee, T. Pascal, L. F. Wan, D. Prendergast, J. B. Neaton, B. Smit, J. B. Kortright, L. Gagliardi, S. Bordiga, J. A. Reimer, J. R. Long, *Nature* **519**, 303 (2015).

[142] T. Chokbunpiam, S. Fritzsche, C. Chmelik, J. Caro, W. Janke, S. Hannongbua, *J. Phys. Chem.* **120**, 23458 (2016).

[143] M. Fujita, Y. J. Kwon, S. Washizu, K. Ogura, *J. Am. Chem. Soc.* **116**, 1151 (1994).

[144] K. Schlichte, T. Kratzke, S. Kaskel, *Micro. Meso. Mater.* **73**, 81 (2004).

[145] F. Vermoortele, M. Vandichel, B. Van de Voorde, R. Ameloot, M. Waroquier, V. Van Speybroeck, D. E. De Vos, *Angew. Chem. Int. Ed.* **51**, 4887 (2012).

[146] A. M. Rasero-Almansa, M. Iglesias, F. Sánchez, *RSC Adv.* **6**, 106790 (2016).

[147] K. Manna, T. Zhang, M. Carboni, C. W. Abney, W. Lin, *J. Am. Chem. Soc.* **136**, 13182 (2014).

[148] G. Lu, S. Li, Z. Guo, O. K. Farha, B. G. Hauser, X. Qi, Y. Wang, X. Wang, S. Han, X. Liu, J. S. DuChene, H. Zhang, Q. Zhang, X. Chen, J. Ma, S. C. J. Loo, W. D. Wei, Y. Yang, J. T. Hupp, F. Huo, *Nat. Chem.* **4**, 310 (2012).

[149] H. Liu, F. C. Strobridge, O. J. Borkiewicz, K. M. Wiaderek, K. W. Chapman, P. J. Chupas, C. P. Grey, *Science* **344**, 1252817 (2014).

[150] A. C. McKinlay, R. E. Morris, P. Horcajada, G. Férey, R. Gref, P. Couvreur, C. Serre, *Angew. Chem. Int. Ed.* **49**, 6260 (2010).

[151] S. Rojas, A. Arenas-Vivo, P. Horcajada, *Coord. Chem. Rev.* **388**, 202 (2019).

[152] H. D. Lawson, S. P. Walton, C. Chan, *ACS Appl. Mater. Interfaces* **13**, 7004 (2021).

[153] P. Jain, V. Ramachandran, R. J. Clark, H. D. Zhou, B. H. Toby, N. S. Dalal, H. W. Kroto, A. K. Cheetham, *J. Am. Chem. Soc.* **131**, 13625 (2009).

[154] W. Li, Z. Zhang, E. G. Bithell, A. S. Batsanov, P. T. Barton, P. J. Saines, P. Jain, C. J. Howard, M. A. Carpenter, A. K. Cheetham, *Acta. Mater.* **61**, 4928 (2013).

[155] C. Schneider, D. Ukaj, R. Koerver, A. A. Talin, G. Kieslich, S. P. Pujari, H. Zuilhof, J. Janek, M. D. Allendorf, R. A. Fischer, *Chem. Sci.* **9**, 7405 (2018).

[156] J.-C. Tan, *Fundamentals of MOF Mechanics & Structure–Mechanical Property Relationships* (The Royal Society of Chemistry, 2023), p. 0.

[157] M. Alhamami, H. Doan, C.-H. Cheng, *Mater.* **7**, 3198 (2014).

[158] J. S. O. Evans, Z. Hu, J. D. Jorgensen, D. N. Argyriou, S. Short, A. W. Sleight, *Science* **275**, 61 (1997).

[159] R. H. Baughman, S. Stafström, C. Cui, S. O. Dantas, *Science* **279**, 1522 (1998).

[160] K. E. Evans, M. A. Nkansah, I. J. Hutchinson, S. C. Rogers, *Nature* **353**, 124 (1991).

[161] G. N. Greaves, A. L. Greer, R. S. Lakes, T. Rouxel, *Nat. Mater.* **10**, 823 (2011).

[162] A. B. Cairns, J. Catafesta, C. Levelut, J. Rouquette, A. van der Lee, L. Peters, A. L. Thompson, V. Dmitriev, J. Haines, A. L. Goodwin, *Nat. Mater.* **12**, 212 (2013).

[163] A. B. Cairns, A. L. Goodwin, *Phys. Chem. Chem. Phys.* **17**, 20449 (2015).

[164] C. Closmann, A. Sleight, J. Haygarth, *J. Solid State Chem.* **139**, 424 (1998).

[165] C. Verdon, D. C. Dunand, *Scr. Mater.* **36**, 1075 (1997).

[166] N. Imanaka, M. Hiraiwa, G. Adachi, H. Dabkowska, A. Dabkowski, *J. Cryst. Gr.* **220**, 176 (2000).

[167] W. J. Clegg, A. Kelly, *Adv. Eng. Mat.* **4**, 388 (2002).

[168] A. Versluis, W. H. Douglas, R. L. Sakaguchi, *Dent. Mater.* **12**, 290 (1996).

[169] K. E. Evans, A. Alderson, *Adv. Mater.* **12**, 617 (2000).

[170] R. H. Baughman, *Nature* **425**, 667 (2003).

[171] J. N. Grima, D. Attard, R. Caruana-Gauci, R. Gatt, *Script. Mater.* **65**, 565 (2011).

[172] A. L. Goodwin, D. A. Keen, M. G. Tucker, *Proc. Natl. Acad. Sci.* **105**, 18708 (2008).

[173] A. D. Fortes, E. Suard, K. S. Knight, *Science* **331**, 742 (2011).

[174] A. L. Goodwin, M. Calleja, M. J. Conterio, M. T. Dove, J. S. O. Evans, D. A. Keen, L. Peters, M. G. Tucker, *Science* **319**, 794 (2008).

[175] A. B. Cairns, A. L. Thompson, M. G. Tucker, J. Haines, A. L. Goodwin, *J. Am. Chem. Soc.* **134**, 4454 (2012).

[176] W. Cai, A. Katrusiak, *Nat. Comm.* **5**, 4337 (2014).

[177] V. K. Peterson, G. J. Kearley, Y. Wu, A. J. Ramirez-Cuesta, E. Kemner, C. J. Kepert, *Angew. Chem. Int. Ed.* **49**, 585 (2010).

[178] P. Serra-Crespo, A. Dikhtiarenko, E. Stavitski, J. Juan-Alcañiz, F. Kapteijn, F.-X. Coudert, J. Gascon, *CrystEngComm* **17**, 276 (2015).

[179] N. Lock, Y. Wu, M. Christensen, L. J. Cameron, V. K. Peterson, A. J. Bridgeman, C. J. Kepert, B. B. Iversen, *J. Phys. Chem. C* **114**, 16181 (2010).

[180] L. H. N. Rimmer, M. T. Dove, A. L. Goodwin, D. C. Palmer, *Phys. Chem. Chem. Phys.* **16**, 21144 (2014).

[181] D. Dubbeldam, K. Walton, D. Ellis, R. Snurr, *Angew. Chem. Int. Ed.* **46**, 4496 (2007).

[182] S. S. Han, W. A. Goddard, *J. Phys. Chem. C* **111**, 15185 (2007).

[183] W. Zhou, H. Wu, T. Yildirim, J. R. Simpson, A. R. H. Walker, *Phys. Rev. B* **78**, 054114 (2008).

[184] J. M. Ogborn, I. E. Collings, S. A. Moggach, A. L. Thompson, A. L. Goodwin, *Chem. Sci.* **3**, 3011 (2012).

[185] A. Marmier, *Anomalous Mechanical Behaviour Arising From Framework Flexibility* (The Royal Society of Chemistry, 2023), p. 0.

[186] M. R. Ryder, B. Civalleri, G. Cinque, J.-C. Tan, *CrystEngComm* **18**, 4303 (2016).

[187] C. Serre, F. Millange, C. Thouvenot, M. Noguès, G. Marsolier, D. Louër, G. Férey, *J. Am. Chem. Soc.* **124**, 13519 (2002).

[188] C. Mellot-Draznieks, C. Serre, S. Surblé, N. Audebrand, G. Férey, *J. Am. Chem. Soc.* **127**, 16273 (2005).

[189] C. Serre, C. Mellot-Draznieks, S. Surblé, N. Audebrand, Y. Filinchuk, G. Férey, *Science* **315**, 1828 (2007).

[190] S. Aguado, G. Bergeret, M. P. Titus, V. Moizan, C. Nieto-Draghi, N. Bats, D. Farrusseng, *New J. Chem.* **35**, 546 (2011).

[191] F.-X. Coudert, *Chem. Phys. Chem.* **18**, 2732 (2017).

[192] T. Ueda, T. Yamatani, M. Okumura, *J. Phys. Chem. C* **123**, 27542 (2019).

[193] K. Biradha, M. Fujita, *Angew. Chem. Int. Ed.* **41**, 3392 (2002).

[194] S. Krause, V. Bon, I. Senkovska, U. Stoeck, D. Wallacher, D. M. Többens, S. Zander, R. S. Pillai, G. Maurin, F.-X. Coudert, S. Kaskel, *Nature* **532**, 348 (2016).

[195] S. B. Choi, H. Furukawa, H. J. Nam, D.-Y. Jung, Y. H. Jhon, A. Walton, D. Book, M. O'Keeffe, O. M. Yaghi, J. Kim, *Angew. Chem. Int. Ed.* **51**, 8791 (2012).

[196] W. Zhou, T. Yildirim, *Phys. Rev. B* **74**, 180301 (2006).

[197] M. Mattesini, J. M. Soler, F. Ynduráin, *Phys. Rev. B* **73**, 094111 (2006).

[198] A. Samanta, T. Furuta, J. Li, *J. Chem. Phys.* **125**, 084714 (2006).

[199] D. F. Bahr, J. A. Reid, W. M. Mook, C. A. Bauer, R. Stumpf, A. J. Skulan, N. R. Moody, B. A. Simmons, M. M. Shindel, M. D. Allendorf, *Phys. Rev. B* **76**, 184106 (2007).

[200] A. J. Graham, D. R. Allan, A. Muszkiewicz, C. A. Morrison, S. A. Moggach, *Angew. Chem. Int. Ed.* **50**, 11138 (2011).

[201] B. Lukose, B. Supronowicz, P. St. Petkov, J. Frenzel, A. B. Kuc, G. Seifert, G. N. Vayssilov, T. Heine, *Phys. Status Solidi B* **249**, 335 (2012).

[202] K. Banlusan, A. Strachan, *J. Chem. Phys.* **146**, 184705 (2017).

[203] J. A. Greathouse, M. D. Allendorf, *J. Phys. Chem. C* **112**, 5795 (2008).

[204] M. Tafipolsky, R. Schmid, *J. Phys. Chem. B* **113**, 1341 (2009).

[205] P. G. Boyd, S. M. Moosavi, M. Witman, B. Smit, *J. Phys. Chem. Lett.* **8**, 357 (2017).

[206] M. Erkartal, M. Durandurdu, *ChemistrySelect* **3**, 8056 (2018).

[207] K. W. Chapman, G. J. Halder, P. J. Chupas, *J. Am. Chem. Soc.* **130**, 10524 (2008).

[208] H. Wu, T. Yildirim, W. Zhou, *J. Phys. Chem. Lett.* **4**, 925 (2013).

[209] A. Gonzalez-Nelson, F.-X. Coudert, M. A. van der Veen, *Nanomaterials* **9**, 330 (2019).

[210] S. L. Gould, D. Tranchemontagne, O. M. Yaghi, M. A. Garcia-Garibay, *J. Am. Chem. Soc.* **130**, 3246 (2008).

[211] M. Tafipolsky, S. Amirjalayer, R. Schmid, *J. Comp. Chem.* **28**, 1169 (2007).

[212] S. Pakhira, M. Takayanagi, M. Nagaoka, *J. Phys. Chem. C* **119**, 28789 (2015).

[213] G. S. Kottas, L. I. Clarke, D. Horinek, J. Michl, *Chem. Rev.* **105**, 1281 (2005).

[214] D. I. Kolokolov, A. G. Stepanov, H. Jobic, *J. Phys. Chem. C* **119**, 27512 (2015).

[215] A. Knebel, B. Geppert, K. Volgmann, D. I. Kolokolov, A. G. Stepanov, J. Twiefel, P. Heitjans, D. Volkmer, J. Caro, *Science* **358**, 347 (2017).

[216] E. Sánchez-González, M. Y. Tsang, J. Troyano, G. A. Craig, S. Furukawa, *Chem. Soc. Rev.* **51**, 4876 (2022).

[217] W. Clegg, A. J. Blake, J. M. Cole, J. S. O. Evans, P. Main, S. Parsons, D. J. Watkin, *Crystal Structure Analysis: Principles and Practice* (Oxford University Press, 2009).

[218] W. Clegg, *X-ray Crystallography* (Oxford University Press, Oxford, 2015), second edn.

[219] A. Authier, G. Chapuis, *A Little Dictionary of Crystallography* (International Union of Crystallography, 2021), third edn.

[220] M. I. Aroyo, ed., *International Tables for Crystallography*, vol. A. (John Wiley & Sons, Ltd, Chichester, 2011), third edn.

[221] A. L. Patterson, *Z. Kristallogr. Cryst. Mater.* **90**, 517 (1935).

[222] J. Karle, H. Hauptman, *Acta Cryst.* **9**, 635 (1956).

[223] L. Palatinus, G. Chapuis, *J. Appl. Cryst.* **40**, 786 (2007).

[224] P. W. Betteridge, J. R. Carruthers, R. I. Cooper, K. Prout, D. J. Watkin, *J. Appl. Cryst.* **36**, 1487 (2003).

[225] O. V. Dolomanov, L. J. Bourhis, R. J. Gildea, J. A. K. Howard, H. Puschmann, *J. Appl. Cryst.* **42**, 339 (2009).

[226] S. R. Hall, F. H. Allen, I. D. Brown, *Acta Cryst. A* **47**, 655 (1991).

[227] A. L. Spek, *J. Appl. Cryst.* **36**, 7 (2003).

[228] G. M. Sheldrick, *Acta Cryst. A* **71**, 3 (2015).

[229] G. M. Sheldrick, *Acta Cryst. C* **71**, 3 (2015).

[230] B. Cernik, *Powder diffraction: theory and practice, edited by Robert E. Dinnebier and Simon Billinge*, vol. 15 (Taylor & Francis, 2009).

[231] G. S. Pawley, *J. Appl. Cryst.* **14**, 357 (1981).

[232] H. M. Rietveld, *J. Appl. Cryst.* **2**, 65 (1969).

[233] A. A. Coelho, *J. Appl. Cryst.* **51**, 210 (2018).

[234] P. Wilmott, *An Introduction to Synchrotron Radiation: Techniques and Applications* (John Wiley & Sons, Ltd, West Sussex, 2019), pp. 51–106.

[235] K. Y. Lonsdale, H. Smith, *Proc. R. Soc. A: Math. Phys. Eng.* **179**, 8 (1997).

[236] T. Weber, *Chimia* **68**, 60 (2014).

[237] T. R. Welberry, T. Weber, *Cryst. Rev.* **22**, 2 (2016).

[238] T. Weber, A. Simonov, *Z. Kristallogr. Cryst. Mater.* **227**, 238 (2012).

[239] T. R. Welberry, *Rep. Prog. Phys.* **48**, 1543 (1985).

[240] T. R. Welberry, B. D. Butler, *Chem. Rev.* **95**, 2369 (1995).

[241] *CrysAlis PRO. Agilent Technologies Ltd, Yarnton, Oxfordshire, England* (2014).

[242] T. R. Welberry, T. Proffen, M. Bown, *Act. Cryst. Sec. A* **54**, 661 (1998).

[243] D. B. Hitchcock, *Am. Stat.* **57**, 254 (2003).

[244] E. J. Chan, D. J. Goossens, *Acta Cryst. B* **68**, 80 (2012).

[245] R. L. McGreevy, *J. Phys. Cond. Mat.* **13**, R877 (2001).

[246] R. G. Parr, S. R. Gadre, L. J. Bartolotti, *Proc. Natl. Acad. Sci.* **76**, 2522 (1979).

[247] L. E. Ratcliff, S. Mohr, G. Huhs, T. Deutsch, M. Masella, L. Genovese, *WIREs Comput. Mol. Sci.* **7**, e1290 (2017).

[248] L. Bellaiche, D. Vanderbilt, *Phys. Rev. B* **61**, 7877 (2000).

[249] T. D. Kühne, M. Iannuzzi, M. Del Ben, V. V. Rybkin, P. Seewald, F. Stein, T. Laino, R. Z. Khaliullin, O. Schütt, F. Schiffmann, D. Golze, J. Wilhelm, S. Chulkov, M. H. Bani-Hashemian, V. Weber, U. Borštnik, M. Taillefumier, A. S. Jakobovits, A. Lazzaro, H. Pabst, T. Müller, R. Schade, M. Guidon, S. Andermatt, N. Holmberg, G. K. Schenter, A. Hehn, A. Bussy, F. Belleflamme, G. Tabacchi, A. Glöß, M. Lass, I. Bethune, C. J. Mundy, C. Plessl, M. Watkins, J. VandeVondele, M. Krack, J. Hutter, *J. Chem. Phys.* **152**, 194103 (2020).

[250] J. P. Perdew, K. Burke, M. Ernzerhof, *Phys. Rev. Lett.* **77**, 3865 (1996).

[251] S. Grimme, J. Antony, S. Ehrlich, H. Krieg, *J. Chem. Phys.* **132**, 154104 (2010).

[252] M. Kobas, T. Weber, W. Steurer, *Phys. Rev. B* **71**, 224205 (2005).

[253] A. Simonov, T. Weber, W. Steurer, *J. Appl. Cryst.* **47**, 1146 (2014).

[254] D. L. Pavia, G. M. Lampman, G. S. Kriz, J. R. Vyvyan, *Introduction to Spectroscopy* (Cengage Learning, 2014), fifth edn.

[255] P. A. Lee, P. H. Citrin, P. Eisenberger, B. M. Kincaid, *Rev. Mod. Phys.* **53**, 769 (1981).

[256] S. Calvin, *XAFS for Everyone* (CRC Press, Boca Raton, 2013), first edn.

[257] J. J. Kas, F. D. Vila, J. J. Rehr, *International Tables for Crystallography* **1** (2020).

[258] A. Bravais, *Analyse mathématique sur les probabilités des erreurs de situation d'un point* (Impr. Royale, 1844).

[259] J. Benesty, J. Chen, Y. Huang, I. Cohen, *Pearson Correlation Coefficient* (Springer Berlin Heidelberg, Berlin, Heidelberg, 2009), pp. 1–4.

[260] G. O. L. F. d'Acapito, A. Puri, A. Laloni, F. L. Manna, E. Dettona, A. D. Luisa, A. Martin, *J. Synchrotron Rad.* **26**, 551 (2019).

[261] K. V. Klementiev, Xafsmass (2012). Freeware: www.desy.de/ klmn/xafsmass.html.

[262] B. Ravel, M. Newville, *J. Synchrotron Rad.* **12**, 537 (2005).

[263] L. D. Hall, *Nuclear Magnetic Resonance* (Aca. Press, 1964), vol. 19, pp. 51–93.

[264] F. A. Bovey, P. A. Mirau, H. S. Gutowksy, *Nuclear Magnetic Resonance Spectroscopy* (Elsevier, 1988).

[265] P. Larkin, *Infrared and Raman Spectroscopy: Principles and Spectral Interpretation* (Elsevier Inc., 2017), second edn.

[266] *LabSolutions IR, Shimadzu Scientific Instruments Inc.* (2015).

[267] *WiRE, Renishaw plc* (2022).

[268] V. A. Blatov, A. P. Shevchenko, D. M. Proserpio, *Cryst. Growth Des.* **14**, 3576 (2014).

[269] S. C. McKellar, S. A. Moggach, *Acta Cryst. B* **71**, 587 (2015).

[270] M. J. Cliffe, A. L. Goodwin, *J. Appl. Cryst.* **45**, 1321 (2012).

[271] J. C. Tan, A. K. Cheetham, *Chem. Soc. Rev.* **40**, 1059 (2011).

[272] W. M. Cohn, *Phys. Rev.* **44**, 326 (1933).

[273] W. Friedrich, P. Knipping, M. von Laue, *Sitz.ber. Bayer. Akad. Wiss.* pp. 303–322 (1912).

[274] W. L. Bragg, *Nature* **90**, 410 (1912).

[275] J. A. Torres, G. Velazquez, *J. Food Eng.* **67**, 95 (2005).

[276] S. A. Moggach, D. R. Allan, S. Parsons, J. E. Warren, *J. Appl. Cryst.* **41**, 249 (2008).

[277] C. E. Weir, E. R. Lippincott, A. Van Valkenburg, E. N. Bunting, *J. Res. Natl. Inst. Stand. Technol.* **63**, 55 (1959).

[278] G. J. Piermarini, *J. Res. Natl. Inst. Stand. Technol.* **106**, 889 (2001).

[279] L. Merrill, W. A. Bassett, *Rev. Sci. Inst.* **45**, 290 (2003).

[280] K. Yokogawa, K. Murata, H. Yoshino, S. Aoyama, *Jpn. J. Appl. Phys.* **46**, 3636 (2007).

[281] R. A. Forman, G. J. Piermarini, J. D. Barnett, S. Block, *Science* **176**, 284 (1972).

[282] A. Dawson, D. R. Allan, S. Parsons, M. Ruf, *J. Appl. Cryst.* **37**, 410 (2004).

[283] Bruker, *Tech. Rep. Bruker AXS Inc., Madison, Wisconsin, USA* (2022).

[284] R. W. Munn, *J. Phys. C.* **5**, 535 (1972).

[285] K. W. Chapman, P. J. Chupas, *J. Am. Chem. Soc.* **129**, 10090 (2007).

[286] R. J. Angel, *Rev. Miner. Geo.* **41**, 35 (2000).

[287] F. Birch, *Phys. Rev.* **71**, 809 (1947).

[288] J. F. Nye, *Physical properties of crystals: their representation by tensors and matrices* (Clarendon Press, Oxford, 1984).

[289] R. E. Newnham, *Properties of materials: anisotropy, symmetry, structure* (Oxford university press, Oxford).

[290] J. B. Pethicai, R. Hutchings, W. C. Oliver, *Phil. Mag. A* **48**, 593 (1983).

[291] G. Pharr, *Mat. Sci. Eng. A* **253**, 151 (1998).

[292] W. Oliver, G. Pharr, *J. Mater. Res.* **19**, 3 (2004).

[293] J. D. Gale, *J. Chem. Soc., Faraday Trans.* **93**, 629 (1997).

[294] J. D. Gale, A. L. Rohl, *Mol. Simul.* **29**, 291 (2003).

[295] R. Gaillac, P. Pullumbi, F.-X. Coudert, *J. Phys. Cond. Mat.* **28**, 275201 (2016).

[296] I. Senkovska, K. A. Cychosz, P. Llewellyn, M. Thommes, S. Kaskel, *Adsorption Methodology* (2016), pp. 575–605.

[297] J. E. Mondloch, O. Karagiaridi, O. K. Farha, J. T. Hupp, *CrystEngComm* **15**, 9258 (2013).

[298] M. Thommes, K. A. Cychosz, *Adsorption* **20**, 233 (2014).

[299] S. Brunauer, P. H. Emmett, E. Teller, *J. Am. Chem. Soc.* **60**, 309 (1938).

[300] M. Thommes, K. Kaneko, A. V. Neimark, J. P. Olivier, F. Rodriguez-Reinoso, J. Rouquerol, K. S. W. Sing, *Pure Appl. Chem.* **87**, 1051 (2015).

[301] S. Sircar, *Ind. Eng. Chem. Res.* **31**, 1813 (1992).

[302] D. Shen, M. Bülow, F. Siperstein, M. Engelhard, A. L. Myers, *Adsorption* **6**, 275 (2000).

[303] A. Nuhnen, C. Janiak, *Dalton Trans.* **49**, 10295 (2020).

[304] R. Clausius, *Ann. Phys.* **155**, 500 (1850).

[305] *3Flex, Micromeritics Instrument Corporation* (2019).

[306] D. Frenkel, B. Smit, *Understanding Molecular Simulation* (Academic Press, San Diego, 2002), second edn.

[307] A. K. Rappe, C. J. Casewit, K. S. Colwell, W. A. I. Goddard, W. M. Skiff, *J. Am. Chem. Soc.* **114**, 10024 (1992).

[308] T. A. Manz, N. G. Limas, *RSC Adv.* **6**, 47771 (2016).

[309] M. Martin, J. Siepmann, *J. Phys. Chem. B* **102**, 2569 (1998).

[310] J. J. Potoff, J. I. Siepmann, *AIChE J.* **47**, 1676 (2001).

[311] D. Dubbeldam, S. Calero, D. E. Ellis, R. Q. Snurr, *Mol. Simul.* **42**, 81 (2016).

[312] C. Healy, K. M. Patil, B. H. Wilson, L. Hermanspahn, N. C. Harvey-Reid, B. I. Howard, C. Kleinjan, J. Kolien, F. Payet, S. G. Telfer, P. E. Kruger, T. D. Bennett, *Coord. Chem. Rev.* **419**, 213388 (2020).

[313] A. P. Shevchenko, A. A. Shabalin, I. Y. Karpukhin, V. A. Blatov, *Sci. Tech. Adv. Mater. Met.* **2**, 250 (2022).

[314] D. Jiang, T. Wen, Y. Guo, J. Liang, Z. Jiang, C. Li, K. Liu, W. Yang, Y. Wang, *Chem. Mater.* **34**, 2764 (2022).

[315] T. Xiao, D. Liu, *Micro. Meso. Mater.* **283**, 88 (2019).

[316] L. Pan, B. Parker, X. Huang, D. H. Olson, Lee, J. Li, *J. Am. Chem. Soc.* **128**, 4180 (2006).

[317] S. A. Jovial, J. Raftery, M. W. Anderson, M. P. Attfield, *Z. Kristallogr. Cryst. Mater.* **233**, 429 (2018).

[318] M. Gupta, M. Ahmad, R. Singh, R. Mishra, J. Sahu, A. K. Gupta, *Polyhedron* **101**, 86 (2015).

[319] N. Wu, Q. Li, J. Li, D. Wu, Y. Li, *Inorg. Chem.* **59**, 9461 (2020).

[320] W. Huang, J. Jiang, D. Wu, J. Xu, B. Xue, A. M. Kirillov, *Inorg. Chem.* **54**, 10524 (2015).

[321] J.-K. Wang, X.-W. Wang, Z.-S. Wang, L.-S. Yao, L.-Z. Niu, Y.-H. Yu, J.-S. Gao, *Polyhedron* **167**, 85 (2019).

[322] H. Hu, J. Zhu, F. Yang, Z. Chen, M. Deng, L. Weng, Y. Ling, Y. Zhou, *Chem. Commun.* **55**, 6495 (2019).

[323] S. Xiaofei, Y. J. X. X. Hong, L. Xiaoju, *Jiegou Huaxue* **34** (2015).

[324] J.-X. Chen, Q.-Y. Fan, *W. Hua. Xue.* **27**, 87 (2011).

[325] C. G. Darwin, *Philos. Mag.* **43**, 800 (1922).

[326] J. Wuttke, *Acta Cryst. A* **70**, 429 (2014).

[327] A. Boulle, D. Chaussende, L. Latu-Romain, F. Conchon, O. Masson, R. Guinebretière, *Appl. Phys. Lett.* **89**, 091902 (2006).

[328] T. G. Mitina, V. A. Blatov, *Cryst. Growth Des.* **13**, 1655 (2013).

[329] G. Chakraborty, I.-H. Park, R. Medishetty, J. J. Vittal, *Chem. Rev.* **121**, 3751 (2021).

[330] N. Stock, S. Biswas, *Chem. Rev.* **112**, 933 (2012).

[331] A. U. Ortiz, A. Boutin, A. H. Fuchs, F.-X. Coudert, *J. Chem. Phys.* **138**, 174703 (2013).

[332] I. E. Collings, M. G. Tucker, D. A. Keen, A. L. Goodwin, *CrystEngComm* **16**, 3498 (2014).

[333] G. Winter, *J. Appl. Cryst.* **43**, 186 (2010).

[334] A. Girard, T. Nguyen-Thanh, S. M. Souliou, M. Stekiel, W. Morgenroth, L. Paolasini, A. Minelli, D. Gambetti, B. Winkler, A. Bosak, *J. Synchrotron Rad.* **26**, 272 (2019).

[335] A. Simonov, Meerkat. version 0.3.6 (2020).

[336] Z. Fang, B. Bueken, D. E. De Vos, R. A. Fischer, *Angew. Chem. Int. Ed.* **54**, 7234 (2015).

[337] A. Simonov, T. De Baerdemaeker, H. L. B. Boström, M. L. Ríos Gómez, H. J. Gray, D. Chernyshov, A. Bosak, H.-B. Bürgi, A. L. Goodwin, *Nature* **578**, 256 (2020).

[338] S. Ehrling, E. M. Reynolds, V. Bon, I. Senkovska, T. E. Gorelik, J. D. Evans, M. Rauche, M. Mendt, M. S. Weiss, A. Pöppl, E. Brunner, U. Kaiser, A. L. Goodwin, S. Kaskel, *Nat. Chem.* **13**, 568 (2021).

[339] T. D. Bennett, A. K. Cheetham, A. H. Fuchs, F.-X. Coudert, *Nat. Chem.* **9**, 11 (2017).

[340] W. Xu, B. Tu, Q. Liu, Y. Shu, C.-C. Liang, C. S. Diercks, O. M. Yaghi, Y.-B. Zhang, H. Deng, Q. Li, *Nat. Rev. Mater.* **5**, 764 (2020).

[341] O. M. Yaghi, M. O'Keeffe, N. W. Ockwig, H. K. Chae, M. Eddaoudi, J. Kim, *Nature* **423**, 705 (2003).

[342] M. O'Keeffe, *Chem. Soc. Rev.* **38**, 1215 (2009).

[343] A. K. Cheetham, T. D. Bennett, F.-X. Coudert, A. L. Goodwin, *Dalton Trans.* **45**, 4113 (2016).

[344] D. S. Sholl, R. P. Lively, *J. Phys. Chem. Lett.* **6**, 3437 (2015).

[345] T. D. Bennett, A. L. Goodwin, M. T. Dove, D. A. Keen, M. G. Tucker, E. R. Barney, A. K. Soper, E. G. Bithell, J.-C. Tan, A. K. Cheetham, *Phys. Rev. Lett.* **104**, 115503 (2010).

[346] D. Umeyama, S. Horike, M. Inukai, T. Itakura, S. Kitagawa, *J. Am. Chem. Soc.* **137**, 864 (2015).

[347] R. Gaillac, P. Pullumbi, K. A. Beyer, K. W. Chapman, D. A. Keen, T. D. Bennett, F.-X. Coudert, *Nat. Mater.* **16**, 1149 (2017).

[348] H. Furukawa, U. Müller, O. M. Yaghi, *Angew. Chem. Int. Ed.* **54**, 3417 (2015).

[349] B. E. G. Lucier, S. Chen, Y. Huang, *Acc. Chem. Res.* **51**, 319 (2018).

[350] D. Zhang, Y. Zhu, L. Liu, X. Ying, C.-E. Hsiung, R. Sougrat, K. Li, Y. Han, *Science* **359**, 675 (2018).

[351] D. N. Johnstone, F. C. N. Firth, C. P. Grey, P. A. Midgley, M. J. Cliffe, S. M. Collins, *J. Am. Chem. Soc.* **142**, 13081 (2020).

[352] S. Ling, R. I. Walton, B. Slater, *Mol. Simul.* **41**, 1348 (2015).

[353] J. P. Dürholt, R. Galvelis, R. Schmid, *Dalton Trans.* **45**, 4370 (2016).

[354] S. M. J. Rogge, *Faraday Discuss.* **225**, 271 (2021).

[355] M. J. Cliffe, W. Wan, X. Zou, P. A. Chater, A. K. Kleppe, M. G. Tucker, H. Wilhelm, N. P. Funnell, F.-X. Coudert, A. L. Goodwin, *Nat. Comm.* **5**, 4176 (2014).

[356] Y. Feng, Q. Chen, M. Jiang, J. Yao, *Ind. Eng. Chem. Res.* **58**, 17646 (2019).

[357] H. Wu, Y. S. Chua, V. Krungleviciute, M. Tyagi, P. Chen, T. Yildirim, W. Zhou, *J. Am. Chem. Soc.* **135**, 10525 (2013).

[358] S. Jakobsen, D. Gianolio, D. S. Wragg, M. H. Nilsen, H. Emerich, S. Bordiga, C. Lamberti, U. Olsbye, M. Tilset, K. P. Lillerud, *Phys. Rev. B* **86**, 125429 (2012).

[359] L. Liu, Z. Chen, J. Wang, D. Zhang, Y. Zhu, S. Ling, K.-W. Huang, Y. Belmabkhout, K. Adil, Y. Zhang, B. Slater, M. Eddaoudi, Y. Han, *Nat. Chem.* **11**, 622 (2019).

[360] A. W. Thornton, R. Babarao, A. Jain, F. Trousselet, F.-X. Coudert, *Dalton Trans.* **45**, 4352 (2016).

[361] K. L. Svane, J. K. Bristow, J. D. Gale, A. Walsh, *J. Mater. Chem. A* **6**, 8507 (2018).

[362] G. C. Shearer, S. Chavan, J. Ethiraj, J. G. Vitillo, S. Svelle, U. Olsbye, C. Lamberti, S. Bordiga, K. P. Lillerud, *Chem. Mater.* **26**, 4068 (2014).

[363] G. Ye, D. Zhang, X. Li, K. Leng, W. Zhang, J. Ma, Y. Sun, W. Xu, S. Ma, *ACS Appl. Mater. Interfaces* **9**, 34937 (2017).

[364] G. C. Shearer, S. Chavan, S. Bordiga, S. Svelle, U. Olsbye, K. P. Lillerud, *Chem. Mater.* **28**, 3749 (2016).

[365] J. M. Taylor, S. Dekura, R. Ikeda, H. Kitagawa, *Chem. Mater.* **27**, 2286 (2015).

[366] M. J. Cliffe, J. A. Hill, C. A. Murray, F.-X. Coudert, A. L. Goodwin, *Phys. Chem. Chem. Phys.* **17**, 11586 (2015).

[367] H. L. B. Boström, G. Kieslich, *J. Phys. Chem. C* **125**, 1467 (2021).

[368] M. Taddei, G. M. Schukraft, M. E. A. Warwick, D. Tiana, M. J. McPherson, D. R. Jones, C. Petit, *J. Mater. Chem. A* **7**, 23781 (2019).

[369] S.-H. Lo, L. Feng, K. Tan, Z. Huang, S. Yuan, K.-Y. Wang, B.-H. Li, W.-L. Liu, G. S. Day, S. Tao, C.-C. Yang, T.-T. Luo, C.-H. Lin, S.-L. Wang, S. J. L. Billinge, K.-L. Lu, Y. J. Chabal, X. Zou, H.-C. Zhou, *Nat. Chem.* **12**, 90 (2020).

[370] L. Sarkisov, *Dalton Trans.* **45**, 4203 (2016).

[371] J. Choi, L.-C. Lin, J. C. Grossman, *J. Phys. Chem. C* **122**, 5545 (2018).

[372] S. Krause, F. S. Reuter, S. Ehrling, V. Bon, I. Senkovska, S. Kaskel, E. Brunner, *Chem. Mater.* **32**, 4641 (2020).

[373] A. Ludi, H. U. Guedel, M. Ruegg, *Inorg. Chem.* **9**, 2224 (1970).

[374] S. S. Kaye, J. R. Long, *J. Am. Chem. Soc.* **127**, 6506 (2005).

[375] P. Franz, C. Ambrus, A. Hauser, D. Chernyshov, M. Hostettler, J. Hauser, L. Keller, K. Krämer, H. Stoeckli-Evans, P. Pattison, H.-B. Bürgi, S. Decurtins, *J. Am. Chem. Soc.* **126**, 16472 (2004).

[376] D. Chernyshov, A. Bosak, *Phase Trans.* **83**, 115 (2010).

[377] M. J. Cliffe, E. N. Keyzer, A. D. Bond, M. A. Astle, C. P. Grey, *Chem. Sci.* **11**, 4430 (2020).

[378] H. L. B. Boström, J. Bruckmoser, A. L. Goodwin, *J. Am. Chem. Soc.* **141**, 17978 (2019).

[379] S.-Y. Zhang, S. Jensen, K. Tan, L. Wojtas, M. Roveto, J. Cure, T. Thonhauser, Y. J. Chabal, M. J. Zaworotko, *J. Am. Chem. Soc.* **140**, 12545 (2018).

[380] S. Abednatanzi, P. Gohari Derakhshandeh, H. Depauw, F.-X. Coudert, H. Vrielinck, P. Van Der Voort, K. Leus, *Chem. Soc. Rev.* **48**, 2535 (2019).

[381] X. Kong, H. Deng, F. Yan, J. Kim, J. A. Swisher, B. Smit, O. M. Yaghi, J. A. Reimer, *Science* **341**, 882 (2013).

[382] S. Yuan, W. Lu, Y.-P. Chen, Q. Zhang, T.-F. Liu, D. Feng, X. Wang, J. Qin, H.-C. Zhou, *J. Am. Chem. Soc.* **137**, 3177 (2015).

[383] S. Canossa, Z. Ji, C. Gropp, Z. Rong, E. Ploetz, S. Wuttke, O. M. Yaghi, *Nat. Rev. Mater.* **8**, 331 (2023).

[384] T. Fukushima, S. Horike, H. Kobayashi, M. Tsujimoto, S. Isoda, M. L. Foo, Y. Kubota, M. Takata, S. Kitagawa, *J. Am. Chem. Soc.* **134**, 13341 (2012).

[385] W. Guo, W. Xia, K. Cai, Y. Wu, B. Qiu, Z. Liang, C. Qu, R. Zou, *Small* **13**, 1702049 (2017).

[386] F. Trousselet, A. Archereau, A. Boutin, F.-X. Coudert, *J. Phys. Chem. C* **120**, 24885 (2016).

[387] M. Taddei, D. Tiana, N. Casati, J. A. van Bokhoven, B. Smit, M. Ranocchiari, *Phys. Chem. Chem. Phys.* **19**, 1551 (2017).

[388] K. A. Lomachenko, J. Jacobsen, A. L. Bugaev, C. Atzori, F. Bonino, S. Bordiga, N. Stock, C. Lamberti, *J. Am. Chem. Soc.* **140**, 17379 (2018).

[389] W. Schrimpf, J. Jiang, Z. Ji, P. Hirschle, D. C. Lamb, O. M. Yaghi, S. Wuttke, *Nat. Comm.* **9**, 1647 (2018).

[390] K. W. P. Orr, S. M. Collins, E. M. Reynolds, F. Nightingale, H. L. B. Boström, S. J. Cassidy, D. M. Dawson, S. E. Ashbrook, O. V. Magdysyuk, P. A. Midgley, A. L. Goodwin, H. H.-M. Yeung, *Chem. Sci.* **12**, 4494 (2021).

[391] Z. Ji, T. Li, O. M. Yaghi, *Science* **369**, 674 (2020).

[392] A. F. Sapnik, H. S. Geddes, E. M. Reynolds, H. H.-M. Yeung, A. L. Goodwin, *Chem. Commun.* **54**, 9651 (2018).

[393] E. M. Reynolds, E. H. Wolpert, A. R. Overy, L. Mizzi, A. Simonov, J. N. Grima, S. Kaskel, A. L. Goodwin, *Faraday Discuss.* **225**, 241 (2021).

[394] T. W. Kemnitzer, C. B. L. Tschense, T. Wittmann, E. A. Rössler, J. Senker, *Langmuir* **34**, 12538 (2018).

[395] P. V. Dau, S. M. Cohen, *Chem. Commun.* **50**, 12154 (2014).

[396] N. Klein, C. Herzog, M. Sabo, I. Senkovska, J. Getzschmann, S. Paasch, M. R. Lohe, E. Brunner, S. Kaskel, *Phys. Chem. Chem. Phys.* **12**, 11778 (2010).

[397] P. S. Petkov, V. Bon, C. L. Hobday, A. B. Kuc, P. Melix, S. Kaskel, T. Düren, T. Heine, *Phys. Chem. Chem. Phys.* **21**, 674 (2019).

[398] J. M. Bermúdez-García, M. Sánchez-Andújar, S. Castro-García, J. López-Beceiro, R. Artiaga, M. A. Señarís-Rodríguez, *Nat. Comm.* **8**, 15715 (2017).

[399] P. Lloveras, E. Stern-Taulats, M. Barrio, J. L. Tamarit, S. Crossley, W. Li, V. Pomjakushin, A. Planes, L. Mañosa, N. D. Mathur, X. Moya, *Nat. Comm.* **6**, 8801 (2015).

[400] P. Schiffer, A. P. Ramirez, D. A. Huse, A. J. Valentino, *Phys. Rev. Lett.* **73**, 2500 (1994).

[401] P. J. Saines, J. A. M. Paddison, P. M. M. Thygesen, M. G. Tucker, *Mater. Horiz.* **2**, 528 (2015).

[402] J. M. Bulled, J. A. M. Paddison, A. Wildes, E. Lhotel, S. J. Cassidy, B. Pato-Doldán, L. C. Gómez-Aguirre, P. J. Saines, A. L. Goodwin, *Phys. Rev. Lett.* **128**, 177201 (2022).

[403] H. L. B. Boström, A. L. Goodwin, *Acc. Chem. Res.* **54**, 1288 (2021).

[404] K. T. Butler, A. Walsh, A. K. Cheetham, G. Kieslich, *Chem. Sci.* **7**, 6316 (2016).

[405] F. C. N. Firth, M. J. Cliffe, D. Vulpe, M. Aragones-Anglada, P. Z. Moghadam, D. Fairen-Jimenez, B. Slater, C. P. Grey, *J. Mater. Chem. A* **7**, 7459 (2019).

[406] S. Leubner, V. E. G. Bengtsson, A. K. Inge, M. Wahiduzzaman, F. Steinke, A. Jaworski, H. Xu, S. Halis, P. Rönfeldt, H. Reinsch, G. Maurin, X. Zou, N. Stock, *Dalton Trans.* **49**, 3088 (2020).

[407] J. Cruddas, B. J. Powell, *J. Am. Chem. Soc.* **141**, 19790 (2019).

[408] M. Eddaoudi, H. Li, O. M. Yaghi, *J. Am. Chem. Soc.* **122**, 1391 (2000).

[409] B. Panella, M. Hirscher, H. Pütter, U. Müller, *Adv. Funct. Mater.* **16**, 520 (2006).

[410] E. V. Perez, K. J. Balkus, J. P. Ferraris, I. H. Musselman, *J. Membr. Sci.* **328**, 165 (2009).

[411] R. B. Potts, *Math. Proc. Cam. Phil. Soc.* **48**, 106 (1952).

[412] P. M. M. Thygesen, J. A. M. Paddison, R. Zhang, K. A. Beyer, K. W. Chapman, H. Y. Playford, M. G. Tucker, D. A. Keen, M. A. Hayward, A. L. Goodwin, *Phys. Rev. Lett.* **118**, 067201 (2017).

[413] J. T. Hughes, A. Navrotsky, *J. Am. Chem. Soc.* **133**, 9184 (2011).

[414] C. K. Brozek, V. K. Michaelis, T.-C. Ong, L. Bellarosa, N. López, R. G. Griffin, M. Dincă, *ACS Central Science* **1**, 252 (2015).

[415] R. B. Neder, T. Proffen, *Diffuse Scattering and Defect Structure Simulations: A cook book using the program DISCUS* (Oxford University Press, Oxford, 2008).

[416] J. A. M. Paddison, *Acta Cryst. A* **75**, 14 (2019).

[417] P. Virtanen, *et al.*, *Nat. Methods* **17**, 261 (2020).

[418] D. Ormrod Morley, A. L. Goodwin, M. Wilson, *Phys. Rev. E* **102**, 062308 (2020).

[419] X. Li, T. Sakai, *Mass Transport in Polymer Gels* (2020), pp. 137–150.

[420] F. A. L. Dullien, *Porous media: Fluid transport and pore structure* (Academic Press, London, 1992), second edn.

[421] C. Coulais, E. Teomy, K. de Reus, Y. Shokef, M. van Hecke, *Nature* **535**, 529 (2016).

[422] K. Liu, R. Sun, C. Daraio, *Science* **377**, 975 (2022).

[423] B. Villemus, J. C. Morel, C. Boutin, *Eng. Struc.* **29**, 2124 (2007).

[424] A. Heyde, L. Guo, C. Jost, G. Theraulaz, L. Mahadevan, *Proc. Natl. Acad. Sci.* **118**, e2006985118 (2021).

[425] F. Kleemiss, S. Grabowsky, O. V. Dolomanov, H. Puschmann, M. Bodensteiner, *Acta Cryst. A* **77**, C906 (2021).

[426] K. W. Chapman, G. J. Halder, P. J. Chupas, *J. Am. Chem. Soc.* **131**, 17546 (2009).

[427] J.-C. Tan, B. Civalleri, C.-C. Lin, L. Valenzano, R. Galvelis, P.-F. Chen, T. D. Bennett, C. Mellot-Draznieks, C. M. Zicovich-Wilson, A. K. Cheetham, *Phys. Rev. Lett.* **108**, 095502 (2012).

[428] M. Erkartal, M. Durandurdu, *Mater. Chem. Phys.* **240**, 122222 (2020).

[429] S. M. J. Rogge, M. Waroquier, V. Van Speybroeck, *Acc. Chem. Res.* **51**, 138 (2018).

[430] Y. H. Hu, L. Zhang, *Phys. Rev. B* **81**, 174103 (2010).

[431] S. Yang, X. Lin, W. Lewis, M. Suyetin, E. Bichoutskaia, J. E. Parker, C. C. Tang, D. R. Allan, P. J. Rizkallah, P. Hubberstey, N. R. Champness, K. Mark Thomas, A. J. Blake, M. Schröder, *Nat. Mater.* **11**, 710 (2012).

[432] M. O. Blunt, J. C. Russell, M. d. C. Giménez-López, J. P. Garrahan, X. Lin, M. Schröder, N. R. Champness, P. H. Beton, *Science* **322**, 1077 (2008).

[433] I. J. Bruno, J. C. Cole, P. R. Edgington, M. Kessler, C. F. Macrae, P. McCabe, J. Pearson, R. Taylor, *Acta Cryst. B* **58**, 389 (2002).

Appendix A: Chapter 3 supplementary information

A1 TRUMOF-1

Table A1.3: Refined site occupancies in TRUMOF-1 obtained in the initial refinement step. The purpose of this refinement was to confirm the interpretation of ligand-site scattering density as reflecting an average over three orientations of 1,3-bdc molecules, each occupied with 25% likelihood. Uncertainties are omitted for constrained variables.

Atom	SOF	$U_{iso}/Å^2$	Wyckoff site	multiplicity	occupancy
Zn1	0.1667	0.0890(13)	$16e$	6	1
O1	0.0417	0.081(8)	$4a$	24	1
O2	0.46(3)	0.118(6)	$96i$	1	0.46(3)
C1	0.23	0.118	$48h$	2	0.46
C2	0.35(2)	0.118	$48h$	2	0.70(4)
C3	0.35	0.118	$48h$	2	0.70

Table A1.4: Crystal data and structure refinement for TRUMOF-1 (at 100 K).

Empirical formula	C_{24} H_{12} O_{13} Zn_4
Formula weight / g mol^{-1}	769.82
Temperature / K	100.0(1)
Crystal system	cubic
Space group	$F\bar{4}3m$
a / Å	15.392(2) Å
α / °	90
V / $Å^3$	3646.3(16)
Z	4
ρ_{calc} / g cm^{-3}	1.4022
μ / mm^{-1}	2.649
F(000)	1520.0
Crystal size / mm^3	0.16 × 0.125 × 0.05
Radiation	MoKα (λ = 0.71073 Å)
2θ range for data collection / °	4.584 – 51.338
Index ranges	$-14 \leq h \leq 18, -18 \leq k \leq 18, -18 \leq l \leq 17$
Reflections collected	6007
Independent reflections	392[R_{int}=0.1096, R_{sigma}=0.0663]
Data/restraints/parameters	392/16/34
Goodness-of-fit on F^2	1.104
Final R indexes [I>2sigma(I)]	R_1 = 0.0615, wR_2 = 0.1569
Final R indexes [all data]	R_1 = 0.0809, wR_2 = 0.1794
Largest diff. peak/hole / e $Å^{-3}$	1.17/–0.51
Flack parameter	0.01(8)

A2 MOX-2

Table A2.5: Crystal data and structure refinement for MOX-2.

Empirical formula	C_{10} H_8 O_5 Zn
Formula weight / g mol^{-1}	273.53
Temperature / K	295.15
Crystal system	orthorhombic
Space group	$P2_12_12_1$
a / Å	11.0562(2)
b / Å	12.6155(2)
c / Å	15.2102(3)
α / °	90
V / Å^3	2121.51(7)
Z	8
ρ_{calc} / g cm^{-3}	1.713
μ / mm^{-1}	2.316
F(000)	1104.0
Crystal size / mm^3	0.18 × 0.40 × 0.40
Radiation	CuKα (λ = 1.54184 Å)
2θ range for data collection / °	6.502 – 61.046
Index ranges	-15 $\leq h \leq$ 13, $-18 \leq k \leq 16, -21 \leq l \leq 19$
Reflections collected	35121
Independent reflections	5669[R_{int}=0.0431, R_{sigma}=0.0327]
Data/restraints/parameters	5669/0/291
Goodness-of-fit on F^2	1.056
Final R indexes [I>2sigma(I)]	R_1 = 0.0431, wR_2 = 0.0327
Final R indexes [all data]	R_1 = 0.0392, wR_2 = 0.0761
Largest diff. peak/hole / e Å^{-3}	0.43/–0.42
Flack parameter	–0.005(6)

A3 MOX-3

Table A3.6: Crystal data and structure refinement for MOX-3 for X = Br.

Empirical formula	C_8 H_3 O_4ZnBr
Formula weight / g mol^{-1}	309.39
Temperature / K	293
Crystal system	trigonal
Space group	$R\bar{3}m$
a / Å	28.4852(3)
b / Å	28.4852(3)
c / Å	7.90520(10)
α / °	90
β / °	90
γ / °	120
V / $Å^3$	5554.97(14)
Z	18
ρ_{calc} / g cm^{-3}	2.127
μ / mm^{-1}	8.292
F(000)	3427.0
Crystal size / mm^3	0.10 × 0.15 × 0.60
Radiation	CuKα (λ = 1.54184 Å)
2θ range for data collection / °	10.758 – 151.982
Index ranges	-35 $\leq h \leq$ 35, $-35 \leq k \leq 34, -7 \leq l \leq 9$
Reflections collected	21620
Independent reflections	1372[R_{int}=0.0644, R_{sigma}=0.068]
Data/restraints/parameters	1372/9/70
Goodness-of-fit on F^2	1.133
Final R indexes [I>2sigma(I)]	R_1 = 0.0613, wR_2 = 0.1998
Final R indexes [all data]	R_1 = 0.0622, wR_2 = 0.2010
Largest diff. peak/hole / e $Å^{-3}$	1.90/–1.70

Table A3.7: Crystal data and structure refinement for MOX-3 for X = Cl.

Empirical formula	C_8 H_3 O_4ZnCl
Formula weight / g mol^{-1}	263.92
Temperature / K	295.15
Crystal system	trigonal
Space group	$R\bar{3}m$
a / Å	28.4445(5)
b / Å	28.4445(5)
c / Å	7.82240(10)
α / °	90
β / °	90
γ / °	120
V / $Å^3$	5481.1(2)
Z	18
ρ_{calc} / g cm^{-3}	1.439
μ / mm^{-1}	4.751
F(000)	2340.0
Crystal size / mm^3	0.10 × 0.15 × 0.60
Radiation	CuKα (λ = 1.54184 Å)
2θ range for data collection / °	10.774 – 151.7
Index ranges	-35 $\leq h \leq$ 35, $-33 \leq k \leq 35$, $-9 \leq l \leq 9$
Reflections collected	24893
Independent reflections	1357[R_{int}=0.0531, R_{sigma}=0.0160]
Data/restraints/parameters	1357/6/69
Goodness-of-fit on F^2	1.124
Final R indexes [I>2sigma(I)]	R_1 = 0.0492, wR_2 = 0.1553
Final R indexes [all data]	R_1 = 0.0515, wR_2 = 0.1576
Largest diff. peak/hole / e $Å^{-3}$	0.94/–0.77

Table A3.8: Crystal data and structure refinement for MOX-3 for X = Cl/Br.

Empirical formula	$C_8\ H_3O_4ZnBr_{0.4}Cl_{0.6}$
Formula weight / g mol^{-1}	282.05
Temperature / K	295.01
Crystal system	trigonal
Space group	$R\bar{3}m$
a / Å	28.4902(4)
b / Å	28.4902(4)
c / Å	7.90730(10)
α / °	90
β / °	90
γ / °	120
V / Å^3	5558.40(17)
Z	18
ρ_{calc} / g cm^{-3}	1.517
μ / mm^{-1}	5.419
F(000)	2472.0
Crystal size / mm^3	0.10 × 0.15 × 0.60
Radiation	CuKα (λ = 1.54184 Å)
2θ range for data collection / °	10.758 – 151.228
Index ranges	-34 $\leq h \leq$ 34, $-34 \leq k \leq 26, -9 \leq l \leq 9$
Reflections collected	7373
Independent reflections	1362[R_{int}=0.0330, R_{sigma}=0.0201]
Data/restraints/parameters	1362/0/70
Goodness-of-fit on F^2	1.103
Final R indexes [I>2sigma(I)]	R_1 = 0.0541, wR_2 = 0.1769
Final R indexes [all data]	R_1 = 0.0560, wR_2 = 0.1792
Largest diff. peak/hole / e Å^{-3}	1.70/–1.14

Table A3.9: Crystal data and structure refinement for MOX-3 for X = I.

Empirical formula	C_8 H_3O_4ZnI
Formula weight / g mol^{-1}	355.37
Temperature / K	290.15
Crystal system	trigonal
Space group	$R\bar{3}m$
a / Å	28.5799(4)
b / Å	28.5799(4)
c / Å	8.09130(10)
α / °	90
β / °	90
γ / °	120
V / $Å^3$	5723.61(18)
Z	18
ρ_{calc} / g cm^{-3}	1.856
μ / mm^{-1}	21.677
F(000)	2988.0
Crystal size / mm^3	0.20 × 0.20 × 0.60
Radiation	CuKα (λ = 1.54184 Å)
2θ range for data collection / °	10.724– 151.978
Index ranges	-35 $\leq h \leq$ 33, $-20 \leq k \leq 35, -10 \leq l \leq 9$
Reflections collected	7511
Independent reflections	1405[R_{int}=0.0194, R_{sigma}=0.0095]
Data/restraints/parameters	1405/8/69
Goodness-of-fit on F^2	1.118
Final R indexes [I>2sigma(I)]	R_1 = 0.0666, wR_2 = 0.2117
Final R indexes [all data]	R_1 = 0.0670, wR_2 = 0.2121
Largest diff. peak/hole / e $Å^{-3}$	3.26/–2.49

A4 MOX-4

Table A4.10: Crystal data and structure refinement for MOX-4.

Empirical formula	C_8 H_6 O_5 S Zn
Formula weight / g mol^{-1}	279.56
Temperature / K	295.109(10)
Crystal system	orthorhombic
Space group	$P2_12_12_1$
a / Å	10.00872(2)
b / Å	13.1876(2)
c / Å	15.0887(2)
α / °	90
V / $Å^3$	2007.19(6)
Z	8
ρ_{calc} / g cm^{-3}	1.850
μ / mm^{-1}	5.382
F(000)	1120.0
Crystal size / mm^3	0.18 × 0.60 × 0.05
Radiation	CuKα (λ = 1.54184 Å)
2θ range for data collection / °	8.906 - 152.082
Index ranges	$-12 \leq h \leq 12, -16 \leq k \leq 8, -18 \leq l \leq 18$
Reflections collected	8263
Independent reflections	3834[R_{int}=0.0358, R_{sigma}=0.0429]
Data/restraints/parameters	3834/0/273
Goodness-of-fit on F^2	1.039
Final R indexes [I>2sigma(I)]	R_1 = 0.0335, wR_2 = 0.0893
Final R indexes [all data]	R_1 = 0.0347, wR_2 = 0.0905
Largest diff. peak/hole / e $Å^{-3}$	0.59/–0.56
Flack parameter	–0.01(2)

A4.1 Comparison MOX-2 and MOX-4 PXRD

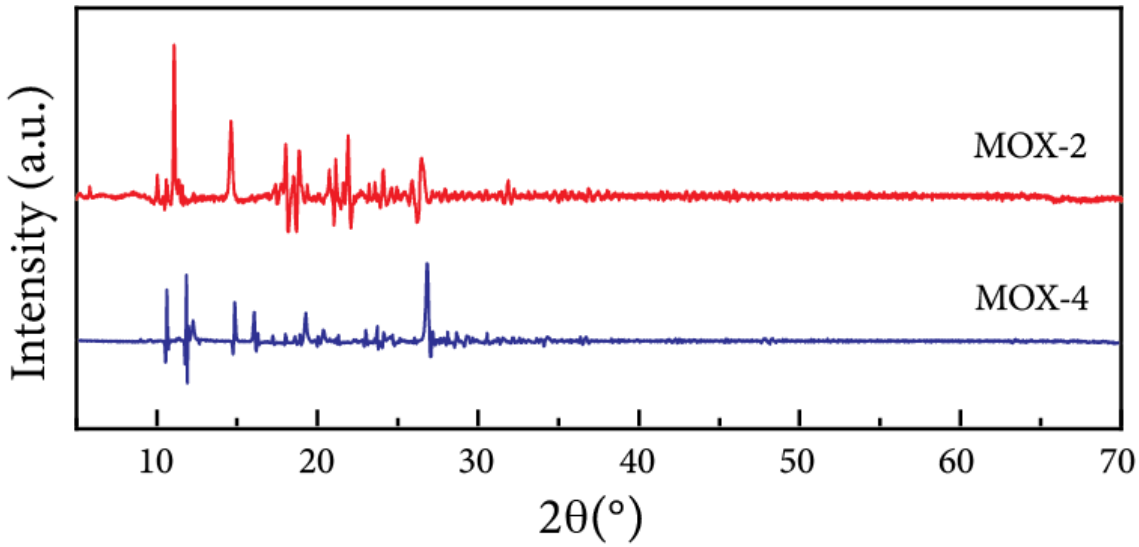

Figure A4.4: Comparison of the difference peaks observed for the Pawley fit for MOX-2 and MOX-4.

A5 MOX-5

Table A5.11: Crystal data and structure refinement for MOX-5.

Empirical formula	C_{11} H_9 O_5NZn
Formula weight / g mol^{-1}	460.38
Temperature / K	300.15
Crystal system	monoclinic
Space group	$P2_1/n$
a / Å	12.8068(2)
b / Å	9.51590(10)
c / Å	16.9226(2)
α / °	90
β / °	111.994(2)
γ / °	90
V / Å^3	1912.24(5)
Z	4
ρ_{calc} / g cm^{-3}	1.599
μ / mm^{-1}	6.815
F(000)	888.0
Crystal size / mm^3	0.05 × 0.40 × 0.70
Radiation	CuKα (λ = 1.54184 Å)
2θ range for data collection / °	7.466 – 152.136
Index ranges	-16 $\leq h \leq$ 16, $-11 \leq k \leq 11, -21 \leq l \leq 20$
Reflections collected	15253
Independent reflections	3947[R_{int}=0.0299, R_{sigma}=0.0277]
Data/restraints/parameters	3947/0/183
Goodness-of-fit on F^2	1.117
Final R indexes [I>2sigma(I)]	R_1 = 0.0300, wR_2 = 0.0898
Final R indexes [all data]	R_1 = 0.0327, wR_2 = 0.0917
Largest diff. peak/hole / e Å^{-3}	0.50/–0.57

Appendix B: Chapter 4 supplementary information

B1 Variable-temperature diffraction data

B1.1 MOX-2 single-crystal variable-temperature data

Table B1.12: Crystal data and structure refinement for MOX-2 at 300 K.

Empirical formula	C_{10} H_7O_5Zn
Formula weight / g mol^{-1}	272.53
Temperature / K	299.99(10)
Crystal system	orthorhombic
Space group	$P2_12_12_1$
a / Å	10.0589(2)
b / Å	12.6127(2)
c / Å	15.2092(2)
α / °	90
V / $Å^3$	2121.42(6)
Z	8
ρ_{calc} / g cm^{-3}	1.713
μ / mm^{-1}	3.286
F(000)	1104.0
Crystal size / mm^3	0.03 × 0.07 × 0.18
Radiation	CuKα (λ = 1.54184 Å)
2θ range for data collection / °	9.108 – 152.014
Index ranges	$-13 \leq h \leq 13, -15 \leq k \leq 15, -19 \leq l \leq 15$
Reflections collected	9516
Independent reflections	4017[R_{int}=0.0312, R_{sigma}=0.0352]
Data/restraints/parameters	4017/0/261
Goodness-of-fit on F^2	1.056
Final R indexes [I>2sigma(I)]	R_1 = 0.0357, wR_2 = 0.1001
Final R indexes [all data]	R_1 = 0.0372, wR_2 = 0.1019
Largest diff. peak/hole / e $Å^{-3}$	0.79/–0.55
Flack parameter	−0.02(2)

Table B1.13: Crystal data and structure refinement for MOX-2 at 250 K.

Empirical formula	C_{10} H_7O_5Zn
Formula weight / g mol^{-1}	272.53
Temperature / K	250.00(10)
Crystal system	orthorhombic
Space group	$P2_12_12_1$
a / Å	10.9191(3)
b / Å	12.5325(4)
c / Å	15.2366(4)
α / °	90
V / Å^3	2096.49(10)
Z	8
ρ_{calc} / g cm^{-3}	1.733
μ / mm^{-1}	3.325
F(000)	1104.0
Crystal size / mm^3	0.03 × 0.07 × 0.18
Radiation	CuKα (λ = 1.54184 Å)
2θ range for data collection / °	9.136 – 140.248
Index ranges	$-13 \leq h \leq 13, -15 \leq k \leq 15, -18 \leq l \leq 11$
Reflections collected	5609
Independent reflections	3254[R_{int}=0.0249, R_{sigma}=0.0351]
Data/restraints/parameters	3254/0/291
Goodness-of-fit on F^2	1.052
Final R indexes [I>2sigma(I)]	R_1 = 0.0309, wR_2 = 0.0820
Final R indexes [all data]	R_1 = 0.0323, wR_2 = 0.0833
Largest diff. peak/hole / e Å^{-3}	0.53/–0.45
Flack parameter	0.03(2)

Table B1.14: Crystal data and structure refinement for MOX-2 at 225 K.

Empirical formula	C_{10} H_7O_5Zn
Formula weight / g mol^{-1}	272.53
Temperature / K	224.99(10)
Crystal system	orthorhombic
Space group	$P2_12_12_1$
a / Å	10.9409(3)
b / Å	12.4881(3)
c / Å	15.2490(3)
α / °	90
V / Å^3	2083.49(9)
Z	8
ρ_{calc} / g cm^{-3}	1.744
μ / mm^{-1}	3.346
F(000)	1104.0
Crystal size / mm^3	0.03 × 0.07 × 0.18
Radiation	CuKα (λ = 1.54184 Å)
2θ range for data collection / °	9.154 – 140.138
Index ranges	$-13 \leq h \leq 13, -15 \leq k \leq 15, -11 \leq l \leq 18$
Reflections collected	5595
Independent reflections	3237[R_{int}=0.0255, R_{sigma}=0.0354]
Data/restraints/parameters	3237/0/291
Goodness-of-fit on F^2	1.063
Final R indexes [I>2sigma(I)]	R_1 = 0.0308, wR_2 = 0.0832
Final R indexes [all data]	R_1 = 0.0322, wR_2 = 0.0843
Largest diff. peak/hole / e Å^{-3}	0.57/–0.45
Flack parameter	−0.03(2)

Table B1.15: Crystal data and structure refinement for MOX-2 at 200 K.

Empirical formula	$C_{10}\ H_7O_5Zn$
Formula weight / g mol^{-1}	272.53
Temperature / K	199.99(10)
Crystal system	orthorhombic
Space group	$P2_12_12_1$
a / Å	10.9004(3)
b / Å	12.4446(3)
c / Å	15.2593(3)
α / °	90
V / Å^3	2069.94(9)
Z	8
ρ_{calc} / g cm^{-3}	1.755
μ / mm^{-1}	3.368
F(000)	1104.0
Crystal size / mm^3	0.03 × 0.07 × 0.18
Radiation	CuKα (λ = 1.54184 Å)
2θ range for data collection / °	9.17 – 140.108
Index ranges	$-13 \leq h \leq 13, -15 \leq k \leq 15, -18 \leq l \leq 11$
Reflections collected	5542
Independent reflections	3221[R_{int}=0.0248, R_{sigma}=0.0359]
Data/restraints/parameters	3221/0/291
Goodness-of-fit on F^2	1.064
Final R indexes [I>2sigma(I)]	R_1 = 0.0305, wR_2 = 0.0838
Final R indexes [all data]	R_1 = 0.0318, wR_2 = 0.0850
Largest diff. peak/hole / e Å^{-3}	0.62/–0.50
Flack parameter	−0.03(2)

Table B1.16: Crystal data and structure refinement for MOX-2 at 175 K.

Empirical formula	C_{10} H_7O_5Zn
Formula weight / g mol^{-1}	272.53
Temperature / K	174.99(10)
Crystal system	orthorhombic
Space group	$P2_12_12_1$
a / Å	10.8710(3)
b / Å	12.4104(3)
c / Å	15.2686(3)
α / °	90
V / Å^3	2059.94(9)
Z	8
ρ_{calc} / g cm^{-3}	1.764
μ / mm^{-1}	3.384
F(000)	1104.0
Crystal size / mm^3	0.03 × 0.07 × 0.18
Radiation	CuKα (λ = 1.54184 Å)
2θ range for data collection / °	9.182 – 140.286
Index ranges	$-13 \leq h \leq 13, -14 \leq k \leq 15, -11 \leq l \leq 18$
Reflections collected	5529
Independent reflections	3224[R_{int}=0.0260, R_{sigma}=0.0378]
Data/restraints/parameters	3224/0/291
Goodness-of-fit on F^2	1.060
Final R indexes [I>2sigma(I)]	R_1 = 0.0315, wR_2 = 0.0854
Final R indexes [all data]	R_1 = 0.0328, wR_2 = 0.0867
Largest diff. peak/hole / e Å^{-3}	0.67/–0.47
Flack parameter	−0.09(2)

Table B1.17: Crystal data and structure refinement for MOX-2 at 150 K.

Empirical formula	C_{10} H_7O_5Zn
Formula weight / g mol^{-1}	272.53
Temperature / K	149.99(10)
Crystal system	orthorhombic
Space group	$P2_12_12_1$
a / Å	10.8500(3)
b / Å	12.3760(3)
c / Å	15.2714(4)
α / °	90
V / Å^3	2050.64(9)
Z	8
ρ_{calc} / g cm^{-3}	1.772
μ / mm^{-1}	3.400
F(000)	1104.0
Crystal size / mm^3	0.03 × 0.07 × 0.18
Radiation	CuKα (λ = 1.54184 Å)
2θ range for data collection / °	9.198 – 140.04
Index ranges	$-13 \leq h \leq 13, -14 \leq k \leq 15, -11 \leq l \leq 18$
Reflections collected	5282
Independent reflections	3181[R_{int}=0.0299, R_{sigma}=0.0434]
Data/restraints/parameters	3181/0/291
Goodness-of-fit on F^2	1.068
Final R indexes [I>2sigma(I)]	R_1 = 0.0356, wR_2 = 0.0991
Final R indexes [all data]	R_1 = 0.0375, wR_2 = 0.1007
Largest diff. peak/hole / e Å^{-3}	0.78/–0.42
Flack parameter	−0.07(2)

Table B1.18: Crystal data and structure refinement for MOX-2 at 125 K.

Empirical formula	C_{10} H_7O_5Zn
Formula weight / g mol^{-1}	272.53
Temperature / K	124.99(10)
Crystal system	orthorhombic
Space group	$P2_12_12_1$
a / Å	10.8240(3)
b / Å	12.3473(4)
c / Å	15.2751(3)
α / °	90
V / Å^3	2041.47(10)
Z	8
ρ_{calc} / g cm^{-3}	1.780
μ / mm^{-1}	3.415
F(000)	1104.0
Crystal size / mm^3	0.03 × 0.07 × 0.18
Radiation	CuKα (λ = 1.54184 Å)
2θ range for data collection / °	9.21 – 140.198
Index ranges	$-13 \leq h \leq 12, -14 \leq k \leq 15, -11 \leq l \leq 18$
Reflections collected	5413
Independent reflections	3174[R_{int}=0.0263, R_{sigma}=0.0384]
Data/restraints/parameters	3174/0/291
Goodness-of-fit on F^2	1.064
Final R indexes [I>2sigma(I)]	R_1 = 0.0342, wR_2 = 0.0895
Final R indexes [all data]	R_1 = 0.0357, wR_2 = 0.0910
Largest diff. peak/hole / e Å^{-3}	0.96/–0.47
Flack parameter	−0.04(3)

Table B1.19: Crystal data and structure refinement for MOX-2 at 100 K.

Empirical formula	C_{10} H_7O_5Zn
Formula weight / g mol^{-1}	272.53
Temperature / K	99.97(12)
Crystal system	orthorhombic
Space group	$P2_12_12_1$
a / Å	10.8044(3)
b / Å	12.3135(4)
c / Å	15.2821(4)
α / °	90
V / Å^3	2033.13(10)
Z	8
ρ_{calc} / g cm^{-3}	1.787
μ / mm^{-1}	3.429
F(000)	1104.0
Crystal size / mm^3	0.03 × 0.07 × 0.18
Radiation	CuKα (λ = 1.54184 Å)
2θ range for data collection / °	9.22 – 139.756
Index ranges	$-13 \leq h \leq 12, -14 \leq k \leq 14, -11 \leq l \leq 18$
Reflections collected	5398
Independent reflections	3169[R_{int}=0.0309, R_{sigma}=0.0440]
Data/restraints/parameters	3169/0/291
Goodness-of-fit on F^2	1.058
Final R indexes [I>2sigma(I)]	R_1 = 0.0355, wR_2 = 0.0938
Final R indexes [all data]	R_1 = 0.0371, wR_2 = 0.0956
Largest diff. peak/hole / e Å^{-3}	1.10/–0.55
Flack parameter	−0.07(3)

B1.2 MOX-4 single-crystal variable-temperature data

Table B1.20: Crystal data and structure refinement for MOX-4 at 300 K.

Empirical formula	$C_8\ H_6O_5SZn$
Formula weight / g mol^{-1}	279.56
Temperature / K	299.99(10)
Crystal system	orthorhombic
Space group	$P2_12_12_1$
a / Å	10.08380(10)
b / Å	12.1797(2)
c / Å	15.0722(2)
α / °	90
V / Å^3	2003.12(5)
Z	8
ρ_{calc} / g cm^{-3}	1.854
μ / mm^{-1}	5.393
F(000)	1120.0
Crystal size / mm^3	0.02 × 0.12 × 0.2
Radiation	CuKα (λ = 1.54184 Å)
2θ range for data collection / °	8.912 – 151.41
Index ranges	$-5 \leq h \leq 12, -16 \leq k \leq 16, -15 \leq l \leq 18$
Reflections collected	6824
Independent reflections	3498[R_{int}=0.0229, R_{sigma}=0.0306]
Data/restraints/parameters	3498/0/273
Goodness-of-fit on F^2	1.053
Final R indexes [I>2sigma(I)]	R_1 = 0.0300, wR_2 = 0.0813
Final R indexes [all data]	R_1 = 0.0307, wR_2 = 0.0820
Largest diff. peak/hole / e Å^{-3}	0.46/–0.59
Flack parameter	−0.000(15)

Table B1.21: Crystal data and structure refinement for MOX-4 at 275 K.

Empirical formula	C_8 H_6O_5SZn
Formula weight / g mol^{-1}	279.56
Temperature / K	274.97(10)
Crystal system	orthorhombic
Space group	$P2_12_12_1$
a / Å	10.09680(10)
b / Å	13.1645(2)
c / Å	15.0383(2)
α / °	90
V / Å^3	1998.88(4)
Z	8
ρ_{calc} / g cm^{-3}	1.858
μ / mm^{-1}	5.404
F(000)	1120.0
Crystal size / mm^3	0.02 × 0.12 × 0.2
Radiation	CuKα (λ = 1.54184 Å)
2θ range for data collection / °	8.928 – 151.282
Index ranges	$-12 \leq h \leq 5, -16 \leq k \leq 16, -18 \leq l \leq 15$
Reflections collected	6799
Independent reflections	3489[R_{int}=0.0222, R_{sigma}=0.0290]
Data/restraints/parameters	3489/0/273
Goodness-of-fit on F^2	1.064
Final R indexes [I>2sigma(I)]	R_1 = 0.0297, wR_2 = 0.0806
Final R indexes [all data]	R_1 = 0.0304, wR_2 = 0.0811
Largest diff. peak/hole / e Å^{-3}	0.41/–0.57
Flack parameter	−0.004(15)

Table B1.22: Crystal data and structure refinement for MOX-4 at 250 K.

Empirical formula	C_8 H_6O_5SZn
Formula weight / g mol^{-1}	279.56
Temperature / K	250.00(10)
Crystal system	orthorhombic
Space group	$P2_12_12_1$
a / Å	10.11000(10)
b / Å	13.1486(2)
c / Å	14.9932(2)
α / °	90
V / Å^3	1993.08(4)
Z	8
ρ_{calc} / g cm^{-3}	1.863
μ / mm^{-1}	5.420
F(000)	1120.0
Crystal size / mm^3	0.02 × 0.12 × 0.2
Radiation	CuKα (λ = 1.54184 Å)
2θ range for data collection / °	8.946 – 151.312
Index ranges	$-12 \leq h \leq 5, -16 \leq k \leq 16, -18 \leq l \leq 15$
Reflections collected	6765
Independent reflections	3479[R_{int}=0.0227, R_{sigma}=0.0300]
Data/restraints/parameters	3479/0/273
Goodness-of-fit on F^2	1.084
Final R indexes [I>2sigma(I)]	R_1 = 0.0290, wR_2 = 0.0769
Final R indexes [all data]	R_1 = 0.0296, wR_2 = 0.0775
Largest diff. peak/hole / e Å^{-3}	0.43/–0.54
Flack parameter	−0.023(14)

Table B1.23: Crystal data and structure refinement for MOX-4 at 225 K.

Empirical formula	C_8 H_6O_5SZn
Formula weight / g mol^{-1}	279.56
Temperature / K	225.00(10)
Crystal system	orthorhombic
Space group	$P2_12_12_1$
a / Å	10.12260(10)
b / Å	13.1330(2)
c / Å	14.9537(2)
α / °	90
V / Å^3	1987.95(4)
Z	8
ρ_{calc} / g cm^{-3}	1.868
μ / mm^{-1}	5.434
F(000)	1120.0
Crystal size / mm^3	0.02 × 0.12 × 0.2
Radiation	CuKα (λ = 1.54184 Å)
2θ range for data collection / °	8.962 – 151.132
Index ranges	$-12 \leq h \leq 5, -16 \leq k \leq 16, -18 \leq l \leq 15$
Reflections collected	6737
Independent reflections	3474[R_{int}=0.0219, R_{sigma}=0.0293]
Data/restraints/parameters	3474/0/273
Goodness-of-fit on F^2	1.066
Final R indexes [I>2sigma(I)]	R_1 = 0.0286, wR_2 = 0.0774
Final R indexes [all data]	R_1 = 0.0294, wR_2 = 0.0782
Largest diff. peak/hole / e Å^{-3}	0.51/–0.55
Flack parameter	0.003(14)

Table B1.24: Crystal data and structure refinement for MOX-4 at 200 K.

Empirical formula	C_8 H_6O_5SZn
Formula weight / g mol^{-1}	279.56
Temperature / K	200.00(10)
Crystal system	orthorhombic
Space group	$P2_12_12_1$
a / Å	10.13240(10)
b / Å	13.1203(2)
c / Å	14.9106(2)
α / °	90
V / Å^3	1982.22(4)
Z	8
ρ_{calc} / g cm^{-3}	1.874
μ / mm^{-1}	5.450
F(000)	1120.0
Crystal size / mm^3	0.02 × 0.12 × 0.2
Radiation	CuKα (λ = 1.54184 Å)
2θ range for data collection / °	8.978 – 151.798
Index ranges	$-5 \leq h \leq 12, -16 \leq k \leq 16, -14 \leq l \leq 18$
Reflections collected	6704
Independent reflections	3452[R_{int}=0.0208, R_{sigma}=0.0280]
Data/restraints/parameters	3452/0/273
Goodness-of-fit on F^2	1.000
Final R indexes [I>2sigma(I)]	R_1 = 0.0295, wR_2 = 0.0851
Final R indexes [all data]	R_1 = 0.0301, wR_2 = 0.0860
Largest diff. peak/hole / e Å^{-3}	0.58–0.61
Flack parameter	−0.016(14)

Table B1.25: Crystal data and structure refinement for MOX-4 at 175 K.

Empirical formula	C_8 H_6O_5SZn
Formula weight / g mol^{-1}	279.56
Temperature / K	174.99(10)
Crystal system	orthorhombic
Space group	$P2_12_12_1$
a / Å	10.13470(10)
b / Å	13.1268(2)
c / Å	14.8388(2)
α / °	90
V / Å^3	1974.10(4)
Z	8
ρ_{calc} / g cm^{-3}	1.881
μ / mm^{-1}	5.472
F(000)	1120.0
Crystal size / mm^3	0.02 × 0.12 × 0.2
Radiation	CuKα (λ = 1.54184 Å)
2θ range for data collection / °	8.994 – 151.282
Index ranges	$-5 \leq h \leq 12, -16 \leq k \leq 16, -14 \leq l \leq 18$
Reflections collected	6669
Independent reflections	3434[R_{int}=0.0219, R_{sigma}=0.0299]
Data/restraints/parameters	3434/0/273
Goodness-of-fit on F^2	1.052
Final R indexes [I>2sigma(I)]	R_1 = 0.0335, wR_2 = 0.0904
Final R indexes [all data]	R_1 = 0.0342, wR_2 = 0.0912
Largest diff. peak/hole / e Å^{-3}	0.61/–0.60
Flack parameter	0.003(15)

Table B1.26: Crystal data and structure refinement for MOX-4 at 150 K.

Empirical formula	C_8 H_6O_5SZn
Formula weight / g mol^{-1}	279.56
Temperature / K	150.00(10)
Crystal system	orthorhombic
Space group	$P2_12_12_1$
a / Å	10.14000(10)
b / Å	13.1252(2)
c / Å	14.7829(2)
α / °	90
V / Å^3	1967.45(4)
Z	8
ρ_{calc} / g cm^{-3}	1.888
μ / mm^{-1}	5.491
F(000)	1120.0
Crystal size / mm^3	0.02 × 0.12 × 0.2
Radiation	CuKα (λ = 1.54184 Å)
2θ range for data collection / °	9.01 – 151.196
Index ranges	$-5 \leq h \leq 12, -16 \leq k \leq 16, -15 \leq l \leq 18$
Reflections collected	6647
Independent reflections	3415[R_{int}=0.0228, R_{sigma}=0.0296]
Data/restraints/parameters	3415/0/273
Goodness-of-fit on F^2	1.033
Final R indexes [I>2sigma(I)]	R_1 = 0.0377, wR_2 = 0.1011
Final R indexes [all data]	R_1 = 0.0384, wR_2 = 0.1020
Largest diff. peak/hole / e Å^{-3}	1.01/–0.57
Flack parameter	−0.014(15)

Table B1.27: Crystal data and structure refinement for MOX-4 at 125 K.

Empirical formula	C_8 H_6O_5SZn
Formula weight / g mol^{-1}	279.56
Temperature / K	12500(10)
Crystal system	orthorhombic
Space group	$P2_12_12_1$
a / Å	10.14780(10)
b / Å	13.1117(2)
c / Å	14.7524(2)
α / °	90
V / Å^3	1962.88(4)
Z	8
ρ_{calc} / g cm^{-3}	1.892
μ / mm^{-1}	5.503
F(000)	1120.0
Crystal size / mm^3	0.02 × 0.12 × 0.2
Radiation	CuKα (λ = 1.54184 Å)
2θ range for data collection / °	9.024 – 151.324
Index ranges	$-5 \leq h \leq 12, -16 \leq k \leq 16, -15 \leq l \leq 18$
Reflections collected	6643
Independent reflections	3416[R_{int}=0.0246, R_{sigma}=0.0320]
Data/restraints/parameters	3416/0/273
Goodness-of-fit on F^2	1.039
Final R indexes [I>2sigma(I)]	R_1 = 0.0377, wR_2 = 0.997
Final R indexes [all data]	R_1 = 0.0383, wR_2 = 0.1003
Largest diff. peak/hole / e Å^{-3}	0.90/–0.61
Flack parameter	0.006(16)

Table B1.28: Crystal data and structure refinement for MOX-4 at 100 K.

Empirical formula	C_8 H_6O_5SZn
Formula weight / g mol^{-1}	279.56
Temperature / K	99.97(16)
Crystal system	orthorhombic
Space group	$P2_12_12_1$
a / Å	10.15680(10)
b / Å	13.1007(2)
c / Å	14.7229(2)
α / °	90
V / Å^3	1959.05(4)
Z	8
ρ_{calc} / g cm^{-3}	1.896
μ / mm^{-1}	5.514
F(000)	1120.0
Crystal size / mm^3	0.02 × 0.12 × 0.2
Radiation	CuKα (λ = 1.54184 Å)
2θ range for data collection / °	9.036 – 151.41
Index ranges	$-5 \leq h \leq 12, -16 \leq k \leq 16, -15 \leq l \leq 18$
Reflections collected	6608
Independent reflections	3407[R_{int}=0.0258, R_{sigma}=0.0337]
Data/restraints/parameters	3407/0/273
Goodness-of-fit on F^2	1.047
Final R indexes [I>2sigma(I)]	R_1 = 0.0378, wR_2 = 0.0998
Final R indexes [all data]	R_1 = 0.0385, wR_2 = 0.1007
Largest diff. peak/hole / e Å^{-3}	0.92/–0.69
Flack parameter	−0.015(17)

B1.3 Structural changes

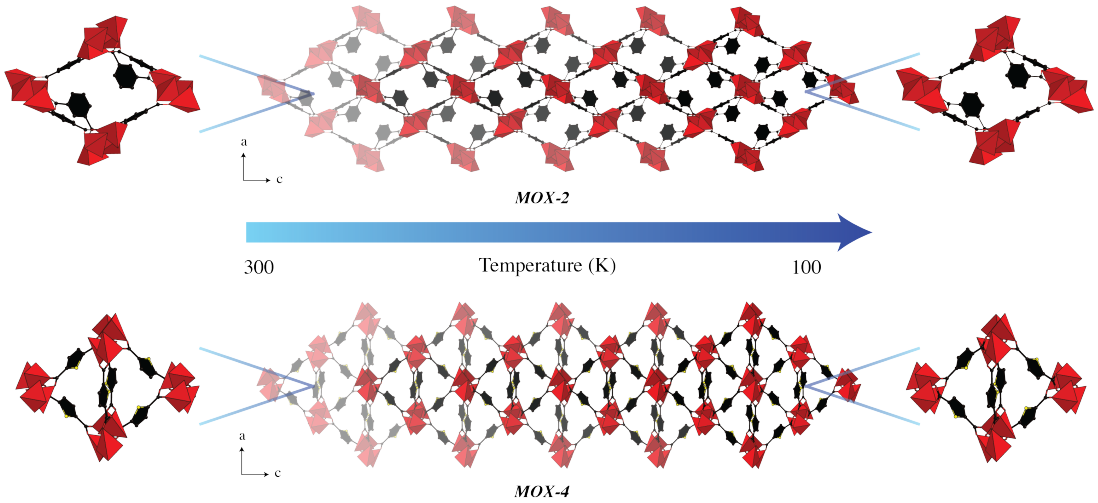

Figure B1.5: Structural changes of MOX-2 (top) and MOX-4 (bottom) as derived from variable-temperature SCXRD, showing the wine-rack structure in the ac-plane.

B2 High-pressure diffraction data

B2.1 MOX-2 single-crystal high-pressure data

Table B2.29: Crystal data and structure refinement for MOX-2 at 0.1(1) GPa.

Empirical formula	$C_{10}\ H_7O_5Zn$
Formula weight / g mol^{-1}	272.53
Temperature / K	293(2)
Crystal system	orthorhombic
Space group	$P2_12_12_1$
a / Å	10.9060(2)
b / Å	12.38910(10)
c / Å	15.22400(10)
α / °	90
V / Å^3	2057.00(4)
Z	8
ρ_{calc} / g cm^{-3}	1.760
μ / mm^{-1}	0.838
F(000)	1096.0
Crystal size / mm^3	0.03 × 0.07 × 0.18
Radiation	(λ = 0.4859 Å)
2θ range for data collection / °	2.898 – 52.426
Index ranges	-12 $\leq h \leq$ 12, $-14 \leq k \leq 16, -22 \leq l \leq 22$
Reflections collected	12276
Independent reflections	4975[R_{int}=0.0467, R_{sigma}=0.0449]
Data/restraints/parameters	4975/0/265
Goodness-of-fit on F^2	1.199
Final R indexes [I>2sigma(I)]	R_1 = 0.0407, wR_2 = 0.1376
Final R indexes [all data]	R_1 = 0.0559, wR_2 = 0.1892
Largest diff. peak/hole / e Å^{-3}	0.71/–0.78
Flack parameter	0.01(4)

Table B2.30: Crystal data and structure refinement for MOX-2 at 0.26(1) GPa.

Empirical formula	$C_{10}H_8O_5Zn$
Formula weight / g mol^{-1}	273.53
Temperature / K	293(2)
Crystal system	orthorhombic
Space group	$P2_12_12_1$
a / Å	10.7947(2)
b / Å	12.22500(10)
c / Å	15.22340(10)
α / °	90
V / Å^3	2008.96(4)
Z	8
ρ_{calc} / g cm^{-3}	1.809
μ / mm^{-1}	0.858
F(000)	1104.0
Crystal size / mm^3	0.03 × 0.07 × 0.18
Radiation	(λ = 0.4859 Å)
2θ range for data collection / °	2.922 – 52.184
Index ranges	-12 $\leq h \leq$ 12, $-14 \leq k \leq 16, -22 \leq l \leq 22$
Reflections collected	12002
Independent reflections	4892[R_{int}=0.0527, R_{sigma}=0.0544]
Data/restraints/parameters	4892/0/261
Goodness-of-fit on F^2	1.094
Final R indexes [I>2sigma(I)]	R_1 = 0.0444, wR_2 = 0.1430
Final R indexes [all data]	R_1 = 0.0609, wR_2 = 0.1911
Largest diff. peak/hole / e Å^{-3}	0.79/–0.87
Flack parameter	0.01(5)

Table B2.31: Crystal data and structure refinement for MOX-2 at 0.52(3) GPa.

Empirical formula	C_{20} H_{16} O_{10} Zn_2
Formula weight / g mol^{-1}	273.53
Temperature / K	293(2)
Crystal system	orthorhombic
Space group	$P2_12_12_1$
a / Å	10.6488(2)
b / Å	11.99100(10)
c / Å	15.2085(2)
α / °	90
V / Å^3	1941.97(5)
Z	8
ρ_{calc} / g cm^{-3}	0.549
μ / mm^{-1}	0.839
F(000)	1104.0
Crystal size / mm^3	0.03 × 0.07 × 0.18
Radiation	(λ = 0.4859 Å)
2θ range for data collection / °	2.956 – 53.224
Index ranges	-12 $\leq h \leq$ 12, $-13 \leq k \leq 16, -22 \leq l \leq 22$
Reflections collected	11572
Independent reflections	4742[R_{int}=0.0480, R_{sigma}=0.0468]
Data/restraints/parameters	4742/0/261
Goodness-of-fit on F^2	1.171
Final R indexes [I>2sigma(I)]	R_1 = 0.0445, wR_2 = 0.1497
Final R indexes [all data]	R_1 = 0.0621, wR_2 = 0.1976
Largest diff. peak/hole / e Å^{-3}	0.62/–0.96
Flack parameter	–0.01(6)

Table B2.32: Crystal data and structure refinement for MOX-2 at 0.72(3) GPa.

Empirical formula	$C_{10}H_8O_5Zn$
Formula weight / g mol^{-1}	273.53
Temperature / K	293(2)
Crystal system	orthorhombic
Space group	$P2_12_12_1$
a / Å	10.5798(2)
b / Å	11.87340(10)
c / Å	15.1917(2)
α / °	90
V / Å^3	1908.35(5)
Z	8
ρ_{calc} / g cm^{-3}	0.605
μ / mm^{-1}	0.854
F(000)	1104.0
Crystal size / mm^3	0.03 × 0.07 × 0.18
Radiation	(λ = 0.4859 Å)
2θ range for data collection / °	2.976 – 52.972
Index ranges	-12 $\leq h \leq$ 12, $-15 \leq k \leq 13, -21 \leq l \leq 21$
Reflections collected	11372
Independent reflections	4679[R_{int}=0.0568, R_{sigma}=0.0630]
Data/restraints/parameters	4679/0/261
Goodness-of-fit on F^2	1.163
Final R indexes [I>2sigma(I)]	R_1 = 0.0420, wR_2 = 0.1413
Final R indexes [all data]	R_1 = 0.0631, wR_2 = 0.1906
Largest diff. peak/hole / e Å^{-3}	0.72/–0.86
Flack parameter	0.00(5)

Table B2.33: Crystal data and structure refinement for MOX-2 at 0.81(4) GPa.

Empirical formula	$C_{10}H_8O_5Zn$
Formula weight / g mol^{-1}	273.53
Temperature / K	293(2)
Crystal system	orthorhombic
Space group	$P2_12_12_1$
a / Å	10.5412(2)
b / Å	11.80700(10)
c / Å	15.1771(2)
α / °	90
V / Å^3	1888.94(5)
Z	4
ρ_{calc} / g cm^{-3}	1.924
μ / mm^{-1}	0.913
F(000)	1104.0
Crystal size / mm^3	0.03 × 0.07 × 0.18
Radiation	(λ = 0.4859 Å)
2θ range for data collection / °	2.988 – 53.142
Index ranges	-12 $\leq h \leq$ 12, $-15 \leq k \leq 13, -22 \leq l \leq 22$
Reflections collected	11235
Independent reflections	4618[R_{int}=0.0567, R_{sigma}=0.0622]
Data/restraints/parameters	4618/0/261
Goodness-of-fit on F^2	1.148
Final R indexes [I>2sigma(I)]	R_1 = 0.0435, wR_2 = 0.1345
Final R indexes [all data]	R_1 = 0.0633, wR_2 = 0.1862
Largest diff. peak/hole / e Å^{-3}	0.64/–0.84
Flack parameter	0.00(2)

Table B2.34: Crystal data and structure refinement for MOX-2 at 0.96(5) GPa.

Empirical formula	$C_{10}H_8O_5Zn$
Formula weight / g mol^{-1}	273.53
Temperature / K	293(2)
Crystal system	orthorhombic
Space group	$P2_12_12_1$
a / Å	10.5021(2)
b / Å	11.73650(10)
c / Å	15.1588(2)
α / °	90
V / Å^3	1868.44(5)
Z	8
ρ_{calc} / g cm^{-3}	1.945
μ / mm^{-1}	0.923
F(000)	1104.0
Crystal size / mm^3	0.03 × 0.07 × 0.18
Radiation	(λ = 0.4859 Å)
2θ range for data collection / °	3 – 53.328
Index ranges	$-12 \leq h \leq 12, -15 \leq k \leq 13, -22 \leq l \leq 22$
Reflections collected	11161
Independent reflections	4579[R_{int}=0.0490, R_{sigma}=0.0533]
Data/restraints/parameters	4579/0/261
Goodness-of-fit on F^2	1.183
Final R indexes [I>2sigma(I)]	R_1 = 0.0456, wR_2 = 0.1483
Final R indexes [all data]	R_1 = 0.0640, wR_2 = 0.1987
Largest diff. peak/hole / e Å^{-3}	0.64/–0.96
Flack parameter	–0.04(6)

Table B2.35: Crystal data and structure refinement for MOX-2 at 1.18(3) GPa.

Empirical formula	$C_{10}H_8O_5Zn$
Formula weight / g mol^{-1}	273.53
Temperature / K	293(2)
Crystal system	orthorhombic
Space group	$P2_12_12_1$
a / Å	10.4499(2)
b / Å	11.64490(10)
c / Å	15.1281(2)
α / °	90
V / Å^3	1840.91(5)
Z	8
ρ_{calc} / g cm^{-3}	1.974
μ / mm^{-1}	0.937
F(000)	1104.0
Crystal size / mm^3	0.03 × 0.07 × 0.18
Radiation	(λ = 0.4859 Å)
2θ range for data collection / °	3.018 – 53.094
Index ranges	-12 $\leq h \leq$ 12, $-13 \leq k \leq 15, -22 \leq l \leq 22$
Reflections collected	10975
Independent reflections	4505[R_{int}=0.0491, R_{sigma}=0.0515]
Data/restraints/parameters	4505/0/261
Goodness-of-fit on F^2	1.167
Final R indexes [I>2sigma(I)]	R_1 = 0.0436, wR_2 = 0.1434
Final R indexes [all data]	R_1 = 0.0615, wR_2 = 0.1920
Largest diff. peak/hole / e Å^{-3}	0.65/–0.76
Flack parameter	0.00(4)

Table B2.36: Crystal data and structure refinement for MOX-2 at 1.42(2) GPa.

Empirical formula	$C_{10}H_8O_5Zn$
Formula weight / g mol^{-1}	273.53
Temperature / K	293(2)
Crystal system	orthorhombic
Space group	$P2_12_12_1$
a / Å	10.3998(2)
b / Å	11.5611(10)
c / Å	15.0947(2)
α / °	90
V / Å^3	1814.88(5)
Z	8
ρ_{calc} / g cm^{-3}	2.002
μ / mm^{-1}	0.950
F(000)	1104.0
Crystal size / mm^3	0.03 × 0.07 × 0.18
Radiation	(λ = 0.4859 Å)
2θ range for data collection / °	3.034 – 52.316
Index ranges	-12 $\leq h \leq$ 12, $-15 \leq k \leq$ 13, $-22 \leq l \leq$ 22
Reflections collected	10797
Independent reflections	4428[R_{int}=0.0504, R_{sigma}=0.0521]
Data/restraints/parameters	4428/0/261
Goodness-of-fit on F^2	1.177
Final R indexes [I>2sigma(I)]	R_1 = 0.0437, wR_2 = 0.1491
Final R indexes [all data]	R_1 = 0.0603, wR_2 = 0.1921
Largest diff. peak/hole / e Å^{-3}	0.78/–0.83
Flack parameter	0.04(5)

Table B2.37: Crystal data and structure refinement for MOX-2 at 1.77(7) GPa.

Empirical formula	$C_{10}H_8O_5Zn$
Formula weight / g mol^{-1}	273.53
Temperature / K	293(2)
Crystal system	orthorhombic
Space group	$P2_12_12_1$
a / Å	10.3353(2)
b / Å	11.44480(10)
c / Å	15.04550(10)
α / °	90
V / Å^3	1779.66(4)(5)
Z	8
ρ_{calc} / g cm^{-3}	2.042
μ / mm^{-1}	0.969
F(000)	1104.0
Crystal size / mm^3	0.03 × 0.07 × 0.18
Radiation	(λ = 0.4859 Å)
2θ range for data collection / °	3.056 – 52.222
Index ranges	-11 $\leq h \leq$ 11, $-15 \leq k \leq 13, -22 \leq l \leq 22$
Reflections collected	10584
Independent reflections	4315[R_{int}=0.0322, R_{sigma}=0.0296]
Data/restraints/parameters	4315/0/261
Goodness-of-fit on F^2	1.123
Final R indexes [I>2sigma(I)]	R_1 = 0.0392, wR_2 = 0.1138
Final R indexes [all data]	R_1 = 0.0442, wR_2 = 0.1264
Largest diff. peak/hole / e Å^{-3}	0.66/–0.87
Flack parameter	0.01(2)

Table B2.38: Crystal data and structure refinement for MOX-2 at 2.00(7) GPa.

Empirical formula	$C_{10}H_8O_5Zn$
Formula weight / g mol^{-1}	273.53
Temperature / K	293(2)
Crystal system	orthorhombic
Space group	$P2_12_12_1$
a / Å	10.2844(2)
b / Å	11.37550(10)
c / Å	15.00620(10)
α / °	90
V / Å^3	1755.58(4)
Z	8
ρ_{calc} / g cm^{-3}	2.070
μ / mm^{-1}	0.982
F(000)	1104.0
Crystal size / mm^3	0.03 × 0.07 × 0.18
Radiation	(λ = 0.4859 Å)
2θ range for data collection / °	3.072 – 51.994
Index ranges	-11 $\leq h \leq$ 11, $-15 \leq k \leq 12, -22 \leq l \leq 22$
Reflections collected	10501
Independent reflections	4218[R_{int}=0.0328, R_{sigma}=0.0338]
Data/restraints/parameters	4218/0/261
Goodness-of-fit on F^2	1.121
Final R indexes [I>2sigma(I)]	R_1 = 0.0386, wR_2 = 0.1193
Final R indexes [all data]	R_1 = 0.0446, wR_2 = 0.1261
Largest diff. peak/hole / e Å^{-3}	0.52/–0.82
Flack parameter	–0.015(17)

B2.2 MOX-4 single-crystal high-pressure data

Table B2.39: Crystal data and structure refinement for MOX-4 at 0.00 GPa.

Empirical formula	$C_8H_6O_5SZn$
Formula weight / g mol^{-1}	279.56
Temperature / K	293(2)
Crystal system	orthorhombic
Space group	$P2_12_12_1$
a / Å	10.093
b / Å	13.17250(10)
c / Å	15.0509(6)
α / °	90
V / Å^3	2001.08(8)
Z	8
ρ_{calc} / g cm^{-3}	1.856
μ / mm^{-1}	0.926
F(000)	1120.0
Crystal size / mm^3	0.02 × 0.07 × 0.18
Radiation	(λ = 0.4859 Å)
2θ range for data collection / °	3.938 – 52.926
Index ranges	-16 $\leq h \leq$ 18, $-19 \leq k \leq 22, -9 \leq l \leq 9$
Reflections collected	11745
Independent reflections	3873[R_{int}=0.0295, R_{sigma}=0.0279]
Data/restraints/parameters	3865/0/243
Goodness-of-fit on F^2	1.072
Final R indexes [I>2sigma(I)]	R_1 = 0.0231, wR_2 = 0.0668
Final R indexes [all data]	R_1 = 0.0238, wR_2 = 0.0670
Largest diff. peak/hole / e Å^{-3}	0.26/–0.42
Flack parameter	0.015(9)

Table B2.40: Crystal data and structure refinement for MOX-4 at 0.15(1) GPa.

Empirical formula	$C_8H_6O_5SZn$
Formula weight / g mol^{-1}	279.56
Temperature / K	293(2)
Crystal system	orthorhombic
Space group	$P2_12_12_1$
a / Å	10.147
b / Å	13.01130(10)
c / Å	14.7748(6)
α / °	90
V / Å^3	1950.58(8)
Z	8
ρ_{calc} / g cm^{-3}	1.904
μ / mm^{-1}	0.950
F(000)	1120.0
Crystal size / mm^3	0.02 × 0.07 × 0.18
Radiation	(λ = 0.4859 Å)
2θ range for data collection / °	3.958 – 52.372
Index ranges	-18 $\leq h \leq$ 16, $-22 \leq k \leq 19$, $-9 \leq l \leq 9$
Reflections collected	11473
Independent reflections	3751[R_{int}=0.0301, R_{sigma}=0.0270]
Data/restraints/parameters	3751/0/243
Goodness-of-fit on F^2	1.054
Final R indexes [I>2sigma(I)]	R_1 = 0.0237, wR_2 = 0.0702
Final R indexes [all data]	R_1 = 0.0247, wR_2 = 0.0706
Largest diff. peak/hole / e Å^{-3}	0.29/–0.38
Flack parameter	0.002(9)

Table B2.41: Crystal data and structure refinement for MOX-4 at 0.24(2) GPa.

Empirical formula	$C_8H_6O_5SZn$
Formula weight / g mol^{-1}	279.56
Temperature / K	293(2)
Crystal system	orthorhombic
Space group	$P2_12_12_1$
a / Å	10.166
b / Å	12.95590(10)
c / Å	14.6643(6)
α / °	90
V / Å^3	1931.35(8)
Z	8
ρ_{calc} / g cm^{-3}	1.923
μ / mm^{-1}	0.960
F(000)	1120.0
Crystal size / mm^3	0.02 × 0.07 × 0.18
Radiation	(λ = 0.4859 Å)
2θ range for data collection / °	3.966 – 52.432
Index ranges	-18 $\leq h \leq$ 16, $-22 \leq k \leq 18, -9 \leq l \leq 9$
Reflections collected	11392
Independent reflections	3711[R_{int}=0.0288, R_{sigma}=0.0257]
Data/restraints/parameters	3711/0/243
Goodness-of-fit on F^2	1.101
Final R indexes [I>2sigma(I)]	R_1 = 0.0248, wR_2 = 0.0714
Final R indexes [all data]	R_1 = 0.0255, wR_2 = 0.00717
Largest diff. peak/hole / e Å^{-3}	0.29/–0.38
Flack parameter	0.001(10)

Table B2.42: Crystal data and structure refinement for MOX-4 at 0.44(3) GPa.

Empirical formula	$C_8H_6O_5SZn$
Formula weight / g mol^{-1}	279.56
Temperature / K	293(2)
Crystal system	orthorhombic
Space group	$P2_12_12_1$
a / Å	10.20580(10)
b / Å	12.84260(10)
c / Å	14.4108(6)
α / °	90
V / Å^3	1888.81(8)
Z	8
ρ_{calc} / g cm^{-3}	1.966
μ / mm^{-1}	0.981
F(000)	1120.0
Crystal size / mm^3	0.02 × 0.07 × 0.18
Radiation	(λ = 0.4859 Å)
2θ range for data collection / °	3.984 – 52.374
Index ranges	-18 $\leq h \leq$ 17, $-18 \leq k \leq 22$, $-9 \leq l \leq 9$
Reflections collected	11141
Independent reflections	3628[R_{int}=0.0290, R_{sigma}=0.0266]
Data/restraints/parameters	3628/0/243
Goodness-of-fit on F^2	1.090
Final R indexes [I>2sigma(I)]	R_1 = 0.0254, wR_2 = 0.0739
Final R indexes [all data]	R_1 = 0.0263, wR_2 = 0.0746
Largest diff. peak/hole / e Å^{-3}	0.30/–0.40
Flack parameter	0.006(8)

Table B2.43: Crystal data and structure refinement for MOX-4 at 0.6 GPa.

Empirical formula	$C_8H_6O_5SZn$
Formula weight / g mol^{-1}	279.56
Temperature / K	293(2)
Crystal system	orthorhombic
Space group	$P2_12_12_1$
a / Å	10.22500(10)
b / Å	12.78550(10)
c / Å	14.2735(8)
α / °	90
V / Å^3	1866.00(11)
Z	8
ρ_{calc} / g cm^{-3}	1.990
μ / mm^{-1}	0.993
F(000)	1120.0
Crystal size / mm^3	0.02 × 0.07 × 0.18
Radiation	(λ = 0.4859 Å)
2θ range for data collection / °	3.35 – 52.136
Index ranges	-17 $\leq h \leq$ 18, $-22 \leq k \leq 18, -9 \leq l \leq 9$
Reflections collected	10986
Independent reflections	3572[R_{int}=0.0283, R_{sigma}=0.0261]
Data/restraints/parameters	3572/0/243
Goodness-of-fit on F^2	1.097
Final R indexes [I>2sigma(I)]	R_1 = 0.0282, wR_2 = 0.0838
Final R indexes [all data]	R_1 = 0.0293, wR_2 = 0.0844
Largest diff. peak/hole / e Å^{-3}	0.36/–0.52
Flack parameter	0.008(9)

Table B2.44: Crystal data and structure refinement for MOX-4 at 0.92(4) GPa.

Empirical formula	$C_8H_6O_5SZn$
Formula weight / g mol^{-1}	279.56
Temperature / K	293(2)
Crystal system	orthorhombic
Space group	$P2_12_12_1$
a / Å	10.261500(10)
b / Å	12.66300(10)
c / Å	14.0487(6)
α / °	90
V / Å^3	1825.51(8)
Z	8
ρ_{calc} / g cm^{-3}	2.034
μ / mm^{-1}	1.015
F(000)	1120.0
Crystal size / mm^3	0.02 × 0.07 × 0.18
Radiation	(λ = 0.4859 Å)
2θ range for data collection / °	3.36 – 52.39
Index ranges	-17 $\leq h \leq$ 18, $-18 \leq k \leq 22$, $-9 \leq l \leq 9$
Reflections collected	10780
Independent reflections	3519[R_{int}=0.0298, R_{sigma}=0.0266]
Data/restraints/parameters	3519/0/243
Goodness-of-fit on F^2	1.091
Final R indexes [I>2sigma(I)]	R_1 = 0.0255, wR_2 = 0.0736
Final R indexes [all data]	R_1 = 0.0263, wR_2 = 0.0741
Largest diff. peak/hole / e Å^{-3}	0.31/–0.44
Flack parameter	-0.004(9)

Table B2.45: Crystal data and structure refinement for MOX-4 at 1.33(4) GPa.

Empirical formula	$C_8H_6O_5SZn$
Formula weight / g mol^{-1}	279.56
Temperature / K	293(2)
Crystal system	orthorhombic
Space group	$P2_12_12_1$
a / Å	10.288
b / Å	12.54640(10)
c / Å	13.8496(6)
α / °	90
V / Å^3	1787.63(8)
Z	8
ρ_{calc} / g cm^{-3}	2.077
μ / mm^{-1}	1.037
F(000)	1120.0
Crystal size / mm^3	0.02 × 0.07 × 0.18
Radiation	(λ = 0.4859 Å)
2θ range for data collection / °	3.5 – 52.096
Index ranges	-17 $\leq h \leq$ 18, $-21 \leq k \leq 18, -8 \leq l \leq 9$
Reflections collected	10579
Independent reflections	3483[R_{int}=0.0270, R_{sigma}=0.0233]
Data/restraints/parameters	3483/0/243
Goodness-of-fit on F^2	1.038
Final R indexes [I>2sigma(I)]	R_1 = 0.0254, wR_2 = 0.0741
Final R indexes [all data]	R_1 = 0.0258, wR_2 = 0.0744
Largest diff. peak/hole / e Å^{-3}	0.30/–0.41
Flack parameter	0.010(9)

Table B2.46: Crystal data and structure refinement for MOX-4 at 1.46(6) GPa.

Empirical formula	$C_8H_6O_5SZn$
Formula weight / g mol^{-1}	279.56
Temperature / K	293(2)
Crystal system	orthorhombic
Space group	$P2_12_12_1$
a / Å	10.29620(10)
b / Å	12.49720(10)
c / Å	13.7711(6)
α / °	90
V / Å^3	1771.98(8)
Z	8
ρ_{calc} / g cm^{-3}	2.096
μ / mm^{-1}	1.046
F(000)	1120.0
Crystal size / mm^3	0.02 × 0.07 × 0.18
Radiation	(λ = 0.4859 Å)
2θ range for data collection / °	3.376 – 52.078
Index ranges	-18 $\leq h \leq$ 17, $-18 \leq k \leq 22$, $-8 \leq l \leq 8$
Reflections collected	10509
Independent reflections	3461[R_{int}=0.0298, R_{sigma}=0.0262]
Data/restraints/parameters	3461/0/243
Goodness-of-fit on F^2	1.072
Final R indexes [I>2sigma(I)]	R_1 = 0.0273, wR_2 = 0.0806
Final R indexes [all data]	R_1 = 0.0278, wR_2 = 0.0809
Largest diff. peak/hole / e Å^{-3}	0.42/–0.43
Flack parameter	–0.008(9)

Table B2.47: Crystal data and structure refinement for MOX-4 at 1.62 GPa.

Empirical formula	$C_8H_6O_5SZn$
Formula weight / g mol^{-1}	279.56
Temperature / K	293(2)
Crystal system	orthorhombic
Space group	$P2_12_12_1$
a / Å	10.302
b / Å	12.44850(10)
c / Å	13.6986(5)
α / °	90
V / Å^3	1756.77(7)
Z	8
ρ_{calc} / g cm^{-3}	2.114
μ / mm^{-1}	1.055
F(000)	1120.0
Crystal size / mm^3	0.02 × 0.07 × 0.18
Radiation	(λ = 0.4859 Å)
2θ range for data collection / °	3.508 – 53.286
Index ranges	-17 $\leq h \leq$ 18, $-22 \leq k \leq 18, -8 \leq l \leq 8$
Reflections collected	10430
Independent reflections	3439[R_{int}=0.0301, R_{sigma}=0.0266]
Data/restraints/parameters	3439/0/243
Goodness-of-fit on F^2	1.050
Final R indexes [I>2sigma(I)]	R_1 = 0.0273, wR_2 = 0.0789
Final R indexes [all data]	R_1 = 0.0278, wR_2 = 0.0793
Largest diff. peak/hole / e Å^{-3}	0.38/–0.38
Flack parameter	–0.006(9)

Table B2.48: Crystal data and structure refinement for MOX-4 at 1.79 GPa.

Empirical formula	$C_8H_6O_5SZn$
Formula weight / g mol^{-1}	279.56
Temperature / K	293(2)
Crystal system	orthorhombic
Space group	$P2_12_12_1$
a / Å	10.309
b / Å	12.39680(10)
c / Å	13.6248(5)
α / °	90
V / Å^3	1741.28(7)
Z	8
ρ_{calc} / g cm^{-3}	2.133
μ / mm^{-1}	1.064
F(000)	1120.0
Crystal size / mm^3	0.02 × 0.07 × 0.18
Radiation	(λ = 0.4859 Å)
2θ range for data collection / °	3.512 – 52.034
Index ranges	-17 $\leq h \leq$ 18, $-18 \leq k \leq 21$, $-8 \leq l \leq 8$
Reflections collected	10307
Independent reflections	3416[R_{int}=0.0274, R_{sigma}=0.0238]
Data/restraints/parameters	3416/0/243
Goodness-of-fit on F^2	1.066
Final R indexes [I>2sigma(I)]	R_1 = 0.0285, wR_2 = 0.0813
Final R indexes [all data]	R_1 = 0.0292, wR_2 = 0.0818
Largest diff. peak/hole / e Å^{-3}	0.46/–0.42
Flack parameter	–0.008(10)

Table B2.49: Crystal data and structure refinement for MOX-4 at 2.09 GPa.

Empirical formula	$C_8H_6O_5SZn$
Formula weight / g mol^{-1}	279.56
Temperature / K	293(2)
Crystal system	orthorhombic
Space group	$P2_12_12_1$
a / Å	10.322
b / Å	12.30560(10)
c / Å	13.4999(5)
α / °	90
V / Å^3	1714.79(7)
Z	8
ρ_{calc} / g cm^{-3}	2.166
μ / mm^{-1}	1.081
F(000)	1120.0
Crystal size / mm^3	0.02 × 0.07 × 0.18
Radiation	(λ = 0.4859 Å)
2θ range for data collection / °	3.386 – 52.034
Index ranges	-18 $\leq h \leq$ 17, $-18 \leq k \leq 21, -8 \leq l \leq 8$
Reflections collected	10157
Independent reflections	3367[R_{int}=0.0281, R_{sigma}=0.0234]
Data/restraints/parameters	3367/0/243
Goodness-of-fit on F^2	1.066
Final R indexes [I>2sigma(I)]	R_1 = 0.0306, wR_2 = 0.0856
Final R indexes [all data]	R_1 = 0.0312, wR_2 = 0.0859
Largest diff. peak/hole / e Å^{-3}	0.49/–0.49
Flack parameter	–0.013(9)

B2.3 Structural changes

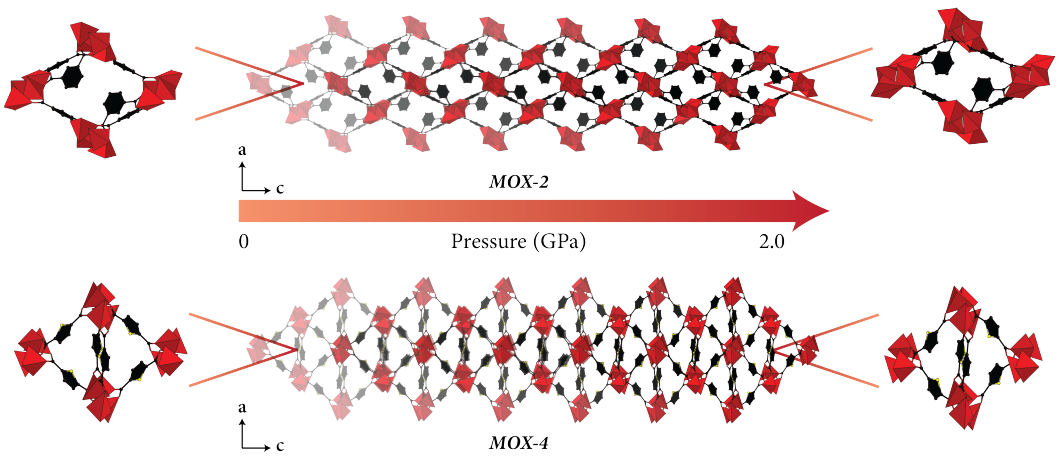

Figure B2.6: Structural changes of MOX-2 (top) and MOX-4 (bottom) as derived from high-pressure SCXRD, showing the wine-rack structure in the ac-plane.

Appendix C: Chapter 7 supplementary information

C1 MOF-5 preparation

C1.1 Synthesis

Single crystals of MOF-5 were synthesised following the method of Ref. [88]. Solutions of $Zn(NO_3)2 \cdot 6\ H_2O$ (0.1 mmol) and 1,4-bdc (0.1 mmol) in dried N,N-diethylformamide (1 mL and 3 mL, respectively) were combined and the resulting mixture placed in a teflon-lined solvothermal vial. The vial was heated to 100 °C for a period of 48 h. On cooling back to room temperature, the vial contained colourless cubic crystals of MOF-5. The crystals were washed three times with dichloromethane. Each washing cycle involved soaking MOF-5 crystals in fresh chloroform for 24 h, followed by filtration.

C1.2 Powder X-ray diffraction

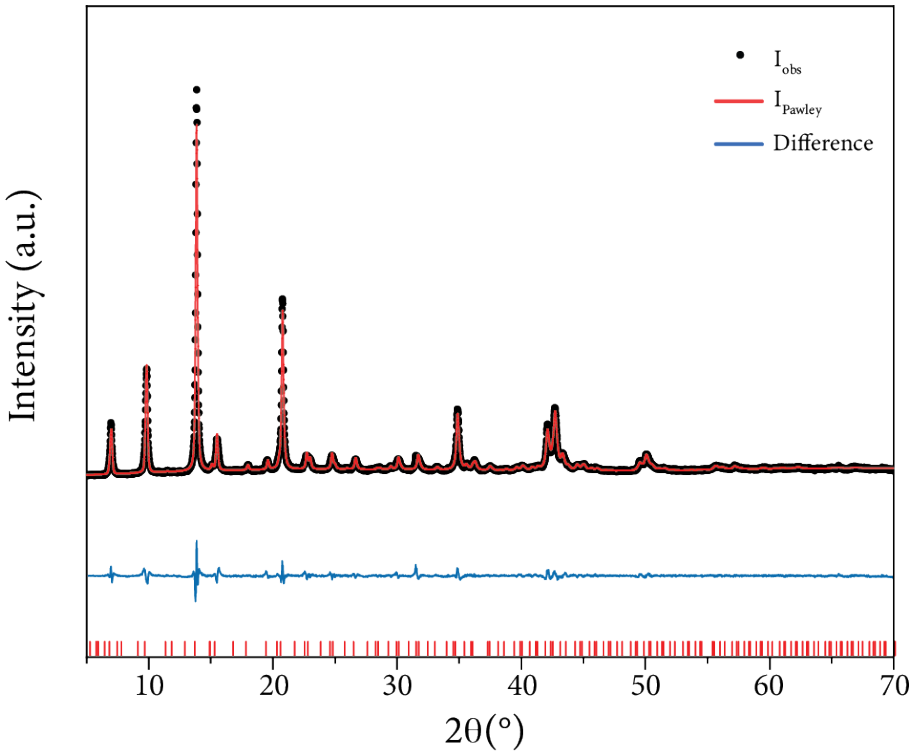

Figure C1.7: Pawley refinement of MOF-5 powder sample, showing an excellent fit. This confirmed the purity and phase of MOF-5, thus suitability for comparison to TRUMOF-1.

C2 EXAFS

EXAFS measurements were performed on TRUMOF-1 and MOF-5 as well as on MOX-3 and MOX-4, performing the same data preparation and collection as outlined in Chapter 2. The reason for also measuring the absorption spectra of MOX-3 and MOX-4 was to ensure that different Zn environments would result in a lower Pearson correlation constant, which is the case (Table C2.50). This result further confirms that the Zn environments of MOF-5 and TRUMOF-1 are very similar.

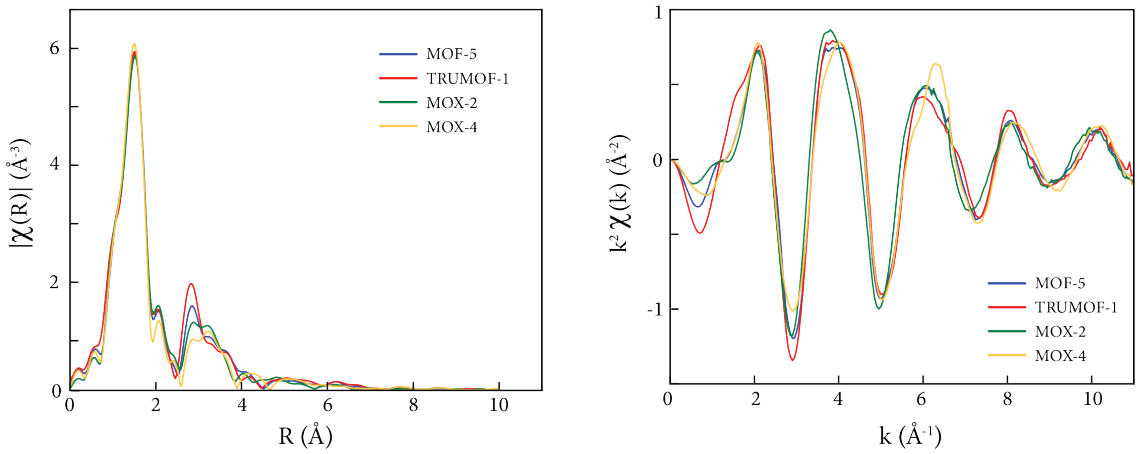

Figure C2.8: Zn K-edge EXAFS measurements and derived functions of MOF-5, TRUMOF-1. MOX-3, and MOX-4.

Table C2.50: Pearson correlation functions calculated from EXAFS data, comparing TRUMOF-1, MOX-3 and MOX-4 to MOF-5.

EXAFS function	Range	TRUMOF-1	MOX-3	MOX-4
$\chi(\mathrm{R})k^3$	$2.4 < \mathrm{R} < 5.5$	0.965	0.876	0.825
$\chi(k)$	full range	0.985	0.963	0.983

C3 Heat of adsorption

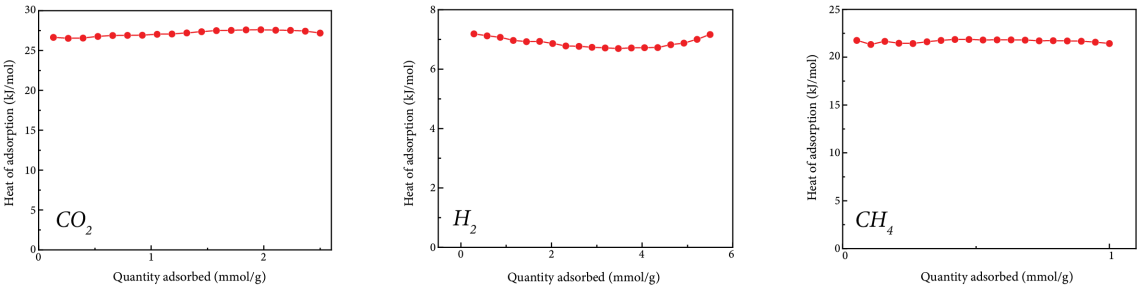

Figure C3.9: Heat of adsorption of TRUMOF-1 as a function of gas quantity adsorbed.

C4 Atomic displacement parameters

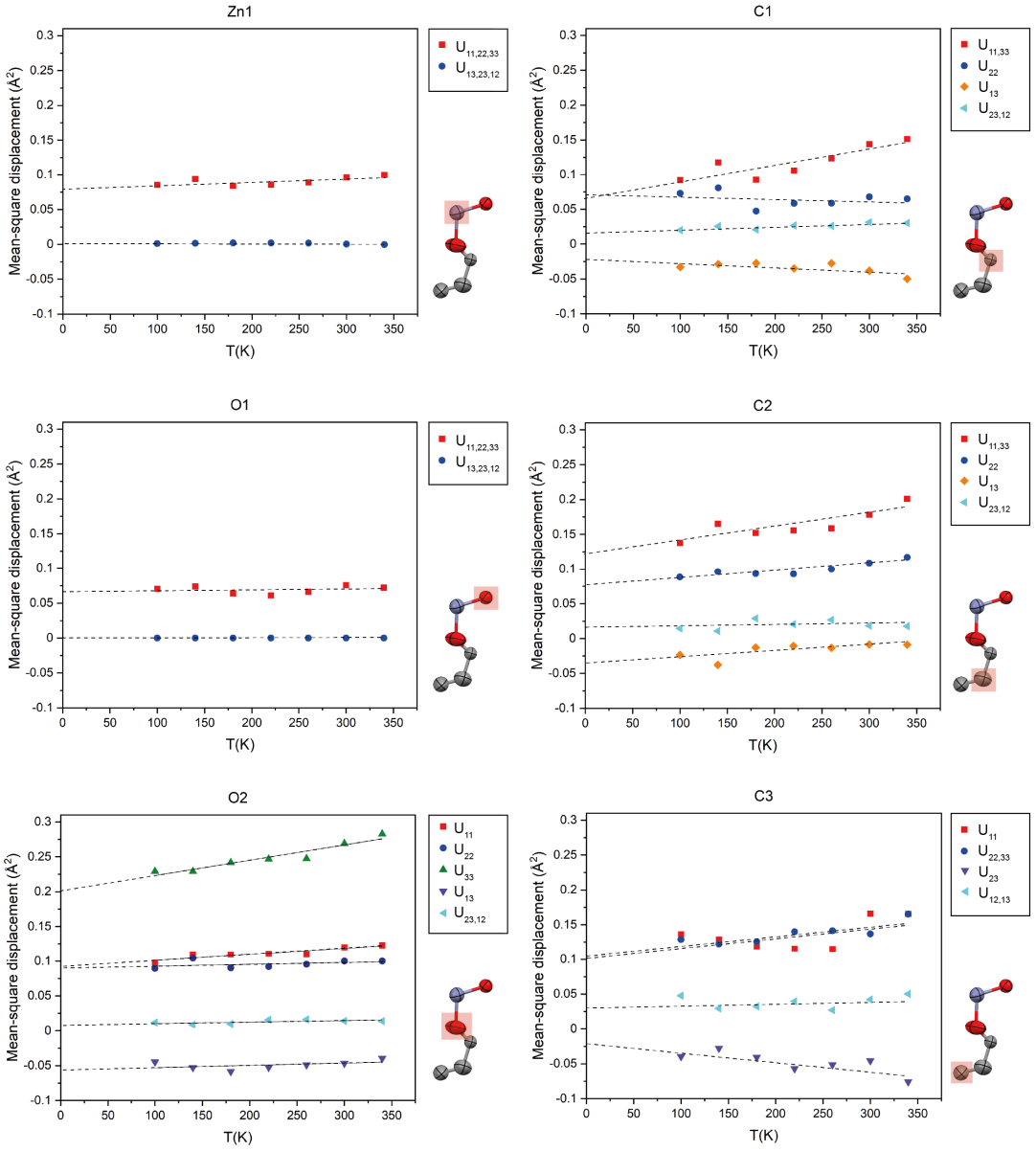

Figure C4.10: U(T) plots used to derive experimental U_{ij} values presented in Fig. 7.9 for all atoms in the asymmetric unit.

C5 High-pressure diffraction data

C5.1 Crystallographic tables

Table C5.51: Crystal data and structure refinement for TRUMOF-1 at 0.11 GPa.

Empirical formula	C_{24} H_9 O_{13} S_2 Zn_4
Formula weight / g mol^{-1}	766.79
Temperature / K	293(2)
Crystal system	cubic
Space group	F$\bar{4}$3m
a / Å	15.4042(4)
α / °	90
V / Å^3	3655.3(3)
Z	4
ρ_{calc} / g cm^{-3}	1.393
μ / mm^{-1}	0.921
F(000)	1508.0
Crystal size / mm^3	0.16 × 0.125 × 0.05
Radiation	synchrotron (λ = 0.4859 Å)
2θ range for data collection / °	3.13 – 35.37
Index ranges	$-19 \leq h \leq 19, -12 \leq k \leq 12, -19 \leq l \leq 19$
Reflections collected	3384
Independent reflections	426[R_{int}=0.01097, R_{sigma}=0.0598]
Data/restraints/parameters	426/12/29
Goodness-of-fit on F^2	1.174
Final R indexes [I>2sigma(I)]	R_1 = 0.0517, wR_2 = 0.1858
Final R indexes [all data]	R_1 = 0.0586, wR_2 = 0.1936
Largest diff. peak/hole / e Å^{-3}	0.48/–0.19
Flack parameter	0.0(3)

Table C5.52: Crystal data and structure refinement for TRUMOF-1 at 0.30(3) GPa.

Empirical formula	C_{24} H_9 O_{13} S_2 Zn_4
Formula weight / g mol^{-1}	766.79
Temperature / K	293(2)
Crystal system	cubic
Space group	$F\bar{4}3m$
a / Å	15.2819(6)
α / °	90
V / $Å^3$	3568.6(4)
Z	4
ρ_{calc} / g cm^{-3}	1.427
μ / mm^{-1}	0.943
F(000)	1508.0
Crystal size / mm^3	0.16 × 0.125 × 0.055
Radiation	Synchrotron (λ = 0.4859 Å)
2θ range for data collection / °	3.156 – 35.314
Index ranges	-19 ≤ h ≤ 19, −12 ≤ k ≤ 12, −19 ≤ l ≤ 19
Reflections collected	2695
Independent reflections	419[R_{int}=0.1105, R_{sigma}=0.0918]
Data/restraints/parameters	419/6/17
Goodness-of-fit on F^2	0.991
Final R indexes [I>2sigma(I)]	R_1 = 0.0668, wR_2 = 0.1719
Final R indexes [all data]	R_1 = 0.0844, wR_2 = 0.1907
Largest diff. peak/hole / e $Å^{-3}$	0.47/–0.37
Flack parameter	–0.1(4)

Table C5.53: Crystal data and structure refinement for TRUMOF-1 at 0.59(1) GPa.

Empirical formula	C_{24} H_9 O_{13} S_2 Zn_4
Formula weight / g mol^{-1}	766.79
Temperature / K	293(2)
Crystal system	cubic
Space group	$F\bar{4}3m$
a / Å	15.1599(6)
α / °	90
V / $Å^3$	3484(14)
Z	4
ρ_{calc} / g cm^{-3}	1.462
μ / mm^{-1}	0.966
F(000)	1508.0
Crystal size / mm^3	0.16 × 0.125 × 0.05
Radiation	Synchrotron (λ = 0.4859 Å)
2θ range for data collection / °	3.182 – 35.2
Index ranges	$-18 \leq h \leq 18, -12 \leq k \leq 12, -18 \leq l \leq 18$
Reflections collected	2627
Independent reflections	404[R_{int}=0.1646, R_{sigma}=0.0953]
Data/restraints/parameters	404/6/29
Goodness-of-fit on F^2	0.976
Final R indexes [I>2sigma(I)]	R_1 = 0.0864, wR_2 = 0.2197
Final R indexes [all data]	R_1 = 0.1153, wR_2 = 0.2554
Largest diff. peak/hole / e $Å^{-3}$	0.48/–0.17
Flack parameter	–0.3(7)

Table C5.54: Crystal data and structure refinement for TRUMOF-1 at 0.73(2) GPa.

Empirical formula	C_{24} H_9 O_{13} S_2 Zn_4
Formula weight / g mol^{-1}	766.79
Temperature / K	293(2)
Crystal system	cubic
Space group	$F\bar{4}3m$
a / Å	15.0989(6)
α / °	90
V / $Å^3$	3442(4)
Z	4
ρ_{calc} / g cm^{-3}	1.480
μ / mm^{-1}	0.978
F(000)	1508.0
Crystal size / mm^3	0.16 × 0.125 × 0.05
Radiation	Synchrotron (λ = 0.4859 Å)
2θ range for data collection / °	3.194 – 35.348
Index ranges	-18 ≤ h ≤ 18, −12 ≤ k ≤ 12, −18 ≤ l ≤ 18
Reflections collected	3296
Independent reflections	405[R_{int}=0.2261, R_{sigma}=0.2165]
Data/restraints/parameters	405/6/17
Goodness-of-fit on F^2	0.862
Final R indexes [I>2sigma(I)]	R_1 = 0.0926, wR_2 = 0.1806
Final R indexes [all data]	R_1 = 0.1246, wR_2 = 0.2068
Largest diff. peak/hole / e $Å^{-3}$	0.50/–0.19
Flack parameter	0.3(5)

Table C5.55: Crystal data and structure refinement for TRUMOF-1 at 1.14(5) GPa.

Empirical formula	C_{24} H_9 O_{13} S_2 Zn_4
Formula weight / g mol^{-1}	766.79
Temperature / K	293(2)
Crystal system	cubic
Space group	$F\bar{4}3m$
a / Å	14.9164(10)
α / °	90
V / $Å^3$	3318.9(7)
Z	4
ρ_{calc} / g cm^{-3}	1.535
μ / mm^{-1}	1.014
F(000)	1508.0
Crystal size / mm^3	0.16 × 0.125 × 0.05
Radiation	Synchrotron (λ = 0.4859 Å)
2θ range for data collection / °	3.234 – 35.324
Index ranges	-18 ≤ h ≤ 18, −18 ≤ k ≤ 18, −12 ≤ l ≤ 11
Reflections collected	2431
Independent reflections	391[R_{int}=0.1754, R_{sigma}=0.1013]
Data/restraints/parameters	391/6/17
Goodness-of-fit on F^2	0.860
Final R indexes [I>2sigma(I)]	R_1 = 0.0901, wR_2 = 0.2562
Final R indexes [all data]	R_1 = 0.1369, wR_2 = 0.3237
Largest diff. peak/hole / e $Å^{-3}$	0.68/–0.28
Flack parameter	0.6(7)

Table C5.56: Crystal data and structure refinement for TRUMOF-1 at 1.35(6) GPa.

Empirical formula	C_{24} H_9 O_{13} S_2 Zn_4
Formula weight / g mol^{-1}	766.79
Temperature / K	293(2)
Crystal system	cubic
Space group	$F\bar{4}3m$
a / Å	14.8504(12)
α / °	90
V / $Å^3$	3275.0(8)
Z	4
ρ_{calc} / g cm^{-3}	1.555
μ / mm^{-1}	1.028
F(000)	1508.0
Crystal size / mm^3	0.16 × 0.125 × 0.05
Radiation	Synchrotron (λ = 0.4859 Å)
2θ range for data collection / °	3.248 – 28.022
Index ranges	-14 ≤ h ≤ 14, −10 ≤ k ≤ 10, −14 ≤ l ≤ 14
Reflections collected	1618
Independent reflections	214[R_{int}=0.5834, R_{sigma}=0.4449]
Data/restraints/parameters	214/7/17
Goodness-of-fit on F^2	1.016
Final R indexes [I>2sigma(I)]	R_1 = 0.1726, wR_2 = 0.2684
Final R indexes [all data]	R_1 = 0.1882, wR_2 = 0.3179
Largest diff. peak/hole / e $Å^{-3}$	0.75/–0.24
Flack parameter	–1.3(10)

Table C5.57: Crystal data and structure refinement for TRUMOF-1 at 1.47(4) GPa.

Empirical formula	C_{24} H_9 O_{13} S_2 Zn_4
Formula weight / g mol^{-1}	766.79
Temperature / K	293(2)
Crystal system	cubic
Space group	$F\bar{4}3m$
a / Å	14.7948(14)
α / °	90
V / $Å^3$	3238.3(9)
Z	4
ρ_{calc} / g cm^{-3}	1.573
μ / mm^{-1}	1.040
F(000)	1508.0
Crystal size / mm^3	0.16 × 0.125 × 0.05
Radiation	Synchrotron (λ = 0.4859 Å)
2θ range for data collection / °	3.26 – 27.932
Index ranges	-14 $\leq h \leq$ 14, $-14 \leq k \leq 14, -10 \leq l \leq 10$
Reflections collected	1310
Independent reflections	208[R_{int}=0.4486, R_{sigma}=0.3995]
Data/restraints/parameters	208/7/17
Goodness-of-fit on F^2	1.029
Final R indexes [I>2sigma(I)]	R_1 = 0.1614, wR_2 = 0.3796
Final R indexes [all data]	R_1 = 0.1751, wR_2 = 0.4208
Largest diff. peak/hole / e $Å^{-3}$	0.40/–0.27
Flack parameter	–1(2)

Table C5.58: Crystal data and structure refinement for TRUMOF-1 at 1.66(1) GPa.

Empirical formula	C_{24} H_9 O_{13} S_2 Zn_4
Formula weight / g mol^{-1}	766.79
Temperature / K	293(2)
Crystal system	cubic
Space group	$F\bar{4}3m$
a / Å	14.7629(14)
α / °	90
V / $Å^3$	3217.5(9)
Z	4
ρ_{calc} / g cm^{-3}	1.583
μ / mm^{-1}	1.046
F(000)	1508.0
Crystal size / mm^3	0.16 × 0.125 × 0.05
Radiation	Synchrotron (λ = 0.4859 Å)
2θ range for data collection / °	3.266 – 21.46
Index ranges	$-8 \leq h \leq 8, -11 \leq k \leq 11, -11 \leq l \leq 11$
Reflections collected	643
Independent reflections	101[R_{int}=0.4891, R_{sigma}=0.3422]
Data/restraints/parameters	101/7/17
Goodness-of-fit on F^2	1.261
Final R indexes [I>2sigma(I)]	R_1 = 0.1663, wR_2 = 0.3257
Final R indexes [all data]	R_1 = 0.1676, wR_2 = 0.3476
Largest diff. peak/hole / e $Å^{-3}$	0.66/–0.54
Flack parameter	1.5(18)

Table C5.59: Crystal data and structure refinement for TRUMOF-1 at 1.81(2) GPa.

Empirical formula	C_{24} H_9 O_{13} S_2 Zn_4
Formula weight / g mol^{-1}	766.79
Temperature / K	293(2)
Crystal system	cubic
Space group	$F\bar{4}3m$
a / Å	14.7185(16)
α / °	90
V / $Å^3$	3188.5(10)
Z	4
ρ_{calc} / g cm^{-3}	1.597
μ / mm^{-1}	1.056
F(000)	1508.0
Crystal size / mm^3	0.16 × 0.125 × 0.05
Radiation	Synchrotron (λ = 0.4859 Å)
2θ range for data collection / °	3.276 – 21.526
Index ranges	$-11 \leq h \leq 11, -7 \leq k \leq 7, -11 \leq l \leq 11$
Reflections collected	640
Independent reflections	101[R_{int}=0.2467, R_{sigma}=0.2442]
Data/restraints/parameters	101/7/17
Goodness-of-fit on F^2	1.613
Final R indexes [I>2sigma(I)]	R_1 = 0.1204, wR_2 = 0.3643
Final R indexes [all data]	R_1 = 0.1244, wR_2 = 0.3800
Largest diff. peak/hole / e $Å^{-3}$	0.66/–0.23
Flack parameter	1(2)

C5.2 High-pressure behaviour

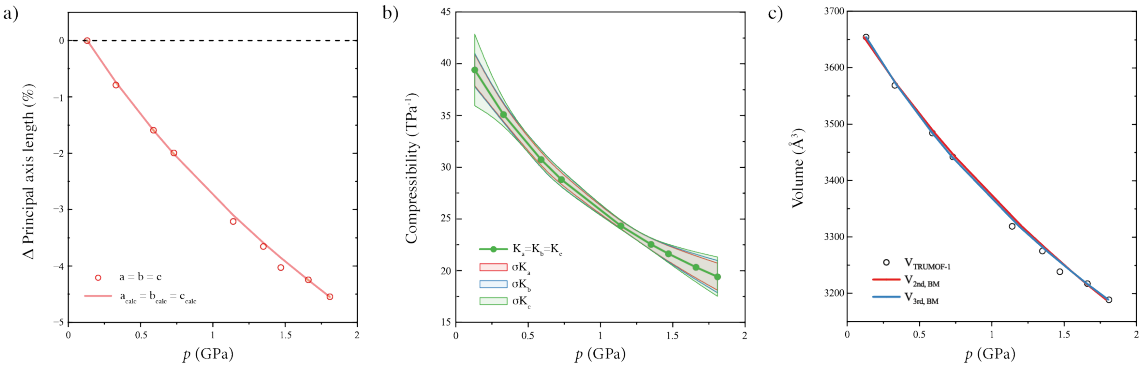

Figure C5.11: Analysis of high-pressure data TRUMOF-1. Change in (a) principal axes length; (b) compressibility; and (c) volume as a function of pressure.

C5.3 Solvent quantity

Table C5.60: TRUMOF-1 pore volume and contents as a function of pressure calculated by the solvent masking algorithm 'NoSphereA2' implemented by Olex2.

p (GPa)	V(Å^3)	no. of e$^-$	V/e$^-$ (Å^3)	DMF molecules / unit cell
0.13(1)	844	115	7.3	3
	104	40	2.6	1
0.33(6)	773	84	9.2	2
	112	40	2.8	1
0.59(1)	721	82	8.8	2
	100	40	2.5	1
0.73(2)	705	115	6.1	3
	88	28	3.1	1

C5.4 Orientationally dependent elastic moduli

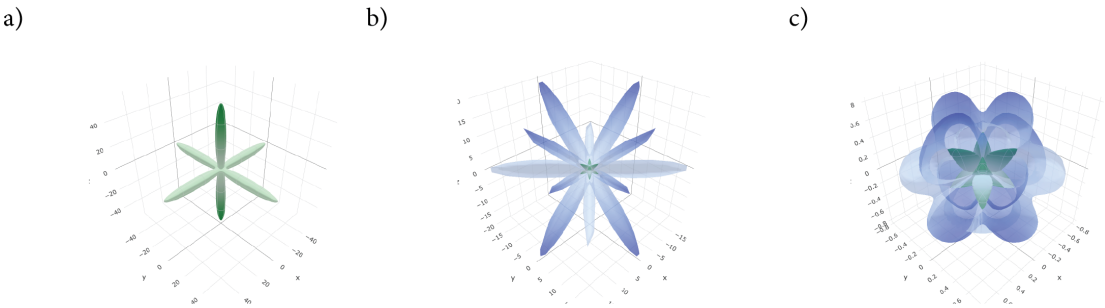

Figure C5.12: The (a) Young's modulus, (b) Shear modulus and (c) Poisson's ratio of MOF-5, as calculated using the ELATE code [295].

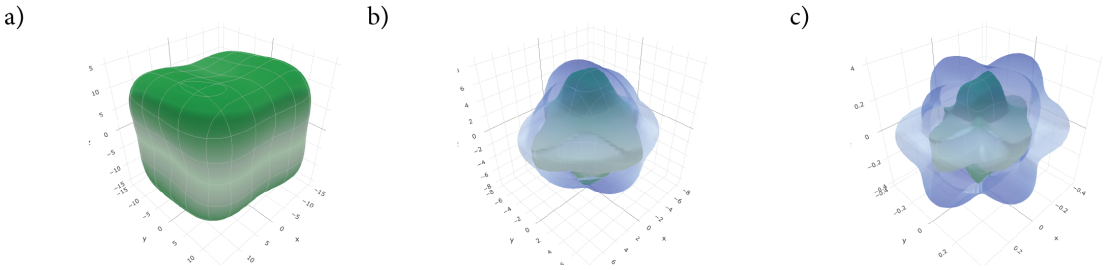

Figure C5.13: The (a) Young's modulus, (b) Shear modulus and (c) Poisson's ratio of TRUMOF-1, as calculated using the ELATE code [295].

Appendix D: Chapter 8 supplementary information

D1 Failed synthesis attempts

Table D1.61: Synthetic parameters for a representative selection of unsuccesful reactions with 1,3-bdc and 0.33 mmol $Zn(NO_3)_2 \cdot H_2O$ salt, at a fixed reaction time of 14 hours.

Linker name and quantity (mmol)	Reaction T (°)	Solvent	Comments
1,3-bdc (0.33)	100	DEF	Small crystals seemingly stuck together in a 'crust'
1,3-bdc (0.33)	110	THF	Red powder
1,3-bdc (0.33)	110	DMSO	No solid product
1,3-bdc (0.33)	110	Chloroform	Small quantity of single opaque crystals
1,3-bdc (0.33)	110	Ethanol	Powder
1,3-bdc (0.33)	110	DCM	Starting material
1,3-bdc (0.33)	110	Hexane	Small amount of powder
1,3-bdc (0.33)	110	Toluence	Starting product
1,3-bdc (0.33)	110	Acetone	Orange powder
1,3-bdc (0.33)	110	Methanol	Starting material

Table D1.62: Synthetic parameters for a representative selection of unsuccesful reactions with 1,3-bdc analogues and 0.33 mmol $Zn(NO_3)_2 \cdot H_2O$ salt, at a fixed reaction time of 14 hours.

Linker name and quantity (mmol)	Reaction T (°)	Solvent	Comments
5-Br-1,3-bdc (0.33)	110	DMF	Single crystals, but unstable in air
4,4'-cis-stilbene (0.33)	110	DMF	Intergrown crystals
4,4'-cis-stilbene (0.33) + acetic acid (20 μL) (0.33)	110	Chloroform	Small and needle-like intergrown crystals
4,4'-cis-stilbene (0.33)	100	DMF	Very small intergrown crystals
2,5-tdc (0.33)	110	Methanol	No solid product
2-I-1,3-bdc (0.33)	110	DMF	One large 'blob'
4,4'-cis-stilbene (0.66)	110	DMF	Intergrown crystals
4,4'-cis-stilbene (0.66) + acetic acid (20 μL)	110	Chloroform	Small and needle-like intergrown crystals
5-NO_2-1,3-bdc (0.33)	110	DMF	No solid product
5-CH_3-1,3-bdc (0.33)	110	DMF	No solid product
5-OH-1,3-bdc (0.33)	110	DMF	No solid product
5-Cl-1,3-bdc (0.33)	110	DMF	No solid product
5-I-1,3-bdc (0.33)	110	DMF	Orange powder
5-F-1,3-bdc (0.33)	110	DMF	No solid product
4,4'-cis-stilbene (0.33)	110	Ethyl acetate	Intergrown crystals
1,1':3',1"-Terphenyl-4,4"-dicarboxylic acid	110	DMF	Very large intergrown crystals
1,1':3',1"-Terphenyl-4,4"-dicarboxylic acid	110	Ethyl acetate	White powder
4,6-Br-1,3-bdc	110	Ethyl acetate	White powder